

NANOCLAY-BASED SELF-HEALING CORROSION PROTECTION COATINGS ON ALUMINUM ALLOYS

AA2024-T4 AND A356.0

THESIS

SUBMITTED IN PARTIAL FULFILMENT OF THE REQUIREMENTS

FOR THE AWARD OF THE DEGREE OF

Doctor of Philosophy

IN

CHEMISTRY

BY

MANASA SAMAVEDAM

(Roll. No: 715095)

RESEARCH SUPERVISORS

Dr. K. V. GOBI

Professor, NITW

Dr. R. SUBASRI

Scientist 'F', ARCI, Hyderabad



Department of Chemistry

NATIONAL INSTITUTE OF TECHNOLOGY, WARANGAL

WARANGAL – 506 004, TELANGANA, INDIA

JULY-2020

DECLARATION

This is to declare that the work presented in the thesis entitled "***Nanoclay-Based Self-Healing Corrosion Protection Coatings on Aluminum Alloys AA2024-T4 and A356.0***", is a bonafide work done by me under the supervision of **Dr. R. Subasri**, Scientist 'F', Centre for Sol-Gel Coatings, ARCI Hyderabad and **Prof. K. V. Gobi**, Professor, Department of Chemistry, NIT Warangal and was not submitted elsewhere for the award of any degree.

I declare that this written submission represents my ideas in my own words and where others' ideas or words have been included, I have adequately cited and referenced the original sources. I also declare that I have adhered to all principles of academic honesty and integrity and have not misrepresented or fabricated or falsified any idea/data/fact/source in my submission.

I understand that any violation of the above will be a cause for disciplinary action by the Institute and can also evoke penal action from the sources which have thus not been properly cited or from whom proper permission has not been taken when needed.



Date: 15-07-2020

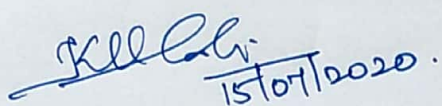
(S. MANASA)

Place: **HYDERABAD**

Roll Number: **715095**

CERTIFICATE

This is to certify that the work presented in the thesis entitled "*Nanoclay-Based Self-healing Corrosion Protection Coatings on Aluminum Alloys AA2024-T4 and A356.0*" is a bonafide work carried out by **Ms. S. Manasa** under our supervision and was not submitted elsewhere for the award of any degree.

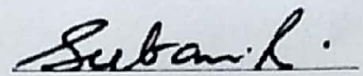


15/07/2020

Prof. K. V. GOBI

(Research Supervisor - Internal)

Professor
Department of Chemistry
NIT Warangal



Dr. R. SUBASRI

(Research Supervisor - External)

Scientist 'F'
Centre for Sol-Gel Coatings
ARCI Hyderabad

ACKNOWLEDGEMENTS

It is with immense pleasure that I express my deep sense of gratitude to my supervisors

Dr. R. Subasri ARCI, Hyderabad and **Prof. K. V. Gobi**, National Institute of Technology, Warangal for their inspiring guidance and invaluable cooperation in the course of my research. The fruitful discussions I had with them on the subject gave me the needed insight into the subject and were very helpful in the preparation of this thesis. I consider myself as very fortunate for being their student and it would have been impossible to achieve this goal without their support and care.

I am grateful to **The Directors**, International Advanced Research Centre for Powder metallurgy and New materials (ARCI), Hyderabad and National Institute of Technology, Warangal for giving me the opportunity to carry out the work and allowing me to submit in the form of thesis. I would like to thank the **Associate Directors**, ARCI, Hyderabad for their encouragement and constant support.

I greatly acknowledge **Science and Engineering Research Board (SERB), Govt. of India** for the financial support **under Grant number SB/S3/ME/007/2014**.

I express my gratitude to the Doctoral Scrutiny Committee members, namely **Prof. P. V. Srilakshmi**, Chairman and Head, Department of Chemistry, NIT Warangal and **Prof. A. Ramachandraiah**, Department of Chemistry, NIT Warangal, **Dr. A. Vishnu Shanker** Department of Chemistry, NIT Warangal and **Dr. Abdul Azeem**, Department of Physics, NIT Warangal for their insightful suggestions. I specially thank **Prof. B. V. Appa Rao, Retired Professor**, former DSC member, Department of Chemistry for his motivation, constant encouragement and valuable suggestions.

I would like to thank **Dr. S. Sathiyarayanan**, Senior Principal Scientist and **Dr. T. Siva**, Research Associate, CECRI, Karaikudi, Tamilnadu for carrying out and helping in the analysis of SVET measurements, **Dr. M. Ramakrishna**, Scientist-D for carrying out TEM

analysis, **Dr. N. Rajalakshmi**, Senior Scientist, CFCT Chennai and **Neha Y. Hebalkar**, Scientist-E for carrying out BET analysis, **Dr. B.V. Sarada**, Scientist-F for carrying out and data analysis of Micro-Raman studies, **Mrs. A. Jyothirmayi** Technical Officer (T.O)-D, for carrying out and helping me in analysis of electrochemical testing at initial stages of work, **Dr. N. Ravi**, Scientist-F and **Dr. K. Suresh**, Scientist-E for carrying out XRD analysis.

I also would like to thank **Mr. G. V. R Reddy**, T.O-D for helping in SEM analysis and **Mr. Ramesh Reddy** T.O-A, for XRD analysis. I specially thank **Mr. K. R. C. Soma Raju**, T.O-E, for carrying out the FESEM analysis.

I would like to thank the members of Centre for sol-gel coatings namely, **Mr. D. S. Reddy**, **Mr. K. S. Rao**, **Mr. J. V. Rao**, **Mr. B. S. Rao** and **Mr. Swapnil H. Adsul**, **Ms. Aarti Gautam**, **Dr. K. Pradeep Premkumar**, **Mr. Ramay Patra** for their friendly behaviour, encouragement and help throughout the research work.

I would like to thank all the faculty members from Chemistry Department, NIT Warangal namely, **Prof. V. Rajeswara Rao**, **Dr. Venkatathri Narayanan**, **Dr. B. Srinivas**, **Dr. K. Hari Prasad**, **Dr. D. Kasinath**, **Dr. Raghu Chitta**, **Dr. Ragha Sudha** and the **other faculty members** for their encouragement throughout the research work.

I convey my special thanks to the seniors **Dr. M. Satyanarayana**, **Dr. K. Vimal Kumar**, **Dr. K. Chaitanya Kumar** from NIT Warangal, for their help in understanding the basics of corrosion testing, continuous support and encouragement in each and every step of my research work. I specially thank **Nabormi Mukhopadhyay** and **S. Pavithra** from ARCI, Hyderabad for their guidance, support and encouragement in early stages of my research work.

I would like to thank my Seniors **Dr. K. Koteshwara Reddy**, **Dr. K. Yugendar Goud**, **V. Sunil Kumar**, **V. V. N. Phani Kumar**, my juniors **K. Shekar**, **K. Sampath Kumar** from NIT Warangal for their continuous support and encouragement

With all happiness I acknowledge the cheerful assistance rendered by all my research colleagues and friends *Mr. S. Suresh, Mrs. R. Hithavani, Mr. A. Madhu. Mr. Ch. Venu, Ms. J. Anitha, Mrs. B. Divya, Ms. Shaik Mubina, Ms. Ch. Prashanthi, Mr. T. Dhanunjay, Mrs. P. Soumya, Mr. Ch. Suman, Mr. G. Srinath, Mr. G. Sripal, Mr. G. Ambedkar* and other co-research scholars for their munificent support.

My heart goes to my beloved **Family Members** who with all their patience, prayers and faith in the Almighty, waited all these long years to see me reaching this stage. Their blessings and care always gave me new fervour and gusto to do something more with perfection.

Finally, I am very much grateful to Almighty, whose abundant grace and spiritual blessings gave me strength and courage to complete my research endeavour successfully.

I always remember and cherish the encouragement and inspiration provided by all my friends and well-wishers during the course of my research work.

A handwritten signature in blue ink, appearing to read "Manasa".

Date: 15-07-2020

S. Manasa

TABLE OF CONTENTS

CHAPTER-1

INTRODUCTION

1.1 Aluminum and its alloys.....	1
1.2 Corrosion in aluminum alloys	3
1.2.1 Types of corrosion	4
1.2.1.1 Pitting corrosion.....	4
1.2.2 Corrosion mechanism in aluminum alloys	5
1.3 Protection of aluminum alloys by surface treatment	6
1.4 Sol-Gel Coatings.....	7
1.4.1 Background of sol-gel process.....	8
1.4.2 Chemistry of sol-gel process.....	9
1.4.3 Advantages of sol-gel coatings	10
1.5 Corrosion inhibitors.....	11
1.6 Sol-gel coatings for Corrosion Protection.....	12
1.7 Self-Healing Coatings	14
1.7.1 Theory of self-healing.....	15
1.7.2 Smart nanocontainers for Self-Healing.....	16
1.7.2.1 Polymeric microcapsules	16
1.7.2.2 Layered double hydroxides.....	18
1.7.2.3. Carbon nanotubes.....	20
1.7.2.4 Halloysite nanotubes	21
1.7.2.5. Montmorillonite nanoclay	27
Objectives of the present work	29
References	31

CHAPTER-2

EXPERIMENTAL

2.1 Synthesis of Matrix sol	44
2.2 Preparation of HNT based Self-healing sol.....	44

2.2.1 Loading of corrosion inhibitors into HNTs and stoppering of loaded HNTs	45
2.2.2 Etching of HNTs	46
2.3 Loading of corrosion inhibitors into MMTs	46
2.4 Preparation of composite sol.....	47
2.5 Substrate cleaning, coating and curing.....	47
2.6 Characterization Techniques.....	48
2.6.1 Electron Microscopy	48
2.6.2 X-ray diffraction studies	49
2.6.3 Fourier Transform-Infrared (FT-IR) spectroscopy	49
2.6.4 Brunauer–Emmett–Teller (BET) surface area and pore volume analysis.	49
2.6.5 Adhesion Test	50
2.6.6 Electrochemical characterization	51
2.6.6.1 Electrochemical impedance spectroscopic (EIS) and Potentiodynamic polarization studies	51
2.6.6.2 Scanning Vibrating Electrode Technique analysis	53
2.6.7 Salt immersion and Salt spray test	54
2.6.8 Weight loss analysis.....	55
2.6.9 Micro-Raman spectroscopic analysis	55
References	57

CHAPTER-3

HALLOYSITE CLAY NANOTUBES AS NANOCONTAINERS FOR SELF-HEALING CORROSION PROTECTION COATINGS ON AA2024-T4 AND A356.0 ALUMINUM ALLOYS

3.1 Characterization of HNT-based powders.....	58
3.1.1 TEM analysis	58
3.1.2 BET surface area and pore volume analysis	60
3.1.3 XRD studies	60
3.2 Results and Discussion of coatings on AA2024-T4 alloy.....	61
3.2.1 Thickness and Adhesion strength of the coatings.....	61
3.2.2 EIS and Potentiodynamic polarization studies	63

3.2.3 Weight loss analysis.....	68
3.2.4 Salt Spray Test (SST) and EDS analysis	69
3.2.5 Salt Immersion Test (SIT) and EDS elemental mapping	70
3.2.6 Scanning vibrating electrode technique (SVET) analysis	74
3.3 Results and discussions of coatings on A356.0 alloy.....	76
3.3.1 Adhesion test.....	76
3.3.2 EIS and Potentiodynamic polarization studies	77
3.3.3 Weight loss studies	85
3.3.4 SST and EDS analysis	86
3.3.5 SVET analysis.....	88
3.3.6 Micro-Raman spectroscopic analysis	90
References	94

CHAPTER-4

LAYERED MONTMORILLONITE NANOCLAY AS NANOCONTAINERS FOR SELF-HEALING COATINGS ON AA2024-T4 AND A356.0

4.1 Characterization of montmorillonite (MMT)-based powders	96
4.1.1 SEM and TEM analyses.....	96
4.1.2 BET surface area and pore volume analysis	99
4.1.3 XRD analysis	99
4.2 Results and Discussion of coatings on AA2024-T4 alloy.....	100
4.2.1 Thickness of coatings.....	100
4.2.2 Adhesion Test	100
4.2.3 Morphology and composition of coatings by SEM and EDS analysis ...	102
4.2.4 EIS and potentiodynamic polarization studies	103
4.2.5 Weight loss experiments	108
4.2.6 SST and EDS analysis	109
4.2.7 SIT and EDS elemental mapping.....	113
4.2.8 SVET analysis.....	118
4.3 Results and discussion of coatings on A356.0 alloy	120

4.3.1 Thickness and adhesion strength of the coatings	120
4.3.2 EIS and potentiodynamic polarization studies	121
4.3.3 Weight loss analysis.....	125
4.3.4 SST and EDS analysis	126
4.4 Performances of corrosion protection of IEM and IMM coatings on AA2024-T4 and A356.0 alloys.....	129
References	131

CHAPTER-5

SYNERGISTIC EFFECT OF HALLOYSITE AND MONTMORILLONITE NANOCONTAINERS FOR THE CORROSION PROTECTION OF AA2024-T4

5.1 Literature Survey.....	132
5.2 Preparation of sols, coating deposition and characterization	134
5.3 Results and Discussion.....	135
5.3.1 Surface morphology of coatings by FESEM analysis	135
5.3.2 Adhesion strength of coatings by tape adhesion test	136
5.3.3 Thickness of the coatings by FESEM analysis	137
5.3.4 EIS and potentiodynamic polarization studies	138
5.3.5 Weight loss studies	148
5.3.6 SST	149
5.3.7 SIT and EDS elemental mapping.....	151
References	153

CHAPTER-6

EFFECT OF ETCHING OF HALLOYSITE NANOTUBES ON LOADING AND CORROSION PROTECTION OF AA2024-T4

6.1 Literature Survey.....	155
6.2 Experimental	158

6.2.1 Etching of HNTs and loading of etched HNTs with corrosion inhibitors	158
6.2.2 Preparation of sols based on modified HNTs and coating deposition.....	159
6.2.3 Characterization of etched HNTs and etched loaded and stoppered HNTs	159
6.3 Results and Discussion.....	159
6.3.1 FT-IR analysis.....	159
6.3.2 XRD analysis	160
6.3.3 BET analysis	161
6.3.4 TEM analysis	163
6.3.5 EIS and potentiodynamic polarization studies	167
References	173

CHAPTER-7

SUMMARY AND CONCLUSIONS

Summary and Conclusions	175
Future scope of the work.....	181

LIST OF PUBLICATIONS	182
Awards Received	183
BIO-DATA.....	1844

LIST OF SYMBOLS AND ABBREVIATIONS

SEM	Scanning Electron Microscopy
FESEM	Field Emission Scanning Electron Microscopy
TEM	Transmission Electron Microscopy
EDX	Energy Dispersive X-ray spectroscopy
XRD	X-ray Diffraction
EIS	Electrochemical Impedance Spectroscopy
SST	Salt Spray Test
SIT	Salt Immersion Test
SVET	Scanning Vibrating Electrode Technique
OCP	Open circuit potential
Z'	Real Impedance
Z''	Imaginary Impedance
kHz	Kilohertz
R_{ct}	Charge transfer resistance
R_s	Solution resistance
CPE	Constant Phase Element
C_{dl}	Double layer capacitance
C_{coat}	Coating capacitance
E_{corr}	Corrosion potential
eV	Electron Volt
i_{corr}	Corrosion current density
μA	Microampere
mmpy	Millimeter per year
mV	Millivolt

cps	Counts per second
Ω	Ohm
$^{\circ}\text{C}$	Degree centigrade
nm	Nanometer
cm^{-1}	Centimeter ⁻¹
mm	millimeter
μm	micrometer
θ	Theta
M	Molarity
s	Second
HNT	Halloysite nanotube
MMT	Montmorillonite clay
SH	Inhibitor loaded halloysite nanotube based self-healing sol
IEM	Inhibitor intercalated montmorillonite
IMM	Inhibitor mixed montmorillonite
HNC	Unloaded halloysite nanotubes dispersed in matrix
MNC	Unloaded montmorillonite clay dispersed in matrix
EH	Etched HNT
ELSH	Etched loaded and stoppered HNT

CHAPTER-1

INTRODUCTION

CHAPTER -1

INTRODUCTION

1.1 Aluminum and its alloys

Aluminum is a light weight metal having the density of 2.7 g/cm^3 which is one third of the density of steel. Hence, it has extensive usage in aerospace, automotive industries, ships and buildings. Aluminum is non-toxic, recyclable and hence it is used as containers for storage of beverages and food. Corrosion resistance of aluminum with respect to uniform corrosion is one more advantage for its important role in construction, heat exchangers and civil engineering, etc. [1]. The annual consumption of aluminum is 64.34 million tons in the year 2018 given by the international aluminum institute (IAI) [2]. However, pure aluminum is soft, which limits its use in various fields and therefore, alloying is carried out by mixing the different alloying elements in order to increase its strength. Aluminum alloys possess outstanding attributes such as (a) good corrosion and oxidation resistance; (b) high thermal and electrical conductivity; (c) high reflectivity and ductility; (d) low density; (e) reasonably high strength and (f) relatively low cost. Hence, these alloys have wide range of applications in various fields such as aerospace, automobile, heat exchangers and construction etc., as given in Fig. 1.1. Aluminum alloys have face centered cubic crystalline structure which contributes to the excellent formability. In addition, they are easy to form and machine when compared to other metals.

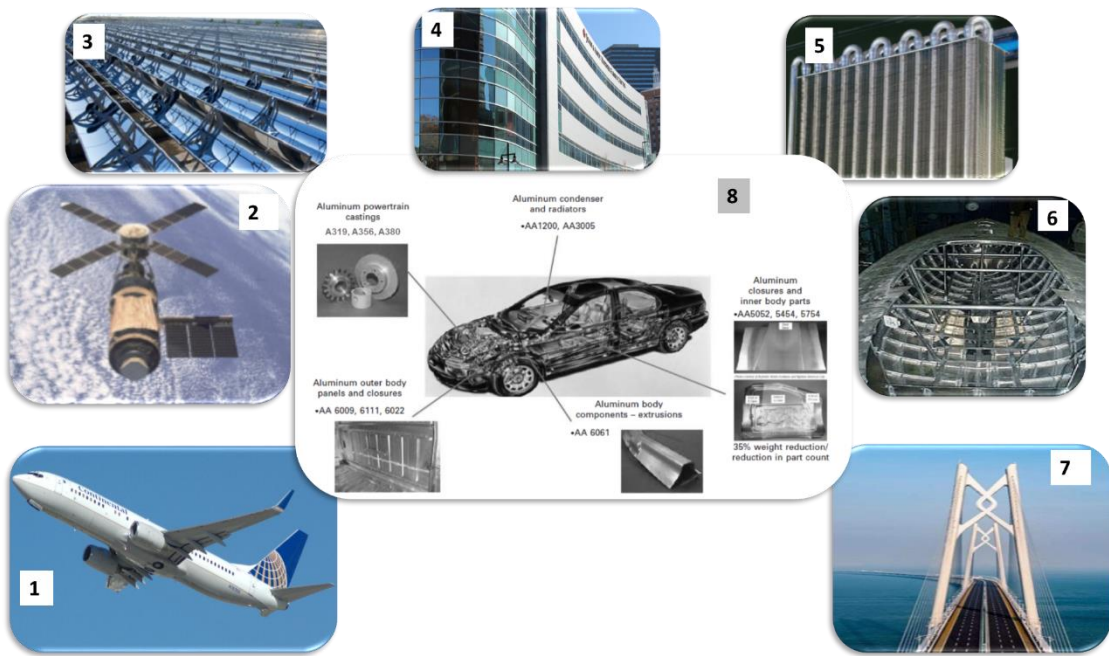


Fig. 1.1. Applications of aluminum and its alloys in various fields: (1) Aircraft; (2) Aerospace; (3) Solar panels; (4) Buildings; (5) Heat exchangers; (6) Ships (7) Bridges and (8) Automobile (source: [3]) industries.

The aluminum alloys are broadly classified into two groups, wrought alloys and cast alloys. The nomenclature for the wrought and cast alloys was given by Aluminum Association. Wrought alloys are designated by four-digit numerical number, for ex. 1xxx, 2xxx, etc. Cast alloys are designated as three-digit number followed by a decimal. The decimal value .0 indicates the alloy is casted, decimal .1 and .2 denotes that they are ingot compositions. The first digit in both types of alloys represents the major alloying element, for example. 1xxx or 1xx.x represents pure aluminum, 2xxx, 2xx.x series represents Cu as the major alloying element and 3xxx or 3xx.x indicates Si as the major alloying element [4]. The alloys are further divided into two sub-groups, heat-treatable and non-heat treatable. Non-heat treatable alloys are hardened by strain hardening or cold working but cannot be heat treated, they include 1xxx (xx.x), 3xxx (xx.x) and 5xxx (xx.x). Heat-treatable alloys strengthened by applying suitable thermal treatment. Alloys with 2xxx (xx.x), 6xxx (xx.x) and 7xxx (xx.x) series are included under heat-treatable alloys. Temper designations are given to both wrought and cast alloys except for ingot alloys based on the sequence of mechanical or thermal treatments or both carried out. Temper designation is mentioned after alloy designation, which is separated by a hyphen. Temper designations are given as O, T, H and F. O represents alloy is annealed to make it softest, T represents aging and heat treatment, H denotes hardened and strengthened. If the alloy is shaped without any control of

hardening, it is designated as F [1,4].

Accordingly, the nomenclature of aluminum alloys AA2024-T4 indicates, it is a wrought alloy, 2 denotes Cu as the major alloying element, 0 indicates there no modification of alloy. The next digits 24 indicates that this alloy is of 2000 series. T4 temper designation denotes, solution heat treated and naturally aged to achieve a stable condition. Similarly, A356.0 alloy indicates, it is a cast alloy, 3 denotes it is having Si as the major alloying element, 56 represents alloy within 3xx.x series. The decimal .0 indicates that it is final shape casted.

1.2 Corrosion in aluminum alloys

Pure aluminum is thermodynamically active, thus in an oxygen containing environment the oxide layer is rapidly formed on its surface [5]. Alumina is one of the most stable of all oxides, with an enthalpy of 21582 $\text{kJ}\cdot\text{mol}^{-1}$, so it is essentially inert and prevents corrosion. It is very difficult to reduce this oxide. Thickness of this oxide film ranges from 2-3 nm at room temperature and it may vary as a function of temperature, environment and alloying elements [6]. Whenever the oxide layer is damaged, a new layer is immediately formed over the bare metal. However, this oxide film gets destabilized due to certain factors such as,

- i) pH: Aluminum forms a passive layer at neutral pH in the range of 4.5-8.0 which is thermodynamically stable as given in the Pourbaix diagram (Fig. 1.2). In acidic environment the aluminum gets corroded uniformly by producing Al^{3+} ions. In alkaline environment aluminate are formed (AlO_2^-) [5].
- ii) Attack of aggressive ions such as chlorides and fluorides.
- iii) Incorporation of elements such as Ga, Sn, Pb, In, Tl in the oxide film which destabilizes it [7].

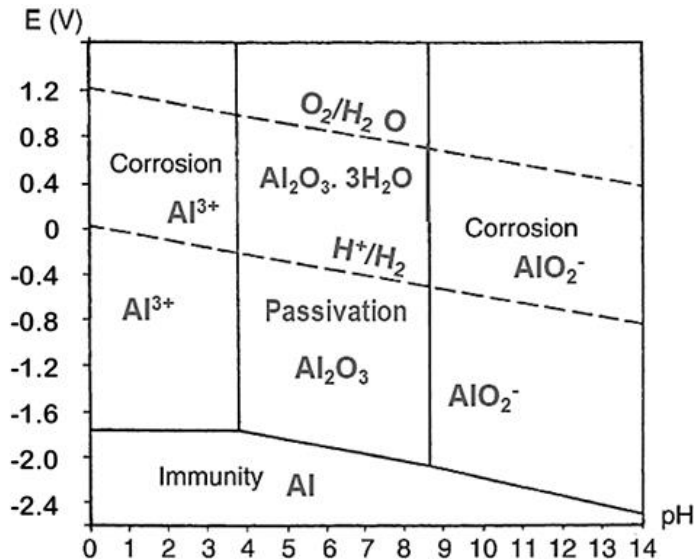


Fig. 1.2. Pourbaix Potential-pH diagram for aluminum [5]

1.2.1 Types of corrosion

Aluminum and its alloys usually undergo localized corrosion such as pitting corrosion or galvanic corrosion at the point of contact, when they are joined with a dissimilar metal. Apart from these, they can undergo other types of corrosion such as uniform, intergranular, filiform, crevice, waterline, microbial, exfoliation and stress corrosion etc. depending on certain factors like exposure medium and service conditions which are intrinsic to the metal.

1.2.1.1 Pitting corrosion

Pitting is a localized form of corrosion, which results in the formation of pits or holes in the metal. This form of corrosion is considered to be more dangerous than uniform corrosion as it is difficult to detect. Therefore, a small narrow pit with a very little loss of metal can lead to the overall system failure. Pits can be of various shapes and sizes such as hemispherical, shallow, elliptical, narrow or completely irregular shape as given in Fig. 1.3. Pits are often covered with corrosion products [8].

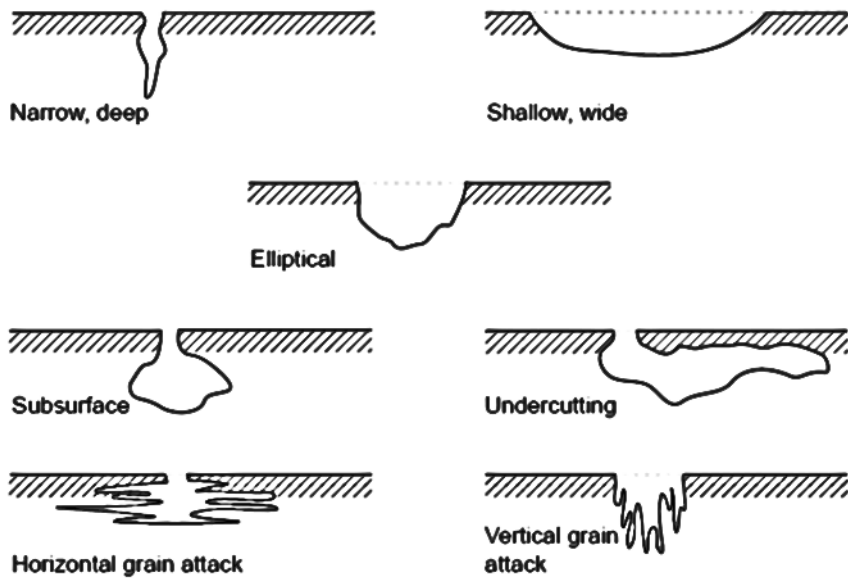


Fig. 1.3. Different shapes of pits formed in pitting corrosion [8]

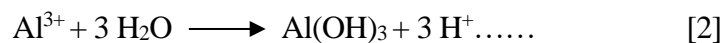
1.2.2 Corrosion mechanism in aluminum alloys

Aluminum alloys are more prone to corrosion when compared to pure aluminum due to the presence of various alloying elements. This occurs because of microstructural heterogeneity in the metal during the alloying process as a result of which, intermetallic (IMC) phases are formed. Most of the commercially used alloys contain several types of intermetallic phases and hence the corrosion in aluminum alloys is essentially a microgalvanic process between these phases and the metal matrix [9]. IMCs are rich in Fe and Cu content compared to the Al matrix, therefore they act as local cathodic sites surrounding aluminum matrix that results in the oxidation of aluminum.

Pitting of aluminum initiates i) due to the attack of aggressive ions such as Cl^- at weak sites in the alumina layer and ii) at the cathodic sites because of the change in the potential difference between IMCs and aluminum matrix. Pits propagate by oxidation of aluminum at the anodic sites as given in the following reactions [1] and [2]. At the cathodic sites, reduction reactions occur by transfer of e^- from anodic site to cathodic site thereby O_2 reduction and H_2 evolution occurs as given in equations [3] and [4]. At the anodic site, as the pit propagates, the pH will decrease due to the formation of Al^{3+} and H^+ ions. In order to balance this, chloride ions will move into the pit resulting in HCl formation. This further accelerates the pit propagation which is explained in Fig. 1.4. At the cathodic IMCs, the reduction reaction causes local alkalinization making the aluminum unstable and hence, aluminum around the particle will dissolve forming

alkaline pits. This may result in the detachment of particles from the surface. In addition, the aluminum part of IMC particles also dissolves, thereby enriching the Fe content and increased cathodic activity [7].

At anode:



At cathode:

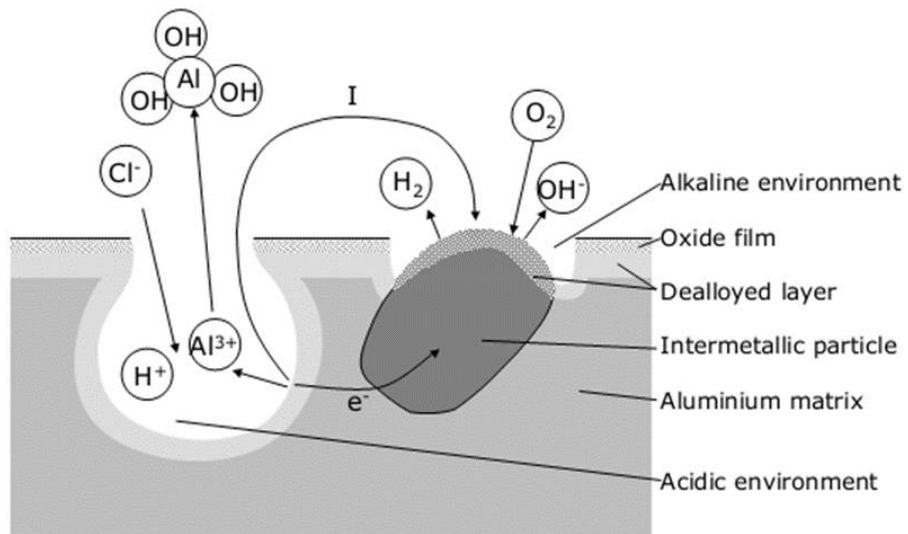


Fig. 1.4. Mechanism of corrosion in aluminum alloys [7, 10]

1.3 Protection of aluminum alloys by surface treatment

Aluminum alloys need to be prevented from getting corroded, as these surfaces constantly get exposed to extreme atmospheric conditions during their usage in various fields, resulting in the deprivation of material with the time. Hence, they must be protected before a heavy loss of material occurs. Paints are generally used to protect these surfaces to provide a barrier protection. However, when the paint layer gets damaged in such a way that it gets removed, thereby exposing the substrate surface and the substrate gets corroded quickly.

Surface treatment or deposition of coatings is the most commonly used strategy to protect the metal/alloy structures. Different methods have been investigated for surface protection such as conversion coatings, vapor deposition methods, anodizing, plasma treatment, laser/electron beam treatment, hot-diffusion alloying, sol-gel coating and organic coating, etc. [11]. Hexavalent chromium-based conversion coatings have been the most effective self-healing coatings used so far, as they are more potent as well as low cost involving simple process of operation [12]. However, due to their carcinogenic nature, chromate conversion coatings have been globally banned. Therefore, these restrictions have drawn enormous efforts to develop chromate-free, self-healing coatings [13]. Hence, researchers are extensively investigating different strategies for the development of new green, smart protective coatings [14–16], keeping in mind that this alternative coating must also possess good adhesion to the substrate, intrinsic durability, flexibility, hardness to withstand mechanical stress and effective corrosion protection. The green alternative should also contain low-VOC (volatile organic compound), low-HAP (Hazardous Air Pollutants) [13]. Sol-gel based coatings are found to be potential replacements for chromate conversion coatings, both from the point of tuning the chemistry to achieve the desired property as well as from the point of ease of deposition on large areas [17].

1.4 Sol-Gel Coatings

Sol-gel method is one of the rapidly developing surface modification methods for obtaining hybrid materials, composite coatings, glass and ceramics. Hence the global market for the sol-gel based products especially coatings is increasing, which is due to the sol-gel coatings possessing many unique characteristic features like good adhesion with the substrate, intrinsic durability, flexibility, hardness to withstand mechanical stress and low temperature curable. Moreover, these coatings are reconcilable with different types of substrates and they can be very thin [18].

“Sol” is a colloidal suspension of solid particles in a liquid medium and “Gel” is a three-dimensional network of the particles. The sol as a liquid phase can be applied on to different surfaces to form a coating by various techniques such as dipping, spinning by rotating the substrates while the sol drops through a nozzle, flowing at an angle, spraying, brushing and electrophoretic deposition by applying voltage. It also can be cast in a mold to obtain self-standing structures. In addition, this sol can be dried to produce different kinds of gels such as aerogels, xerogels and ceramics. The sol being relatively stable, can be stored for certain

time and used further [13]. Fig. 1.5. depicts various routes for obtaining sol-gel coatings.

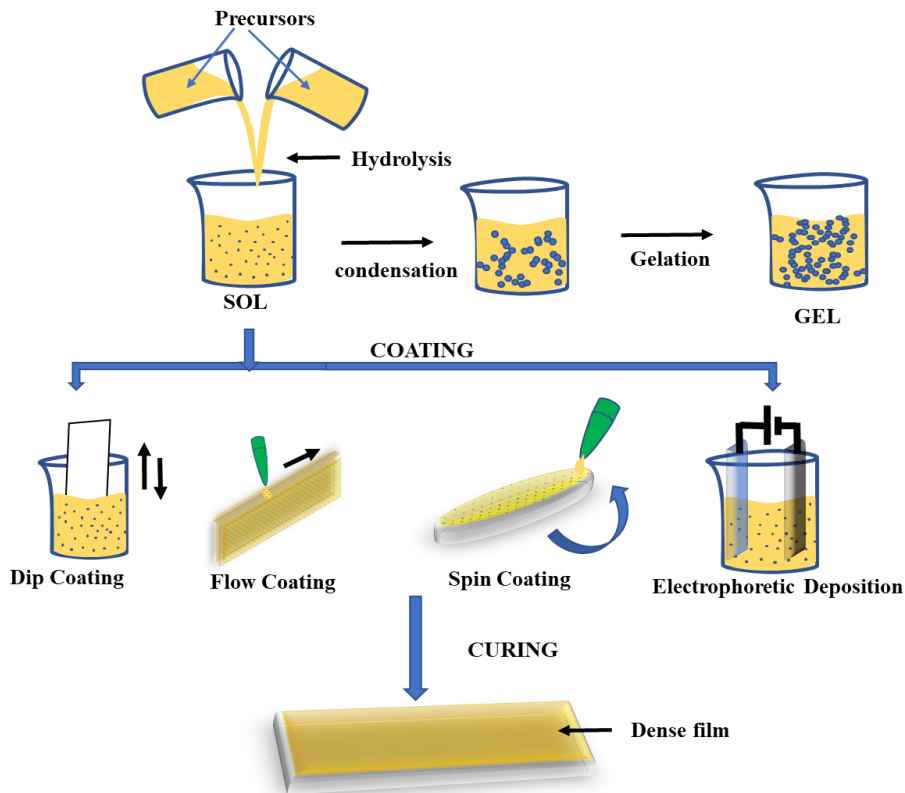


Fig. 1.5. Various sol-gel coating process routes [19].

1.4.1 Background of sol-gel process

Sol-gel process is a wet chemical synthesis method in which an oxide network is formed by progressive condensation reactions of molecular precursors (silicon or metal alkoxide) from a liquid medium [20–22]. M. Ebelmann was the first one to observe the formation of transparent glass form of silyl ester when exposed to moisture in the year 1846. The term Sol-Gel was coined by Graham in 1864 and the first patent on sol-gel process was filed in 1939 by Jenaer Glaswerke Schott & Gen. In 1930s, Geffcken and Berger from Schott company established a process for the formation of sol-gel oxide layers from the metal containing precursors on industrial glasses. In 1970s, Dislich [23] synthesized borosilicate glass lens from oxide powders by low temperature heating sol-gel process, which has drawn interest among scientists for the development of sol-gel technology. The commercialization of sol-gel process started in 1980s first by Japanese companies. Intense research on organic-inorganic hybrid systems was carried out from 1985 onwards, after H. Schmidt from Germany and G.L. Wilkes from USA independently reported the organic-inorganic hybrid

sol-gel systems [24,25].

1.4.2 Chemistry of sol-gel process

The conversion of sol to gel in hybrid materials generally involves four steps. i) Hydrolysis of metal oxides in which alkoxy groups (-OR) are replaced by hydroxyl (-OH) groups; ii) Condensation and polymerization of monomer particles to form chains and particles; iii) Growth of the particles and iv) Agglomeration of particles to form an extended 3-dimensional network resulting in the gel formation as given in Fig. 1.6. The hydrolysis and condensation reactions both occur simultaneously once the hydrolysis has started. The small molecules like alcohol and water will be produced as the by-products of these reactions [20].

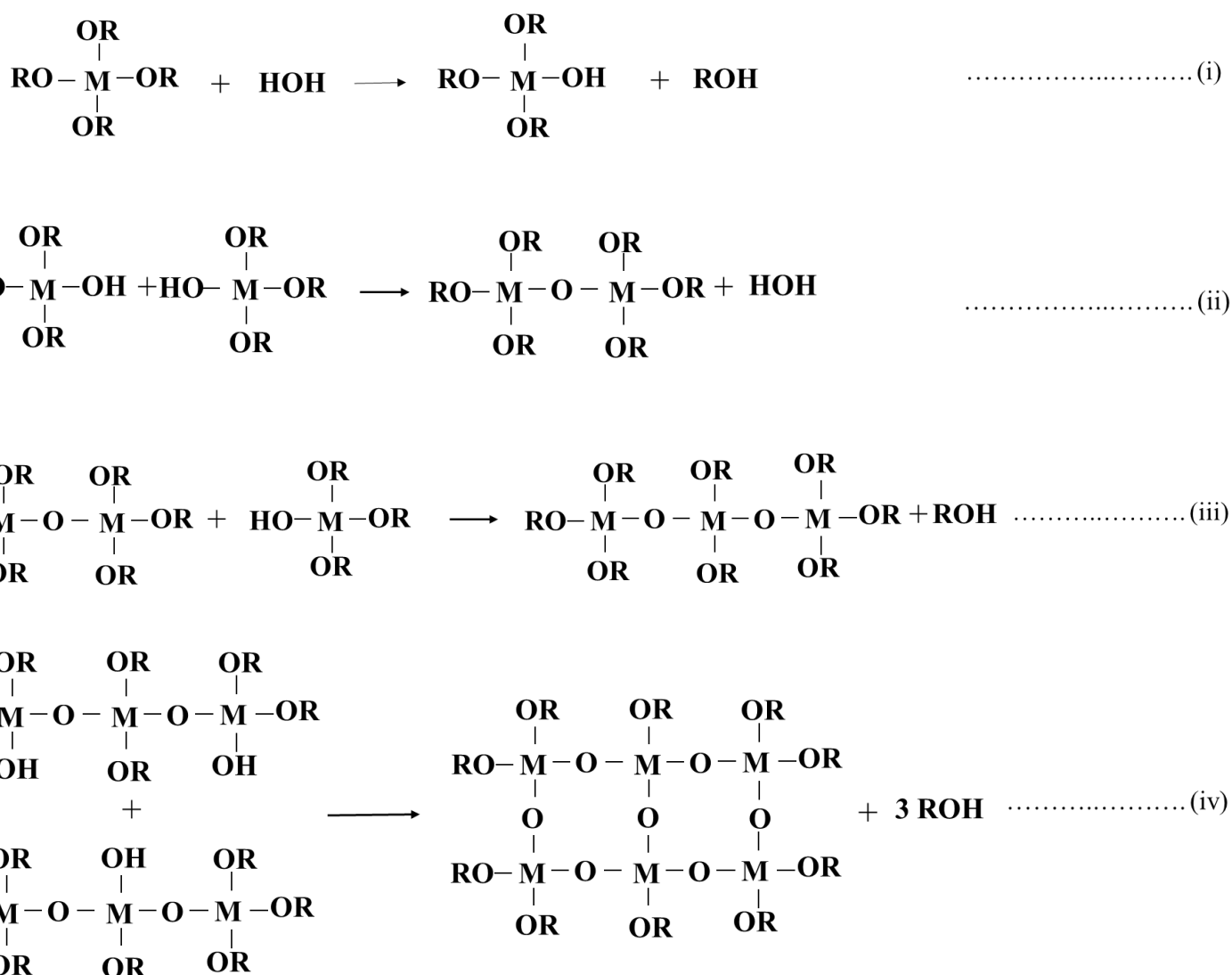
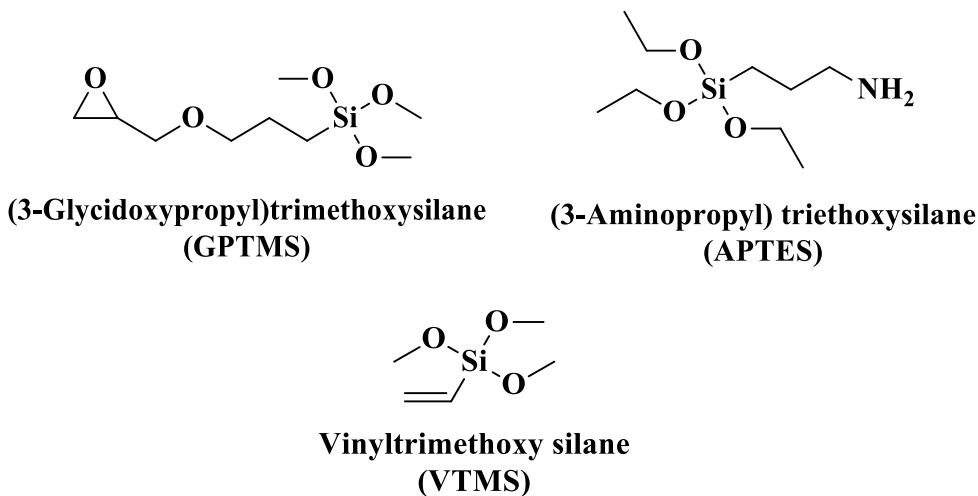


Fig.1.6. Mechanism of sol-gel process

Metal alkoxides such as tetraethoxy silane, zirconium-n-propoxide, titanium tetraisopropoxide, aluminum sec-butoxide etc., are the widely used starting precursor molecules for the synthesis of silica, zirconia, titania and alumina sols respectively. Use of these precursors result in inorganic coatings as they have good strength and corrosion resistance. However, their brittleness and high processing temperature limits the usage in wide range [26]. This process was found to be one of the most efficient way for the preparation of organic-inorganic hybrid coatings because of their excellent physical, chemical and corrosion protection properties [24,27–29]. Hence, the organic precursors such as alkyl alkoxysilanes are being used to develop the flexible and low temperature curable coatings. Some of the examples of organically modified silanes are given in Fig 1.7. The hybrid sol-gel coatings contain combination of inorganic and organic precursors, in which, the inorganic part offer strength and barrier property and organic part provide the flexibility [26].



1.7. Structures of different organic-inorganic silanes.

1.4.3 Advantages of sol-gel coatings

The coatings developed from sol-gel process are found to be most effective, solvent-free and eco-friendly coatings. These coatings are considered to be chrome-free coatings, which have good mechanical properties and excellent adhesion strength. Materials with high porosity and high specific surface area can be obtained, which allows the incorporation of inhibitors. The processing temperature is very low so that thermal volatilization and degradation of compounds or entrapped materials are reduced [20,22,30]. As the precursor molecules are mostly in liquid form, it is possible to cast coating in complex shapes and produce the coating without any melting process or machining [13]. Presence of three-dimensional network silica

as the main component of the coating structure can provide a dense coating having an excellent barrier property. Corrosion inhibitors can be used as additives to sol-gel coatings in order to improve the corrosion protection property of sol-gel coatings. Multifunctionality can be achieved in a single layer of coating.

1.5 Corrosion inhibitors

Inhibitor is a substance or combination of two or more substances when added in low concentrations to an environment or to a coating mitigates the reaction of metal to the environment. Similarly, corrosion inhibitors are chemical substances that decrease the corrosion rate of the system. The efficiency of an inhibitor can be expressed by the following formula.

$$\text{Inhibition efficiency (\%)} = \frac{\text{CR}_{\text{without inhibitor}} - \text{CR}_{\text{with inhibitor}}}{\text{CR}_{\text{without inhibitor}}} \times 100$$

Where CR = Corrosion Rate

Inhibitors act either by i) surface modification of the system i.e., by adsorbing on the surface of metals and by forming a surface film on the metal or by ii) arresting the cathodic or anodic reactions or even both at the same time. They form monomolecular layer on the metal creating a barrier to the environment.

Inhibitors have been classified into organic and inorganic inhibitors. These are again divided based on their functionalities such as cationic and anionic.

Inorganic inhibitors: Anionic inhibitors such as vanadates, phosphates, molybdates and cationic inhibitors mostly rare earth compounds such as cerium salts, lanthanum and zirconium etc. are widely used.

Organic inhibitors: Anionic inhibitors derived from thiazole moieties such 2-mercapto benzothiazole (2-MBT), triazoles (Benzotriazole) are widely used. Apart from these, imidazoles (Benzimidazole-BIA and 2-mercaptopbenzimidazole) and quinolines (8-hydroxyquinoline) are also investigated as given Fig.1.8. Cationic inhibitors such as compounds containing aliphatic or aromatic amines are used [1,8].

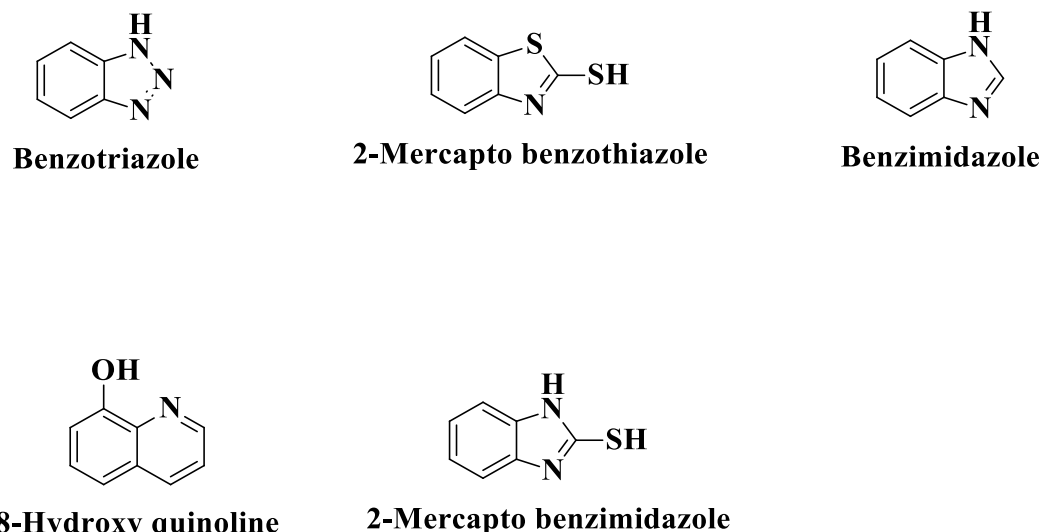


Fig. 1.8. Structures of organic inhibitors.

1.6 Sol-gel coatings for Corrosion Protection

Sol-gel coatings have been extensively reported as “green” alternatives for chromate conversion coatings for different metals such as steel, aluminum and magnesium alloys. The pure inorganic parts containing silane matrix are not suitable for the corrosion protection as they are porous and require high temperatures for densification [31]. However, inorganic-organic hybrid coatings being flexible, dense, exhibiting superior barrier nature and having less curing temperature were found to be desirable as anti-corrosion coatings. Castro et al [32] have developed crack-free, homogenous coatings by dip and electrophoretic deposition (EPD) using tetraethoxy silane (TEOS) and methyltriethoxysilane (MTES) as the precursors on AISI 304 steel substrates. They reported that the coatings were thicker and provided better corrosion protection by EPD. Acid catalyzed hydrolytic condensation of MTES and tri-isopropoxy(methyl)silane to produce polysilsequioxanes was reported by Gunji et al [33].

Presence of organically modified functional groups i.e., organo-alkoxysilanes such as epoxy, vinyl and methacrylic groups leads to polymerization, resulting in the higher density, enhanced barrier and corrosion protection properties than hybrid sol-gel coatings with non-functional organosilanes. Parkhil et al [34] have prepared epoxy based silane films on 2024-T3 aluminum alloy substrates. They have reported superior barrier properties and good corrosion protection when compared with chrome-based coatings. Hybrid coatings by two step acid catalyzed co-polymerization of TEOS and 3-methacryloxypropyltrimethoxysilane (MPTMS) on 316 and 304 stainless steel substrates have been reported by Chou et al [35]. These coatings were found to be flexible, uniform without any defects with good adhesion strength and

excellent corrosion protection. A two-step co-polymerization of 2-methacryloyloxyethyl-phosphate and 3-methacryloxypropyltrimethoxysilane (MEMO) was reported by Kannan et al [36]. This hybrid coating was found to provide enhanced corrosion protection on mild steel due to the presence of strong interactions of phosphate groups with the substrate. Criado et al [37] have synthesized the sol-gel coatings using different mixtures such as TEOS and MPTS, TEOS and MTES, TMOS and MPTS or TMOS and MTES. However, aqueous based sols have also been reported recently. Kirtay et al [38] have prepared aqueous based hybrid silica coatings using GPTMS and APTES sols on mild steel and Santana et al. [39] have used TEOS and GPTMS on carbon steel. Moreover, introduction of organic components in the sol-gel coatings produces thicker, crack-free coatings with enhanced corrosion protection. The functional groups such as phenyl, methyl groups can be incorporated to increase the hydrophobicity of the coatings [40]. The amino groups have ability to react with epoxy groups and provide compatibility with organic primer. Presence of amino derived cross linking agents in epoxy based hybrid silane coatings permits formation of organic network at low temperatures [41]. Vreugdenhil [42] have studied the corrosion behavior of epoxy silane coatings using an amine cross linking agent diethylenetriamine (DETA) on AA2024-T3 alloy. DETA was a low temperature curable cross-linking agent and was found to produce dense coating which provided better corrosion protection. Donley et al [43] have prepared epoxy silane coatings cross-linked with amino-silanes and these coatings were found to provide improved corrosion protection when compared to those of DETA cross-linked ones. In addition to amino silanes, other amines have been used as the alternatives to DETA such as branched amines [44,45] and di-amines with long carbon chains [46], which were found show better corrosion protection. In the absence of these cross-linking agents, epoxy-based hybrid coatings require more temperatures above 100° C by thermal curing for the formation of network. However, these coatings have poor mechanical strength and wear resistance. Therefore, to overcome these drawbacks various strategies have been adopted such as addition of inorganic particles like silica, aluminum oxide and other oxides [47,48]. Formation of nanoparticles or nanostructured films by in situ process through controlled hydrolysis or condensation of precursors during sol-gel synthesis is another strategy [43,49–53]. Zheludkevich et al [52] have synthesized hybrid coatings incorporated with zirconia nanoparticles using GPTMS, TEOS and ZrTPO as the precursors. Lamaka et al [53] have synthesized nanostructured porous titania layer which was covered by epoxy-zirconia-silane based sol-gel film. They reported that, the presence of nanostructured components in the sol-gel film resulted in enhancement of barrier and

mechanical properties. Moreover, these nanostructured compounds can be used to introduce the corrosion inhibitors into sol-gel coatings.

Incorporation of corrosion inhibitors into the sol-gel matrix is an alternate method to achieve the self-healing ability for replacement of hazardous chrome-based coatings. Initially, investigations were focused on the direct addition of corrosion inhibitors like benzotriazole, thiazole groups or cerium salts into the sol-gel matrix, in order to prolong the corrosion protection whenever there was a defect in the paint layer. However, it was found that direct loading of corrosion inhibitors in the matrix has a detrimental effect on the coating, which enhances the corrosion rate of the substrate. Due to direct loading in the sol-gel matrix, the inhibitor is released in an uncontrolled manner and hence the corrosion protection is rendered only for a short duration of time [54,55]. More recent studies have been focusing on encapsulating the corrosion inhibitor to enable a controlled release of the same, which takes place only on demand, i.e., whenever there is a defect in the coating. Different types of encapsulating materials like porous nanoparticles [56,57], naturally occurring clay minerals like montmorillonite, bentonite halloysite clays [58], carbon nanotubes [59], layered double hydroxides [60,61] have been investigated. Shi et al [62] used various nanoparticles such as silica, iron oxide, zinc and halloysite nanoclays for the preparation of anticorrosion coatings on steel substrates. These nanoparticles were individually dispersed in epoxy matrix, dip coated on steel substrates and cured at room temperature for 7 days. Mechanical properties of coatings were studied by atomic force microscopy and the anticorrosion behaviour was studied by electrochemical impedance spectroscopy (EIS) and potentiodynamic polarization experiments. They reported that all the nanoparticles were able to significantly improve the corrosion resistance of steel. However, SiO_2 nanoparticles exhibited improved stiffness of the coating, whereas, Fe_2O_3 and halloysite clay nanoparticle-based coatings provided better corrosion protection.

1.7 Self-Healing Coatings

Self-healing coatings can be developed by encapsulation/loading of active anticorrosion species in host containers, which will be subsequently dispersed into the matrix and can be polymeric or sol-gel based [63]. These self-healing coatings are also called as smart coatings, as they act by releasing corrosion inhibiting species from containers only on demand whenever there is a damage to substrates, without unnecessary leakage [64]. The

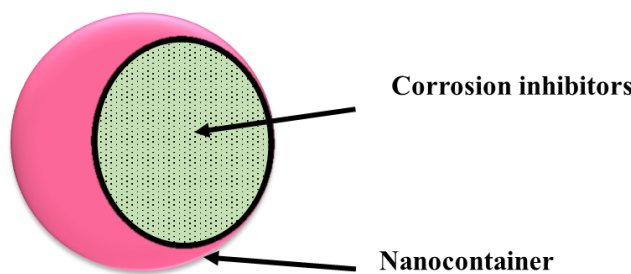
containers act as reservoirs by storing the functional species till the time of their release. Self-healing materials as the protective coating can increase material's lifetime, reduce replacement costs and improve product safety. Hence, the use of smart and functional coatings have been found to be one of the effective ways of achieving high performance anticorrosion properties [65].

1.7.1 Theory of self-healing

The inspiration for development of self-healing coatings has come from the natural self-repairing activity taking place along the wounds and cuts in living species. The biomimetic of this complex mechanism to engineering materials is done to achieve the release of corrosion inhibitors on demand so as to recover their mechanical properties after damage.

The self-healing coatings render a good barrier property as well as extended corrosion protection when applied on to the materials. In these coatings, the active species such as corrosion inhibitors, monomers, catalysts, etc. are loaded into the nanocontainers and are further dispersed into the matrix. On the onset of damage to coating such that the substrate gets exposed, the damage/crack ruptures the nanocontainers resulting in the release of corrosion inhibitors and passivate the damaged area by polymerization of monomers or by formation of oxide and hydroxides. In addition to this, local pH in the damage area will change, which is the driving force for the release of corrosion inhibitors into the scratch. The schematic mechanism of self-healing is given in Fig. 1.9.

In order to provide a self-healing behaviour, the nanocontainers chosen must have good compatibility with the coating matrix, they must be stable and be able to store the active agents for long time, thereby releasing the inhibitors only when required. This approach is also being used for developing multifunctionalities in the protective coatings, viz antibacterial and anti-fouling properties etc. [65].



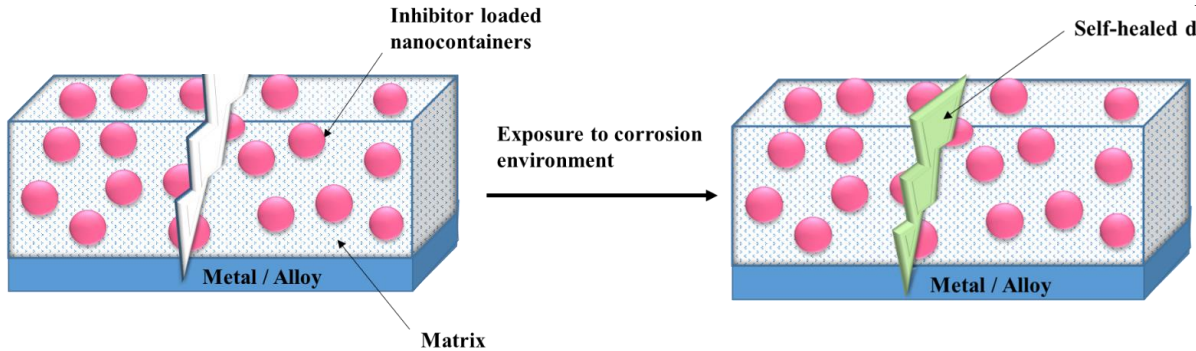


Fig. 1.9. Mechanism of self-healing action using smart nanocontainers.

1.7.2 Smart nanocontainers for Self-Healing

Different micro/nanocontainers have been widely investigated for corrosion protection applications such as polymeric microcapsules, carbon nanotubes, layered double hydroxides, halloysite nanotubes and montmorillonite nanoclays, etc.

1.7.2.1 Polymeric microcapsules

Polymeric microcapsules are the most widely used containers for the controlled release of active agents. These capsules are small spherical particles, which contain two components i.e., inner core and outer shell [66] as shown in Fig. 1.10. The process of encapsulation of solid, liquid or gases inside the core is called encapsulation, which separates and protects the active material from the environment [67]. In case of microcapsules, their diameter widely ranges from 3-800 μm and can contain 10-90 wt % of inner core materials. They have been used in several industries such as adhesives, insecticides, cosmetics, pharmaceuticals and carbon less copying papers [68].

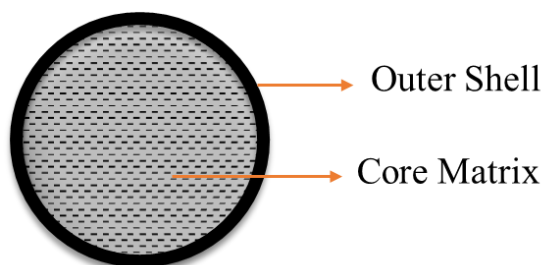


Fig. 1.10. Schematic representation of microcapsule

Scott R. White's group have carried out pioneering work on microcapsules as the containers for self-healing polymers [69–72]. Following this, there have been several other reports on the use of microcapsules for self-healing corrosion protection coatings. Maia et al [73] have used polyurea microcapsules for encapsulating MBT corrosion inhibitor. These inhibitor loaded microcapsules were added to a hybrid sol-gel matrix for corrosion protection of AA2024 alloy. The corrosion resistance of developed coatings from MBT loaded microcapsules were compared with that from coatings developed by adding MBT directly to the matrix. EIS results showed that, coatings containing MBT loaded microcapsules provided good corrosion protection and the self-healing action was confirmed by SVET. Cotting et al [74] have synthesized polystyrene based microcapsules by the solvent evaporation method from a double emulsion. These microcapsules were loaded with octyl silane and Ce (III) ions, which were dispersed in epoxy resin and coatings applied onto carbon steel. Thanawala et al [75] have encapsulated linseed oil into the poly-urea formaldehyde microcapsules by in-situ polymerization, which were dispersed into a polymer matrix for coating deposition. These self-healing coatings on mild steel substrates showed good resistance to corrosion assisted blistering till 500 h of immersion in 3.5 % NaCl solution. The adhesion strength of the coatings was found to be enhanced due to the addition of microcapsules. Ataeia et al [76] have used alkyd resin based on coconut oil and incorporated into poly (melamine-urea-formaldehyde) (PMUF) microcapsules, that were subsequently dispersed into epoxy resin. These coatings were applied on stainless steel panels. The concentration of loaded microcapsules incorporated into epoxy resin was varied from 5-15 %. They have observed that the increase in the concentration of these microcapsules in epoxy resin resulted in decrease in gloss and adhesion strength as well as a reduction in bending elongation of coatings. Epoxy resin containing 10 % microcapsules showed better corrosion protection. Sun et al [77] have prepared microcapsules by loading 4,4'-bis-methylene cyclohexane diisocyanate into them, which are chemically and thermally stable. These loaded microcapsules possessed self-healing and self-lubricating property. Incorporation of encapsulated isocyanates improved corrosion resistance as well as self-lubricating performance. Huang et al (77) have synthesized poly-urea formaldehyde microcapsules by in-situ polymerization in an oil-water emulsion, which were loaded with 1H,1H,2H,2H-perfluoroctyl triethoxysilane (POTS) - a hydrolysable organic silane. POTS microcapsules were incorporated into epoxy resin and coated on a steel substrate. These coatings have provided good corrosion protection due to self-healing action. Yang et al [79] have studied the effectiveness of the epoxy resin filled microcapsules in self-healing of the cracks

generated in the coating. Microcapsules were prepared by in-situ polymerization of urea-formaldehyde resin to form a shell over the epoxy resin. These microcapsules were added into the paint and applied on cold-rolled steel substrates. The microcapsules had rough morphology and provided good anchoring between paint matrix and microcapsules. They exhibited good storage stability at room temperature (stable up to 200° C) and also self-healing ability after the paint got cracked under simulated mechanical action.

Izadi et al [80] have used green inhibitor loaded nanocontainers (GIN) i.e., nettle leaves extract for corrosion protection of steel. Polyaniline- polyacrylic acid based shells were used as the nanocontainers and these loaded nanocontainers were dispersed in hybrid sol-gel matrix. The active inhibition was observed from GIN-epoxy coatings on steel. Blaiszik et al [71] prepared dicyclopentadiene (DCPD) loaded urea-formaldehyde (UF) nanocapsules by in-situ encapsulation and ultrasonication. They have reported formation of nanocapsules with the diameter ranging from 200 nm-1.65 μ m and having smooth surface. These nanocapsules contain nearly 94 % inner core material and were thermally stable up to 150° C. Epoxy matrix dispersed with these nanocapsules has shown increase in fracture toughness by approximately 59 % for the capsules with the volume fraction (ϕ_f) of 0.015.

1.7.2.2 Layered double hydroxides

Layered double hydroxides (LDH) consist of mixed metals and hydroxide molecules separated by exchangeable anions and water molecules [54]. These LDHs act as smart nanocontainers by exchanging the intercalated anions by other anions under given conditions. Hence they have wide range of applications in the field of drug delivery [81] and catalysis [82]. Use of LDHs as nanocontainers for loading the inhibitors were reported to be promising in self-healing corrosion protective coatings, as they play a dual role by releasing inhibitors (I^-) as well as entrapping the corrosive chloride ion [58]. The schematic representation of self-healing of damage of the coatings with LDH is shown in Fig. 1.11.

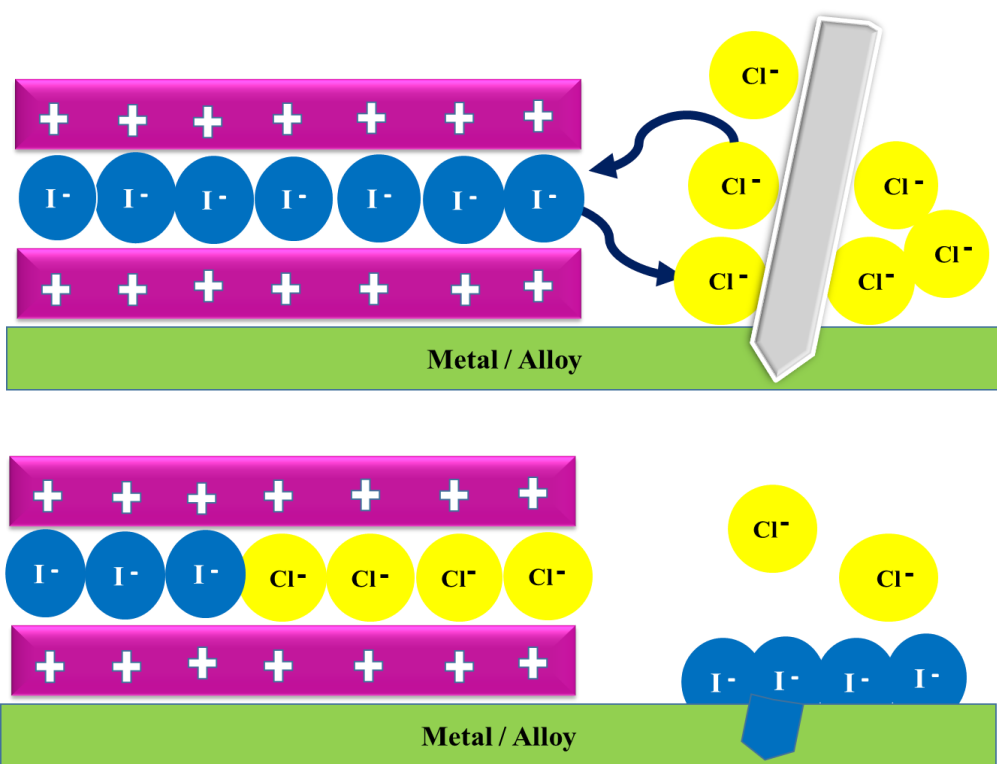


Fig. 1.11. Self-healing mechanism using LDH as nanocontainers [83].

There are several reports on use of LDHs as nanocontainers for self-healing coatings. Tedim et al [84] have used combination of LDHs loaded with different inhibitors such as vanadate, phosphate and MBT. The inhibitor loaded LDHs were dispersed into sol-gel matrix and applied onto AA2024 substrates. LDHs loaded with vanadate, phosphate, vanadate and MBT anions were shown to confer a synergistic anticorrosion effect on AA2024. Mixture of inhibitors in LDH was seen to exhibit better corrosion protection than individual systems. Liu et al [85] have dispersed Ce doped ZnAl-LDH nanoparticles in hybrid sol-gel matrix and deposited on AA2024. Ce was doped into LDH sheets at various concentrations. A two phase mixture of Ce-loaded LDH and CeO₂ was formed. ZnAlCe-LDH nanoparticles got distributed uniformly in sol-gel matrix. The coating embedded with LDH-0.1 Ce particles exhibited best anti-corrosion ability due to the synergistic inhibiting action by the dissolution of ZnAlCe-LDHs and CeO₂ nanoparticles. Hu et al [86] have synthesized decavanadate intercalated ZnAl-LDH, modified with γ - aminopropyltriethoxysilane (APTS) which were grafted using polyaniline (PANI) on mild steel substrates, labelled as PANI/AD-LDH. PANI/AD-LDH has got higher corrosion resistant property than the coatings containing only decavanadate intercalated-LDH and PANI. Montemor et al [61] have used two different nanocontainers i.e., LDH and Ce molybdate hollow microspheres, which were loaded with

2-MBT. These loaded nanocontainers were dispersed in the sol-gel matrix and applied on to galvanized steel. A mixture of these two nanocontainers has shown synergistic effect on corrosion protection. In-situ growth of LDH directly on AA2024 substrates was also carried out by Tedim et al [60]. In this work, LDH was loaded with vanadate inhibitor and it was found that direct growth of LDH has an advantage of better adhesion than ex-situ application of LDH in the form of coating. This inhibitor loaded in-situ grown LDH layer has formed nanostructured container islands in the zones of intermetallic phases which are the most susceptible for localised corrosion attack.

1.7.2.3. Carbon nanotubes

Carbon nanotubes (CNTs) have attracted much attention due to their superior electrical [87], mechanical [88] and thermal properties [89]. CNT have tubular nanoscale morphology, possessing high strength, light weight and high specific area [90,91]. These CNTs are made up of hundreds of concentric shells of carbons with adjacent shells separation of 0.34 nm [91]. In combination with active materials, they have been used for the corrosion protection [92,93].

Nezamdoust et al [94] have developed sol-gel nanocomposites using hydroxylated multiwalled carbon nanotubes (OH-MWCNT), which were embedded in phenyl-trimethoxysilane (PTMS) at different concentrations. These nanocomposites have been deposited on magnesium alloy AM60B for corrosion protection. The sol-gel coating without nanoparticles has shown cracks, whereas the nanocomposite coating with OH-MWCNT embedded in it was without any cracks. The corrosion resistance and hydrophobic nature of this nanocomposite film was improved due to the chemical interaction between incorporated OH-MWCNT and silane matrix, by filling the defects in the coating by embedded nanoparticles. Cui et al [95] have dispersed functionalized multiwalled carbon nanotubes (MWCNT) in epoxy matrix (EP) to develop fabricated MWCNT/EP nanocomposites on Q235 carbon steel electrode. The non-covalent functionalisation of MWCNT was carried out using poly (2-butylaniline) (PBA) to improve dispersion. The incorporation of dispersed MWCNT into the epoxy resulted in a decrease in the water absorption capacity, the noble open circuit potential (0.028 V) and high impedance modulus. These nanocomposites exhibited decrease in friction coefficient and wear rate compared to blank EP. He et al [96] synthesized multi-walled carbon nanotubes and β -cyclodextrin based functional nano-reservoir through a new and facile chemical method. These functional nano-reservoirs were loaded with green

inhibitor benzimidazole (BIA), which was subsequently dispersed in epoxy resin and then coated on steel substrates. Inhibitor loaded functional nano-reservoirs significantly improved corrosion resistance due to the self-healing action by releasing the encapsulated inhibitor. Yeole et al [97] have developed a three step process of layer-by-layer deposition of polypyrrole coating on CNT, loading of 2-MBT as corrosion inhibitor and poly acrylic acid layer on mild steel substrates to provide improved corrosion protection. The nanocontainers/epoxy system provided better corrosion protection than only epoxy system alone due to the interaction between nanocontainers and corrosive medium. Arora et al [98] have reported direct growth of multi-walled carbon nanotubes over mild steel substrates. The MWCNTS were directly grown on the substrates by the decomposition of ferrocene-benzene mixture. A significant improvement of corrosion resistance was observed due to protective and highly hydrophobic nature of the directly grown MWCNT coating.

1.7.2.4 Halloysite nanotubes

Halloysite clay is a two layered alumino silicate having 1:1 ratio of alumina and silicate layers possessing chemical similarity to kaolin. It has hollow tubular structure in the sub micrometer range [99] and presence of a monolayer of water in the interlayer makes it morphologically different from kaolin [100]. It is an abundantly available natural mineral in New Zealand, Australia, USA, China, Mexico and Brazil with various morphological forms such as platy, spherical and tubular. The size of halloysite nanotubes (HNTs) ranges from 0.2-1 microns of length, with inner lumen diameter of 15-30 nm and outer diameter 50-70 nm. The molecular formula of HNT is $\text{Al}_2(\text{OH})_4\text{Si}_2\text{O}_5 \cdot n\text{H}_2\text{O}$. HNTs outer and inner surfaces consists of tetrahedral silica layer which negatively charged and octahedral alumina layer which positively charged respectively as shown in Fig. 1.12. The zeta potential of inner lumen is positive at $\text{pH} < 8$, which allows the loading of negatively charged active materials into the lumen. However, when these loaded HNTs get exposed to surroundings or aggressive Cl^- environment having the $\text{pH} > 8.5$, the inner lumen of HNT becomes negatively charged, which in turn driving the release of loaded active materials on the damaged area [101,102]. The self-healing mechanism using HNTs as the nanocontainers is depicted in Fig. 1.13.

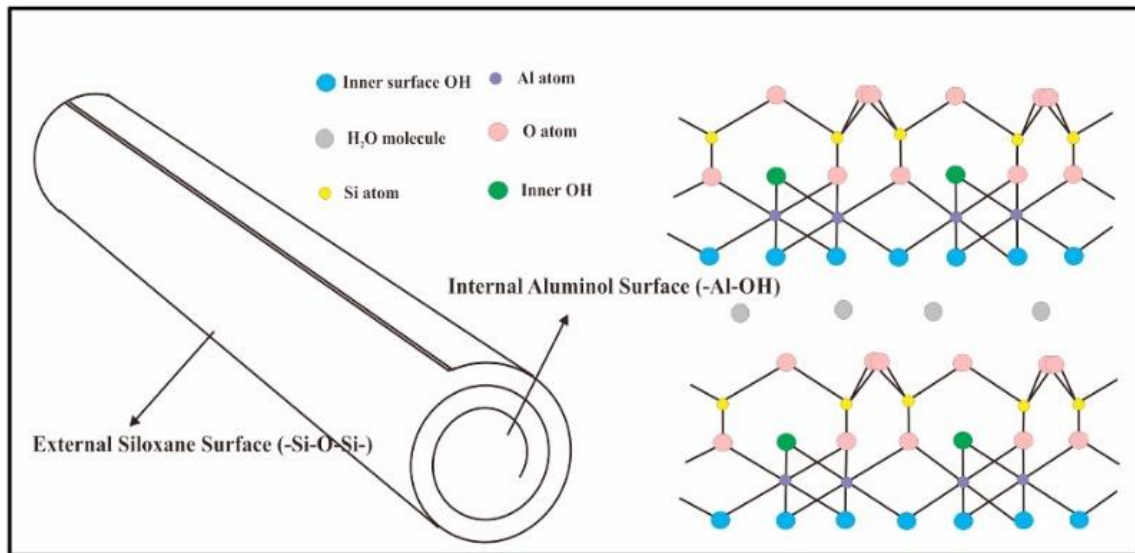


Fig. 1.12. (a) Schematic representation of structure [102]

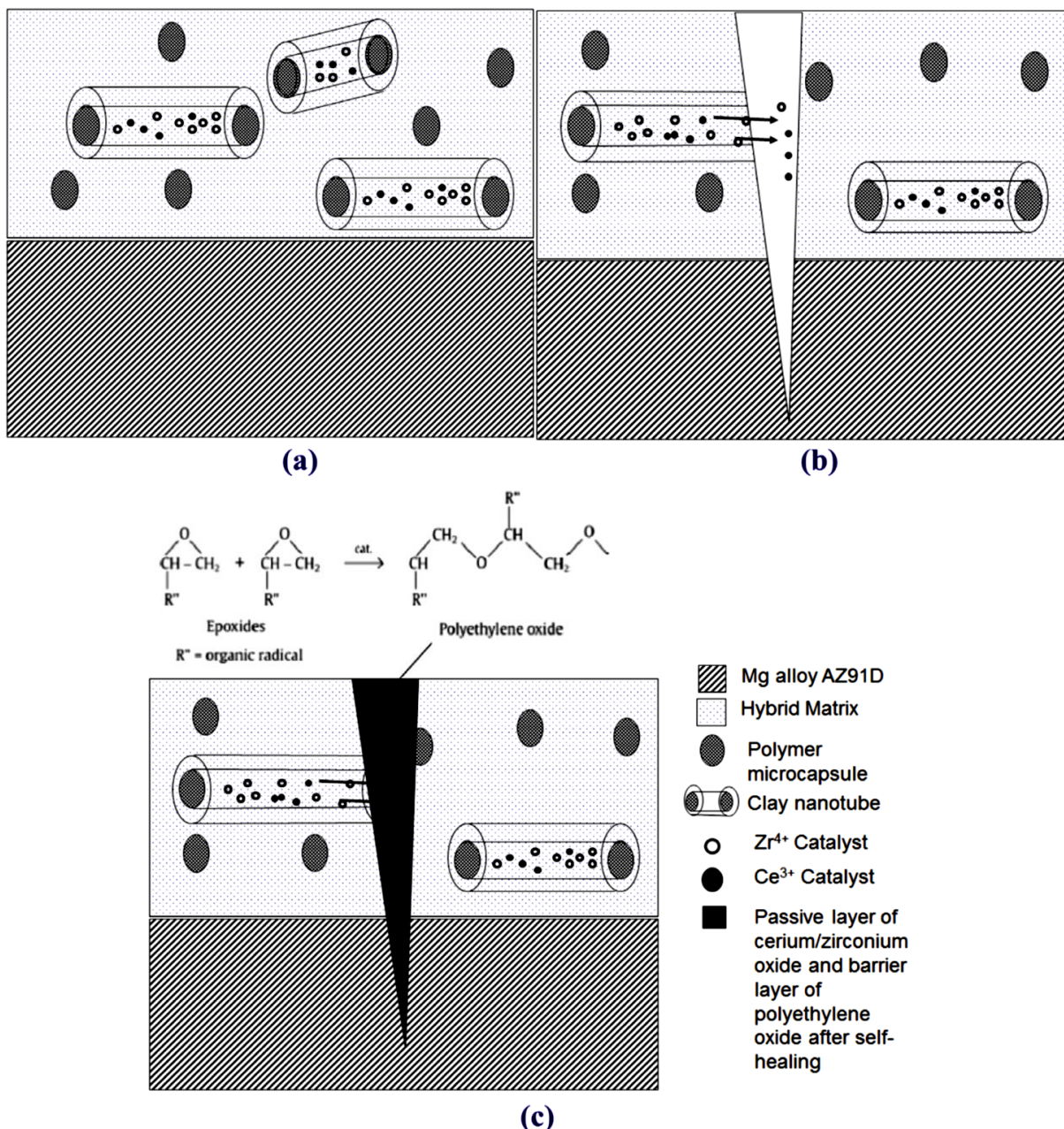


Fig. 1.13. Schematic representation of HNTs as nano reservoirs for self-healing mechanism (a) as-generated coating, (b) after crack initiation and (c) self-healing layer formation [103].

Use of HNTs as smart nano containers have been found to be promising because of their ability to load various active agents like corrosion inhibitors, drugs, catalysts and monomers, etc. In addition, being biocompatible and cost-effective makes HNTs a promising carrier [100]. These nanotubes possess larger surface area and pore volumes and it can be increased by acid treatment of lumen, which further enhances the loading capacity [104].

Several investigations have been carried out on loading of various corrosion inhibitors into halloysite nanotubes. The corrosion inhibitors such as 2-mercaptobenzothiazole (2-MBT), benzotriazole (BTA), 8-hydroxyquinoline, inorganic phosphates, iron oxide, Pr and dodecylamine etc., have been loaded into the lumen of HNTs.

Abdullayev et al [105] have carried out loading of HNTs with different anionic corrosion inhibitors such as BTA, 2-mercaptobenzimidazole and 2-MBT. These loaded HNTs have been doped into polyurethane and acrylic paints for the corrosion protection of copper alloys. Shchukin et al [99] have incorporated 2-MBT into HNTs and the loaded HNTs have been modified by several alternate polyelectrolyte layers of (poly(allylamine hydrochloride)/poly(styrene sulfonate)). The corrosion protection ability of these loaded and modified HNTs was studied by dispersing into silica-zirconia sol-gel matrix. The coatings were applied on to AA2024-T3 alloy substrates. Zahidah et al [106] have used benzimidazole as the corrosion inhibitor to load inside the HNT lumen. They have studied the corrosion protection ability of these loaded HNTs which are dispersed into epoxy matrix and applied on carbon steel substrates. Benzimidazole HNT-epoxy coatings exhibited higher corrosion resistance after 6 days of exposure to 3.5% NaCl solution. Fix et al [107] have studied the anticorrosion properties of coatings containing BTA and 8-hydroxyquinoline (8-HQ) loaded HNTs in ZrO_2 - SiO_2 hybrid sol-gel matrix which were generated on AA2024 substrates. The self-healing property of these coatings were evaluated by using scanning vibrating electrode technique (SVET) and found that coatings generated with loaded HNT exhibited better corrosion protection property than only sol-gel coating and pure HNT dispersed sol-gel coating. A comparative study on effect of different inhibitors loaded HNTs for the corrosion protection of steel substrates was carried out by Shchukina et al [108]. Three different corrosion inhibitors Halox 520, Korantin SMK and $(NH_4)_2TiF_6$ were loaded into HNTs and dispersed in poly epoxy based matrix. 1 wt % of inhibitor loaded HNTs based polyepoxy coatings were compared with standard polyepoxy coating having 20 wt % of zinc phosphate as inhibiting pigment. Corrosion performance of these coatings were tested by Neutral salt spray. It has been found that encapsulated HNTs based coatings have shown similar corrosion protection compared to standards even though in very low concentrations due to effective isolation of corrosion inhibitor from matrix because of nanocontainers. Shchukina et al [109] have developed polyester powder coatings containing HNTs and mesoporous silica nanoparticles as the nanocontainers that were loaded with 8-HQ on low carbon steel. They have reported that 2 wt % of loaded HNT/mesoporous silica nanoparticles decreased the delamination effect more than four times than that of only commercial polyester coating and

also the direct addition of inhibitor resulted in delamination of coating in neutral salt spray test. Dong et al [110] have generated epoxy coatings on copper substrates, in which two types of pH responsive corrosion inhibitors L-valine and 2-MBT encapsulated into HNTs. 2-MBT loaded HNTs were further covered with poly electrolyte layer. The corrosion inhibition efficiency was found to be more in case of 2-MBT loaded HNTs than L-valine loaded HNTs with 20 mM concentration. However, the artificial cross scratch experiment has revealed that coatings derived from L-valine loaded HNTs have shown four times more corrosion resistance than 2-MBT loaded HNTs. Vijayan et al [111] have reported the use of HNTs as the multifunctional filler in epoxy coatings. In this, epoxy monomer loaded HNTs were incorporated into epoxy coating together with the amine hardener immobilized mesoporous silica. The loaded HNTs were found to have the reduced wettability and thus improved the waterproofing properties. The increased amount of loaded HNTs improved the barrier property of coatings by reducing the porosity and altering the diffusion path. Sun et al [112] have developed plasma electrolytic oxidation (PEO) coatings on AM50 Mg alloy using silicate based electrolyte containing BTA loaded HNTs. The PEO coatings with BTA-HNT were found to give the superior corrosion protection and could inhibit the pitting by self-healing action. The corrosion rate initially increased, but later the self-healing was achieved by formation of a dense $Mg(OH)_2$ formation mediated by BTA in the corrosion sites. Joshi et al [113] studied effect of different triazole-based corrosion inhibitors loaded HNTs on ASTM A366 mild steel plates. In this, three corrosion inhibitors BTA, MBI and 2-MBT have been incorporated into HNTs. The loaded HNTs were then capped at the ends of the tubes using urea-formaldehyde (UF) and copper ions and were dispersed in oil-based alkyd paint. Release kinetics revealed that MBI released slowly and provided better corrosion resistance when compared to other inhibitors. Presence of tube end stoppers resulted in the controlled release. SVET results showed that MBI and BTA loaded and stoppered HNTs contained in paint exhibited significant improvement of corrosion protection.

Zheng et al [114] have shown that iron oxide nanoparticles can be loaded into the lumen of HNTs. They synthesized Fe_2O_3 particles selectively inside the lumen of HNTs by the diffusion of Fe^{3+} and Fe^{2+} ions into the lumen of HNTs, due to the alkaline environment created because of hydrolysis of urea in presence of urease catalyst. Fe_2O_3 were formed inside the lumen and they reported that, these Fe_2O_3 loaded HNTs can be used for immobilization of photocatalysis and adsorption of contaminants. The HNTs can be removed easily after the adsorption of contaminants by applying the magnetic field. Mahmoudi et al [115] have reported praseodymium (Pr) loaded HNTs for the corrosion protection of magnesium alloy

AZ31. The Pr inhibitor was loaded after etching the HNT lumen with H_2SO_4 to enhance the lumen diameter. Pr loaded HNTs and encapsulated with urea-formaldehyde to prevent the release of inhibitors and were dispersed in the silane matrix. The corrosion protection performance of nanocontainer-based silane coatings was investigated with and without epoxy matrix. Pr loaded silane coatings were found to provide good corrosion protection by forming a passive layer of oxides/ hydroxides of Pr. Falcón et al [116] have used dodecylamine loaded HNTs as the nanocontainers for corrosion protection of AISI 1020 carbon steel substrates. The inhibitor loaded HNTs were dispersed into alkyd primer and coated substrates were tested for their anticorrosion property by EIS and SVET measurements. These results revealed that dodecylamine loaded HNT-based coating were able to provide the self-healing corrosion protection.

In order to enhance the loading of active materials inside the lumen as well as their surface adsorption, researchers from different fields like drug industry, corrosion protection and catalysis have been focusing on the etching of HNTs. HNTs being tubular in nature with rolled sheets of inner alumina and outer silica, the lumen can be selectively etched by using different acids [117] .

Garcia-Garcia et al [117] have used different acids such as sulphuric, acetic and acrylic acid to study the effect of these acids on the selective surface etching of HNTs. Zhang et al [118] have carried out systematic investigation on effect of sulphuric acid on physico-chemical and pore characteristics of HNTs for adsorption of methylene blue. They have studied the effect of acid treatment by etching for 21 h. BET analysis has shown that the surface area and pore volume increase till 13 h and decreased thereafter, which was found due to disaggregation of silica layers. TEM analysis showed that after acid treatment, the obtained HNTs were in the form of porous nanorods of amorphous silica. Shu et al. [119] have carried out selective etching of inner alumina lumen or outer silicate layer by using acid (HCl) and alkali (NaOH) and pre-calcination. They have reported that, meso or microporous silica nanotubes were obtained by acid etching and pre-calcination at 850° C. Mesoporous alumina rich nanotubes were obtained by alkali etching and pre-calcination at 1000° C. These modified HNTs were found to exhibit improved methylene blue dye adsorption. Moeinpour et al [120] have carried out selective etching of HNT lumen using 2 M H_2SO_4 and calcined HNT to increase loading capacity of losartan, a high blood pressure controlling drug.

1.7.2.5. Montmorillonite nanoclay

Montmorillonite (MMT) layered clays are naturally occurring materials belong to smectite group and most common components of soil. MMT has three-dimensional plates, containing thousands of silicates belonging to 2:1 phyllosilicates [121]. It is made up of negatively charged layers composed of two tetrahedral silica sheets sandwiching a central octahedral sheet containing cations. The existence of isomorphous substitutions in the central octahedral sheet is the origin of the negative charge in the silicate layers, which is compensated by cations (exchangeable cations) as other framework ions located in the interlayer space as given in Fig. 1.14. Hence, the cationic corrosion inhibitors can be incorporated to into the interlayers of MMT to generate the corrosion protection coatings [122].

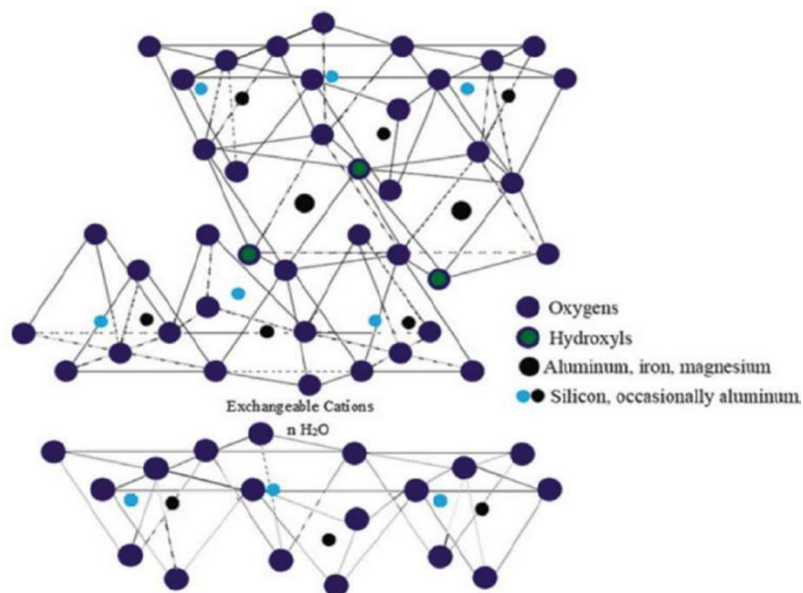


Fig. 1.14. Structure of montmorillonite clay [123].

Cationic inhibitor incorporated montmorillonite clays also have been investigated extensively for corrosion protection studies [124,125]. Deflorian et al [124] have studied the barrier properties of montmorillonite dispersed with different amounts in the sol-gel matrix and also the effect of CeO_2 and Ce_2O_3 enriched montmorillonite on galvanized steel sheet. Carbonell et al [125] have studied the barrier property and corrosion protection behaviour of different inhibitors like BTA, Na-(diethyl(dithiocarbamate)), piperazine in sol-gel matrix and Ce(III) modified montmorillonite in sol-gel matrix by scanning electrochemical microscopy

on AA2024-T3. Coatings based on Ca^{2+} modified Na-bentonite clay dispersed in alkyd primer for aluminum 1050 plates have been developed by Vega et al [126]. EIS studies revealed that the formation of passive layer between coating and surface due to the release of Ca^{2+} and formation of insoluble calcium deposits. The coated panels with Ca-bentonite in salt spray test have shown blisters and slight delamination of coating at shorter durations of exposure, whereas these Ca-bentonite-based coatings were found to have better barrier properties in condensing humidity test and Kesternich test, Bohm et al [127] have carried out Ca^{2+} exchange with Na-bentonite, dispersed in polyester-resin based primer having the pigment with volume concentration of 19%. The calcium exchanged silica pigment (Shieldex) and strontium chromate primer systems were coated on Zn pre-treated galvanized steel followed by a topcoat of polyester. They have used scanning reference electrode technique (SRET) to measure the electrical potential in solution at known distance above a corroding metal surface, relative to a remote reference electrode. These SRET potentials are determined by the flow of ionic current flux through the electrolyte between sites of localised anodic and cathodic activity. SRET measurements in 5 wt % NaCl up to 24 h have shown that Ce-exchanged bentonite exhibited better localised inhibition efficiency than that of strontium chromate and shieldex. Salt spray test results showed that, after 1000 h of exposure, Ce and Ca exchanged bentonites showed very less delamination rate of coatings near cut edge of panels than that of chromates and shieldex based primer coatings. Dong et al [128] have synthesized Ca exchanged MMT from Na-MMT and Mg-Al-LDH modified with NaVO_3 . Ca-MMT and Mg-Al-LDH were dispersed in epoxy resin and deposited over steel Q345 panels. EIS results indicated that the Ca-MMT based epoxy coatings found to have better corrosion protection than that of Mg-Al-LDH based coatings. Ghazi et al [129] have used Na-MMT for exchanging zinc cations and BIA with Na ions. The protective performance the developed coatings were studied by dispersing the individual modified MMTs as well as combinedly in epoxy ester matrix. EIS results indicated that both Zn and BIA intercalated MMT based epoxy ester coatings exhibited better corrosion resistance after 25 days of exposure to 3.5 wt % NaCl solution. The self-healing behaviour of coatings was evaluated by artificially scribing on the coating and exposing to 3.5 wt % for 5 h and 8 h. They have reported that Zn and BIA were found to leach from coating near the scratched area After 5 h of exposure and it was observed that and after 8 h, the inhibitors were found in scribed area as observed from EDS elemental mapping.

Darmiani et al [130] have studied synergistic effect of montmorillonite, cerium nitrate nanocomposites based epoxy coatings on cold rolled steel panels. These coatings have shown

better corrosion protection by inhibited corrosion activity in the scribed area. Motte et al [131] modified Na-MMT by rare earth salt such as Ce (Ce-MMT) and dispersed in three different silanes for corrosion protection of hot dip galvanized steel. The modified clay was analysed for intercalation using X-ray fluorescence spectroscopy (XRF) and XRD. A comparative corrosion resistance study of coatings composed of 2 wt % of Na-MMT and Ce-MMT was carried out by EIS in 0.1 M NaCl solution for 96 h. Ce-MMT was found to inhibit the progressive loss of barrier property of silane coatings for longer durations of exposure to the corrosive medium. Swapnil et al [132] intercalated $\text{Ce}^{3+}/\text{Zr}^{4+}$ cations in to Al pillared MMT, dispersed the loaded MMT into hybrid silica matrix and generated coatings on Mg alloy. The intercalation of cations into pillared clay was confirmed by small angle X-ray scattering (SAXS) analysis and XRD patterns. The anticorrosion properties and self-healing ability of coatings were evaluated by EIS/polarization and SVET, respectively.

Objectives of the present work

In view of the aforementioned discussion on the urgent need for replacement of hexavalent chrome-based coatings on aluminum alloys, the present work was carried out. The objective of the work was to find out an “environment friendly and cost-effective” replacement for chromium conversion coatings on aluminum alloys. In this context, halloysite nanotubes and montmorillonite nanoclay have been chosen as the nanocontainers due to their ease of use and being biocompatible, environment friendly and cost-effective. Two different cationic corrosion inhibitors namely Ce^{3+} and Zr^{4+} ions for encapsulation into the nanoclays have been investigated. The organic-inorganic hybrid sol was used as the matrix formulation for dispersion of loaded nanocontainers. The coatings were deposited onto the aluminum alloys AA2024-T4 and A356.0, which are used as structural materials in aircraft and automobile industries respectively. Extensive analysis of the protective and self-healing efficiencies of the inhibitor loaded nanocontainer-based sol-gel coatings have been carried out by electrochemical techniques such as electrochemical impedance spectroscopy, potentiodynamic polarization and accelerated salt spray tests. Localized analytical techniques like scanning vibrating electrode technique was employed to study the self-healing property. A comparison of performance of halloysite nanotubes and layered nanoclays as smart nanocontainers was made with respect to their self-healing abilities. Further studies were extended to use combination of loaded nanocontainers and modification of inner lumen of HNTs by etching. The corrosion protection behavior of these

coatings was investigated to arrive at efficient strategies for the fabrication of self-healing coatings on AA2024-T4 and A356.0 alloys. Therefore, this present research work has been organized as seven thesis chapters as mentioned below.

- ❖ CHAPTER - 1: Introduction
- ❖ CHAPTER - 2: Experimental
- ❖ CHAPTER - 3: Halloysite Clay Nanotubes as Nanocontainers for Self-healing Corrosion Protection Coatings on A2024-T4 and A356.0.
- ❖ CHAPTER - 4: Layered Montmorillonite Nanoclay as Nanocontainers for Self-healing Coatings on AA2024-T4 and A356.0.
- ❖ CHAPTER - 5: Synergistic Effect of Halloysite and Montmorillonite Nanocontainer-based Coatings for the Corrosion Protection of AA2024-T4.
- ❖ CHAPTER - 6: Effect of Etching of Halloysite Nanotubes on Loading and Corrosion Protection of AA2024-T4.
- ❖ CHAPTER - 7: Summary and Conclusions.

References

- [1] C. Vargel, Corrosion of Aluminium, Elsevier, (2004) 1-626. doi:10.1016/B978-0-08-044495-6.X5000-9.
- [2] Global aluminium production growth brakes sharply in 2018, (2019) 1–7.
- [3] J.C. Benedyk, Aluminum alloys for lightweight automotive structures, Materials, Design and Manufacturing for Lightweight Vehicles, Elsevier, (2010) 79–113. doi:10.1533/9781845697822.1.79.
- [4] J.R. Davis, Corrosion of aluminum and aluminum alloys, ASM International, (1999) 73–2798. doi:10.1361/caaa1999p001.
- [5] M. Pourbaix, Atlas of electrochemical equilibria in aqueous solutions, Journal of Electroanalytical Chemistry and Interfacial Electrochemistry, (1974) 644.
- [6] K. Shimizu, R.C. Furneaux, G.E. Thompson, G.C. Wood, A. Gotoh, K. Kobayashi, On the nature of “easy paths” for the diffusion of oxygen in thermal oxide films on aluminum, Oxidation of Metals. 35 (1991) 427–439. doi:10.1007/BF00664713.
- [7] G. Svenningsen, Corrosion of Aluminium Alloys, 1 (1992) 7491.
- [8] P.R. Roberge, Handbook of corrosion engineering, McGraw-Hill, (2000) 335-337. doi:10.5860/choice.37-5122
- [9] K. Nisancioglu, Corrosion of aluminium alloys, in: Proceedings of ICAA3, (1992) 239–259.
- [10] J.R. et al Davis, Metals Handbook, 9th ed., ASM International, (1987) 583-609.
- [11] P. Droniou, W.E. Fristad, J.L. Liang, Nanoceramic-based conversion coating, Metal Finishing. 103 (2005) 41–43. doi:10.1016/S0026-0576(05)80849-9.
- [12] J. Zhao, L. Xia, A. Sehgal, D. Lu, R.L. McCreery, G.S. Frankel, Effects of chromate and chromate conversion coatings on corrosion of aluminum alloy 2024-T3, Surface and Coatings Technology. 140 (2001) 51–57. doi:10.1016/S0257-8972(01)01003-9.
- [13] R. Figueira, I. Fontinha, C. Silva, E. Pereira, Hybrid Sol-Gel Coatings: Smart and Green Materials for Corrosion Mitigation, Coatings. 6 (2016) 12. doi:10.3390/coatings6010012.
- [14] A.A.O. Magalhães, B. Tribollet, O.R. Mattos, I.C.P. Margarit, O.E. Barcia, Chromate conversion coatings formation on zinc studied by electrochemical and electrohydrodynamical impedances, Journal of the Electrochemical Society. 150 (2003) 16–25. doi:10.1149/1.1528196.
- [15] B.L. Bramfitt, Carbon and Alloy Steels, in: M. Kutz (Ed.), Handbook of Materials

Selection, John Wiley & Sons, Inc., Hoboken, NJ, USA, (2002) 27–64. doi:10.1002/0471777447.ch1.

- [16] J.H. Osborne, Observations on chromate conversion coatings from a sol-gel perspective, *Progress in Organic Coatings*. 41 (2001) 280–286. doi:10.1016/S0300-9440(01)00143-6.
- [17] D. Wang, G.P. Bierwagen, Sol-gel coatings on metals for corrosion protection, *Progress in Organic Coatings*. 64 (2009) 327–338. doi:10.1016/j.porgcoat.2008.08.010.
- [18] B. Babiarczuk, A. Szczurek, A. Donesz-Sikorska, I. Rutkowska, J. Krzak, The influence of an acid catalyst on the morphology, wettability, adhesion and chemical structure properties of TiO₂ and ZrO₂ sol–gel thin films, *Surface and Coatings Technology*. 285 (2016) 134–145. doi:10.1016/j.surfcoat.2015.11.030.
- [19] C. Sanchez, P. Belleville, M. Popall, L. Nicole, Hybrid materials themed issue, *Chemical Society Reviews*. 40 (2011) 453–1152.
- [20] C.J. Brinker, G.W. Scherer, *Sol gel science: The Physics and Chemistry of Sol-Gel Processing*, Academic Press, Boston ,USA, 1990 1-228..
- [21] M.A. Aegerter, M. Menning, *Sol-Gel Technologies for Glass Producers and Users*, Springer US, Boston, MA, (2004) 3-486. doi:10.1007/978-0-387-88953-5_21.
- [22] D. Balgude, A. Sabnis, Sol-gel derived hybrid coatings as an environment friendly surface treatment for corrosion protection of metals and their alloys, *Journal of Sol-Gel Science and Technology*. 64 (2012) 124–134. doi:10.1007/s10971-012-2838-z.
- [23] H. Dislich, Glassy and crystalline systems from gels: Chemical basis and technical application, *Journal of Non-Crystalline Solids*. 57 (1983) 371–388. doi:10.1016/0022-3093(83)90425-8.
- [24] J. Wen, G.L. Wilkes, Organic/inorganic hybrid network materials by the sol-gel approach, *Chemistry of Materials*. 8 (1996) 1667–1681. doi:10.1021/cm9601143.
- [25] H. Schmidt, G. Jonschker, S. Goedicke, M. Menning, The Sol-Gel Process as a Basic Technology for Nanoparticle-Dispersed-Inorganic-Organic Composites, *Journal of Sol-Gel Science and Technology*. 19 (2000) 39–51. doi:10.1023/A:1008706003996.
- [26] S.K. Rahimi, R. Potrekar, N.K. Dutta, N.R. Choudhury, Anticorrosive interfacial coatings for metallic substrates, *Surface Innovations*. 1 (2013) 112–137. doi:10.1680/si.13.00004.
- [27] T.P. Chou, C. Chandrasekaran, S.J. Limmer, S. Seraji, Y. Wu, Organic - inorganic hybrid coatings for corrosion protection, *Journal of Non-Crystalline Solids*. 290 (2001) 153–162.

- [28] P. Innocenzi, G. Brusatin, M. Guglielmi, R. Bertani, New synthetic route to (3-glycidoxypropyl)trimethoxysilane-based hybrid organic-inorganic materials, *Chemistry of Materials*. 11 (1999) 1672–1679. doi:10.1021/cm980734z.
- [29] D. Wang, G.P. Bierwagen, Sol-gel coatings on metals for corrosion protection, *Progress in Organic Coatings*. (2009) 327-338. doi:10.1016/j.porgcoat.2008.08.010.
- [30] C.J. Brinker, A.J. Hurd, P.R. Schunk, G.C. Frye, C.S. Ashley, Review of sol-gel thin film formation, *Journal of Non-Crystalline Solids*. 147&148 (1992) 424–436. doi:10.1016/S0022-3093(05)80653-2.
- [31] A. Conde, A. Durán, J.J. De Damborenea, Polymeric sol-gel coatings as protective layers of aluminium alloys, *Progress in Organic Coatings*. 46 (2003) 288–296. doi:10.1016/S0300-9440(03)00014-6.
- [32] Y. Castro, B. Ferrari, R. Moreno, A. Durán, Corrosion behaviour of silica hybrid coatings produced from basic catalysed particulate sols by dipping and EPD, *Surface and Coatings Technology*. 191 (2005) 228–235. doi:10.1016/j.surfcoat.2004.03.001.
- [33] T. Gunji, Y. Iizuka, K. Arimitsu, Y. Abe, Preparation and properties of alkoxy(methyl)silsesquioxanes as coating agents, *Journal of Polymer Science, Part A: Polymer Chemistry*. 42 (2004) 3676–3684. doi:10.1002/pola.20233.
- [34] R.L. Parkhill, E.T. Knobbe, M.S. Donley, Application and evaluation of environmentally compliant spray-coated ormosil films as corrosion resistant treatments for aluminum 2024-T3, *Progress in Organic Coatings*. 41 (2001) 261–265. doi:10.1016/S0300-9440(01)00138-2.
- [35] T.P. Chou, C. Chandrasekaran, G.Z. Cao, Sol-gel-derived hybrid coatings for corrosion protection, *Journal of Sol-Gel Science and Technology*, 26 (2003) 321–327. doi:10.1023/A:1020736107842.
- [36] A.G. Kannan, N.R. Choudhury, N.K. Dutta, Electrochemical performance of sol-gel derived phospho-silicate-methacrylate hybrid coatings, *Journal of Electroanalytical Chemistry*. 641 (2010) 28–34. doi:10.1016/j.jelechem.2010.01.016.
- [37] M. Criado, I. Sobrados, J. Sanz, J.M. Bastidas, Steel protection using sol-gel coatings in simulated concrete pore solution contaminated with chloride, *Surface and Coatings Technology*. 258 (2014) 485–494. doi:10.1016/j.surfcoat.2014.08.051.
- [38] S. Kirtay, Preparation of hybrid silica sol–gel coatings on mild steel surfaces and evaluation of their corrosion resistance, *Progress in Organic Coatings*. (2014). doi:10.1016/j.porgcoat.2014.06.016.
- [39] I. Santana, A. Pepe, E. Jimenez-Pique, S. Pellice, S. Ceré, Silica-based hybrid coatings

for corrosion protection of carbon steel. Part I: Effect of pretreatment with phosphoric acid, *Surface and Coatings Technology*. 236 (2013) 476–484. doi:10.1016/j.surfcoat.2012.07.086.

[40] N. Kumar, A. Jyothirmayi, K.R.C. Soma Raju, R. Subasri, Effect of functional groups (methyl, phenyl) on organic-inorganic hybrid sol-gel silica coatings on surface modified SS 316, *Ceramics International*. 38 (2012) 6565–6572. doi:10.1016/j.ceramint.2012.05.040.

[41] S.R. Davis, A.R. Brough, A. Atkinson, Formation of silica/epoxy hybrid network polymers, *Journal of Non-Crystalline Solids*. 315 (2003) 197–205. doi:10.1016/S0022-3093(02)01431-X.

[42] A.J. Vreugdenhil, V.N. Balbyshev, M.S. Donley, Nanostructured silicon sol-gel surface treatments for Al 2024-T3 protection, *Journal of Coatings Technology*. 73 (2001) 35–43. doi:10.1007/bf02730029.

[43] M.S. Donley, R.A. Mantz, A.N. Khramov, V.N. Balbyshev, L.S. Kasten, D.J. Gaspar, The self-assembled nanophase particle (SNAP) process: A nanoscience approach to coatings, *Progress in Organic Coatings*. 47 (2003) 401–415. doi:10.1016/j.porgcoat.2003.08.017.

[44] E. Roussi, A. Tsetsekou, D. Tsiorvas, A. Karantonis, Novel hybrid organo-silicate corrosion resistant coatings based on hyperbranched polymers, *Surface and Coatings Technology*. 205 (2011) 3235–3244. doi:10.1016/j.surfcoat.2010.11.037.

[45] S.S. Pathak, A.S. Khanna, Investigation of anti-corrosion behavior of waterborne organosilane-polyester coatings for AA6011 aluminum alloy, *Progress in Organic Coatings*. 65 (2009) 288–294. doi:10.1016/j.porgcoat.2008.12.006.

[46] T.L. Metroke, O. Kachurina, E.T. Knobbe, Spectroscopic and corrosion resistance characterization of GLYMO-TEOS Ormosil coatings for aluminum alloy corrosion inhibition, *Progress in Organic Coatings*. 44 (2002) 295–305. doi:10.1016/S0300-9440(02)00063-2.

[47] N.C. Rosero-Navarro, S.A. Pellice, A. Durán, M. Aparicio, Effects of Ce-containing sol-gel coatings reinforced with SiO₂ nanoparticles on the protection of AA2024, *Corrosion Science*. 50 (2008) 1283–1291. doi:10.1016/j.corsci.2008.01.031.

[48] Y.J. Du, M. Damron, G. Tang, H. Zheng, C.J. Chu, J.H. Osborne, Inorganic/organic hybrid coatings for aircraft aluminum alloy substrates, *Progress in Organic Coatings*. 41 (2001) 226–232. doi:10.1016/S0300-9440(01)00133-3.

[49] M.L. Zheludkevich, I.M. Salvado, M.G.S. Ferreira, Sol-gel coatings for corrosion

protection of metals, *Journal of Materials Chemistry*. 15 (2005) 5099–5111. doi:10.1039/b419153f.

[50] N. Pirhady Tavandashti, S. Sanjabi, T. Shahrabi, Corrosion protection evaluation of silica/epoxy hybrid nanocomposite coatings to AA2024, *Progress in Organic Coatings*. 65 (2009) 182–186. doi:10.1016/j.porgcoat.2008.10.010.

[51] N.N. Voevodin, N.T. Grebasch, W.S. Soto, L.S. Kasten, J.T. Grant, F.E. Arnold, M.S. Donley, An organically modified zirconate film as a corrosion-resistant treatment for aluminum 2024-T3, *Progress in Organic Coatings*. 41 (2001) 287–293. doi:10.1016/S0300-9440(01)00156-4.

[52] M.L. Zheludkevich, R. Serra, M.F. Montemor, I.M. Miranda Salvado, M.G.S. Ferreira, Corrosion protective properties of nanostructured sol-gel hybrid coatings to AA2024-T3, *Surface and Coatings Technology*. 200 (2006) 3084–3094. doi:10.1016/j.surfcoat.2004.09.007.

[53] S. V Lamaka, M.L. Zheludkevich, K.A. Yasakau, M.F. Montemor, P. Cecílio, M.G.S. Ferreira, TiO_x self-assembled networks prepared by templating approach as nanostructured reservoirs for self-healing anticorrosion pre-treatments, *Electrochemistry Communications*. 8 (2006) 421–428. doi:10.1016/j.elecom.2005.12.019.

[54] D.G. Shchukin, M. Zheludkevich, K. Yasakau, S. Lamaka, M.G.S. Ferreira, H. Möhwald, Layer-by-layer assembled nanocontainers for self-healing corrosion protection, *Advanced Materials*. 18 (2006) 1672–1678. doi:10.1002/adma.200502053.

[55] J. Tedim, S.K. Poznyak, A. Kuznetsova, D. Raps, T. Hack, M.L. Zheludkevich, M.G.S. Ferreira, Enhancement of active corrosion protection via combination of inhibitor-loaded nanocontainers, *ACS Applied Materials and Interfaces*. 2 (2010) 1528–1535. doi:10.1021/am100174t.

[56] T.T.H. Nguyen, B.T. Le, T.A. Nguyen, Inhibitor-loaded silica nanoparticles for self-healing metal coating, *Smart Nanocontainers*, Elsevier, (2020) 431–441. doi:10.1016/B978-0-12-816770-0.00025-3.

[57] E. V. Skorb, D. Fix, D. V. Andreeva, H. Möhwald, D.G. Shchukin, Surface-modified mesoporous SiO₂ containers for corrosion protection, *Advanced Functional Materials*. 19 (2009) 2373–2379. doi:10.1002/adfm.200801804.

[58] T. Mishra, A.K. Mohanty, S.K. Tiwari, Recent Development in clay based functional coating for corrosion protection, *Key Engineering Materials*. 571 (2013) 93–109. doi:10.4028/www.scientific.net/KEM.571.93.

[59] G. Lanzara, Y. Yoon, H. Liu, S. Peng, W.I. Lee, Carbon nanotube reservoirs for self-healing materials, *Nanotechnology*. 20 (2009) 335704- 335710. doi:10.1088/0957-4484/20/33/335704.

[60] J. Tedim, M.L. Zheludkevich, A.N. Salak, A. Lisenkov, M.G.S. Ferreira, Nanostructured LDH-container layer with active protection functionality, *Journal of Materials Chemistry*. 21 (2011) 15464–15470. doi:10.1039/c1jm12463c.

[61] M.F. Montemor, D. V. Snihirova, M.G. Taryba, S. V. Lamaka, I.A. Kartsonakis, A.C. Balaskas, G.C. Kordas, J. Tedim, A. Kuznetsova, M.L. Zheludkevich, M.G.S. Ferreira, Evaluation of self-healing ability in protective coatings modified with combinations of layered double hydroxides and cerium molibdate nanocontainers filled with corrosion inhibitors, *Electrochimica Acta*. 60 (2012) 31–40. doi:10.1016/j.electacta.2011.10.078.

[62] X. Shi, T.A. Nguyen, Z. Suo, Y. Liu, R. Avci, Effect of nanoparticles on the anticorrosion and mechanical properties of epoxy coating, *Surface and Coatings Technology*. 204 (2009) 237–245. doi:10.1016/j.surfcoat.2009.06.048.

[63] H. Wei, Y. Wang, J. Guo, N.Z. Shen, D. Jiang, X. Zhang, X. Yan, J. Zhu, Q. Wang, L. Shao, H. Lin, S. Wei, Z. Guo, Advanced micro/nanocapsules for self-healing smart anticorrosion coatings, *Journal of Materials Chemistry A*. 3 (2015) 469–480. doi:10.1039/c4ta04791e.

[64] T.A. Nguyen, A.A. Assadi, Smart Nanocontainers: Preparation, Loading/Release Processes and Applications, *Kenkyu Journal of Nanotechnology & Nanoscience*. 4 (2018) 10–13. doi:10.31872/2018/KJNN-S1-100101.

[65] M.F. Montemor, Functional and smart coatings for corrosion protection : A review of recent advances, *Surface and Coatings Technology*. 258 (2014) 17–37. doi:10.1016/j.surfcoat.2014.06.031.

[66] A.A. Nazeer, M. Madkour, Potential use of smart coatings for corrosion protection of metals and alloys: A review, *Journal of Molecular Liquids*. 253 (2018) 11–22. doi:10.1016/j.molliq.2018.01.027.

[67] S.K. Ghosh, Functional Coatings by polymer microencapsultion, Wiley-VCH Verlag GmbH & Co. KGaA, (2006) 1-357. doi:10.1002/3527608478.

[68] M. Samadzadeh, S.H. Boura, M. Peikari, S.M. Kasiriha, A. Ashrafi, A review on self-healing coatings based on micro/nanocapsules, *Progress in Organic Coatings*. 68 (2010) 159–164. doi:10.1016/j.porgcoat.2010.01.006.

[69] A.S. Jones, J.D. Rule, J.S. Moore, N.R. Sottos, S.R. White, Life extension of self-healing polymers with rapidly growing fatigue cracks, *Journal of the Royal Society Interface*. 4

(2007) 395–403. doi:10.1098/rsif.2006.0199.

[70] M.M. Caruso, B.J. Blaiszik, H. Jin, S.R. Schelkopf, D.S. Stradley, N.R. Sottos, S.R. White, J.S. Moore, Robust, double-walled microcapsules for self-healing polymeric materials, *ACS Applied Materials and Interfaces.* 2 (2010) 1195–1199. doi:10.1021/am100084k.

[71] B.J. Blaiszik, N.R. Sottos, S.R. White, Nanocapsules for self-healing materials, *Composites Science and Technology.* 68 (2008) 978–986. doi:10.1016/j.compscitech.2007.07.021.

[72] S.R. White, N.R. Sottos, P.H. Geubelle, J.S. Moore, M.R. Kessler, S.R. Sriram, E.N. Brown, S. Viswanathan, Autonomic healing of polymer composites, *Nature.* 409 (2001) 794–797. doi:10.1038/35057232.

[73] F. Maia, K.A. Yasakau, J. Carneiro, S. Kallip, J. Tedim, T. Henriques, A. Cabral, J. Venâncio, M.L. Zheludkevich, M.G.S. Ferreira, Corrosion protection of AA2024 by sol-gel coatings modified with MBT-loaded polyurea microcapsules, *Chemical Engineering Journal.* 283 (2016) 1108–1117. doi:10.1016/j.cej.2015.07.087.

[74] F. Cotting, I.V. Aoki, Smart protection provided by epoxy clear coating doped with polystyrene microcapsules containing silanol and Ce (III) ions as corrosion inhibitors, *Surface and Coatings Technology.* 303 (2016) 310–318. doi:10.1016/j.surfcoat.2015.11.035.

[75] K. Thanawala, N. Mutneja, A.S. Khanna, R.K. Singh Raman, Development of self-healing coatings based on linseed oil as autonomous repairing agent for corrosion resistance, *Materials.* 7 (2014) 7324–7338. doi:10.3390/ma7117324.

[76] S. Ataei, S.N. Khorasani, R. Torkaman, R.E. Neisiyan, M.S. Koochaki, Self-healing performance of an epoxy coating containing microencapsulated alkyd resin based on coconut oil, *Progress in Organic Coatings.* 120 (2018) 160–166. doi:10.1016/j.porgcoat.2018.03.024.

[77] D. Sun, Y.B. Chong, K. Chen, J. Yang, Chemically and thermally stable isocyanate microcapsules having good self-healing and self-lubricating performances, *Chemical Engineering Journal.* 346 (2018) 289–297. doi:10.1016/j.cej.2018.04.046.

[78] M. Huang, H. Zhang, J. Yang, Synthesis of organic silane microcapsules for self-healing corrosion resistant polymer coatings, *Corrosion Science.* 65 (2012) 561–566. doi:10.1016/j.corsci.2012.08.020.

[79] Y. Zhao, W. Zhang, L.P. Liao, S.J. Wang, W.J. Li, Self-healing coatings containing microcapsule, *Applied Surface Science.* 258 (2012) 1915–1918.

doi:10.1016/j.apsusc.2011.06.154.

[80] M. Izadi, T. Shahrabi, B. Ramezanzadeh, Active corrosion protection performance of an epoxy coating applied on the mild steel modified with an eco-friendly sol-gel film impregnated with green corrosion inhibitor loaded nanocontainers, *Applied Surface Science*. 440 (2018) 491–505. doi:10.1016/j.apsusc.2018.01.185.

[81] S.Y. Kwak, W.M. Kriven, M.A. Wallig, J.H. Choy, Inorganic delivery vector for intravenous injection, *Biomaterials*. 25 (2004) 5995–6001. doi:10.1016/j.biomaterials.2004.01.056.

[82] D. Carriazo, C. Martín, V. Rives, Thermal Evolution of a MgAl Hydrotalcite-Like Material Intercalated with Hexaniobate, *European Journal of Inorganic Chemistry*. 2006 (2006) 4608–4615. doi:10.1002/ejic.200600580.

[83] R. Subasri, S.H. Adsul, S. Manasa, Smart Nanocontainers For Anticorrosion Applications, *Smart Nanocontainers*, Elsevier, (2020) 399–412. doi: 10.1016/b978-0-12-816770-0.00023-x.

[84] J. Tedim, S.K. Poznyak, A. Kuznetsova, D. Raps, T. Hack, M.L. Zheludkevich, M.G.S. Ferreira, Enhancement of active corrosion protection via combination of inhibitor-loaded nanocontainers, *ACS Applied Materials and Interfaces*. 2 (2010) 1528–1535. doi:10.1021/am100174t.

[85] J. Liu, Y. Zhang, M. Yu, S. Li, B. Xue, X. Yin, Influence of embedded ZnAlCe-NO₃-layered double hydroxides on the anticorrosion properties of sol-gel coatings for aluminum alloy, *Progress in Organic Coatings*. 81 (2015) 93–100. doi:10.1016/j.porgcoat.2014.12.015.

[86] J. Hu, M. Gan, L. Ma, Z. Li, J. Yan, J. Zhang, Synthesis and anticorrosive properties of polymer-clay nanocomposites via chemical grafting of polyaniline onto Zn-Al layered double hydroxides, *Surface and Coatings Technology*. 240 (2014) 55–62. doi:10.1016/j.surfcoat.2013.12.012.

[87] A. Sanli, R. Ramalingame, O. Kanoun, Piezoresistive pressure sensor based on carbon nanotubes / epoxy composite under cyclic loading, 2018 IEEE International Instrumentation and Measurement Technology Conference (I2MTC). (2018) 1–5. doi:10.1109/I2MTC.2018.8409527.

[88] M. Ahmadi, O. Zabihi, M. Masoomi, M. Naebe, Synergistic effect of MWCNTs functionalization on interfacial and mechanical properties of multi-scale UHMWPE fibre reinforced epoxy composites, *Composites Science and Technology*. 134 (2016) 1–11. doi:10.1016/j.compscitech.2016.07.026.

[89] P.K. Ghosh, K. Kumar, N. Chaudhary, Influence of ultrasonic dual mixing on thermal and tensile properties of MWCNTs-epoxy composite, *Composites Part B: Engineering*. 77 (2015) 139–144. doi:10.1016/j.compositesb.2015.03.028.

[90] Y. Zhou, J. Wang, Y. Hu, R. O’Hayre, Z. Shao, A porous LiFePO₄ and carbon nanotube composite, *Chemical Communications*. 46 (2010) 7151. doi:10.1039/c0cc01721c.

[91] V.D. Punetha, S. Rana, H.J. Yoo, A. Chaurasia, J.T. McLeskey, M.S. Ramasamy, N.G. Sahoo, J.W. Cho, Functionalization of carbon nanomaterials for advanced polymer nanocomposites: A comparison study between CNT and graphene, *Progress in Polymer Science*. 67 (2017) 1–47. doi:10.1016/j.progpolymsci.2016.12.010.

[92] S.J. Richard Prabakar, M. Pyo, Corrosion protection of aluminum in LiPF₆ by poly(3,4-ethylenedioxythiophene) nanosphere-coated multiwalled carbon nanotube, *Corrosion Science*. 57 (2012) 42–48. doi:10.1016/j.corsci.2011.12.036.

[93] M. Ioni, A. Prun, Polypyrrole/carbon nanotube composites: Molecular modeling and experimental investigation as anti-corrosive coating, *Progress in Organic Coatings*. 72 (2011) 647–652. doi:10.1016/j.porgcoat.2011.07.007.

[94] S. Nezamdoust, D. Seifzadeh, Z. Rajabalizadeh, PTMS/OH-MWCNT sol-gel nanocomposite for corrosion protection of magnesium alloy, *Surface and Coatings Technology*. 335 (2018) 228–240. doi:10.1016/j.surfcoat.2017.12.044.

[95] M. Cui, S. Ren, S. Qiu, H. Zhao, L. Wang, Q. Xue, Non-covalent functionalized multi-wall carbon nanotubes filled epoxy composites: Effect on corrosion protection and tribological performance, *Surface and Coatings Technology*. 340 (2018) 74–85. doi:10.1016/j.surfcoat.2018.02.045.

[96] Y. He, C. Zhang, F. Wu, Z. Xu, Fabrication study of a new anticorrosion coating based on supramolecular nanocontainer, *Synthetic Metals*. 212 (2016) 186–194. doi:10.1016/j.synthmet.2015.10.022.

[97] K. V. Yeole, I.P. Agarwal, S.T. Mhaske, The effect of carbon nanotubes loaded with 2-mercaptobenzothiazole in epoxy-based coatings, *Journal of Coatings Technology and Research*. 13 (2016) 31–40. doi:10.1007/s11998-015-9730-z.

[98] S. Arora, M.Y. Rekha, A. Gupta, C. Srivastava, High Corrosion Resistance Offered by Multi-Walled Carbon Nanotubes Directly Grown Over Mild Steel Substrate, *JOM*. 70 (2018) 2590–2595. doi:10.1007/s11837-018-2768-5.

[99] D.G. Shchukin, S. V. Lamaka, K.A. Yasakau, M.L. Zheludkevich, M.G.S. Ferreira, H. Möhwald, Active anticorrosion coatings with halloysite nanocontainers, *Journal of Physical Chemistry C*. 112 (2008) 958–964. doi:10.1021/jp076188r.

[100] Q. Wang, J. Zhang, Y. Zheng, A. Wang, Adsorption and release of ofloxacin from acid- and heat-treated halloysite, *Colloids and Surfaces B: Biointerfaces*. 113 (2014) 51–58. doi:10.1016/j.colsurfb.2013.08.036.

[101] K. Thanawala, A.S. Khanna, R.K.S. Raman, S. Bohm, Smart anti-corrosive self-healing coatings using halloysite nanotubes as host for entrapment of corrosion inhibitors, *Australasian Corrosion Association Annual Conference: Corrosion and Prevention 2015, ACA 2015*. (2015).

[102] K.A. Zahidah, S. Kakooei, M.C. Ismail, P. Bothi Raja, Halloysite nanotubes as nanocontainer for smart coating application: A review, *Progress in Organic Coatings*. 111 (2017) 175–185. doi:10.1016/j.porgcoat.2017.05.018.

[103] S.H. Adsul, T. Siva, S. Sathiyanarayanan, S.H. Sonawane, R. Subasri, Self-healing ability of nanoclay-based hybrid sol-gel coatings on magnesium alloy AZ91D, *Surface and Coatings Technology*. 309 (2017) 609–620. doi:10.1016/j.surfcoat.2016.12.018.

[104] E. Abdullayev, A. Joshi, W. Wei, Y. Zhao, Y. Lvov, Enlargement of halloysite clay nanotube lumen by selective etching of aluminum oxide, *ACS Nano*. 6 (2012) 7216–7226. doi:10.1021/nn302328x.

[105] E. Abdullayev, V. Abbasov, A. Tursunbayeva, V. Portnov, H. Ibrahimov, G. Mukhtarova, Y. Lvov, Self-healing coatings based on halloysite clay polymer composites for protection of copper alloys, *ACS Applied Materials and Interfaces*. 5 (2013) 4464–4471. doi:10.1021/am400936m.

[106] K.A. Zahidah, S. Kakooei, M. Kermanioryani, H. Mohebbi, M.C. Ismail, P.B. Raja, Benzimidazole-loaded halloysite nanotube as a smart coating application, *International Journal of Engineering and Technology Innovation*. 7 (2017) 243–254.

[107] D. Fix, D. V Andreeva, Y.M. Lvov, D.G. Shchukin, H. Möhwald, Application of inhibitor-loaded halloysite nanotubes in active anti-corrosive coatings, *Advanced Functional Materials*. 19 (2009) 1720–1727. doi:10.1002/adfm.200800946.

[108] E. Shchukina, D. Grigoriev, T. Sviridova, D. Shchukin, Comparative study of the effect of halloysite nanocontainers on autonomic corrosion protection of polyepoxy coatings on steel by salt-spray tests, *Progress in Organic Coatings*. 108 (2017) 84–89. doi:10.1016/j.porgcoat.2017.03.018.

[109] E. Shchukina, D. Shchukin, D. Grigoriev, Effect of inhibitor-loaded halloysites and mesoporous silica nanocontainers on corrosion protection of powder coatings, *Progress in Organic Coatings*. 102 (2017) 60–65. doi:10.1016/j.porgcoat.2016.04.031.

[110] C. Dong, M. Zhang, T. Xiang, L. Yang, W. Chan, C. Li, Novel self-healing anticorrosion

coating based on L-valine and MBT-loaded halloysite nanotubes, *Journal of Materials Science*. 53 (2018) 7793–7808. doi:10.1007/s10853-018-2046-5.

[111] P.P. Vijayan, Y.M. Hany El-Gawady, M.A.S.A. Al-Maadeed, Halloysite Nanotube as Multifunctional Component in Epoxy Protective Coating, *Industrial and Engineering Chemistry Research*. 55 (2016) 11186–11192. doi:10.1021/acs.iecr.6b02736.

[112] M. Sun, A. Yerokhin, M.Y. Bychkova, D. V Shtansky, E.A. Levashov, A. Matthews, Self-healing plasma electrolytic oxidation coatings doped with benzotriazole loaded halloysite nanotubes on AM50 magnesium alloy, *Corrosion Science*. 111 (2016) 753–769. doi:10.1016/j.corsci.2016.06.016.

[113] A. Joshi, E. Abdullayev, A. Vasiliev, O. Volkova, Y. Lvov, Interfacial modification of clay nanotubes for the sustained release of corrosion inhibitors, *Langmuir*. 29 (2013) 7439–7448. doi:10.1021/la3044973.

[114] P. Zheng, Y. Du, X. Ma, Selective fabrication of iron oxide particles in halloysite lumen, *Materials Chemistry and Physics*. 151 (2015) 14–17. doi:10.1016/j.matchemphys.2014.11.075.

[115] R. Mahmoudi, P. Kardar, A.M. Arabi, R. Amini, P. Pasbakhsh, The active corrosion performance of silane coating treated by praseodymium encapsulated with halloysite nanotubes, *Progress in Organic Coatings*. 138 (2020) 105404. doi:10.1016/j.porgcoat.2019.105404.

[116] J.M. Falcón, T. Sawczen, I.V. Aoki, Dodecylamine-loaded halloysite nanocontainers for active anticorrosion coatings, *Frontiers in Materials*. 2 (2015) 1–13. doi:10.3389/fmats.2015.00069.

[117] D. Garcia-Garcia, J.M. Ferri, L. Ripoll, M. Hidalgo, J. Lopez-Martinez, R. Balart, Characterization of selectively etched halloysite nanotubes by acid treatment, *Applied Surface Science*. 422 (2017) 616–625. doi:10.1016/j.apsusc.2017.06.104.

[118] A.B. Zhang, L. Pan, H.Y. Zhang, S.T. Liu, Y. Ye, M.S. Xia, X.G. Chen, Effects of acid treatment on the physico-chemical and pore characteristics of halloysite, *Colloids and Surfaces A: Physicochemical and Engineering Aspects*. 396 (2012) 182–188. doi:10.1016/j.colsurfa.2011.12.067.

[119] Z. Shu, Y. Chen, J. Zhou, T. Li, D. Yu, Y. Wang, Nanoporous-walled silica and alumina nanotubes derived from halloysite : controllable preparation and their dye adsorption applications, *Applied Clay Science*. 112–113 (2015) 17–24. doi:10.1016/j.clay.2015.04.014.

[120] F. Moeinpour, F. Soofivand, F.S. Mohseni-Shahri, Controlled release of losartan from

acid- and heat-treated halloysite nanotubes, *Medicinal Chemistry Research.* 28 (2019) 160–168. doi:10.1007/s00044-018-2273-y.

[121] H.A. Patel, *Nanoclays: Synthesis, Characterization and Applications*, Astral International (P) Ltd, (2014).1-20.

[122] J.M. Cases, I. Bérend, M. François, L.P. Uriot, L.J. Michot, F. Thomas, Mechanism of Adsorption and Desorption of Water Vapor by Homoionic Montmorillonite: 3. the Mg²⁺, Ca²⁺, Sr²⁺ and Ba²⁺ Exchanged Forms, *Clays and Clay Minerals.* 45 (1997) 8–22. doi:<https://doi.org/10.1346/CCMN.1997.0450102>.

[123] F. Deflorian, S. Rossi, M. Fedel, C. Motte, Electrochemical investigation of high-performance silane sol–gel films containing clay nanoparticles, *Progress in Organic Coatings.* 69 (2010) 158–166. doi:10.1016/j.porgcoat.2010.04.007.

[124] F. Deflorian, S. Rossi, M. Fedel, C. Motte, Electrochemical investigation of high-performance silane sol–gel films containing clay nanoparticles, *Progress in Organic Coatings.* 69 (2010) 158–166. doi:10.1016/j.porgcoat.2010.04.007.

[125] D.J. Carbonell, A. García-Casas, J. Izquierdo, R.M. Souto, J.C. Galván, A. Jiménez-Morales, Scanning electrochemical microscopy characterization of sol-gel coatings applied on AA2024-T3 substrate for corrosion protection, *Corrosion Science.* 111 (2016) 625–636. doi:10.1016/j.corsci.2016.06.002.

[126] J.M. Vega, N. Granizo, J. Simancas, I. Díaz, M. Morcillo, D. de la Fuente, Exploring the corrosion inhibition of aluminium by coatings formulated with calcium exchange bentonite, *Progress in Organic Coatings.* 111 (2017) 273–282. doi:10.1016/j.porgcoat.2017.04.046.

[127] S. Bohm, H.N. McMurray, S.M. Powell, D.A. Worsley, Novel environment friendly corrosion inhibitor pigments based on naturally occurring clay minerals, *Materials and Corrosion* 52 (2001) 896–903. doi:10.1002/1521-4176(200112)52:123.0.CO;2-8.

[128] Y. Dong, L. Ma, Q. Zhou, Effect of the incorporation of montmorillonite-layered double hydroxide nanoclays on the corrosion protection of epoxy coatings, *Journal of Coatings Technology Research.* 10 (2013) 909–921. doi:10.1007/s11998-013-9519-x.

[129] A. Ghazi, E. Ghasemi, M. Mahdavian, B. Ramezan-zadeh, M. Rostami, The application of benzimidazole and zinc cations intercalated sodium montmorillonite as smart ion exchange inhibiting pigments in the epoxy ester coating, *Corrosion Science.* 94 (2015) 207–217. doi:10.1016/j.corsci.2015.02.007.

[130] E. Darmiani, G.R. Rashed, D. Zaarei, I. Danaee, Synergistic Effects of

Montmorillonite/Cerium Nitrate Additives on the Corrosion Performance of Epoxy-Clay Nanocomposite Coatings, *Polymer - Plastics Technology and Engineering*. 52 (2013) 980–990. doi:10.1080/03602559.2013.763373.

- [131] C. Motte, M. Poelman, A. Roobroeck, M. Fedel, F. Deflorian, M.-G. Olivier, Improvement of corrosion protection offered to galvanized steel by incorporation of lanthanide modified nanoclays in silane layer, *Progress in Organic Coatings*. 74 (2012) 326–333. doi:10.1016/j.porgcoat.2011.12.001.
- [132] S.H. Adsul, T. Siva, S. Sathiyanarayanan, S.H. Sonawane, R. Subasri, Aluminum pillared montmorillonite clay-based self-healing coatings for corrosion protection of magnesium alloy AZ91D, *Surface and Coatings Technology*. 352 (2018) 445–461. doi:10.1016/j.surfcoat.2018.08.034.

CHAPTER-2

EXPERIMENTAL

CHAPTER-2

EXPERIMENTAL

2.1 Synthesis of Matrix sol

3-glycidoxypolypropyltrimethoxysilane (GPTMS, Gelest Inc., USA, 98%) and tetraethoxysilane (TEOS, Gelest Inc., 98%) were used as the starting materials. 0.1 N HCl as catalyst and de-ionized (DI) water were used for the synthesis of 100 g of matrix sol.

Organic-inorganic hybrid matrix sol was synthesized by taking 69.66 g of GPTMS which was co-hydrolysed with 21.29 g of TEOS in a molar ratio of 3.5:1 by using 2.30 g of 0.1 N HCl, which was added dropwise. It became turbid after the addition of HCl, this was then followed by the addition of 6.75 g of DI water under constant stirring for 1 h until a transparent matrix sol was obtained [1].

2.2 Preparation of HNT based Self-healing sol

Halloysite nanotubes (HNTs) and Montmorillonite nanoclay (MMT, aluminum pillared clay) supplied by Sigma-Aldrich, USA were used as the nano reservoirs for the self-healing material. Conc. H₂SO₄ supplied by SD Fine Chemicals, India of 98% purity, was used as the stock for the preparation of 1 M and 2M H₂SO₄ solutions, using which, inner lumen of HNTs was etched. Ce(NO₃)₃.6H₂O (Loba Chemie, India, 99.9%) and zirconium n-propoxide (Gelest Inc., USA, 70% in n-propanol) were used as the source of Ce³⁺ and Zr⁴⁺ cationic corrosion inhibitors. Methacrylic acid (MAA, ABCR GmbH KG, Germany, 99%) stabilized with 100–250 ppm hydroquinone or 4-methoxy phenol was added as a complexing agent along with cationic corrosion inhibitors. Urea, formaldehyde and resorcinol procured from Fisher Scientific, India. Ammonium chloride procured from SD Fine Chemicals and polyvinyl alcohol obtained from Alfa Aesar were used for the synthesis of polymeric urea-formaldehyde microcapsules (UF) for capping open ends of the loaded HNTs. All the above-mentioned starting materials were used as-received without further purification.

2.2.1 Loading of corrosion inhibitors into HNTs and stoppering of loaded HNTs

The cationic corrosion inhibitor mixture was synthesized by adding $\text{Ce}(\text{NO}_3)_3$ and Zr -n-propoxide with the molar ratio of $\text{Ce}^{3+}/\text{Zr}^{4+}$ as 1:23 along with 0.029 moles of MAA. The cationic inhibitors were loaded inside the HNTs by dispersing 2 g of as-received HNTs/etched HNTs in a solution of the mixture of inhibitors followed by ultrasonication for 15 min. Evacuation was carried out inside a vacuum desiccator for about 3 h, during which fizzing occurs indicating that the inhibitor solution is loading into the lumen of HNTs [2]. Evacuation process was stopped after the fizzing stops. The solution was then centrifuged at 6500 rpm for 5 min by washing with IPA for 3 times to separate the inhibitor loaded HNT powder. The obtained powder was dried at 60 °C for 15 min and grinded to get fine particles as given in the scheme below (Fig. 2.1).

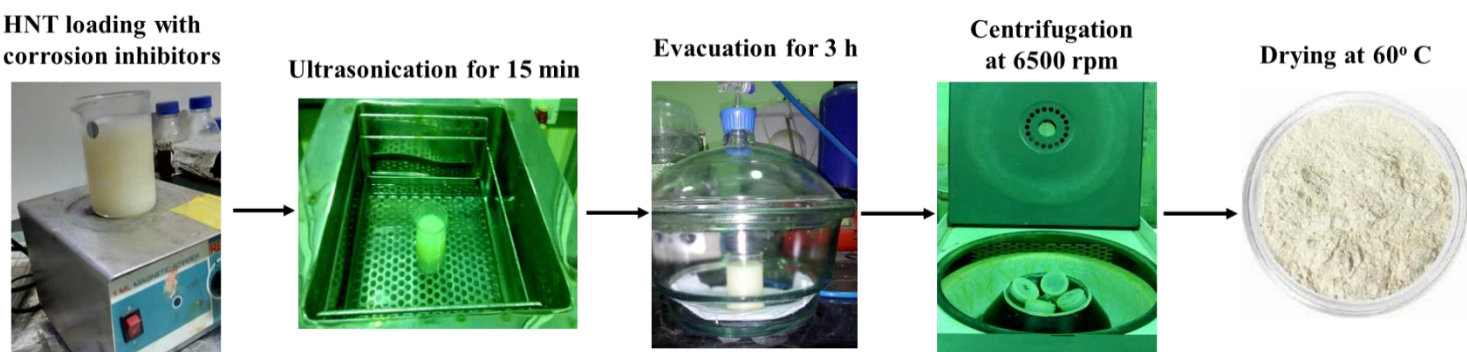


Fig. 2.1. Schematic representation of loading of corrosion inhibitors into HNTs.

The ends of loaded HNTs were stoppered by using urea-formaldehyde microcapsules. Urea solution was prepared by adding 7 g of urea, 0.5 g of resorcinol and 0.5 g of ammonium chloride to 75 g of DI water, which was stirred to obtain clear homogenous solution by adding by 75 g more DI water. Further, 5 wt % polyvinyl alcohol solution, GPTMS mixture (~30 g) and 18.91 g of 37 % formaldehyde solution were added to the above prepared urea solution and the emulsion was stabilized for 15 min under constant stirring. The temperature of the solution was raised to 60 °C and maintained for 6 h under stirring. The solution was brought to room temperature and centrifuged at 6500 rpm for 5 min by washing with deionized water to separate microcapsules from the suspension [3,4]. The obtained microcapsules were dispersed in 25 ml of isopropanol (IPA).

2 g of inhibitor loaded HNTs and 25 ml of UF microcapsules dispersion were added to 98 g of hybrid matrix sol and stirred for 4 h to synthesize self-healing sol, which is hereafter abbreviated as SH sol.

2.2.2 Etching of HNTs

The selective etching of inner aluminol layer in the lumen of HNT was carried out using H_2SO_4 as etching agent. Experimental procedure includes, adding 1 g of HNTs in 500 ml of 1 M or 2 M H_2SO_4 solution for 3 days with continuous stirring while maintaining the temperature at 60 °C using water bath. The solution was then centrifuged at 6500 rpm for 5 min, washed with deionized water till neutral pH was obtained in the supernatant solution and dried in order to get an enlarged lumen diameter [5,6]. These experiments were carried out in order to incorporate more amount of corrosion inhibitors into the lumen and to study the effect of different concentrations of sulphuric acid on the efficiency of etching.

The loading of cationic corrosion inhibitors into the etched HNTs and stoppering the ends of etched HNTs were carried out by same procedure as that followed for as-received HNTs as mentioned in the section 2.2.1.

2 g of inhibitor loaded etched HNTs and 25 ml of UF microcapsules dispersion were added to 98 g of hybrid matrix sol and stirred for 4 h to synthesize self-healing sol using etched HNTs, which will be hereafter abbreviated as ELSH sol.

2.3 Loading of corrosion inhibitors into MMTs

Loading of cationic inhibitors into the montmorillonite clays was carried out by two different methods: 1) by physical mixing of alcoholic solutions of the corrosion inhibitor compounds with montmorillonite and 2) by addition of inhibitors to montmorillonite clay followed by evacuation to enable intercalation of cationic inhibitors into the interlayer space. The cationic corrosion inhibitor mixture was prepared by similar procedure as that followed for HNTs, mentioned in the section 2.2.1. For the preparation of inhibitor mixed MMT (IMM), 2 g of as-received MMT powder was added to the prepared inhibitor solution and stirred for 1 h. The inhibitor solution was prepared by addition of 4.3 g of MAA to 25.29 g of Zr-n propoxide while stirring. 1.08 g of cerium nitrate dissolved in 15 ml of IPA, and it was added to the above solution and stirred for 45 min. The mixture was then centrifuged at 6500 rpm for 5 min for 3-4 times and dried at 60° C for 15 min. Inhibitor evacuated MMT (IEM) was prepared by adding 2 g of as-received MMT to inhibitor solution, followed by

stirring and evacuating at room temperature for 3 h using vacuum desiccator. The resulting mixture was then centrifuged at 6500 rpm for 3 times by washing with IPA each time and dried at 60 °C for 15 min. The loaded clays as mentioned in (1) and (2) were subsequently dispersed in hybrid matrix sol.

2.4 Preparation of composite sol

The composite sol was prepared by mixing the cationic inhibitor loaded HNT and inhibitor loaded MMT nanoclay powders in 1:1 wt. ratio and this powder was then dispersed in the hybrid matrix sol as 2 wt % and is abbreviated as M+H sol.

2.5 Substrate cleaning, coating and curing

Aluminium alloy coupons of A356.0 and AA2024-T4 of dimensions 20 mm x 20 mm x 3 mm were used for the experiments. The composition of the aluminium alloy AA2024-T4 substrates in wt % was determined to be Cu 4.9, Mg 1.6, Mn 0.6, Si 0.5, Fe 0.5, Zn 0.25, Ti 0.15 and remaining Al. For A356.0 aluminum alloy, the composition was Al 82.6, Si 16.0, Mg 0.3, Ti 0.3, Fe 0.2, Sn 0.44 and Pb 0.15. All the substrate coupons were sequentially polished with 1000 grit emery paper to remove the oxide layer and ultrasonically degreased with acetone for 20 min prior to coating.

The coatings were deposited using dip coating technique by employing 1 mm/s withdrawal speed followed by thermal curing at 130 °C for 1 h in air using a drying oven. The schematic representation of the preparation of HNT/MMT based sols, coating and curing procedure is given in Fig.2.2.

Bilayer coatings have been generated as two configurations H|M and M|H by depositing SH (H)/ IEM (M) sols each layer at 1 mm/s withdrawal speed. Each layer was thermally cured subsequently at 130 °C for 1 h after dip coating.

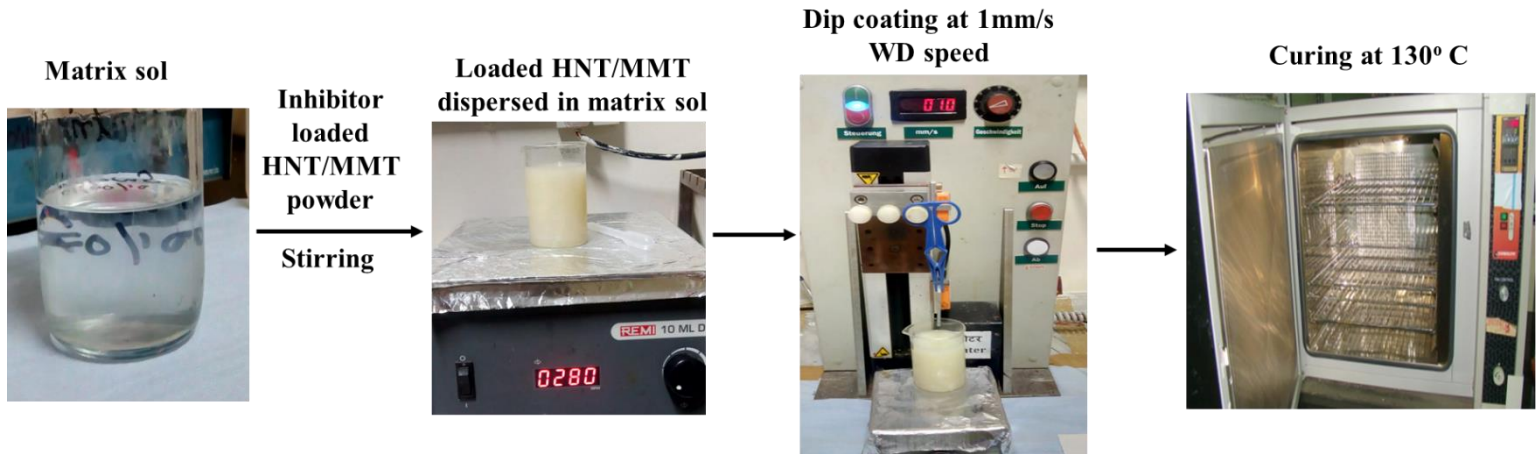


Fig. 2.2. Preparation of HNT/MMT based sols, coating and curing of the coated Al substrates.

2.6 Characterization Techniques

2.6.1 Electron Microscopy

Scanning electron microscopy (SEM, Hitachi, model-S3400N) was used to observe the surface morphology and coating composition of all coated and uncoated substrates in the magnification range of 1000-2000X. EDAX analysis for HNT and MMT-based powder samples was carried out to find out the composition of clays and confirm the loading of corrosion inhibitors into the clays. EDAX analysis as well as elemental mapping for coated and uncoated AA2024-T4 and A356.0 substrates before and after immersion test and salt spray test was carried at 100 to 500X magnification. The working distance of the samples was kept at 13-15 mm and the accelerating voltage was at 20 - 50 kV. Field emission SEM (FESEM) – Zeiss Gemini 500 having a hot Schottky field emission (FE) gun, was used for observing the morphology and size of the microcapsules and coating cross sectional images. The magnification range used was 10 k - 20 kX. For the analysis of powder samples, powders were dispersed in ethanol and ultrasonicated for 5 min, after which, few drops of supernatant solution was dropped on the carbon tape containing stubs and dried until solvent gets evaporated. The coated substrates of $2\text{ cm} \times 2\text{ cm}$ were sputtered with gold for 30 s before the analysis to avoid the charging and blurring of images during SEM analysis.

The lumen diameter and length of the nanotubes for the as-received, etched and inhibitor loaded HNTs and the size, interlayer space and crystalline nature of the montmorillonite clay were determined using a transmission electron microscope (TEM, Tecnai 200 G2, FEI, Netherlands). Small amount of powder samples was dispersed into ethyl

alcohol, ultrasonicated for 5 min and 50 μ l of suspension was added onto the C coated Cu grids using micro-pipette and dried under dust-free environment before the analysis.

2.6.2 X-ray diffraction studies

The crystalline or amorphous nature of the HNT and MMT powders and the intercalation of corrosion inhibitors into HNT and MMT nanoclays were confirmed by X-ray diffraction studies using Bruker AXS D8 Advance, USA (shown in Fig. 2.3). The diffraction analysis was carried out in the 2-theta range of 2-80°, in a step scan mode with step size of 0.1°. The instrument is equipped with Cu source and a high speed 1D Lynx Eye detector mounted on a vertical goniometer and the XRD profiles were acquired in symmetric geometry [7]. The obtained XRD profiles were analyzed using Match® software to obtain peak data.



Fig. 2.3. X-ray diffractometer - Bruker AXS D8 Advance

2.6.3 Fourier Transform-Infrared (FT-IR) spectroscopy

FT-IR spectra were recorded for HNT powders collected at different time intervals of etching (etched HNT with 1 M and 2 M H_2SO_4). Perkin Elmer Spectrum 100 FT-IR spectrophotometer was used for recording the infrared spectra using KBr pellet technique [8,9] in the range of 600 to 4000 cm^{-1} .

2.6.4 Brunauer–Emmett–Teller (BET) surface area and pore volume analysis

BET surface area and pore volume measurements for the as-received, etched, loaded and stoppered HNTs and as-received, inhibitor loaded MMTs were carried out using a

Gemini (11-2370), Micromeritics ASAP 2020, USA surface area and porosimetry analyser. The analysis was carried out by nitrogen adsorption-desorption at 77 K. All the samples were degassed at 300 °C under vacuum for 6 h prior to adsorption experiments. The specific surface area was determined by the Brunauer–Emmett–Teller procedure. The pore volume was determined by the nitrogen adsorption volume at a relative pressure (P/P_0).

2.6.5 Adhesion Test

Adhesion test of coated AA2024-T4 and A356.0 substrates was investigated by cross-hatch cutter as per ASTM D3359-17 test procedure [10]. The surface was scribed in the form of 1 mm^2 grid lines using cutter. A pressure sensitive adhesive tape was applied over the grid and pulled off rapidly at an angle close to 180°. The samples were inspected for any removal of the coating using optical microscope (Olympus BX51M). The extent of detachment of coating and the presence of flakes in the tape determines the coating quality, based on which grades 1B to 5B are given indicating poor to good adhesion, respectively as depicted in Fig. 2.4.

CLASSIFICATION OF ADHESION TEST RESULTS		
CLASSIFICATION	PERCENT AREA REMOVED	SURFACE OF CROSS-CUT AREA FROM WHICH FLAKING HAS OCCURRED FOR SIX PARALLEL CUTS AND ADHESION RANGE BY PERCENT
5B	0% None	
4B	Less than 5%	
3B	5 – 15%	
2B	15 – 35%	
1B	35 – 65%	
0B	Greater than 65%	

Fig. 2.4. Classification of ranks based on % removal of coating after tape adhesion test.

2.6.6 Electrochemical characterization

2.6.6.1 Electrochemical impedance spectroscopic (EIS) and Potentiodynamic polarization studies

Electrochemical analyses have been performed to study the corrosion protection properties of HNT and MMT based coatings on AA2024-T4 and A356.0 substrates.

Initially the electrochemical experiments were carried out for bare and HNT-based sol coated A356.0 substrates using a Solartron electrochemical interface SI 1287 with Impedance

Analyzer Solartron SI 1260. The corrosion cell had the classic configuration of three electrodes with a Pt coil as counter electrode, a saturated calomel electrode as reference electrode and the uncoated/coated aluminum alloy samples as the working electrode. EIS and potentiodynamic polarization studies of the coated/uncoated substrates were carried out at 25°C using 3.5 wt % NaCl solution with an exposure of 1 h, 72 h, 120 h, 168 and 216 h. Prior to exposure of samples to corrosive medium, the solution was purged with N₂ for 1 h to remove any dissolved oxygen. The substrates of 1 cm² area were exposed and the remaining area was insulated using cellophane tape. These substrates were then immersed into 3.5 wt % NaCl solution. Potentiodynamic scans were recorded by applying potentials over a range of ± 1.5 V with respect to open circuit potential (OCP) at a scan rate of 1 mV/s. The electrochemical impedance analysis was carried out using an AC signal of 10 mV amplitude applied over a bandwidth from 100 kHz to 0.01 Hz with 10 steps/decade frequency. The electrochemical impedance spectroscopic data obtained were analyzed using Zview 2[®] and the potentiodynamic polarization data were analyzed using Corrvie 2[®] software [11,12].

Later the experiments have been continued on CH instrument (Model 604E supplied by CH instruments, USA) for HNT and MMT-based sol coated AA2024-T4 and MMT based sol coated A356.0 substrates. The corrosion cell had a flat cell set up as shown in Fig. 2.5, with same electrode configuration as mentioned above. EIS and polarization studies of the coated/uncoated substrates were carried out at 25 °C after exposure to 3.5 wt % NaCl solution in atmospheric environment for 1 h, 72 h and 120 h and further extended up to 216 h. The EIS measurements were carried out using 10 mV amplitude AC signal applied over a bandwidth of 100 kHz - 0.01 Hz having 12 steps/decade frequency. Potentiodynamic polarization scans were recorded by applying potentials over a range of ± 1.5 V with respect to OCP at a scan rate of 1 mV/s. The EIS data obtained were analyzed using Zsimpwin[®] software to obtain Nyquist, Bode and phase angle plots. The potentiodynamic polarization data were analyzed using the CH604E software for determining corrosion potentials and corrosion currents. The substrates were insulated along the edges with cellophane tape before the immersion. The electrochemical tests were performed by exposing 1 cm² area of substrates (working electrode) to electrolyte. OCP analysis was run for 40 min until the potential got stabilized.

Two dip coated samples, i.e. four coated surfaces, for each set were used for corrosion testing to ascertain the reproducibility of data.

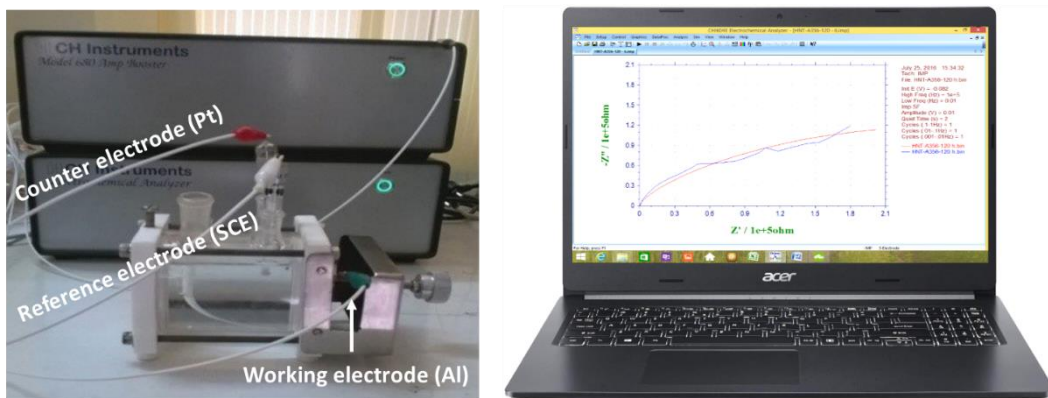


Fig. 2.5. Photograph of CH Instruments electrochemical work station.

2.6.6.2 Scanning Vibrating Electrode Technique analysis

The self-healing ability of the developed coatings on AA2024-T4 and A356.0 was analyzed using scanning vibrating electrode technique (SVET), which uses Biologic SCV 470 control unit. This is a localized electrochemical analysis on the electrode surface. Samples prepared for SVET measurement were of dimensions 1 cm x 1 cm and a scan area of $4000 \times 4000 \mu\text{m}$ with 64 x 48 points along X and Y axes was considered for the measurements. The samples were scribed prior to the measurements, in order to introduce an artificial defect to an area ranging from 0.1 to 0.3 mm². The sample was mounted in a teflon holder and the 3.5 wt % NaCl electrolyte solution was added as shown in Fig. 2.6. Scans were initiated within 5 min of exposure to the electrolyte solution and the data were collected for various durations of exposure. Each scan consists of 400 data points on a 20 x 20 grid with an integration time of 1s per point. A complete scan required 30 min, followed by a 5 min rest period prior to the next scan. Frequency of the vibrating electrode was 100 Hz. The current density maps were plotted in 3D format over the scan area with positive and negative current densities representing anodic and cathodic regions, respectively [13]. The measurements were obtained at the OCP.

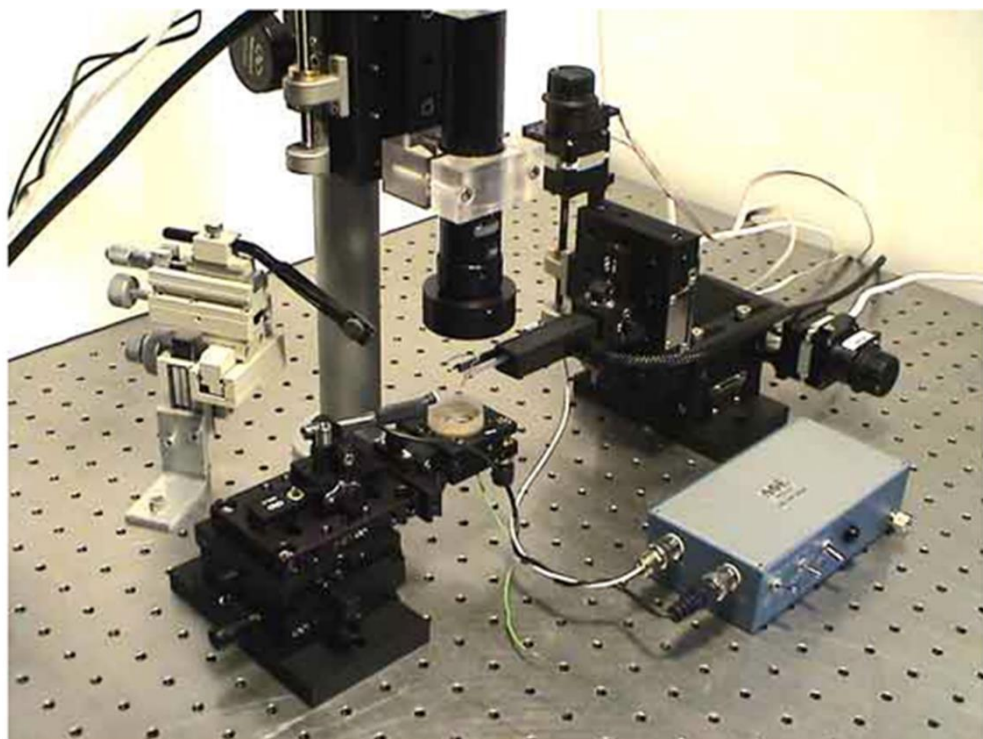


Fig. 2.6. SVET instrumental set up

2.6.7 Salt immersion and Salt spray test

Salt immersion test and salt spray tests were performed on uncoated and coated Al substrates. Samples were scratched as 'X' shape using metallic forceps with sharp ends. The coated and uncoated substrates were insulated using cellophane tape along edges before test to prevent the propagation of corrosion from ends. For salt immersion test, substrates were immersed in 3.5 wt % NaCl for 120 h and for salt spray test, substrates were exposed to 5 wt % NaCl solution for 168 h according to ASTM B117 method [14]. The salt spray test was carried out in a cycling corrosion cabinet of model CCX 2000 and made by Atlas Material Testing solutions, USA, as shown in Fig. 2.7. The samples were rinsed with DI water and dried after the tests. EDAX elemental mapping was carried out for these samples, before and after immersion/spray on the scribed areas along X area using SEM.



Fig. 2.7. Photograph of salt spray test chamber

2.6.8 Weight loss analysis

Weight loss experiments were carried out by immersing the coated and uncoated substrates in 3.5 wt % NaCl solution for 120 h according to the ASTM G31 standards [15] and cleaning of the substrates after the immersion was carried out as per the ASTM G1-90 standard cleaning method [16]. The samples were weighed before and after immersion and weight loss was calculated. The following expression was used to determine the corrosion rate of substrates in millimeters per year (mmpy).

$$\text{Corrosion rate} = \frac{8.76 \times 10^4 \times w}{t \times A \times \rho}$$

Where, w is weight loss in grams (g), t is exposure time in hours (h), A is exposed area in cm^2 and ρ is density of the alloy in g/cm^3 . Density of aluminium alloys is $2.78 \text{ g}/\text{cm}^3$.

2.6.9 Micro-Raman spectroscopic analysis

Micro-Raman spectroscopic analysis was carried out to confirm the mechanism of self-healing action. The analysis was carried out on uncoated and coated A356.0 substrates in the scribed region before and after immersion in 3.5 wt % NaCl for 150 h. The data was

obtained using Horiba Jobin-Yvon LabRam HR800 Raman spectrometer as shown in Fig. 2.8, with Ar ion laser of 514 nm as the light source over the scan range of 100-2000 cm^{-1} [17]. Phase mapping was carried out in the scribed region at room temperature on an active area of $20 \mu\text{m}^2$.



Fig. 2.8. Pictorial representation of Micro-Raman spectrophotometer.

References

- [1] L. Sowntharya, R.C. Gundakaram, K.R.C. Soma Raju, R. Subasri, Effect of addition of surface modified nanosilica into silica-zirconia hybrid sol-gel matrix, *Ceramics International*. 39 (2013) 4245–4252. doi:10.1016/j.ceramint.2012.10.276.
- [2] E. Abdullayev, Y. Lvov, Clay nanotubes for corrosion inhibitor encapsulation: Release control with end stoppers, *Journal of Materials Chemistry*. 20 (2010) 6681–6687. doi:10.1039/c0jm00810a.
- [3] S.R. White, N.R. Sottos, P.H. Geubelle, J.S. Moore, M.R. Kessler, S.R. Sriram, E.N. Brown, S. Viswanathan, Autonomic healing of polymer composites, *Nature*. 409 (2001) 794–797. doi:10.1038/35057232.
- [4] T. Siva, S. Sathiyanarayanan, Self healing coatings containing dual active agent loaded urea formaldehyde (UF) microcapsules, *Progress in Organic Coatings*. 82 (2015) 57–67. doi:10.1016/j.porgcoat.2015.01.010.
- [5] E. Abdullayev, A. Joshi, W. Wei, Y. Zhao, Y. Lvov, Enlargement of Halloysite Clay Nanotube Lumen by Selective Etching of Aluminum Oxide, *ACS Nano*. 6 (2012) 7216–7226. doi:10.1021/nn302328x.
- [6] Y. Lvov, W. Wang, L. Zhang, R. Fakhrullin, Halloysite Clay Nanotubes for Loading and Sustained Release of Functional Compounds, *Advanced Materials*. 28 (2016) 1227–1250. doi:10.1002/adma.201502341.
- [7] C. Suryanarayana, M.G. Norton, *X-ray diffraction: a practical approach*. Springer Science & Business Media. (2013).
- [8] S. Wartewig, *Basic principles of vibrational spectroscopy, IR and Raman Spectroscopy: Fundamental Processing*, Wiley VCH erlag GmbH & Co. KGaA. (2003). doi: 10(3527601635).
- [9] R. Salzer, H.W. Siesler, *Infrared and Raman Spectroscopic Imaging*, 2nd Edition, John Wiley & Sons. (2014) 1-180.
- [10] ASTM D3359-17, Standard Test Methods for Rating Adhesion by Tape Test (2009) 1-9.
- [11] R.G. Kelly, J.R. Scully, D. Shoesmith, R.G. Buchheit, *Electrochemical Techniques in Corrosion Science and Engineering*, CRC Press. (2002) 319-340.
- [12] M.G.S. Ferreira, C.A. Melendres (Eds.), *Electrochemical and Optical Techniques for the Study and Monitoring of Metallic Corrosion*, Springer Science. 203 (2013) 484-520.
- [13] S.H. Adsul, T. Siva, S. Sathiyanarayanan, S.H. Sonawane, R. Subasri, Self-healing

ability of nanoclay-based hybrid sol-gel coatings on magnesium alloy AZ91D, *Surface and Coatings Technology*. 309 (2017) 609–620. doi:10.1016/j.surfcoat.2016.12.018.

- [14] ASTM B117-16, Standard Practice for Operating Salt Spray (Fog) Apparatus, (2011) 1-12.
- [15] ASTM G31-72, Standard Guide for Laboratory Immersion Corrosion Testing of Metals, (2004) 1-8.
- [16] ASTM G1-90, Standard Practice for Preparing, Cleaning and Evaluation Corrosion Test Specimens, (1999).
- [17] J. Popp, T. Mayerhöfer (Eds.), *Micro-Raman Spectroscopy: Theory and Application*, Walter de Gruyter GmbH & Co KG. (2020).

CHAPTER-3

**Halloysite Clay Nanotubes as
Nanocontainers for Self-healing Corrosion
Protection Coatings on AA2024-T4 and
A356.0 Aluminum Alloy**

CHAPTER-3

Halloysite Clay Nanotubes as Nanocontainers for Self-healing Corrosion Protection Coatings on AA2024-T4 and A356.0 Aluminum Alloys

Chapter 3 includes results and discussions of halloysite nanotubes-based, sol-gel coatings on AA2024-T4 and A356.0 alloys. The halloysite nanotubes (HNTs) after loading with Ce³⁺ and Zr⁴⁺ corrosion inhibitors have been characterized by TEM - EDS, SEM, XRD and BET-surface area and pore volume analyses to confirm the loading of corrosion inhibitors into the inner lumen of HNTs. The corrosion protection behaviour of the developed coatings was analysed through electrochemical tests such as electrochemical impedance spectroscopy and potentiodynamic polarization studies. In addition, weight loss, salt immersion test and salt spray test have also been carried out. The self-healing property has been evaluated by Scanning Vibrating Electrode Technique. The mechanism of self-healing was confirmed by micro-Raman spectroscopic studies.

3.1 Characterization of HNT-based powders

3.1.1 TEM analysis

As-received HNT as well as inhibitor loaded and stoppered HNTs were observed through TEM for their morphology and lumen diameter. EDS analysis was carried out to check the presence of corrosion inhibitors after loading. The as-received HNTs appeared as tubular structures of various lengths ranging from 0.1 -1.0 μm , with a hollow lumen having diameter of 10-15 nm as shown in Fig. 3.1 (a) and (b). The elemental analysis was carried out on HNT, an aluminosilicate as given in Fig. 3.1 (c), which confirmed the presence of aluminium and silicon. These HNTs were loaded with corrosion inhibitors [1], which were then stoppered by urea-formaldehyde microcapsules at the open ends in order to prevent the leakage of loaded corrosion inhibitors.[2]. TEM images of the tubes after loading with inhibitors and stoppering are shown in Fig. 3.1 (d) and (e). The EDS analysis of the loaded and stoppered HNT has shown the percentage weight ratios for Al, Si, O, Ce and Zr were

70.3, 18.2, 10.9, 0.16 and 0.28 respectively. The microcapsules were found to be spherical in shape as shown in SEM image in Fig. 3.2.

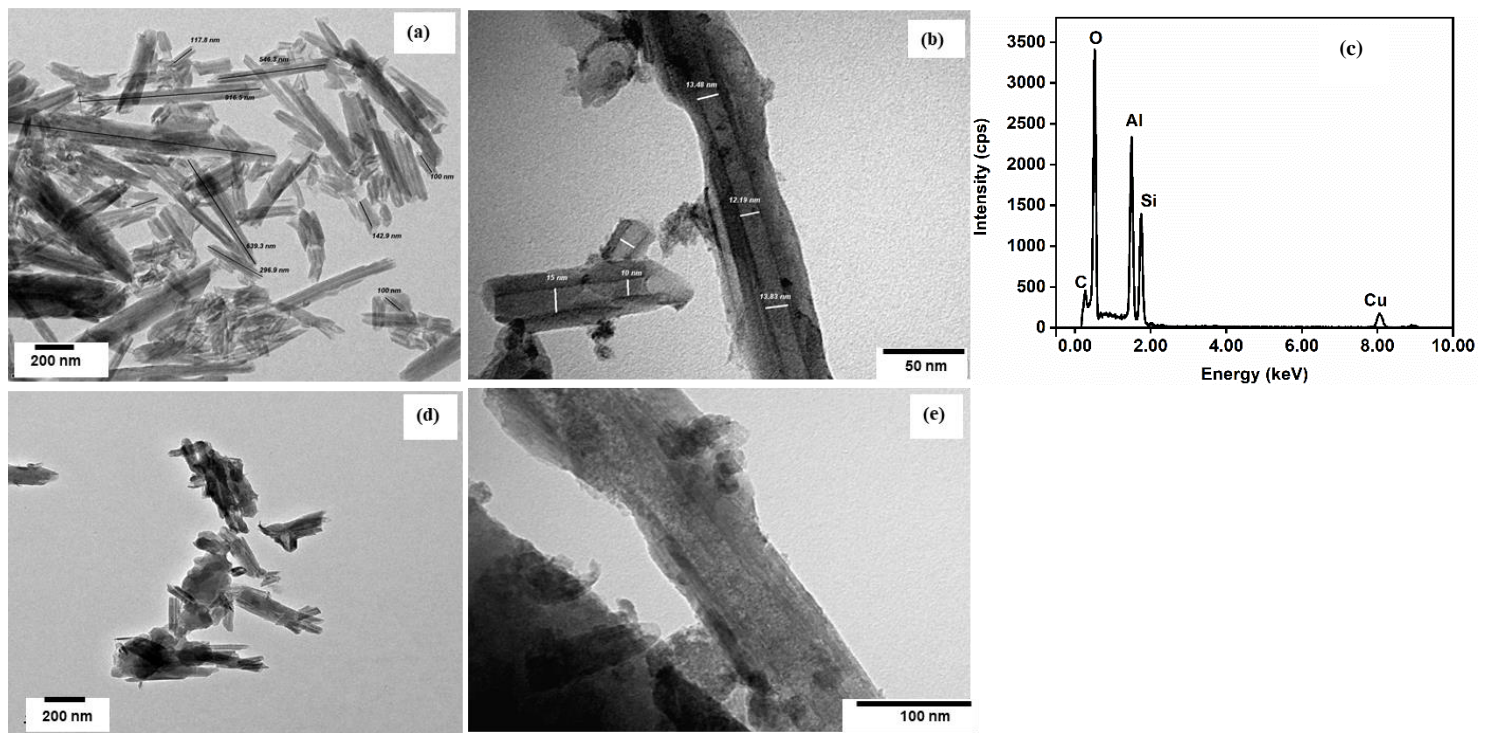


Fig. 3.1. TEM images of (a) and (b) as-received HNT, (d) and (e) inhibitor loaded HNTs and (c) EDS spectrum of as-received halloysite nanotubes respectively.

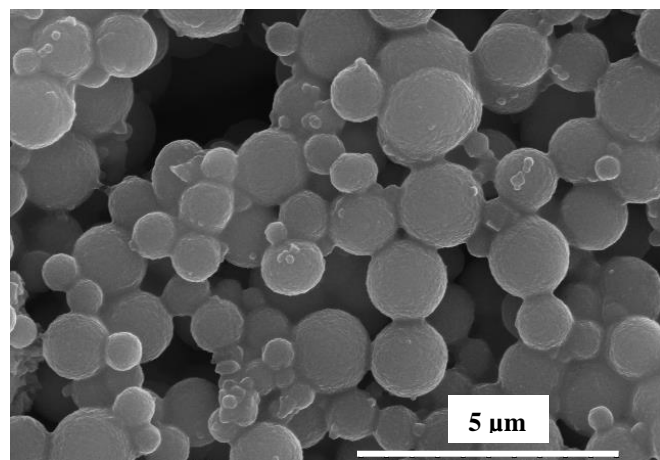


Fig. 3.2. SEM image of the urea-formaldehyde microcapsule tube stoppers.

3.1.2 BET surface area and pore volume analysis

BET surface area and pore volume analysis was carried out to confirm the loading of corrosion inhibitors into the lumen of HNTs. A comparison of pore volume as a function of pore diameter for as-received and inhibitor loaded and stoppered HNT is shown in Fig. 3.3. Pore volumes for as-received and inhibitor loaded and stoppered HNT were measured to be 0.145 and 0.029 cm³/g respectively, and surface area were 41.4 and 14.52 m²/g respectively. The decrease in the pore volume for loaded and stoppered HNT unequivocally confirmed that, the loading of the inhibitors inside the lumen of HNTs has taken place.

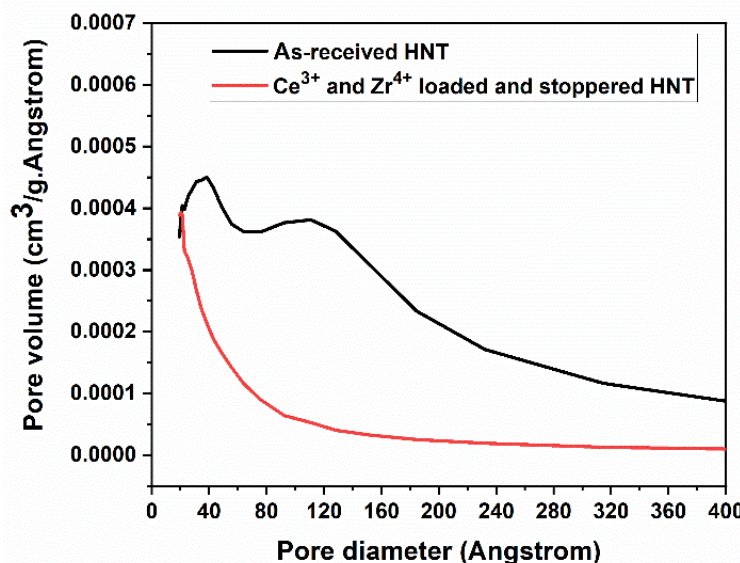


Fig. 3.3. Pore volume versus pore diameter of as received and inhibitor loaded stoppered HNTs.

3.1.3 XRD studies

XRD spectra of as-received and inhibitor loaded and stoppered HNTs are depicted in Fig. 3.4. Inhibitor loaded and stoppered HNTs have shown a very similar XRD pattern with d_{001} and d_{002} peaks as that of as-received HNTs, without any shift in the 2θ values. The peak position at $2\theta = 12.2^\circ$ corresponds to d_{001} plane that represents the multilayer wall packing and peak at $2\theta = 20.5^\circ$ corresponding to d_{002} plane, represents the tubular nature of HNT. These results are in accordance with that reported by Joshi et. al [3], who also observed that, a nil shift in the d_{001} and d_{002} planes and that indicated, the loading of corrosion inhibitors inside HNTs mainly because of the precipitation within the lumen and that no intercalation within the interlayer space had taken place.

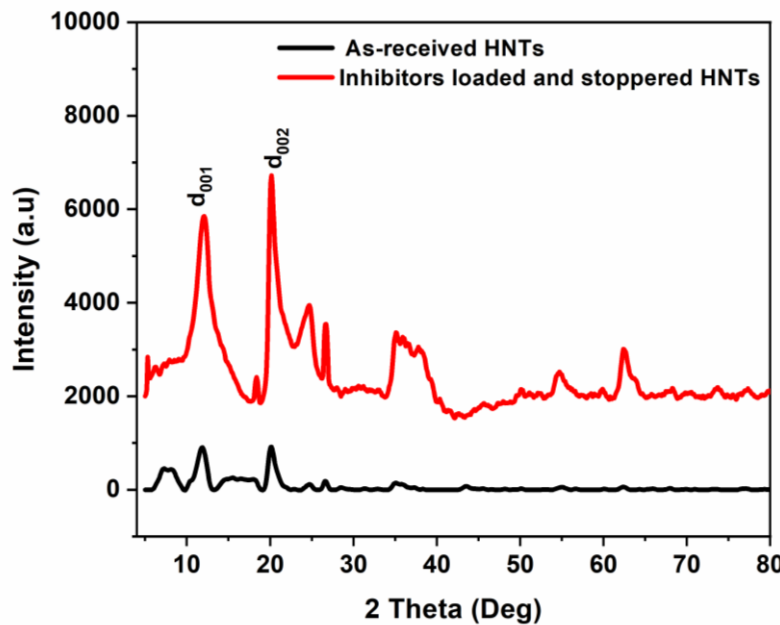


Fig. 3.4. XRD patterns of as-received and inhibitor loaded halloysite nanotubes.

3.2 Results and Discussion of coatings on AA2024-T4 alloy

3.2.1 Thickness and Adhesion strength of the coatings

SEM cross sectional image of loaded and stoppered HNT (labelled as SH) sol coated AA2024-T4 substrate was recorded and is shown in Fig. 3.5. Thickness of the SH sol-based coating was determined to be $4.5 (\pm 0.1) \mu\text{m}$, which was measured through SEM cross sectional images as given in Fig. 3.5.

The adhesion strengths of hybrid matrix (Mat) sol, unloaded HNT-based sol (HNC) and SH sol coatings applied on AA2024-T4 substrates were determined by tape adhesion test as per ASTM D3359-17 procedure [4]. In this test, the substrates surface was scribed in the form of 1 mm^2 grid lines by using cross-hatch cutter. A pressure sensitive adhesive tape was applied over the scribed area and pulled off rapidly at an angle close to 180° . The samples were observed under the optical microscope for removal of the coating, if any.

The SH, Mat and HNC coatings have shown very good adhesion with the substrate and there was no removal of any coating after tape test as shown in Fig. 3.6 and hence the adhesion strength of all the coatings was ranked as 5B.

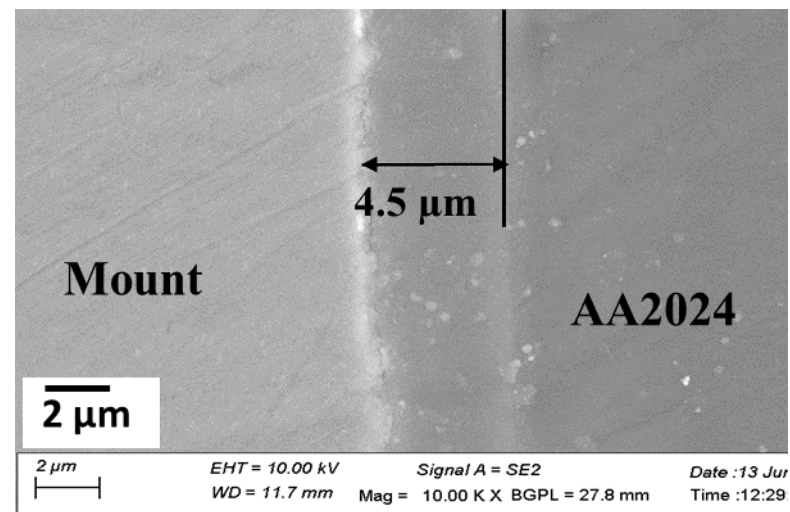


Fig. 3.5. SEM cross sectional image of SH sol coated AA2024-T4 substrate.

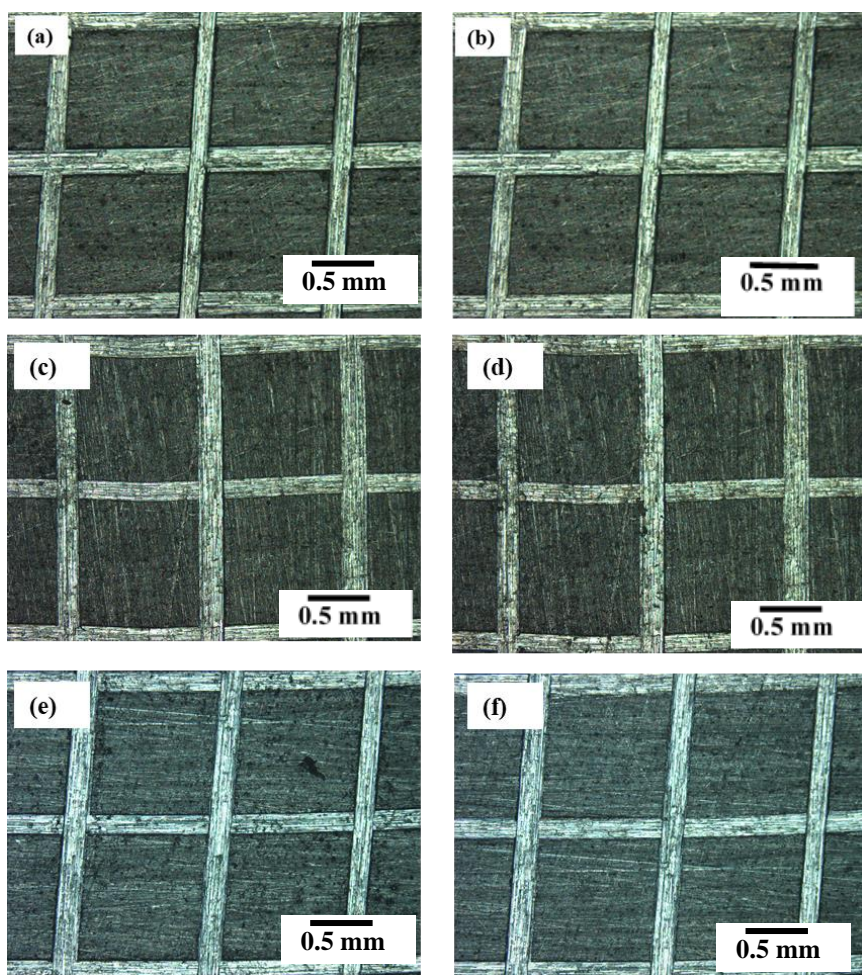


Fig. 3.6. Microscopic images of SH (a, b), Mat (c, d) and (d) and HNC sol coated (e, f) AA2024-T4 substrates before (a, c, e) and after (b, d, f) the tape adhesion test.

3.2.2 EIS and Potentiodynamic polarization studies

EIS and potentiodynamic polarization studies were performed to check the corrosion behaviour of all the coatings generated on AA2024-T4 substrates and compare with that of the bare substrates. These experiments were carried out for SH, HNC, Mat sol coated and uncoated AA2024-T4 substrates after exposing them to 3.5 wt % NaCl solution for 1, 72, 120, 168 and 216 h.

EIS results of HNT clay-based coatings on AA2024-T4 are shown as Nyquist plots in Fig. 3.7 and the fit parameters obtained after fitting with the equivalent electrical circuit are presented in Table 3.1. The equivalent electrical circuit for fitting the EIS data is given in Fig. 3.8, where the charge transfer resistance (R_{ct}) is in parallel with a double-layer capacitance (CPE_{dl}), which is in series with $R_{oxide/coat}$. CPE_{oxide/coat} and $R_{oxide/coat}$ correspond to capacitance and resistance of the oxide/coating, in which oxide layer is for uncoated and coating layer for coated substrates. There is a formation of thin aluminum oxide passive layer on uncoated substrates, indicating two interfaces. Therefore, the results were fitted with two-time constants for both uncoated and coated substrates. Constant phase element (CPE) was used in this equivalent electrical circuit instead of a pure capacitor, as all the Nyquist plots given in Fig. 3.7 deviated from the ideal semi-circle shape. This non-ideal frequency response is attributed to the inhomogeneity of the metal surface arising from interfacial phenomena or surface roughness. The value of pseudo capacitance C ($C_{oxide}/C_{coat}/C_{dl}$) was calculated from CPE parameter values Q_o , n and resistance R , using the following expression. Similar equivalent circuit was also reported by other researchers [5–8].

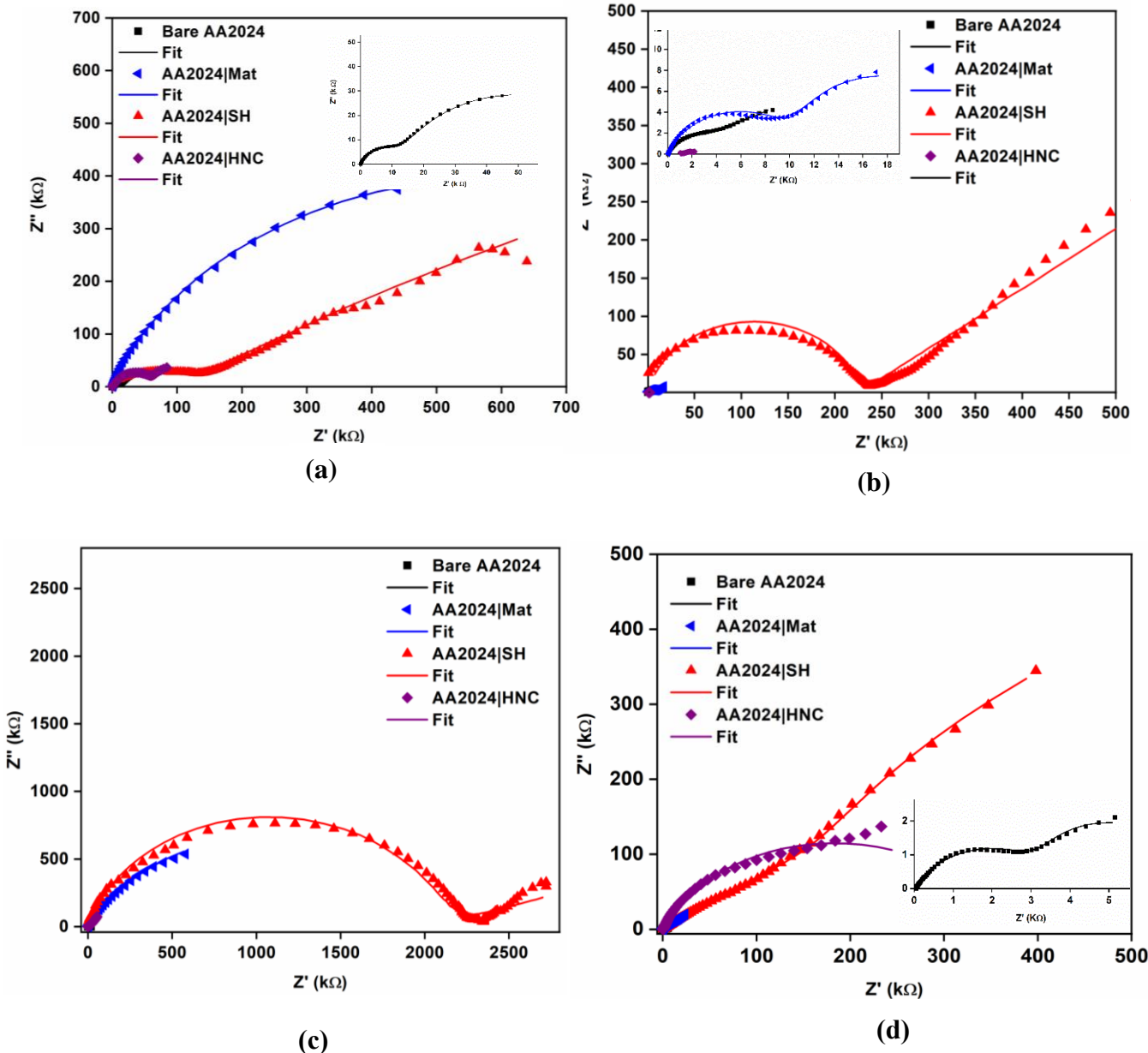
$$C = (Q_o \times R)^{(1/n)} (1/R)$$

The R_{ct} for Mat coated substrates (Table 3.1 and Fig. 3.8) was high at 1 h of exposure to corrosive medium, which has got decreased on prolonged duration of exposure due to loss of barrier property. SH sol coated substrates have exhibited an increase in R_{ct} as the duration of exposure to corrosive medium was prolonged and it was highest among all after 120 h of exposure to corrosive medium. HNC sol coated substrates exhibited least R_{ct} at all exposure times. These results indicated that, SH sol coated substrates were able to provide prolonged corrosion protection when compared to the matrix and HNC sol coated substrates.

Potentiodynamic polarization curves depicted in Fig. 3.9 and polarization data is presented in Table 3.2. HNC sol coated substrates have shown least corrosion currents

initially, but on prolonged duration of exposure, the corrosion currents were seen to increase. However, SH sol coated substrates exhibited lower corrosion currents initially which further decreased upon increasing the exposure time to corrosive medium.

The above studies clearly indicated that SH sol coated substrates provided prolonged corrosion protection due to the release of corrosion inhibitors.



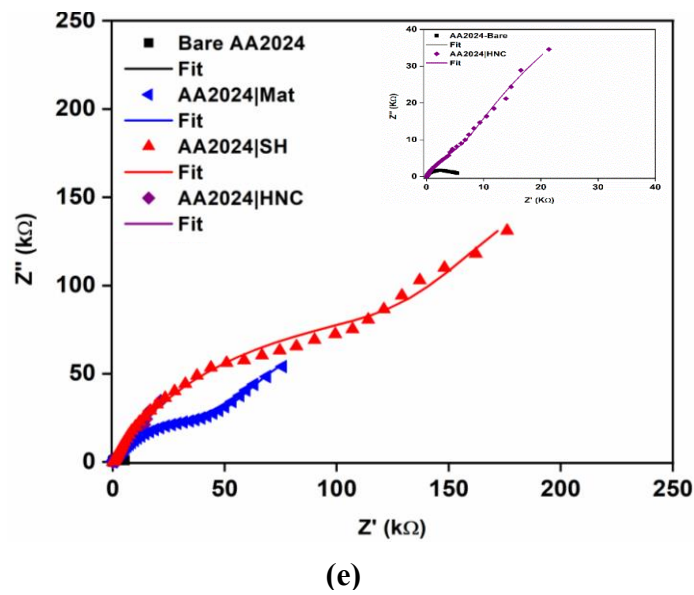


Fig. 3.7. Nyquist plots of coated and uncoated AA2024-T4 substrates after (a) 1 h, (b) 72 h, (c) 120 h, (d) 168 h and (e) 216 h of exposure to 3.5 wt % NaCl solution.

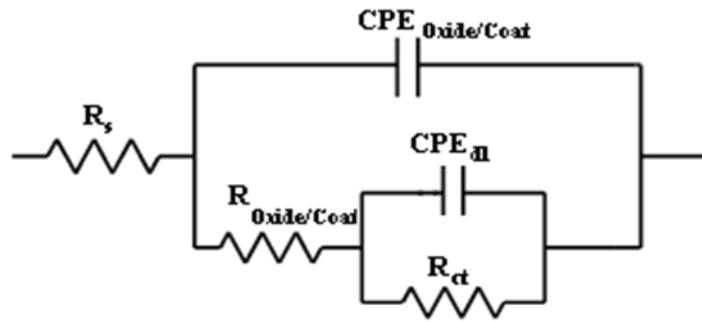


Fig. 3.8. Equivalent electrical circuit used for fitting the EIS data.

Table 3.1. EIS fit data obtained after fitting with the equivalent electrical circuit for coated and uncoated AA2024-T4 substrates at different exposure durations

Exposure time to 3.5 wt% NaCl	Sample name	$R_{oxide/coat}$ k Ω .cm 2	R_{ct} k Ω .cm 2	$C_{oxide/coat}$ μ F/cm 2	C_{dl} μ F/cm 2	CHI square error
1 h	Bare	6.04	36.7	0.126	0.040	1.37×10^{-3}
	AA2024 SH	111.0	410.0	0.00035	258.0	1.60×10^{-3}
	AA2024 Mat	272.0	223.0	0.00011	603.0	0.80×10^{-3}
	AA2024 HNC	47.9	77.9	2.78	37.0	2.86×10^{-3}
72 h	Bare	5.34	7.9	0.496	0.0932	3.64×10^{-3}
	AA2024 SH	5.75	234.0	1.03	1.15	1.57×10^{-3}
	AA2024 Mat	11.5	14.2	25.7	112.0	4.80×10^{-3}
	AA2024 HNC	0.51	2.534	5700.0	6870	0.35×10^{-3}
120 h	Bare	1.36	15.8	6.34	3.80	0.44×10^{-3}
	AA2024 SH	19.1	2800	0.72	0.00072	1.72×10^{-3}
	AA2024 Mat	2.093	942.0	0.0043	6.66	2.60×10^{-3}
	AA2024 HNC	34.36	715.0	24.8	192.0	0.57×10^{-3}
168 h	Bare	3.72	3.35	117.0	4100	0.49×10^{-3}
	AA2024 SH	783.0	441.0	33.1	6.23	1.43×10^{-3}
	AA2024 Mat	26.03	84.76	114.1	725.1	1.61×10^{-3}
	AA2024 HNC	0.22	343.8	0.23	7.60	2.63×10^{-3}
216 h	Bare	5.34	17.9	49.6	932.0	3.64×10^{-3}
	AA2024 SH	225.3	372.3	16.87	111.6	4.74×10^{-3}
	AA2024 Mat	53.50	67.60	38.7	259.0	1.91×10^{-3}
	AA2024 HNC	22.4	17.8	16.2	22.2	1.59×10^{-3}

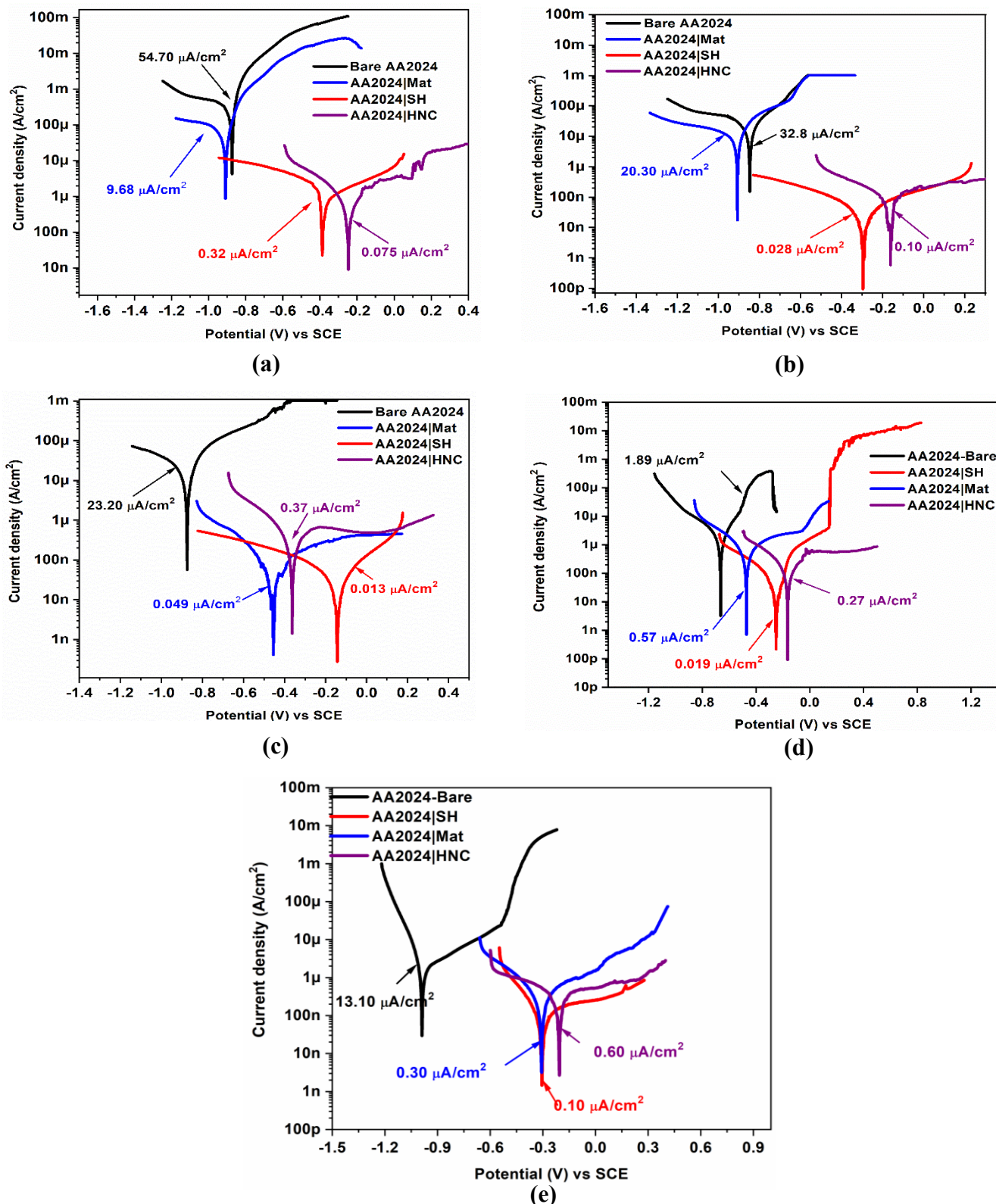


Fig. 3.9. Polarization curves of coated and uncoated AA2024 –T4 substrates after (a) 1h, (b) 72 h and (c) 120 h of exposure to 3.5 wt % NaCl solution.

Table 3.2. Polarization data of coated and uncoated AA2024-T4 substrates at different exposure durations to 3.5 wt % NaCl.

Sample name	Time of immersion in 3.5 wt % NaCl	i_{corr} ($\mu\text{A}/\text{cm}^2$)	E_{corr} (V vs. SCE)
Bare	1 h	54.70	-0.869
AA2024 SH		0.32	-0.388
AA2024 Mat		9.68	-0.909
AA2024 HNC		0.075	-0.247
Bare	72 h	32.80	-0.847
AA2024 SH		0.028	-0.296
AA2024 Mat		20.30	-0.907
AA2024 HNC		0.10	-0.162
Bare	120 h	23.20	-0.875
AA2024 SH		0.013	-0.202
AA2024 Mat		0.049	-0.455
AA2024 HNC		0.37	-0.363
Bare	168 h	1.89	-0.664
AA2024 SH		0.019	-0.251
AA2024 Mat		0.57	-0.472
AA2024 HNC		0.27	-0.252
Bare	216 h	13.10	-0.746
AA2024 SH		0.10	-0.305
AA2024 Mat		0.30	-0.307
AA2024 HNC		0.60	-0.206

3.2.3 Weight loss analysis

The corrosion rate (mmpy) of coated and uncoated substrates was determined by weight loss studies after 5 days of immersion in 3.5 wt % NaCl according to GSTM-G31 standard procedure [9,10]. A comparison of corrosion rates determined for coated and uncoated AA2024-T4 substrates is shown in Fig. 3.10. SH sol coated substrates have shown the least corrosion rate after 120 h. Matrix coated substrates exhibited corrosion rate next to the SH coated substrates. However, HNC sol coated substrates showed highest corrosion rate, which is even higher than bare substrates.

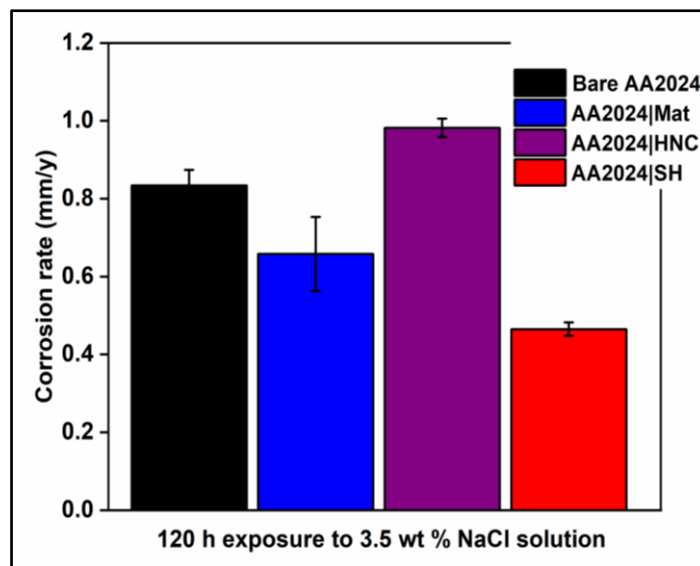


Fig. 3.10. Comparison of corrosion rate of coated AA2024-T4 substrates from weight loss analysis.

3.2.4 Salt Spray Test (SST) and EDS analysis

EDS elemental analysis was carried out for salt spray tested coated and uncoated AA2024-T4 substrates before and after exposure to 5 wt % NaCl according to ASTM-B117 standard method [11]. An 'X' shaped artificial damage was created by means of scribing the surface with a sharp tool before exposing them to salt spray. The results of the EDS analysis in the scribed area are shown in Table 3.3. Bare substrates showed increase in the O amount after SST in the scratched area due to the accumulation of corrosion product. Mat and HNC sol coated substrates showed an increase in the C and O content after SST. Presence Mg and Cu represents the alloying elements in AA2024 alloy. SH sol coated substrates have shown an increase in the amount of C, O, Si along with Ce and Zr, which indicated that the corrosion inhibitors have got released into the scratch region by self-healing mechanism.

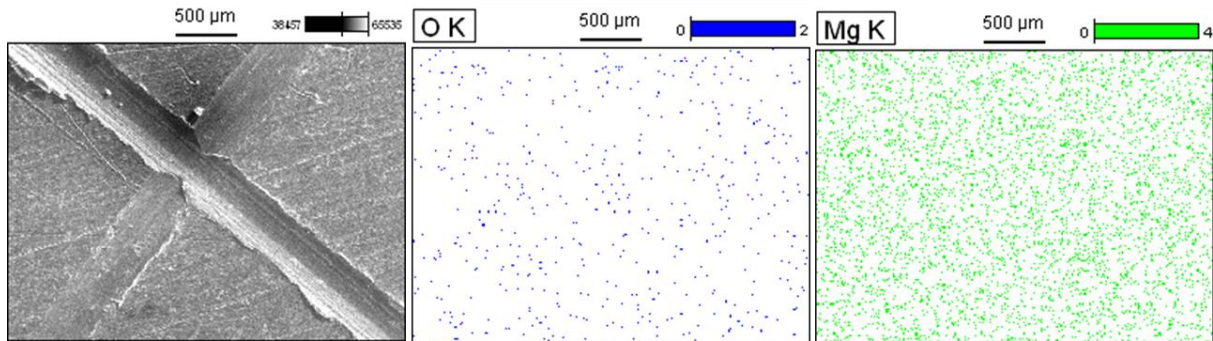
Table 3.3. EDS analysis of coated uncoated AA2024-T4 substrates in the scribed region, before and after exposure to 5 wt % NaCl solution for 168 h

Sample name	SST	% weight ratio of elements in the scratched area									
		C	O	Na	Mg	Al	Si	Cl	Cu	Zr	Ce
Bare	Before	-	0.61	-	1.56	92.32	-	-	5.51	-	-
	After	-	27.83	0.60	0.49	37.70	-	6.48	26.90	-	-
Matrix sol coated	Before	0.00	0.39	-	1.26	92.35	1.27	-	4.73	-	-
	After	6.62	26.75	0.48	1.07	52.21	0.50	2.04	10.32	-	-
HNC sol coated	Before	0.00	0.90	-	1.25	92.85	0.00	-	5.00	-	-
	After	12.63	33.24	8.16	0.00	39.65	3.85	0.35	2.12	-	-
SH sol coated	Before	0.00	0.27	-	0.00	96.94	0.04	-	2.75	0.00	0.00
	After	25.77	12.45	0.12	0.00	54.01	2.84	2.65	1.88	0.22	0.06

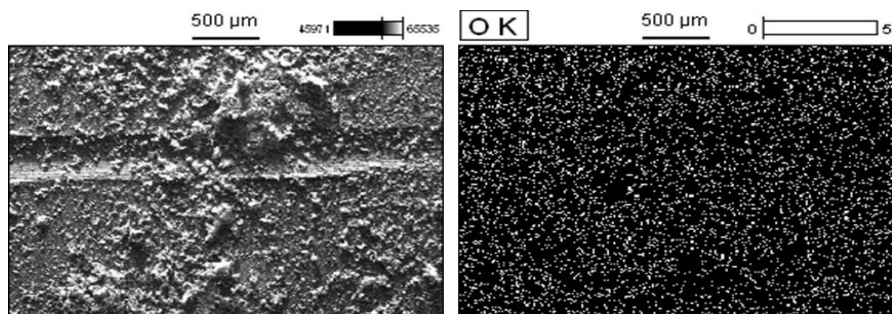
3.2.5 Salt Immersion Test (SIT) and EDS elemental mapping

The uncoated and all coated AA2024-T4 substrates were immersed in 3.5 wt % NaCl solution for 120 h after making an artificial scratch. EDS elemental mapping was carried out to check the release of corrosion inhibitors into the scratch area as depicted in Fig. 3.11. Bare substrate before immersion (Fig. 3.11. (a)), has shown presence of Mg and Cu along with Al and O indicating the alloying elements in AA2024-T4. After SST there is an increased amount of O for bare (Fig. 3.11 (b)) indicating the formation of corrosion product. Mat and HNC coated substrates showed increased amounts of O, Al, Si in the scribed area as shown in Fig. 3.11 (d) and (f) respectively. SH sol coated substrates showed increased amounts of Ce and Zr along with the C, O, Al and Si in the scribed area (Fig. 3.11 (h)), indicating that the corrosion inhibitors have got released into the scratch region after exposing the damage

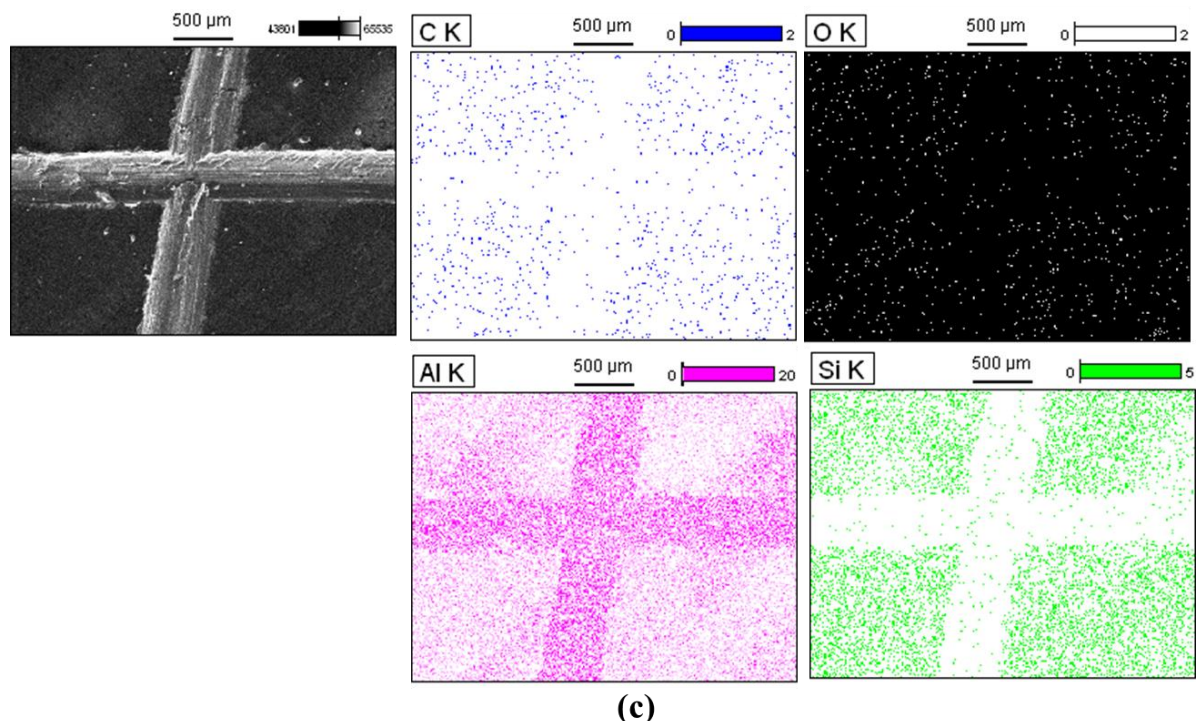
to corrosion medium. Increase in the amount of C and O indicated that the monomers added inside the HNTs along with inhibitors have also got polymerised to form a polymeric passive layer in the presence of inhibitors.



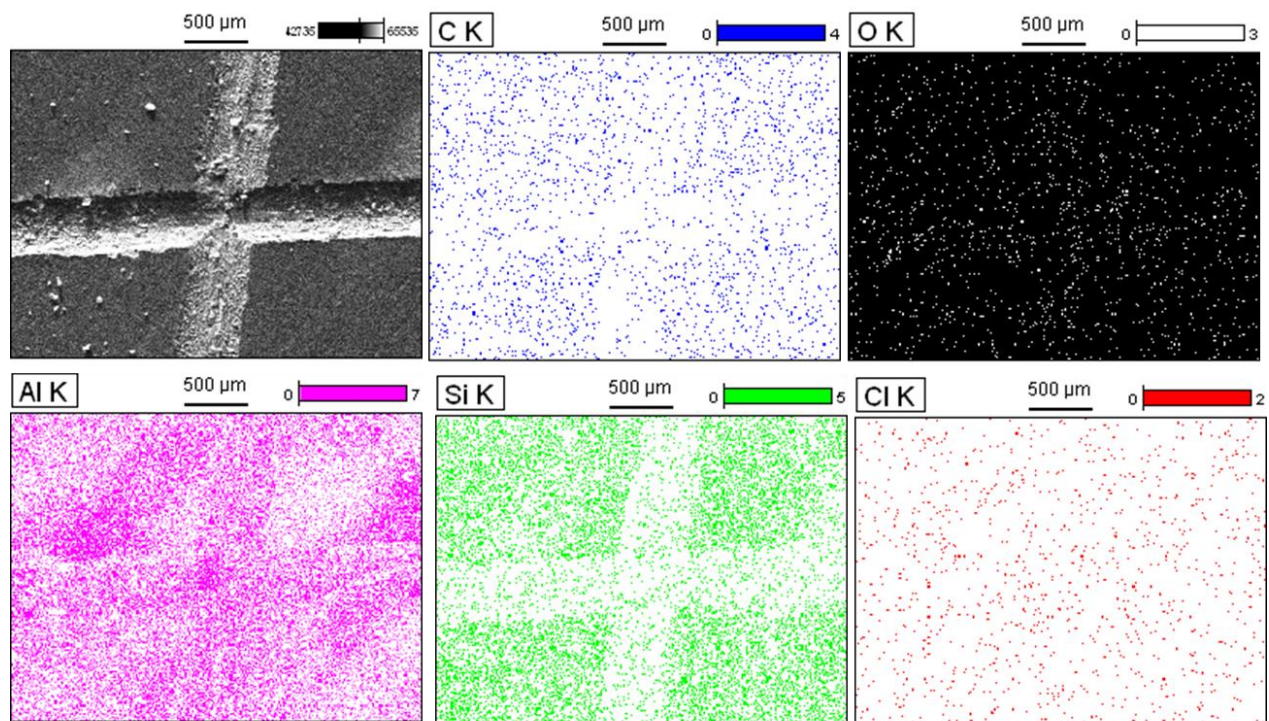
(a)



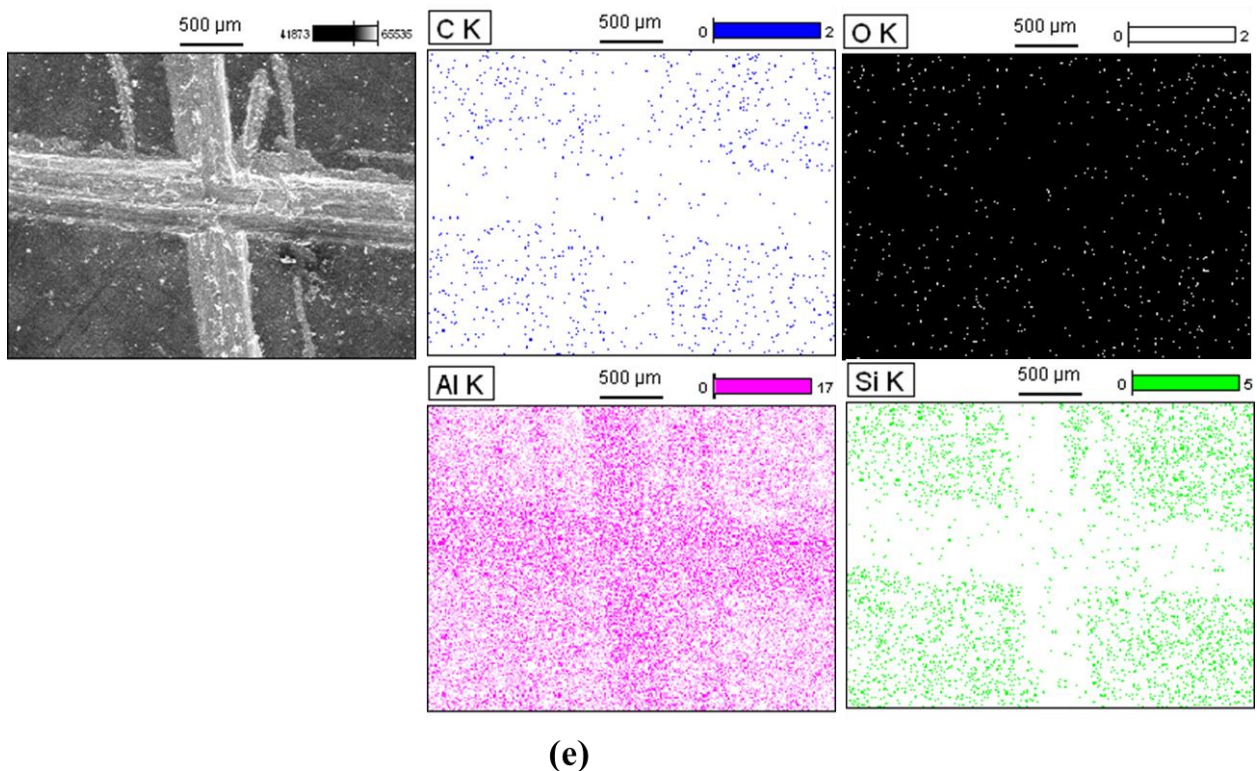
(b)



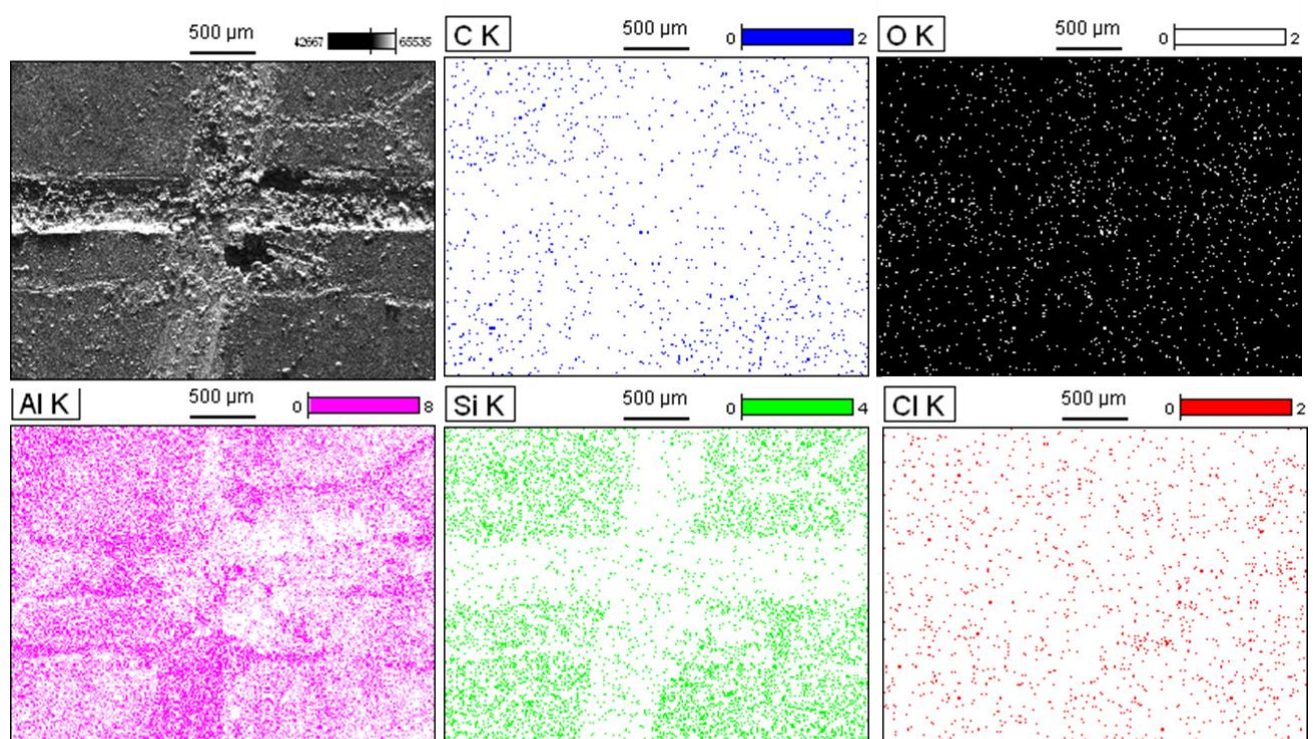
(c)



(d)



(e)



(f)

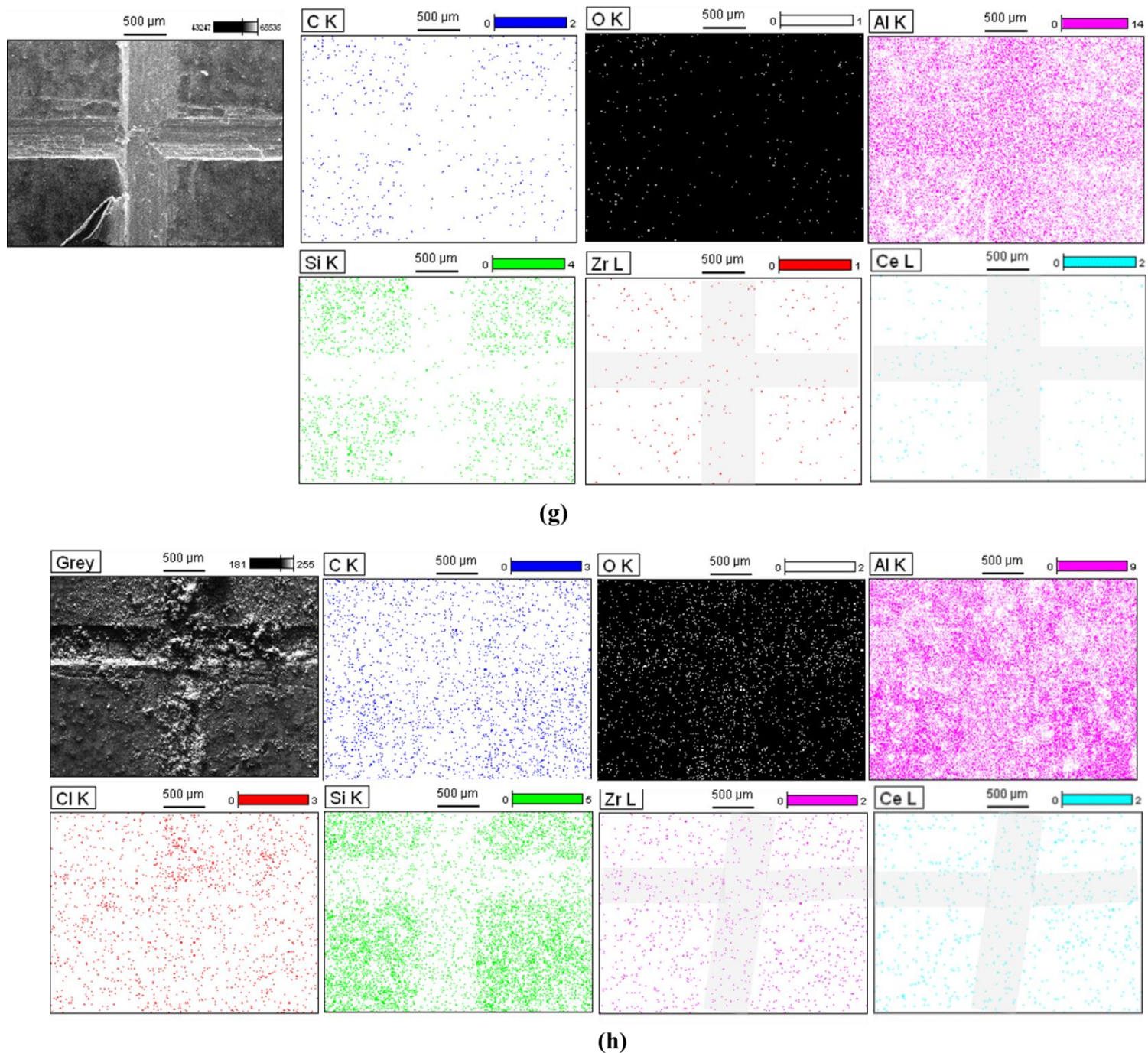


Fig. 3.11. EDS elemental mapping of bare AA2024-T4 substrate (a) before; (b) after salt immersion, Mat sol coated substrate (c) before; (d) after salt immersion, HNC sol coated substrate (e) before; (f) after salt immersion and SH sol coated substrate (g) before; (h) after salt immersion.

3.2.6 Scanning vibrating electrode technique (SVET) analysis

The self-healing property of the developed inhibitor loaded HNT-based coatings has been evaluated by a localized electrochemical testing method known as scanning vibrating electrode technique (SVET). The current density maps obtained after exposing the scribed

region of coated substrates to 3.5 wt % NaCl solution at different time intervals are given in Fig. 3.12. For uncoated substrates, there is a rapid increase in the anodic current with the exposure time indicating that more corrosion has taken place as there is no protection. Mat sol coated substrates did not show any anodic current initially due to its barrier nature, but the anodic current got increased as the time of exposure to corrosive medium is increased. HNC sol coated substrates have shown increased anodic current with increased duration of exposure to corrosive medium, indicating the absence of self-healing property. However, for SH sol coated substrates there is initially a small anodic current due to the attack of corrosive species, which gets suppressed as a function of time. This indicated that SH sol coated substrates having cationic inhibitors, were able to provide self-healing action when there is a damage to the coating and hence a longer duration of corrosion protection.

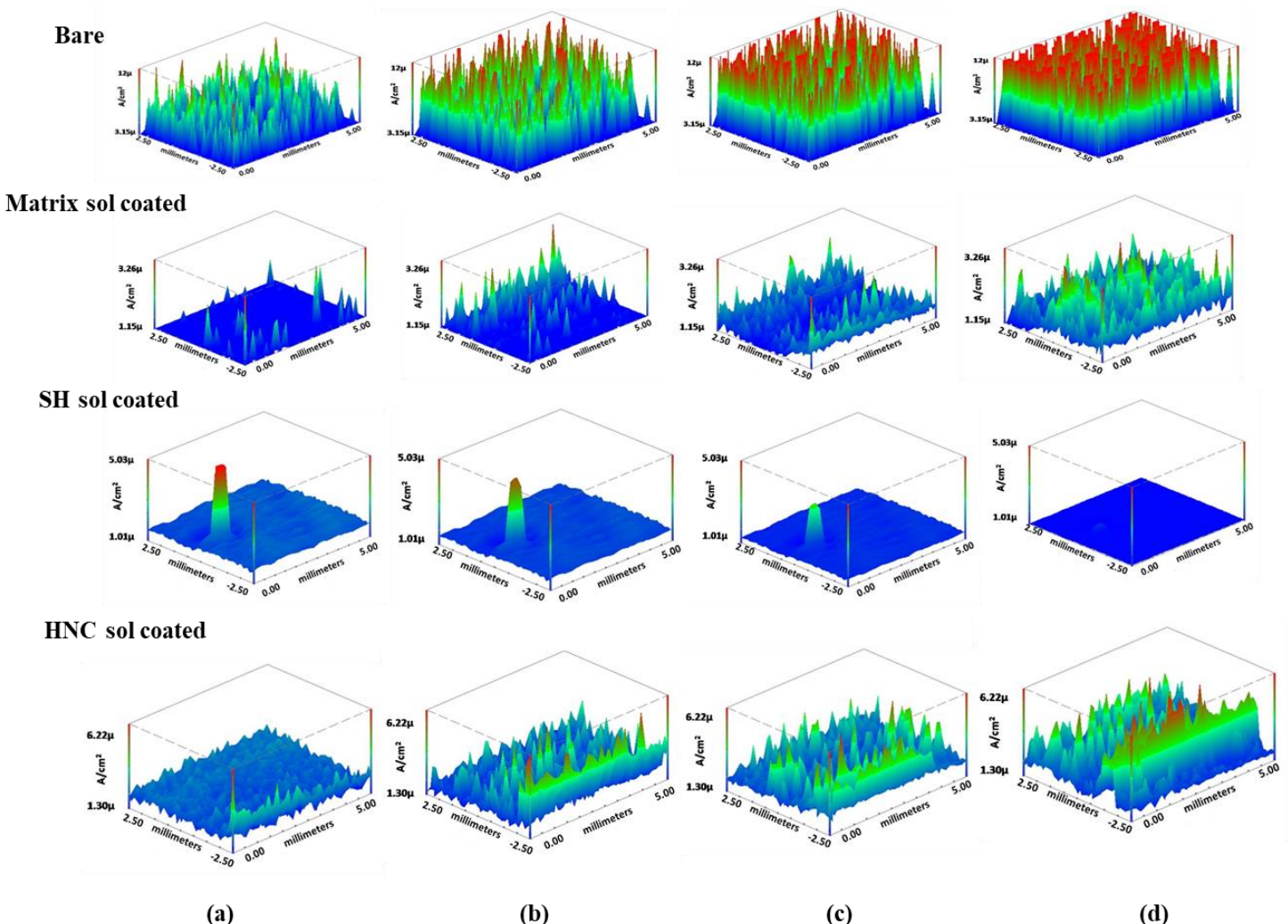


Fig. 3.12. Current density maps obtained in the scribed region at a) initially, b) 1 h, c) 12 h and d) 24 h of exposure to 3.5 wt % NaCl solution.

3.3 Results and discussions of coatings on A356.0 alloy

3.3.1 Adhesion test

Fig. 3.13 depicts optical microscopic images of coatings on A356.0 substrates after making the grid lines using cross-hatch cutter, before and after tape adhesion peel off test. The Mat sol coatings (Fig. 3.13 (a) and (b)) have shown removal of the coating up to 15 % along the edges of grids after the tape was peeled off and hence, the adhesion strength of these coatings were ranked as 3B. Similarly, HNC sol coated substrates ((Fig. 3.13 (c) and (d)) have also shown removed coating along the edges of the grids, the area of removal was up to a level of 5 %. Therefore, adhesion strength of HNC coatings was ranked as 4B. However, SH sol coatings (Fig. 3.13 (e) and (f)), have not shown any removal of coating after tape peel off and had very good adhesion with substrates and hence, adhesion strength of SH coatings was ranked as 5B.

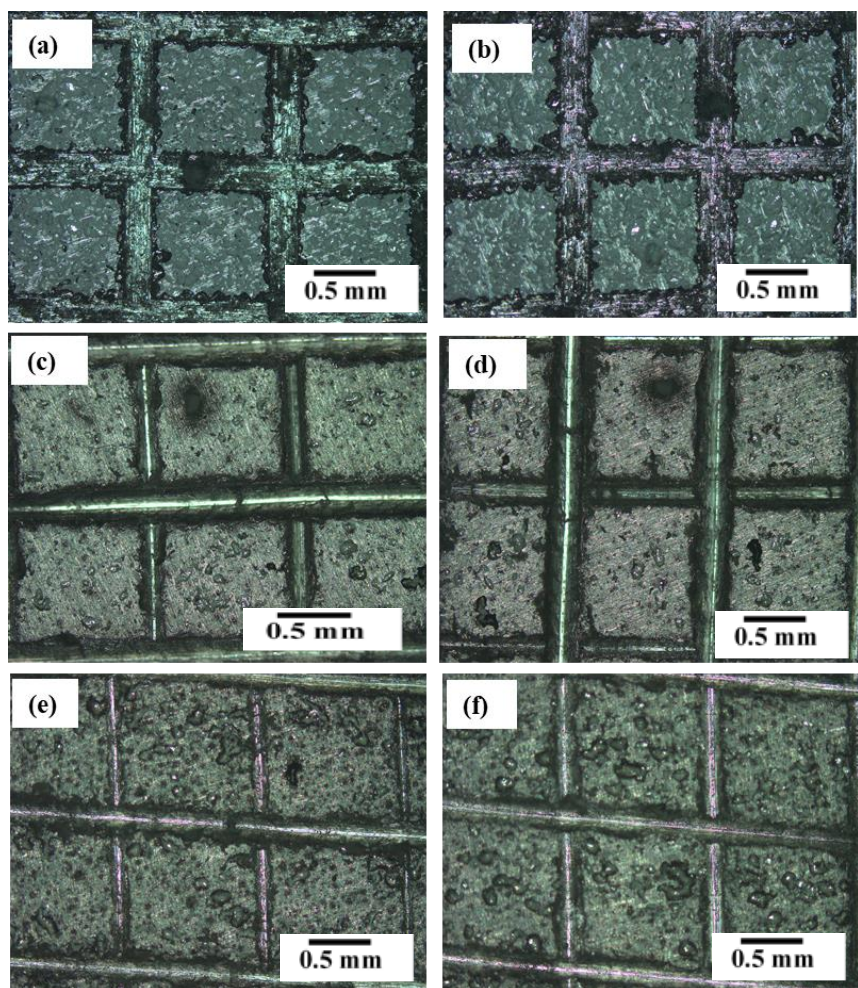


Fig. 3.13. Microscopic images of Mat sol coated (a, b), HNC sol coated (c, d) and SH sol coated (e, f) substrates before putting on tape (a, c, e) and after removal of tape (b, d, f).

3.3.2 EIS and Potentiodynamic polarization studies

EIS and potentiodynamic polarization studies were carried out for SH, HNC and Mat sol coated A356.0 substrates along with the uncoated (Bare) substrates after exposing them to 3.5 wt % NaCl solution for 1, 72, 120, 168 and 216 h. The equivalent electric circuit used for fitting the EIS data of uncoated and coated substrates is shown in Fig. 3.14.

Nyquist plots for coated and uncoated substrates are shown in Fig. 3.15. The charge-transfer resistance (R_{ct}) determined after fitting the EIS data with the equivalent electric circuit is plotted as a function of exposure time as shown Fig. 3.16 and the fit parameters are given in Table 3.4. The magnitude of impedance and phase angle are shown in Bode plots is as given in Fig. 3.17. From Fig. 3.15, 3.16 and 3.17, it can be seen that, the Mat and HNC sol coated substrates exhibited higher R_{ct} values at initial time period (1 h) than SH sol coated substrates, implying higher corrosion resistance for the matrix sol coated and HNC sol coated substrates. The R_{ct} values of matrix coated substrates were found to decrease as the function of exposure to time to corrosion medium, indicating that the barrier protection lasts only for short durations until there is no damage to the coating. HNC sol coated substrates exhibited least R_{ct} value at 72 h, after which there is not much increase in the R_{ct} values. This indicated the poor corrosion resistance of the HNC coating. In overall, corrosion resistance of HNC sol coatings is inferior to that of Mat sol coatings. These observations were in accordance with the studies reported by Huttunen-Saarivirta et al. who studied the corrosion resistance of coatings generated from HNT dispersed in an epoxy matrix on carbon steel substrates [12]. They reported that the barrier and corrosion protection properties get compromised when the empty halloysite nanotubes were embedded in epoxy matrix. The reason for this was attributed to the random orientation of nanotubes, resulting in a less favourable aspect ratio, thereby leading to increased water permeability, which in turn led to poor corrosion protection. On the other hand, the SH sol coated substrates exhibited highest the R_{ct} after prolonged time of exposure. The barrier property of the SH sol coatings was initially low when compared to HNC coated substrates due to the above-mentioned reason and because of which, there is an initiation of corrosion at defective areas. However, on prolonged exposure to the corrosion medium, there is a change in the pH at areas where corrosion gets initiated, and this change in pH acts as a trigger for the release of inhibitors from the loaded HNTs in SH sol. Once the corrosion inhibitors are released, there is a formation of passive layer at the defective area, thereby providing corrosion protection. Therefore, the R_{ct} values of SH sol coated substrates after 120 h or more times of

exposure (168 and 216 h) were enormously high compared to those of all the coated and also uncoated substrates.

The phase angle data from Bode plots (Fig. 3.17) indicates that the SH sol coated substrates exhibited phase angle maximum around 60° at 1, 72 h and which got decreased to 50° at 120 h. The phase angle maximum of SH coated substrates was found to be highest among all after prolonged durations of exposure such as 168 and 216 h. On the other hand, Mat and HNC sol coated substrates though exhibited high phase angle maximum values initially, they were decreased at prolonged durations. It can also be observed that, two phase angle maxima were observed for SH coated substrates after 168 and 216 h, clearly indicating that there is formation of a passive layer by the release of inhibitors by self-healing mechanism and hence two-time constants were seen.

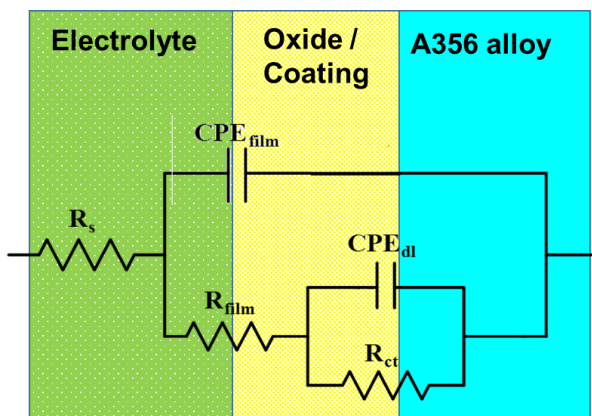


Fig. 3.14. Equivalent electrical used for fitting EIS data of A356.0 substrates

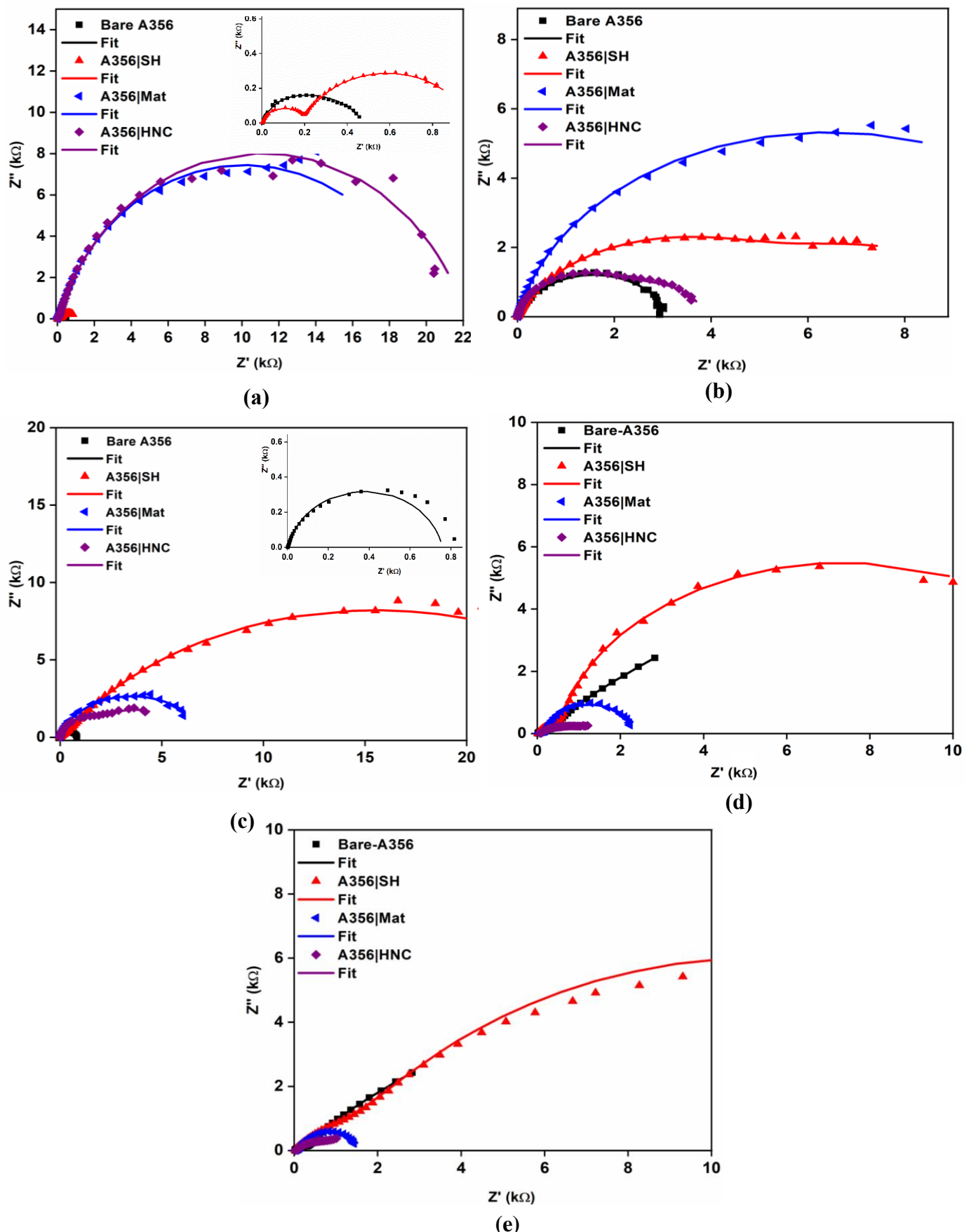


Fig. 3.15. Nyquist plots coated and uncoated A356.0 substrates after (a) 1 h, (b) 72 h, (c) 120 h, (d) 168 h and (e) 216 h.

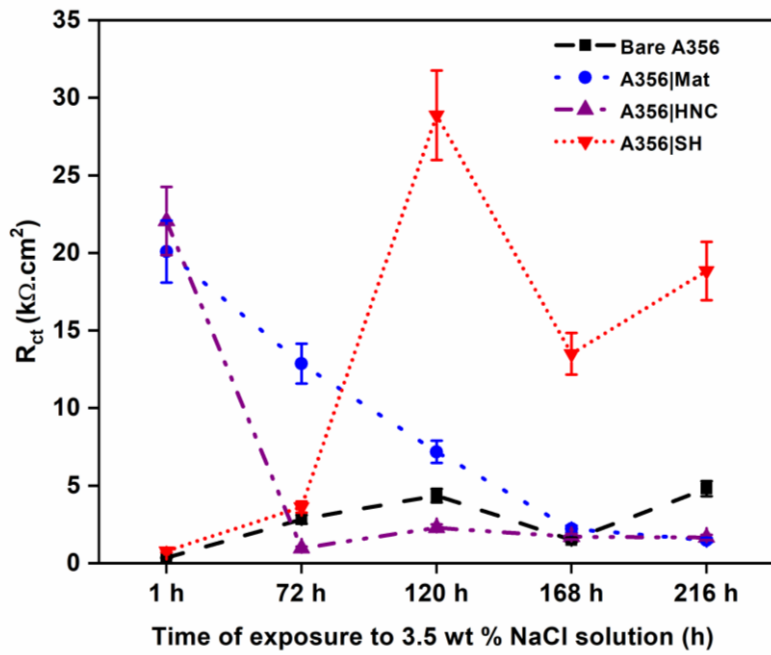
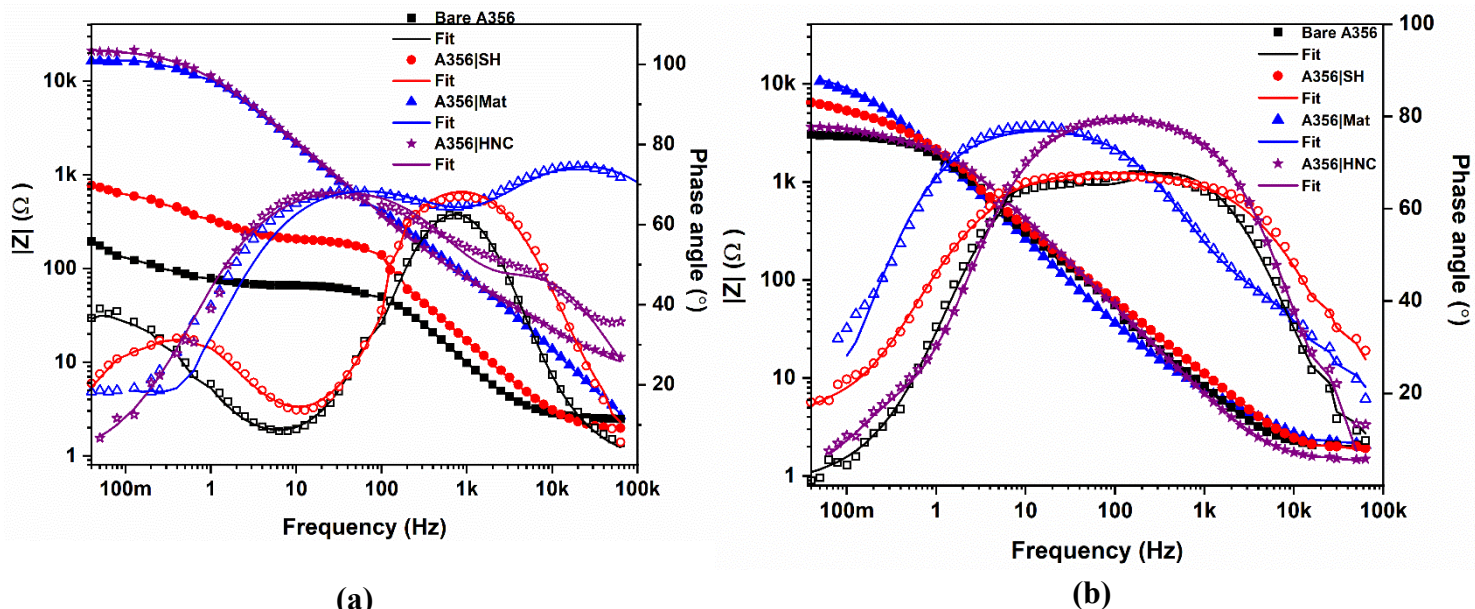


Fig. 3.16. Comparison of charge transfer resistance of coated and uncoated substrates as a function of exposure time to 3.5 wt % NaCl solution. (Note: The lines connecting the data points are just guidelines for the eye)



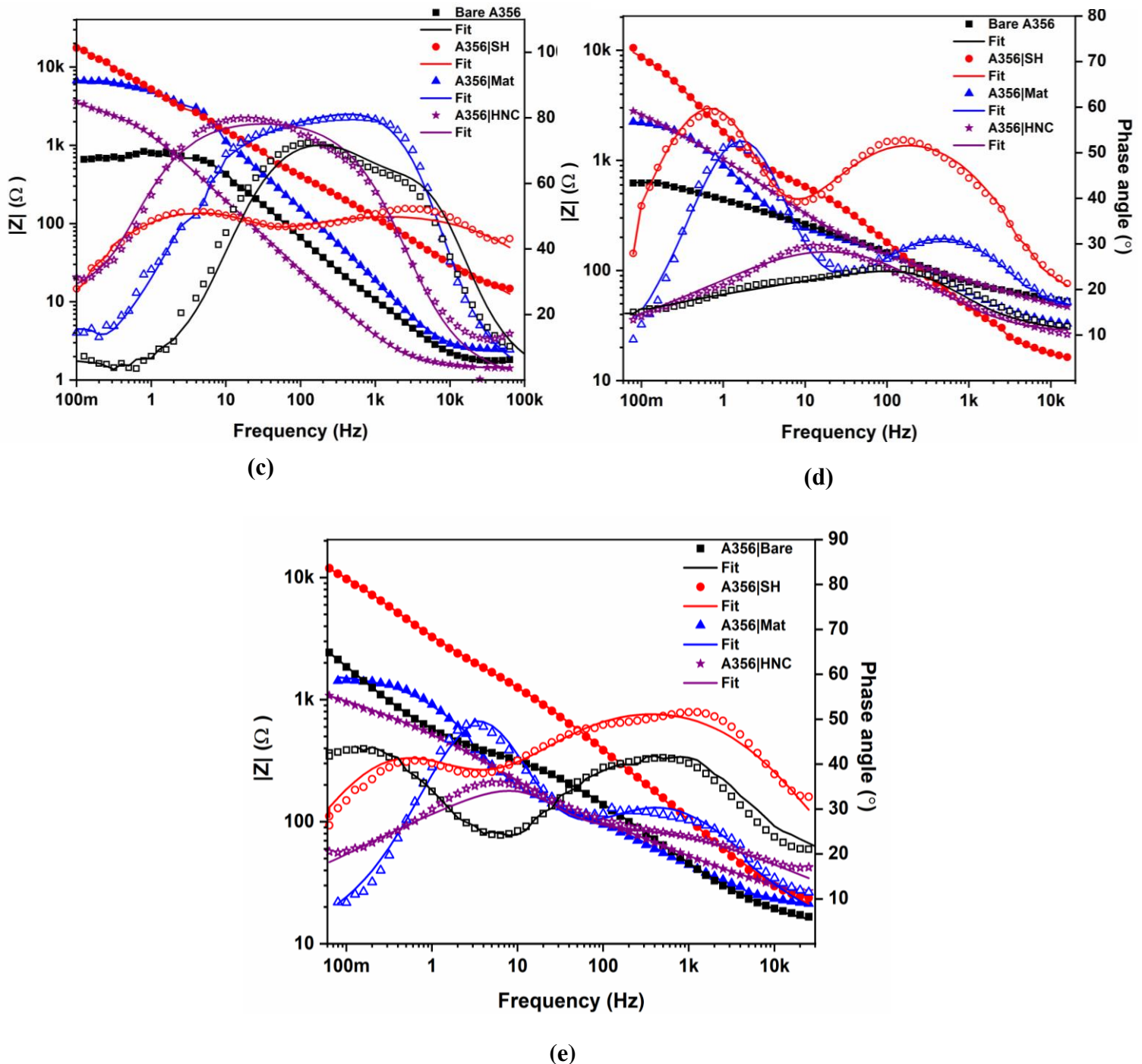


Fig. 3.17. Bode plots for coated and uncoated A356.0 substrates after (a) 1 h, (b) 72 h, (c) 120 h, (d) 168 h and (e) 216 h of exposure to 3.5 wt % NaCl solution.

Table 3.4. EIS fit data of coated and uncoated A356.0 substrates at different exposure durations, obtained after fitting with an equivalent electrical circuit.

Sample	Duration of exposure to 3.5 wt % NaCl	C _{coat} μF/cm ²	R _{coat} kΩ.cm ²	n	C _{dl} μF/cm ²	R _{ct} kΩ.cm ²	n	CHI Sqr error
Bare	1 h	48.2	0.64	0.93	0.0097	0.351	0.84	0.7×10^{-3}
MAT		3.51	0.20	0.88	7.67	20.08	0.76	2.5×10^{-3}
HNC		9.00	0.10	0.77	6.64	22.05	0.82	0.4×10^{-4}
SH		23.9	0.20	0.87	160.0	0.77	0.79	1.2×10^{-3}
Bare	72 h	31.7	0.28	0.84	16.80	2.82	0.84	1.4×10^{-3}
MAT		12.00	0.004	0.71	29.0	12.85	0.88	2.0×10^{-3}
HNC		53.4	287.50	0.90	106.0	0.96	0.95	6.5×10^{-3}
SH		39.4	637.20	0.77	708.0	3.61	0.80	1.9×10^{-3}
Bare	120 h	44.5	5.080	0.78	635.0	4.36	1	2.0×10^{-3}
MAT		25.4	0.072	1	88.9	7.17	0.71	1.4×10^{-3}
HNC		124.0	3.36	0.89	1140.0	2.28	0.75	0.9×10^{-3}
SH		38.8	2.88	0.60	4.76	28.88	0.85	1.8×10^{-3}
Bare	168 h	9.09	0.13	0.28	3.59	1.49	0.80	2.0×10^{-3}
MAT		7.44	0.25	0.61	99.0	2.23	0.99	1.7×10^{-3}
HNC		3000.0	0.10	0.23	710.0	1.70	0.54	0.8×10^{-3}
SH		49.0	1.26	0.68	32.5	13.49	1	1.6×10^{-3}
Bare	216 h	18.30	0.70	0.61	58.3	4.80	0.75	2.7×10^{-3}
MAT		163.0	0.16	0.61	13.80	1.47	0.93	1.7×10^{-3}
HNC		731.0	0.42	0.40	26.60	1.65	0.70	0.8×10^{-3}
SH		34.80	2.79	0.63	63.70	18.84	0.92	1.4×10^{-3}

From the impedance parameters as given in Table 3.4, we can also observe a change in the 'n' value corresponding to R_{ct}. The 'n' value corresponding to R_{ct} for SH coated substrates has been shifted towards higher values from 1 h to 216 h. When the value of 'n' is very close to 1, it indicates that the protective film is highly homogeneous. In case of HNC

coated substrates, the n values decreased as the function of time, which indicates mass transport because of the degradation of coating due to the absence of inhibitors. It also has been observed from these fit parameters that, the R_{coat} of SH sol coated substrates were highest among all the coated and uncoated substrates after prolonged durations of exposure.

A similar trend was observed when the potentiodynamic polarization data was analysed. Polarization curves are depicted in Fig. 3.18 and the polarization experimental results are given in Table 3.5. Bare substrates showed the highest corrosion current among all the substrates for 1 h exposure to corrosive medium. It is interesting to note that the matrix sol coated substrates exhibited nearly equal values of corrosion current (i_{corr}) and corrosion potential up to 120 h of exposure to corrosive medium. The corrosion current got increased more and more after 168 h and after 216 h, it was even higher than the bare. This indicates that the matrix sol rendered excellent undeterred barrier protection to the substrates until it got damaged. However, when HNTs, whether inhibitor loaded or unloaded are added to the matrix sol, the i_{corr} are higher initially and are of the same order. This indicates that there is a slight deterioration in the barrier properties of the matrix sol coating upon the addition of HNTs. The corrosion current and corrosion potential of both SH sol coated and HNC sol coated was nearly equal to each other at initial time periods.

However, after exposure to 120 h, the i_{corr} value of SH sol coated substrates decreased enormously and is almost two orders lesser compared to that of HNC sol coatings. Moreover, the E_{corr} shifted towards positive value after 168 h and slightly shifted to negative value after 216 h. This clearly indicates that self-healing action was indeed taking place. On further prolonged exposure up to 216 h, the SH sol coated substrates exhibited least i_{corr} values, when compared to other coated and uncoated substrates. On the other hand, it may be noted that on prolonged exposure, the HNC coated substrates showed higher currents. This indicates that an optimum corrosion protection is achieved when coatings are generated from SH sol

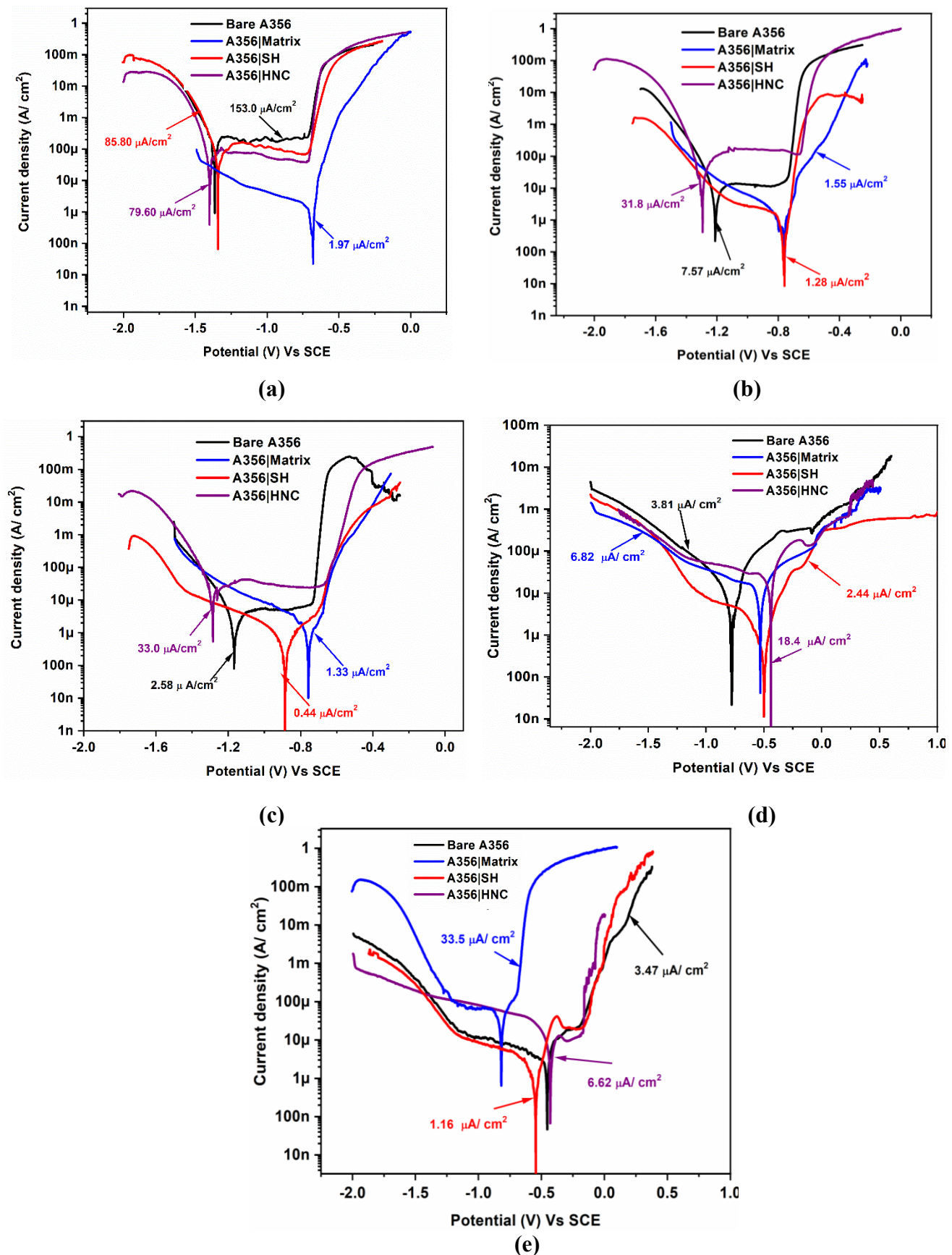


Fig. 3.18. Polarization curves for coated and uncoated A356.0 substrates after (a) 1 h, (b) 72 h, (c) 120 h, (d) 168 h and (e) 216 h of exposure to 3.5 wt % NaCl solution.

Table 3.5. Corrosion current and corrosion potential data for coated and uncoated A356.0 substrates at different times of exposure to 3.5 wt % NaCl solution.

Sample	Time of immersion in 3.5 % NaCl	i_{corr} ($\mu\text{A}/\text{cm}^2$)	E_{corr} (V) vs SCE
Bare	1 h	153.0	-1.365
A356 Mat		1.97	-0.686
A356 HNC		79.6	-1.339
A356 SH		85.8	-1.340
Bare	72 h	7.57	-1.209
A356 Mat		1.55	-0.763
A356 HNC		31.8	-1.297
A356 SH		1.28	-0.768
Bare	120 h	2.58	-1.165
A356 Mat		1.33	-0.756
A356 HNC		33.0	-1.288
A356 SH		0.43	-0.886
Bare	168 h	3.81	-0.776
A356 Mat		6.82	-0.532
A356 HNC		18.3	-0.448
A356 SH		2.44	-0.466
Bare	216 h	3.47	-0.463
A356 Mat		33.5	-0.822
A356 HNC		6.62	-0.428
A356 SH		1.16	-0.550

3.3.3 Weight loss studies

The EIS and potentiodynamic polarization observations were further corroborated by weight loss measurements and the results are shown in Fig. 3.19. SH sol coated substrates have shown the least corrosion rate and HNC sol coated substrates have shown highest corrosion rate among all.

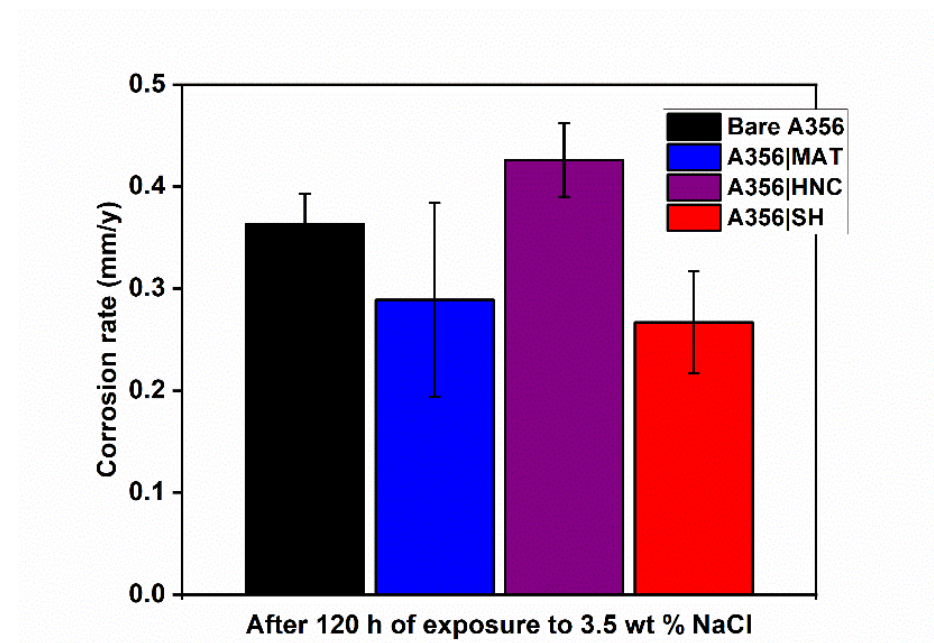


Fig. 3.19. Comparison of corrosion rate of A356.0 substrates determined by weight loss experiments.

3.3.4 SST and EDS analysis

SEM images for uncoated and coated A356.0 substrates, before and after SST for 168 h as per ASTM B-117 standard procedure are shown in Fig. 3.20. A comparison of the amounts of C, Si, O, Ce and Zr from EDS analysis on the scribed area before and after the SST was made and is given in Table 3.6. The bare substrates after scribing showed the presence of primarily Al and Si with a low amount of O (Fig. 3.20 (a,b) and Table 3.6). Mat and HNC sol coated substrates (Fig. 3.20 (d,f)) have shown higher amounts of O after SST compared to SH sol coated substrates. The amount of O in the scribed area has increased after exposure to the corrosive medium, indicating the formation of corrosion products. After exposure, it could be seen in Fig. 3.20 (h) and Table 3.6 that there were increased amounts of C, Si, O, Ce and Zr in the scribed area for SH sol coated substrates, which confirm the possible formation of a passive oxide layer of Ce and Zr along with a polyethylene oxide product resulted by the cationic ($\text{Ce}^{3+}/\text{Zr}^{4+}$) initiated polymerization of epoxy groups of the epoxy silane present in the matrix sol.

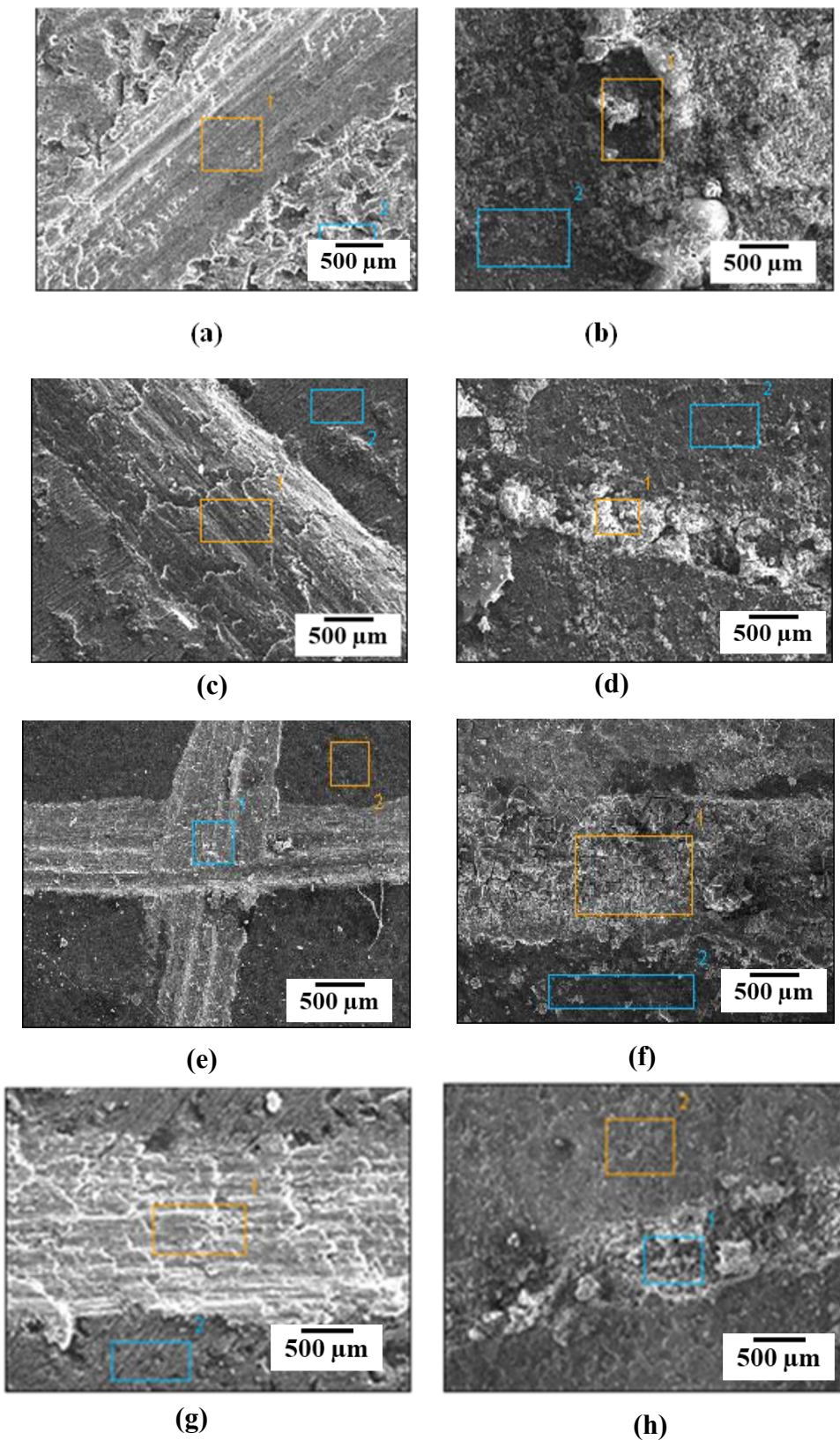


Fig. 3.20. SEM images of bare (a, b), matrix sol coated (c, d), HNC sol coated (e, f) and SH sol coated (g, h) A356.0 substrates before (a, c, e, g) and after (b, d, f, h) 168 h exposure to 5 wt % NaCl solution.

Table 3.6. EDS analysis of uncoated and coated substrates, before and after SST for 168 h in 5 wt % NaCl solution.

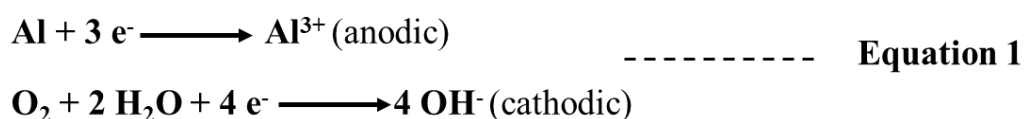
Sample name	SST	% weight ratio of elements in the scratched area							
		C	O	Na	Al	Si	Cl	Zr	Ce
Bare	Before	-	4.33	-	85.51	10.16	-	-	-
	After	-	41.38	1.33	43.00	9.69	4.61	-	-
Mat sol coated	Before	1.86	0.10	-	89.81	8.23	-	-	-
	After	8.57	46.14	0.52	36.61	3.53	4.63	-	-
HNC sol coated	Before	12.65	2.17	-	73.80	11.38	-	-	-
	After	16.85	37.45	0.30	37.11	4.73	3.56	-	-
SH sol coated	Before	3.80	2.21	-	81.63	12.36	-	0.00	0.00
	After	9.29	20.01	0.67	25.29	41.48	2.76	0.25	0.25

3.3.5 SVET analysis

The current density maps obtained from SVET measurements for different substrates at different exposure times are shown in Fig. 3.21. The bare substrate has shown a steep increase in the anodic current in the flaw area from 12 h of exposure, indicating an accelerated corrosion due to continuous dissolution of aluminum at the anodic sites given in the equation 1, as there is absence of any protection. Mat sol coated substrates have shown less anodic current up to 12 h, after which there is an increase in the anodic current flow. This indicates the good barrier protection by matrix sol coating initially, which becomes less protective on increasing the exposure time to corrosive medium. The SH sol coated substrates initially have shown only a small anodic current flow in the flaw area due to initiation of corrosion in the

scratched area because of Cl^- ions at the scratch. However, after 12 h, the anodic current was seen to be decreased which was completely suppressed after 24 h. This can be explained as follows. The local pH change in the environment due to the attack of Cl^- ion medium acts as a driving force for the release of cationic inhibitors (Ce^{3+}) from the HNTs forming an insoluble passive layer as given in the equation 2, Subsequently, the released cationic inhibitors act as catalyst promoting the polymerization of epoxy monomers added into the matrix as shown in equation 3, which further stops the corrosion of metal. Therefore, the anodic current got completely suppressed after 24 h. This further confirmed that the proposed self-healing property of SH sol coatings.

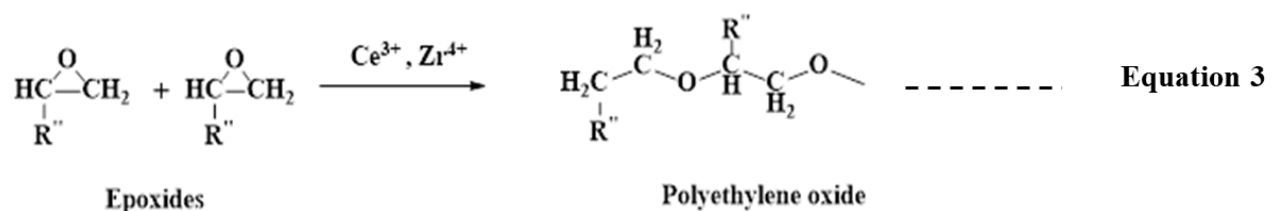
The corrosion reaction in metal



In presence of cationic inhibitor



Mechanism of cationic polymerization



R'' = Organic radical

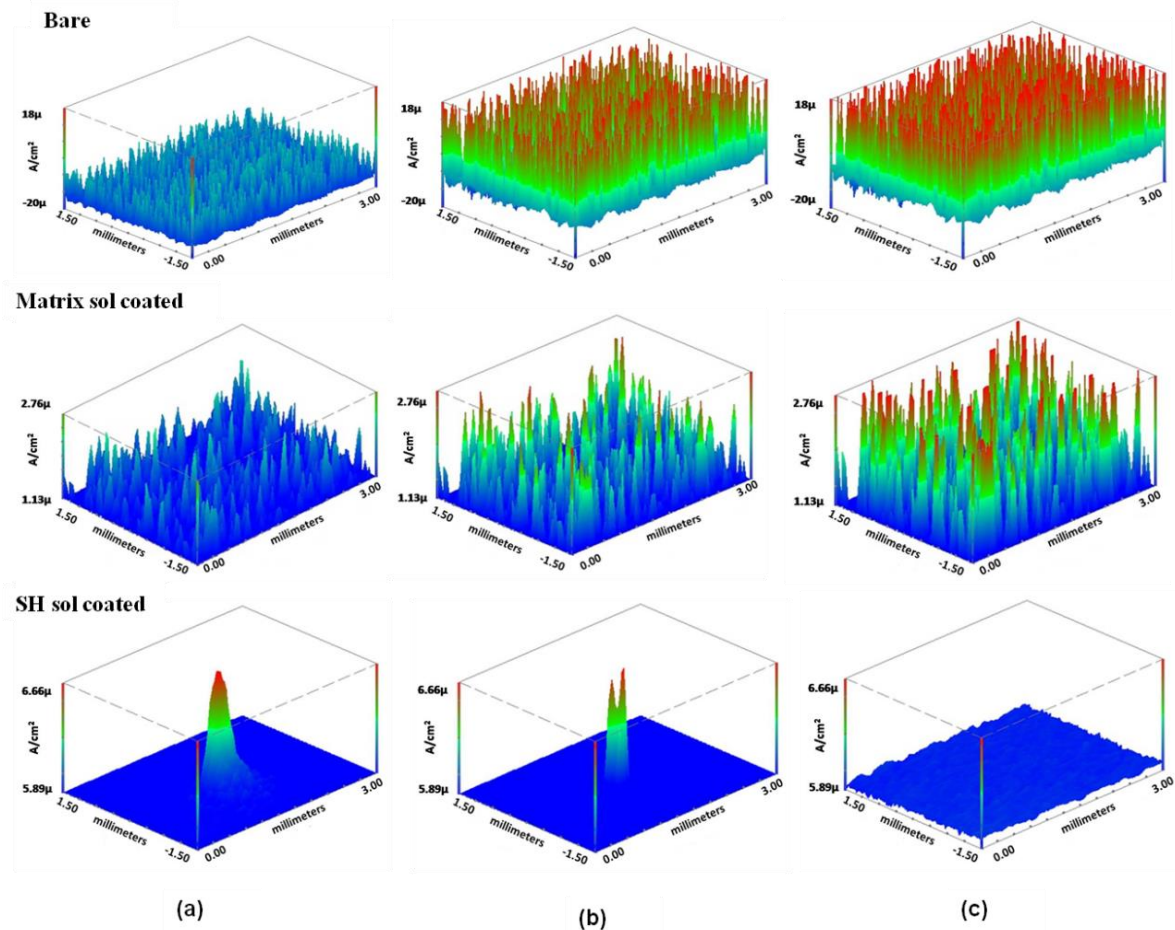


Fig. 3.21. Current density maps for uncoated, matrix and SH sol coated A356.0 substrates for (a) 0, (b) 12 and (c) 24 h of exposure to 3.5 wt % NaCl solution.

3.3.6 Micro-Raman spectroscopic analysis

Micro-Raman spectroscopic analysis was carried for confirming the mechanism of self-healing action. This analysis was carried out after immersion of substrates in 3.5 wt% NaCl solution for 120 h. The uncoated and SH coated substrates were scribed in the form of 'X' shape prior to the NaCl exposure. The Micro-Raman analysis was carried out for pure aluminum substrates also along with A356.0 substrates to find out the phase composition of corrosion product in bare aluminum and polyethylene oxide polymer formation in SH coated substrates.

The Raman spectrum of bare pure aluminum substrate after immersion as shown in Fig. 3.22, has exhibited only one peak at 860 cm^{-1} , which corresponds to alumina [13]. This indicated the formation of corrosion product on exposure to the corrosive medium. The scribed region of SH coated substrate showed few dark spots after immersion as depicted in Fig. 3.23 (a). The micro-Raman spectrum for the dark region as given in Fig. 3.23 (b) has

shown peaks at ~ 231 , 286 and 580 cm^{-1} corresponding to zirconia [14] and a broad peak at 450 - 517 cm^{-1} corresponding to both ceria and zirconia phases [14,15]. A sharp, highly intense peak at 1440 cm^{-1} , which corresponds to $\delta(\text{CH}_2)$ stretching frequency of poly ethylene oxide (PEO) and a broad peak in the region 1520 - 1590 cm^{-1} [16], corresponding to C=C-stretching of acrylic group were observed [17]. The mapping for this spectrum as shown in Fig. 3.23 (c) indicated the presence of ceria, zirconia and PEO. This clearly confirmed that the inhibitors have got released into the scratch from nearby the scratch to self-heal the material by a) polymerization of epoxy group in the matrix and the acrylic group from halloysite nanotubes to form a thick layer and b) by formation of a passive CeO_2 and ZrO_2 layers.

The micro-Raman spectrum for SH coated A356.0 after immersion as given in Fig. 3.24 has shown a sharp, highly intense peak at 521 cm^{-1} corresponding to crystalline silicon belonging to alloying element Si in A356.0 alloy, and peaks at 232 cm^{-1} and 294 cm^{-1} correspond to zirconia [14]. Peaks corresponding for ceria and PEO were not seen in this spectrum due to the domination of crystalline silicon present in this alloy. The Raman phase mapping for the spectrum (Fig. 3.24 (a)) is given in Fig. 3.25 (b), and it shows the presence of red, green and blue colours corresponding to heated amorphous zirconia and crystalline zirconia respectively. This observation showed that the different phases of zirconia were present uniformly all over the scratch. This indicated that Zr^{4+} has got released into the scratch from locations in the vicinity of the scratch to self-heal the damage by the formation of passive ZrO_2 layer.

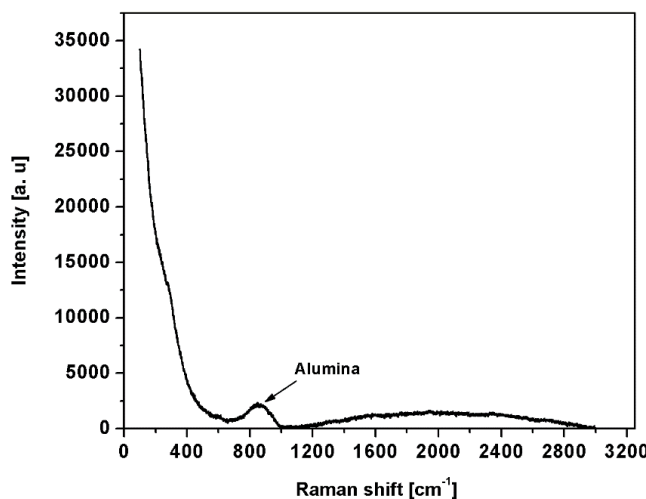
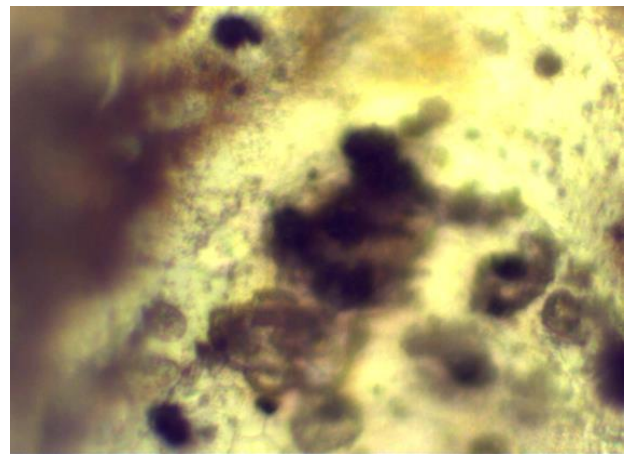
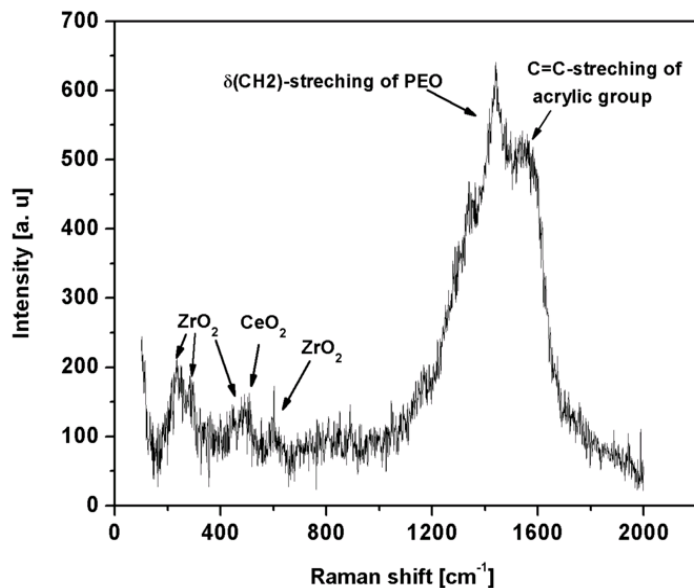


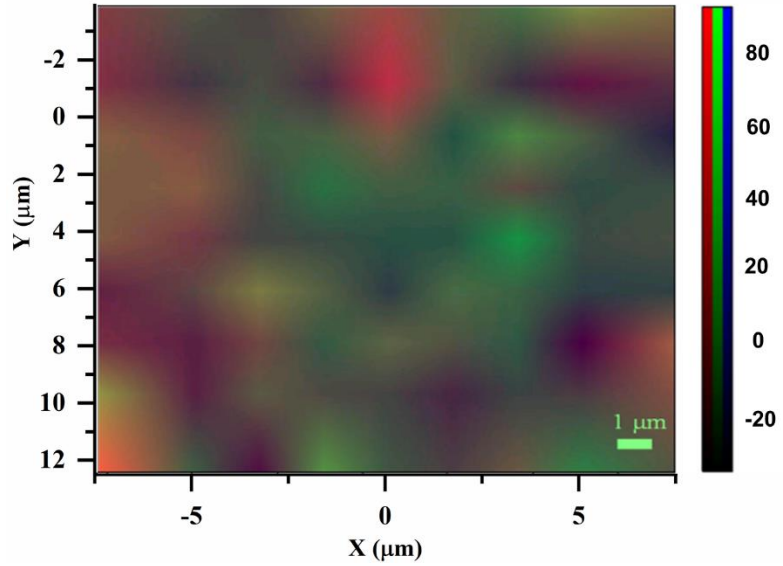
Fig. 3.22. Micro Raman spectrum of uncoated aluminum in the scratched region after immersion in 3.5 wt % NaCl solution for 120 h.



(a)



(b)



(c)

Fig. 3.23. (a) Image of scratch region, (b) Raman spectrum and (c) phase mapping corresponding to the dark spots in the scratch (red-zirconia; green- ceria; blue- PEO).

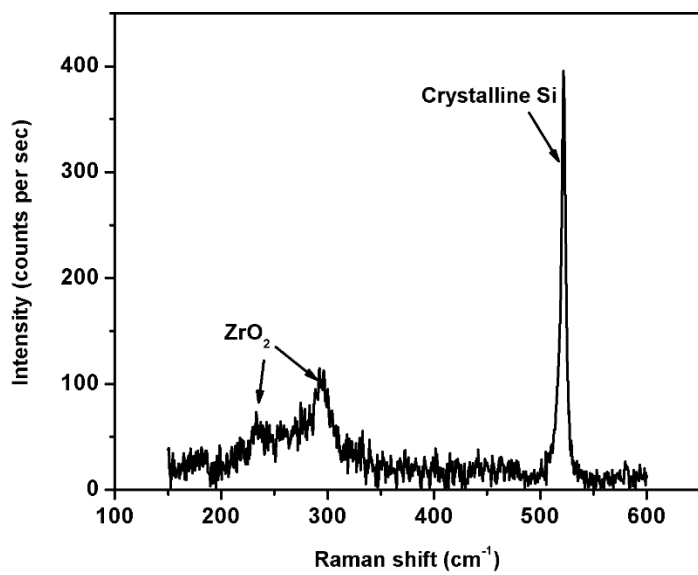


Fig. 3.24. Micro-Raman spectrum of SH coated A356.0 substrate in the scribed area, after exposure to 3.5 wt % NaCl for 120 h.

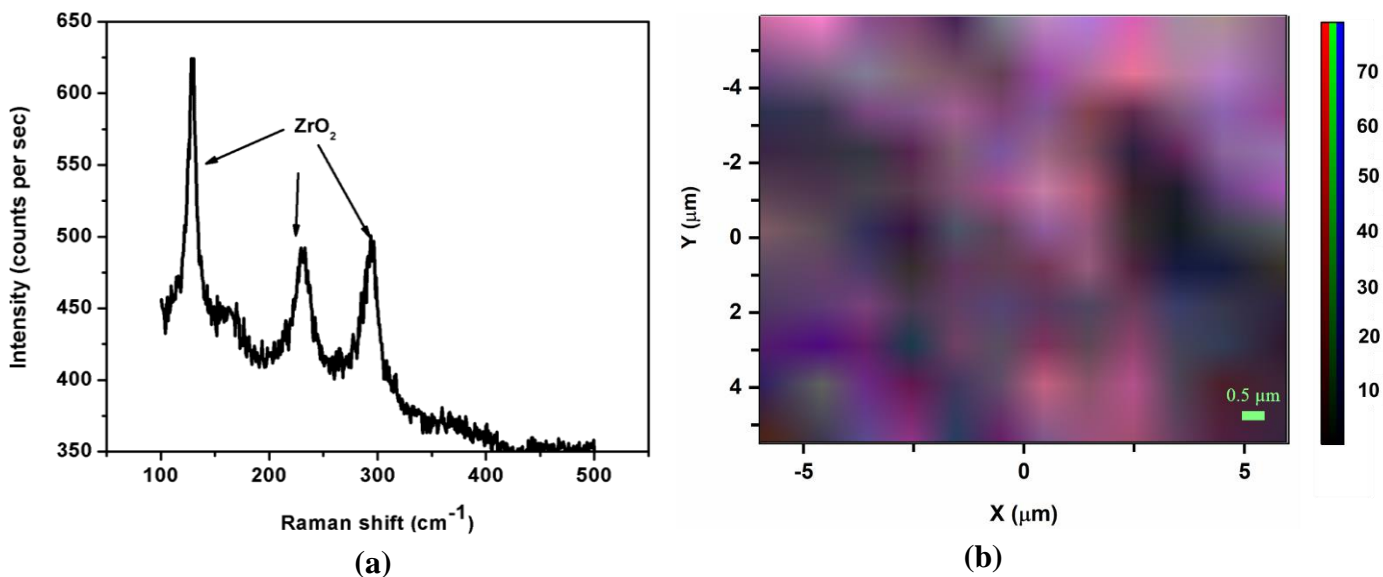


Fig. 3.25. (a) Micro-Raman spectrum and (b) phase mapping of SH coated A356.0 substrate in the scribed area, after exposure to 3.5 wt % NaCl for 120 h.

References

- [1] E. Abdullayev, Y. Lvov, Clay nanotubes for corrosion inhibitor encapsulation: Release control with end stoppers, *Journal of Materials Chemistry*. 20 (2010) 6681–6687. doi:10.1039/c0jm00810a.
- [2] S.R. White, N.R. Sottos, P.H. Geubelle, J.S. Moore, M.R. Kessler, S.R. Sriram, E.N. Brown, S. Viswanathan, Autonomic healing of polymer composites, *Nature*. 409 (2001) 794–797. doi:10.1038/35057232.
- [3] A. Joshi, E. Abdullayev, A. Vasiliev, O. Volkova, Y. Lvov, Interfacial modification of clay nanotubes for the sustained release of corrosion inhibitors, *Langmuir*. 29 (2013) 7439–7448. doi:10.1021/la3044973.
- [4] ASTM D3359-17 Standard Test Methods for Rating Adhesion by Tape Test, (2009) 1–9. doi:10.1520/D3359-17.
- [5] J. Hu, M. Gan, L. Ma, Z. Li, J. Yan, J. Zhang, Synthesis and anticorrosive properties of polymer-clay nanocomposites via chemical grafting of polyaniline onto Zn-Al layered double hydroxides, *Surface and Coatings Technology*. 240 (2014) 55–62. doi:10.1016/j.surfcoat.2013.12.012.
- [6] J. Liu, Y. Zhang, M. Yu, S. Li, B. Xue, X. Yin, Influence of embedded ZnAlCe-NO₃-layered double hydroxides on the anticorrosion properties of sol-gel coatings for aluminum alloy, *Progress in Organic Coatings*. 81 (2015) 93–100. doi:10.1016/j.porgcoat.2014.12.015.
- [7] R. Naderi, M. Fedel, F. De, M. Poelman, M. Olivier, Synergistic effect of clay nanoparticles and cerium component on the corrosion behavior of eco-friendly silane sol – gel layer applied on pure aluminum, *Surface and Coatings Technology*. 224 (2013) 93–100. doi:10.1016/j.surfcoat.2013.03.005.
- [8] S.H. Adsul, T. Siva, S. Sathiyanarayanan, S.H. Sonawane, R. Subasri, Self-healing ability of nanoclay-based hybrid sol-gel coatings on magnesium alloy AZ91D, *Surface and Coatings Technology*. 309 (2017) 609–620. doi:10.1016/j.surfcoat.2016.12.018.
- [9] ASTM G31-12, Standard Guide for Laboratory Immersion Corrosion Testing of Metals 1, (2012). doi:10.1520/G0031-12A.
- [10] ASTM G1-90, Standard Practice for Preparing, Cleaning and Evaluation Corrosion Test Specimens, (1999).
- [11] ASTM B117-16, Standard Practice for Operating Salt Spray (Fog) Apparatus, (2016). doi:10.1520/B0117-16.2.

- [12] E. Huttunen-Saarivirta, G. V Vaganov, V.E. Yudin, J. Vuorinen, Characterization and corrosion protection properties of epoxy powder coatings containing nanoclays, *Progress in Organic Coatings*. 76 (2013) 757–767. doi:10.1016/j.porgcoat.2013.01.005.
- [13] J. Gangwar, B.K. Gupta, S.K. Tripathi, A.K. Srivastava, Phase dependent thermal and spectroscopic responses of Al_2O_3 nanostructures with different morphogenesis, *Nanoscale*. 7 (2015) 13313–13344. doi:10.1039/C5NR02369F.
- [14] V.G. Keramidas, william B. White, Raman Scattering Study of the Crystallization and Phase Transformations of ZrO_2 , *Journal of the American Ceramic Society*. 57 (1974) 22–24.
- [15] F. Zhang, S. Chan, J.E. Spanier, E. Apak, Q. Jin, R.D. Robinson, H.P. Irving, Cerium oxide nanoparticles : Size-selective formation and structure analysis, *Applied Physics Letters*. 80 (2002) 127–129. doi:10.1063/1.1430502.
- [16] J. Maxfield, I.W. Shepherd, Conformation of poly(ethylene oxide) in the solid state , melt and solution measured by Raman scattering, *Polymer*. 16 (1975) 505–509.
- [17] A. Kulbida, M.N. Ramos, M. Rasanen, J. Nieminen, O. Schrems, R. Fausto, Rotational Isomerism in Acrylic Acid, *Journal of Chemical Society Faraday Transactions*. 91 (1995) 1571–1585.

CHAPTER-4

Layered Montmorillonite

Nanoclay as Nanocontainers

for Self-healing Coatings on

AA2024-T4 and A356.0

CHAPTER-4

Layered Montmorillonite Nanoclay as Nanocontainers for Self-healing Coatings on AA2024-T4 and A356.0

The chapter-4 deals with the experimental results and discussions of self-healing, corrosion protection coatings developed using layered montmorillonite nanoclay as nanocontainers to accommodate the corrosion inhibitors, Ce^{3+} and Zr^{4+} . The coatings with the use of inhibitor loaded montmorillonite clay have been deposited on AA2024-T4 and A356.0 alloys for their corrosion protection. Loading of corrosion inhibitors into montmorillonite clay was carried out by two methods: i) by intercalation of corrosion inhibitors into the inter layer spaces of montmorillonite clay, ii) by physical mixing of inhibitors with montmorillonite clay, as per the procedures mentioned in Chapter-2.

Ce^{3+} and Zr^{4+} inhibitors loaded montmorillonite nanoclay powders have been characterized by SEM and TEM along with EDS, BET and XRD for confirming the loading of the corrosion inhibitors into montmorillonite. Further, the corrosion behaviour of the coated samples was examined by electrochemical methods, such as electrochemical impedance spectroscopy and potentiodynamic polarization studies. Weight loss study, salt spray test and salt immersion test have also been carried out. The self-healing activity of the developed coatings was established by these analyses and was further confirmed by SVET analysis.

4.1 Characterization of montmorillonite (MMT)-based powders

4.1.1 SEM and TEM analyses

SEM analysis along with EDS was carried out for as-received MMT, inhibitor mixed MMT (IMM) and inhibitor intercalated MMT (IEM) powders. SEM images depicted in Fig. 4.1 showed that IEM powder possessed a layered structure, having morphological similarities with as-received MMT. On the other hand, IMM powder did not show any flake like appearance. The elemental analysis as presented in Table 4.1 indicated that IMM powder has more amounts of Ce, Zr and very less amounts of Al, Si than in IEM powder. However, IEM has shown Al, Si ratios nearly similar to that of as-received MMT along with the presence of Ce and Zr in it. The amounts of inhibitors, Ce^{3+} and Zr^{4+} , are exceedingly high in IMM nanoclays with the decrease in the elemental contents of Al and Si. This elemental composition

of IMM nanoclay resulted with EDS analysis could infer that the inhibitors, Ce^{3+} and Zr^{4+} , were present widely in the exteriors of IMM nanoclay. Subsequently, it could be well expected that IEM nanoclay contained Ce^{3+} and Zr^{4+} in the interlayer spaces of MMT clay (*vide infra*). TEM results given in Fig. 4.2 have further confirmed that IEM had structural similarity with as received MMT as that seen in SEM. However, IMM has shown the presence of more amount of Zr and the layered structure was lost. Presence of Cu in the EDS spectra was from Cu-based TEM grid on which the MMT powders were dispersed.

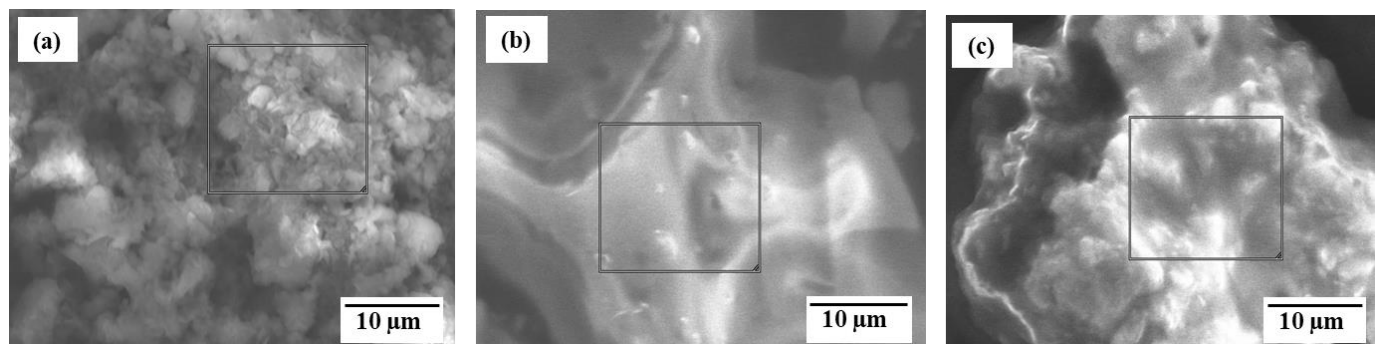


Fig. 4.1. SEM images of a) as-received MMT, b) IMM and c) IEM powders.

Table 4.1. Elemental composition in % weight from EDS spectra for a) as-received MMT, b) IMM and c) IEM.

Sample	O	Na	Mg	Al	Si	Zr	Ce
As-received MMT	38.19	0.38	1.94	15.69	43.81	-	-
IMM	32.67	0.15	0.21	0.68	15.10	48.98	2.19
IEM	34.68	0.00	1.55	15.14	44.34	3.58	0.71

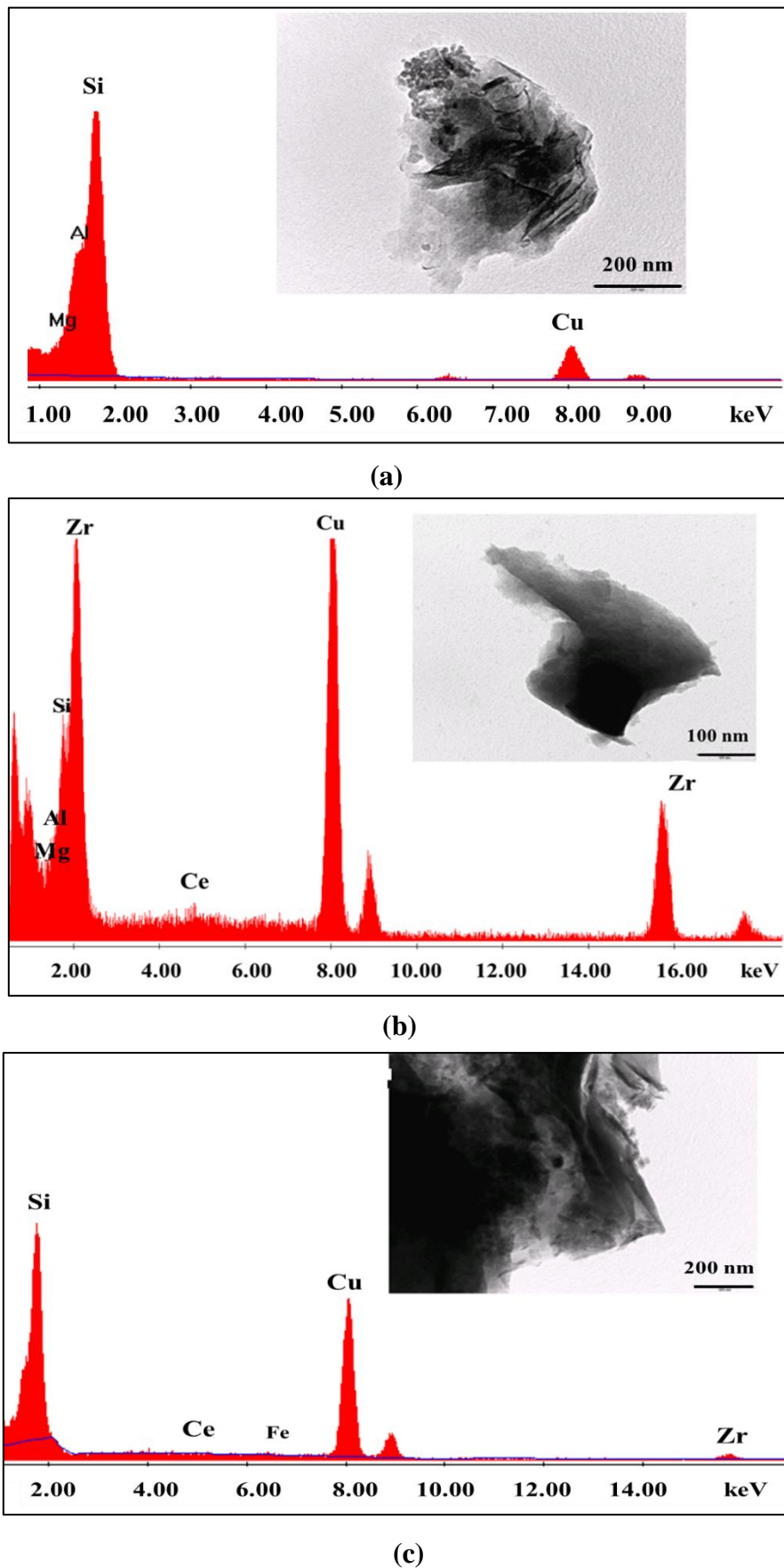


Fig. 4.2. EDS spectra and TEM images (inset) of a) as-received MMT, b) IMM and c) IEM powders.

4.1.2 BET surface area and pore volume analysis

BET surface area and pore volume analysis was carried out to find out the change in the pore volume and surface area after loading of inhibitors for IMM and IEM with respect to as-received MMT. BET surface area and pore volume for a) as-received MMT, b) IMM and c) IEM were found to be $221.39 \text{ m}^2/\text{g}$ and $0.256 \text{ cm}^3/\text{g}$, $10.44 \text{ m}^2/\text{g}$ and $0.0122 \text{ cm}^3/\text{g}$, $173.67 \text{ m}^2/\text{g}$ and $0.229 \text{ cm}^3/\text{g}$, respectively. The surface area and pore volume for IEM powder have decreased when compared to as-received MMT as shown in Fig. 4.3, indicating that intercalation of inhibitors has taken place. In case of IMM, the surface area and pore volume have decreased substantially when compared to as-received MMT and IEM. This large decrease in the surface area as well as pore volume of IMM and the presence of more amount of Zr from EDS analysis, as shown Table 4.1, indicated that zirconium might have been adsorbed on the exteriors of clay particles instead of getting intercalated in between the layers (*vide supra*). This could be the reason for a substantial decrease in the surface area and pore volume of IMM.

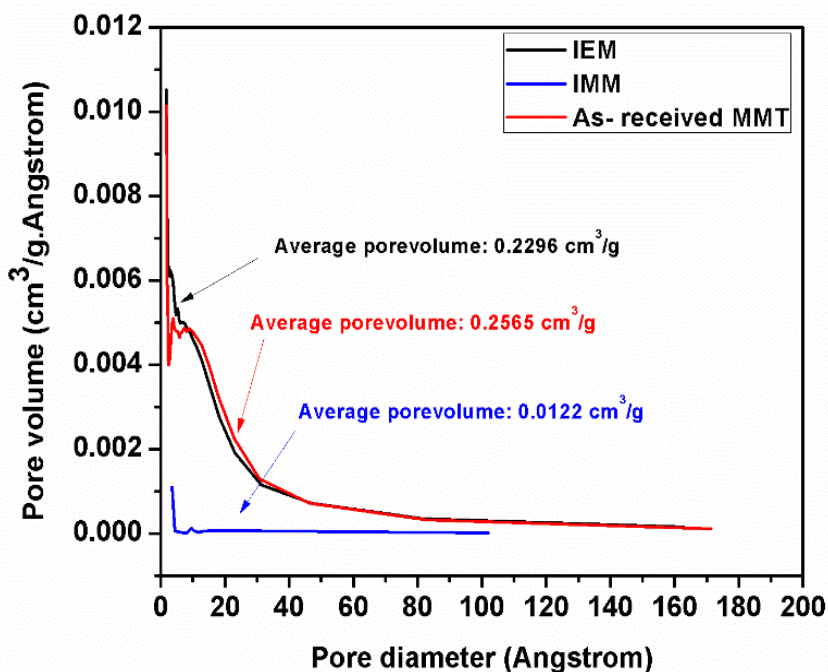


Fig. 4.3. BET pore volume versus pore diameter for as-received, IMM and IEM powders

4.1.3 XRD analysis

XRD patterns for as-received, IMM and IEM powders are depicted in Fig. 4.4. As-received MMT has shown a high intensity sharp peak at 2θ value 4.9° , which corresponds to the layered

structure of montmorillonite. IEM powder has shown a sharp peak at the same 2θ value as that of as-received MMT, thus indicating that the layered structure is intact in IEM. However, the IMM has shown a broadened and extended peak [1–3] which indicates that the delamination of some of the MMT layers had taken place and the inhibitor had got covered by the delaminated sheets, and hence there was a decrease in pore volume and surface area.

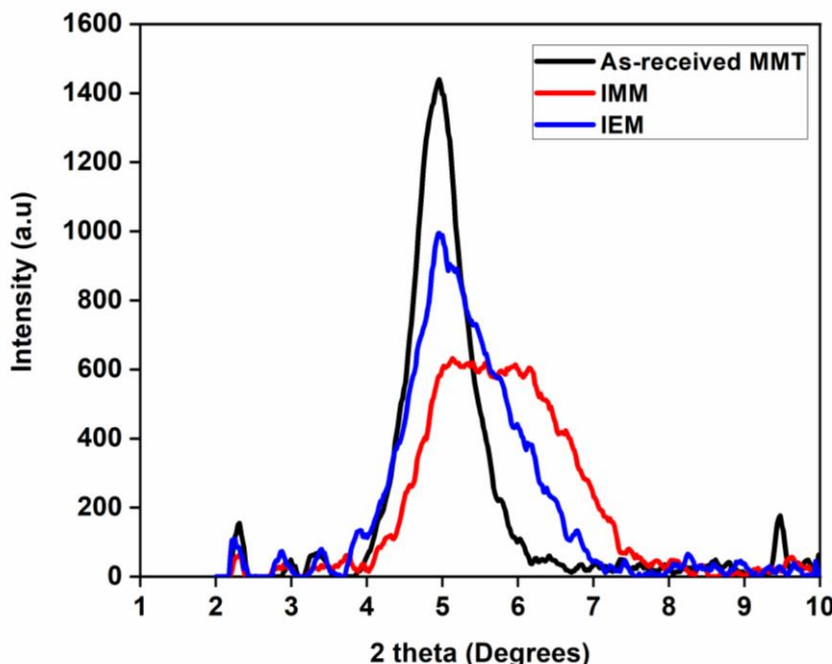


Fig. 4.4. XRD spectrum of as-received and modified MMT powders.

4.2 Results and Discussion of coatings on AA2024-T4 alloy

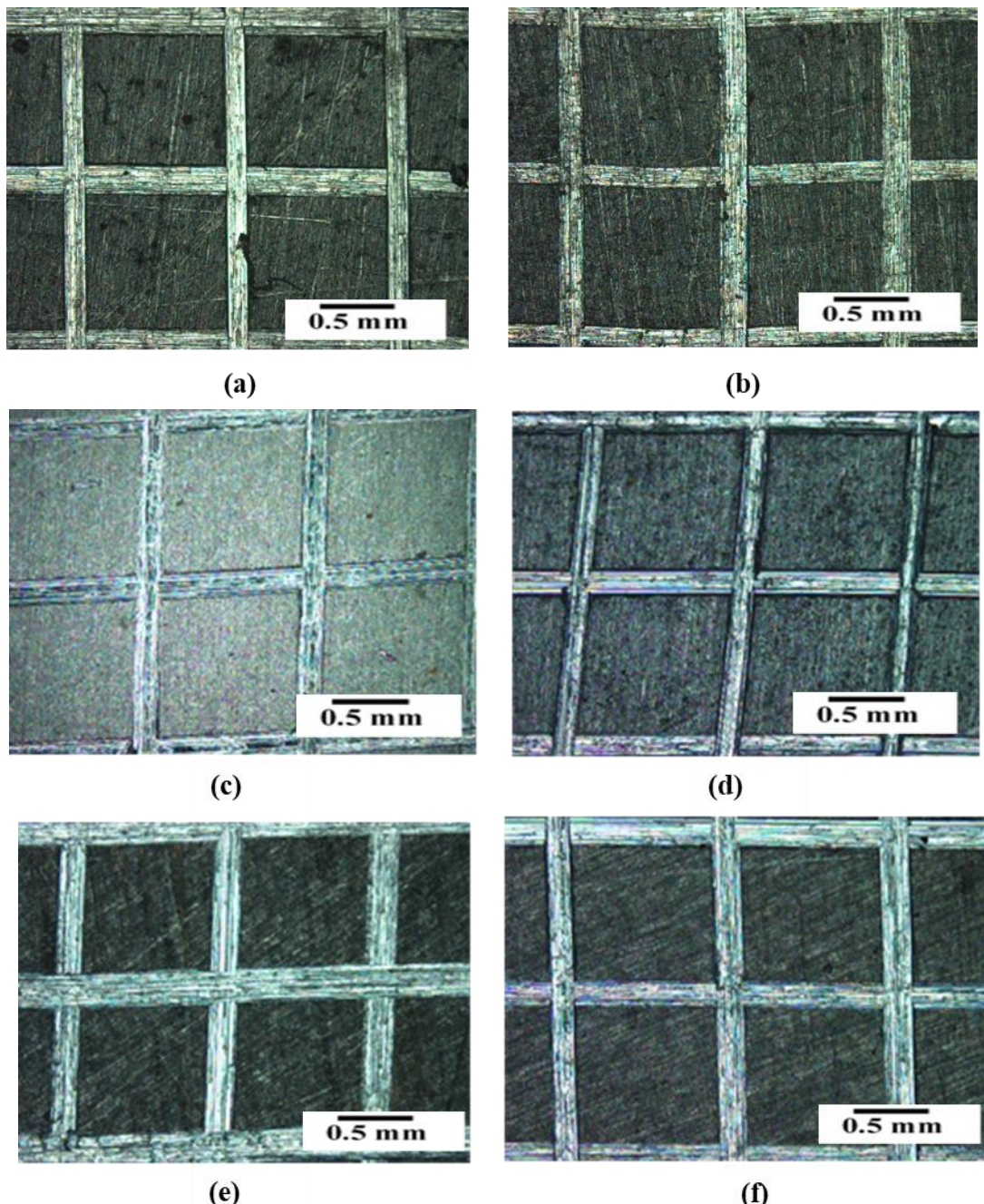
4.2.1 Thickness of coatings

Thickness was measured for all coated substrates using PosiTector, which is a non-destructive method. The measured thickness for Matrix sol coated (henceforth abbreviated as Mat) was $3.6 (\pm 0.2) \mu\text{m}$, IEM sol coated was $4.0 (\pm 0.15) \mu\text{m}$ and IMM sol was $4.2 (\pm 0.2) \mu\text{m}$, whereas MNC sol coated substrates have shown the thickness of $5.3 (\pm 0.3) \mu\text{m}$.

4.2.2 Adhesion Test

The optical microscopic images of coated AA2024-T4 substrates after carrying out adhesion test are given in Fig. 4.5. Mat sol coated substrates (Fig 4.5 a, b) have shown no peeling off (0% removal) of the material after the adhesion tape was removed, hence its adhesion is

adjudged as 5B rank, which represented best adhesion property according to ASTM D3359-17 [4]. Similarly, IEM and IMM sol coated substrates as given in Fig. 4.5 c-f have also not shown any removal of coating material and the adhesion strength of these coatings was ranked as 5B. However, MNC sol coatings (Fig 4.5 g, h) had up to 35 % removal of the coated area after the tape was removed, and hence the adhesion strength was ranked as 2B.



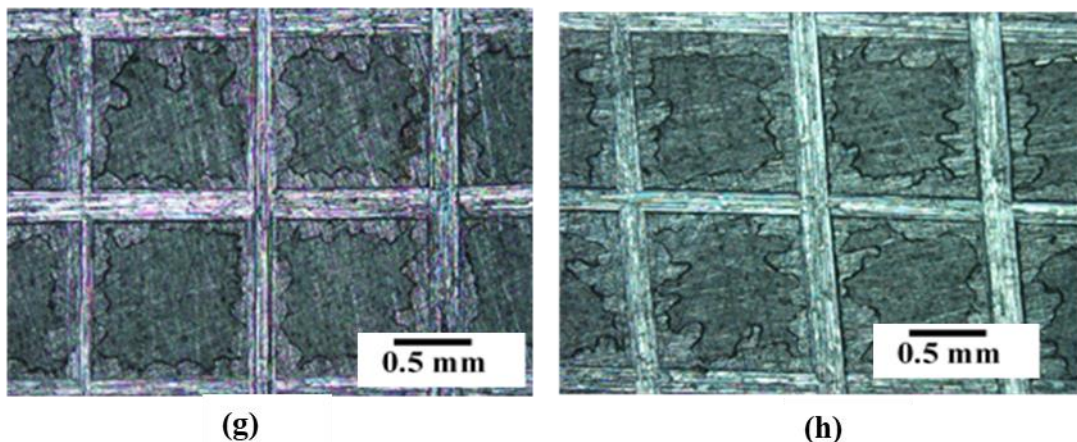


Fig. 4.5. Adhesion test micrographs of (a, b) Mat sol coated, (c, d) IEM sol coated, (e, f) IMM sol coated and (g, h) MNC sol coated substrates before putting on tape (a, c, e, g) and after removal of tape (b, d, f, h).

4.2.3 Morphology and composition of coatings by SEM and EDS analysis

SEM images of IMM, IEM, MNC and Matrix sol coatings are shown in Fig. 4.6. All the coated substrates have shown smooth surfaces without any cracks. These coatings did not show any surface features as the matrix is amorphous in nature. Results of the EDS analysis of all the coatings are presented in Table 4.2, indicating that IMM coated substrates have shown more amount of Zr than IEM coated substrates.

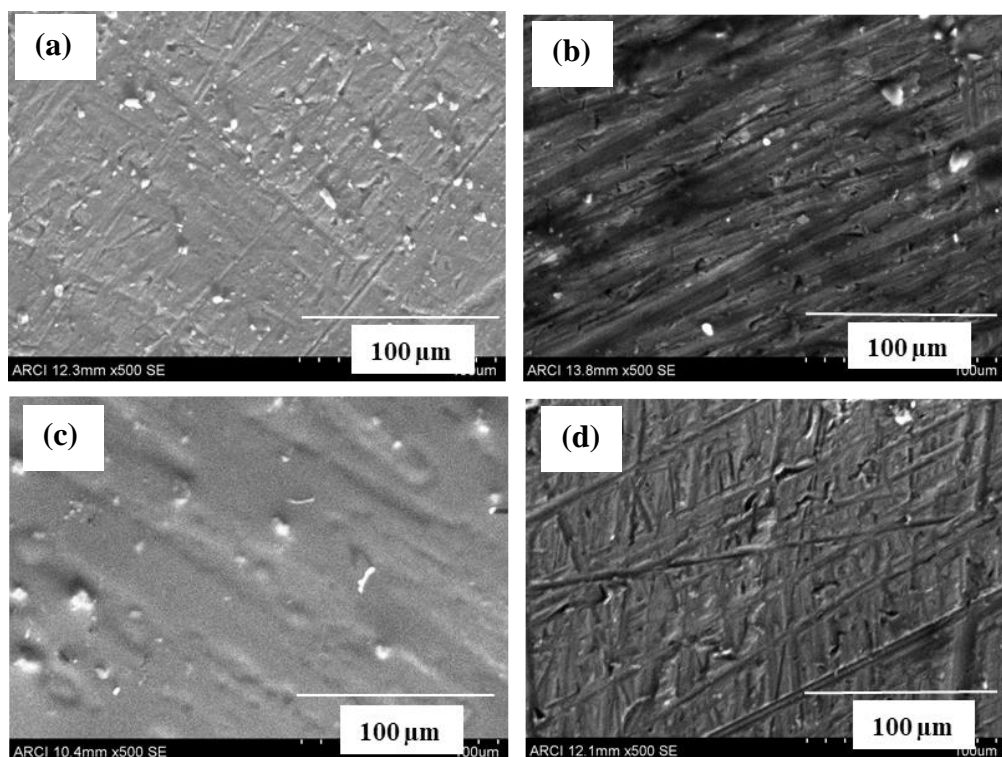


Fig. 4.6. SEM images of a) IMM, b) IEM, c) MNC and d) Mat sol coated AA2024-T4 substrates.

Table 4.2. Elemental composition of different coatings in % weight from EDS analysis

Name of the coating	C	O	Al	Si	Zr	Ce
IMM	14.70	4.42	76.13	1.71	1.49	0.07
IEM	36.68	6.52	50.03	5.41	0.34	0.08
MNC	44.17	16.22	24.40	14.82	-	-
Mat	35.27	3.98	57.62	3.12	-	-

4.2.4 EIS and potentiodynamic polarization studies

EIS and potentiodynamic polarization studies were carried out after exposing the samples to 3.5 wt % NaCl solution for 1, 72, 120, 168 and 216 h. The equivalent electrical circuit used for fitting the impedance data of uncoated and coated substrates is given in Fig. 4.7. Nyquist plots for coated and uncoated substrates are depicted in Fig. 4.8, and the fit data obtained after fitting with an equivalent circuit are given in Table 4.3. After 1 h of exposure to 3.5 wt % NaCl solution, Mat coated substrates have shown the R_{ct} values, which indicated a very good adhesion to substrate thereby providing excellent barrier protection. IEM and IMM coated substrates have shown nearly equal R_{ct} values after 1 h. The charge transfer resistance of IEM coated substrates has got increased as a function of duration of exposure to the corrosive medium.

After 72 h of exposure to corrosive medium, the R_{coat} and R_{ct} values for IEM coated substrates, as given in Table 4.3, were found to be highest among all substrates. After 120 h of exposure, the R_{ct} of IEM was still the highest compared to all substrates, followed by MNC coated substrates. On the other hand, the IMM coated substrates were found to exhibit least R_{ct} than all coated substrates after a prolonged duration of exposure. From above observations, it could be concluded that IEM coated substrates were able to exhibit very good corrosion protection even on prolonged duration of exposure to the corrosive medium. Hence, further studies after 168 h and 216 h were continued for only IEM. MNC coated substrates also were able to withstand as that of IEM coated substrates. Mat coated substrates were initially able to provide high corrosion resistance with an R_{ct} value of $2.23 \times 10^4 \text{ k}\Omega\text{.cm}^2$ due to their excellent barrier nature, but the barrier property was lost after longer durations of exposure to corrosive medium.

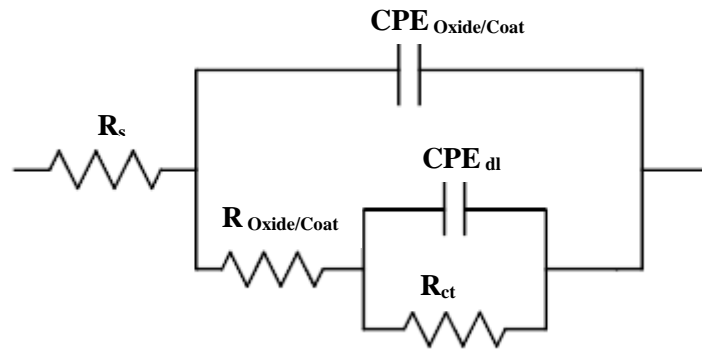


Fig. 4.7. Equivalent electrical circuit used for fitting EIS data.

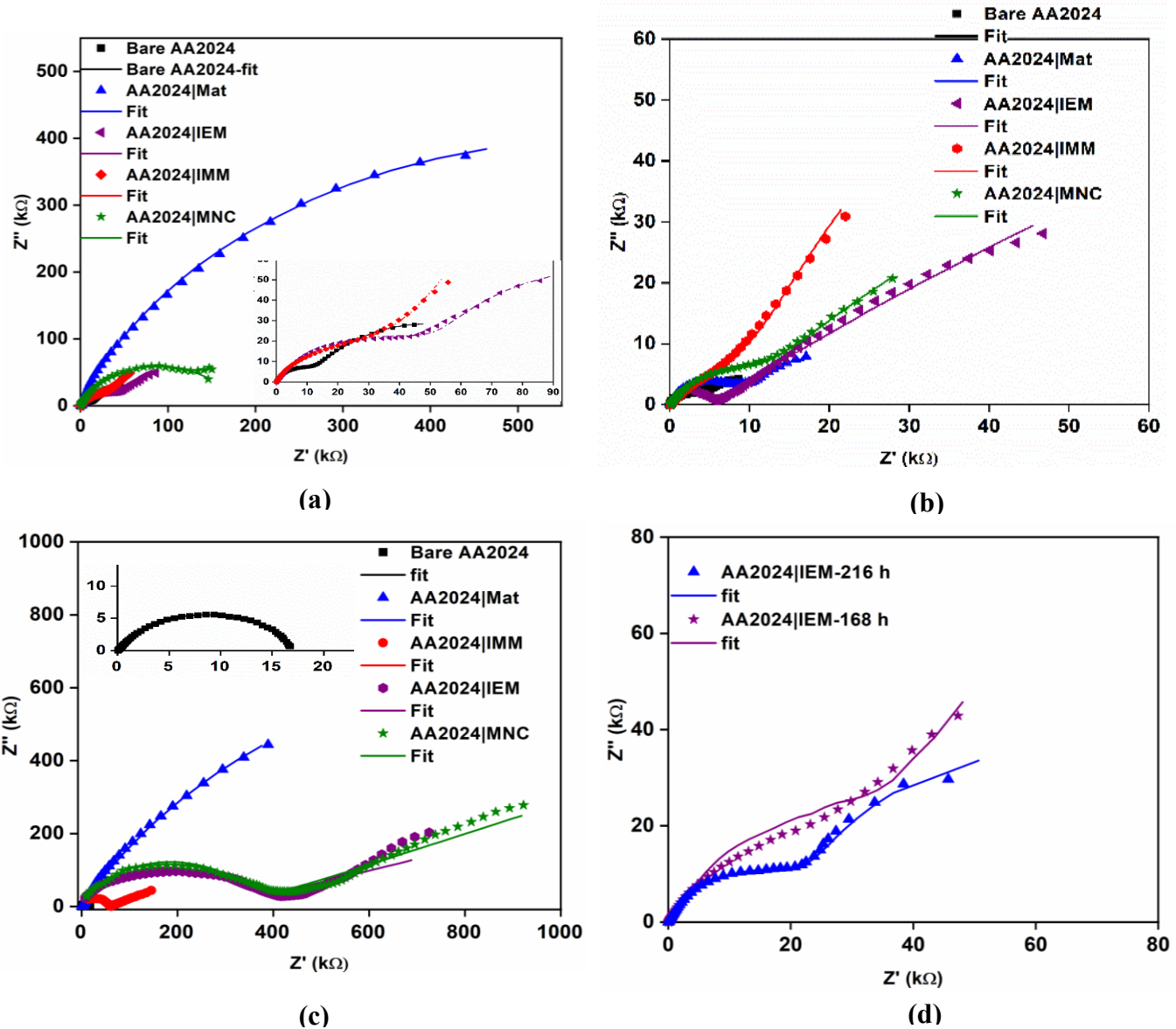


Fig. 4.8. Nyquist plots of uncoated and coated AA2024-T4 substrates after a) 1 h, b) 72 h, c) 120 h and IEM coated substrates after (d) 168 h and 216 h of exposure to 3.5 wt % NaCl solution.

Table 4.3. EIS fit data of coated and uncoated AA2024-T4 substrates at different exposure durations, obtained after fitting with an equivalent electrical circuit.

Sample	Time of immersion in 3.5 wt % NaCl	$R_{coat/Oxide}$ k Ω .cm 2	R_{ct} k Ω .cm 2	$C_{coat/Oxide}$ μ F/cm 2	C_{dl} μ F/cm 2
Bare	1 h	6.04	36.7	12.6	409.0
AA2024 Mat		272.0	22300	0.00011	603.0
AA2024 IEM		68.0	102.0	10.3	199.0
AA2024 IMM		35.4	122.0	19.4	1940.0
AA2024 MNC		8.53	500.0	0.00052	20.7
Bare	72 h	5.34	17.9	49.6	932.0
AA2024 Mat		11.5	14.2	25.7	1120
AA2024 IEM		110.0	1040.0	127.0	63.6
AA2024 IMM		17.2	210.0	51.7	342.0
AA2024 MNC		15.6	126.0	24.8	979.0
Bare	120 h	1.36	15.80	6.34	3.80
AA2024 Mat		541.0	6.94X10 ⁶	6.56	85.8
AA2024 IEM		184.0	1.12X10 ¹¹	8.56X10 ⁻⁵	1.67X10 ¹²
AA2024 IMM		79.9	1270.0	3480	57.80
AA2024 MNC		620.0	4.37X10 ¹⁰	0.00013	1.64X10 ¹¹
AA2024 IEM	168 h	53.5	143.0	36.6	182.0
AA2024 IEM	216 h	7.90	119.0	1.52	7.93

Potentiodynamic polarization results have also followed the same trend as that of EIS studies. The polarization curves with corrosion currents obtained for coated and uncoated substrates at different durations of exposure are depicted in Fig. 4.9, and polarization data are given in Table 4.4. MNC coated substrates exhibited least i_{corr} initially, and the i_{corr} got increased after 72 h, after which on prolonged exposure to 120 h it got decreased. Mat coated substrates have shown higher i_{corr} values up to 72 h due to loss of barrier property, as the polarization is a destructive process involving the application of voltage to damage the coating. After 120 h, the corrosion current of Mat coated substrates got decreased, which can be attributed due to the accumulation of corrosion product. The i_{corr} values for IEM and IMM coated substrates were found to be nearly same at initial exposure time i.e., at 1 h. However,

IEM coated substrates have shown least corrosion currents after 72 h and which got further decreased as the duration of exposure increased to 120 h. It also can be observed from the polarization graphs that the anodic curves for IEM coated substrates were having passive region till 120 h. The polarization studies were extended to 168 h and 216 h for IEM coated substrates as seen from Fig. 4.8 d. The i_{corr} values started increasing slowly after 120 h to 168 h and decreased after 216 h. The anodic curves started showing the active region as the time prolonged from 168 h to 216 h indicating that, the breakdown of the passive layer.

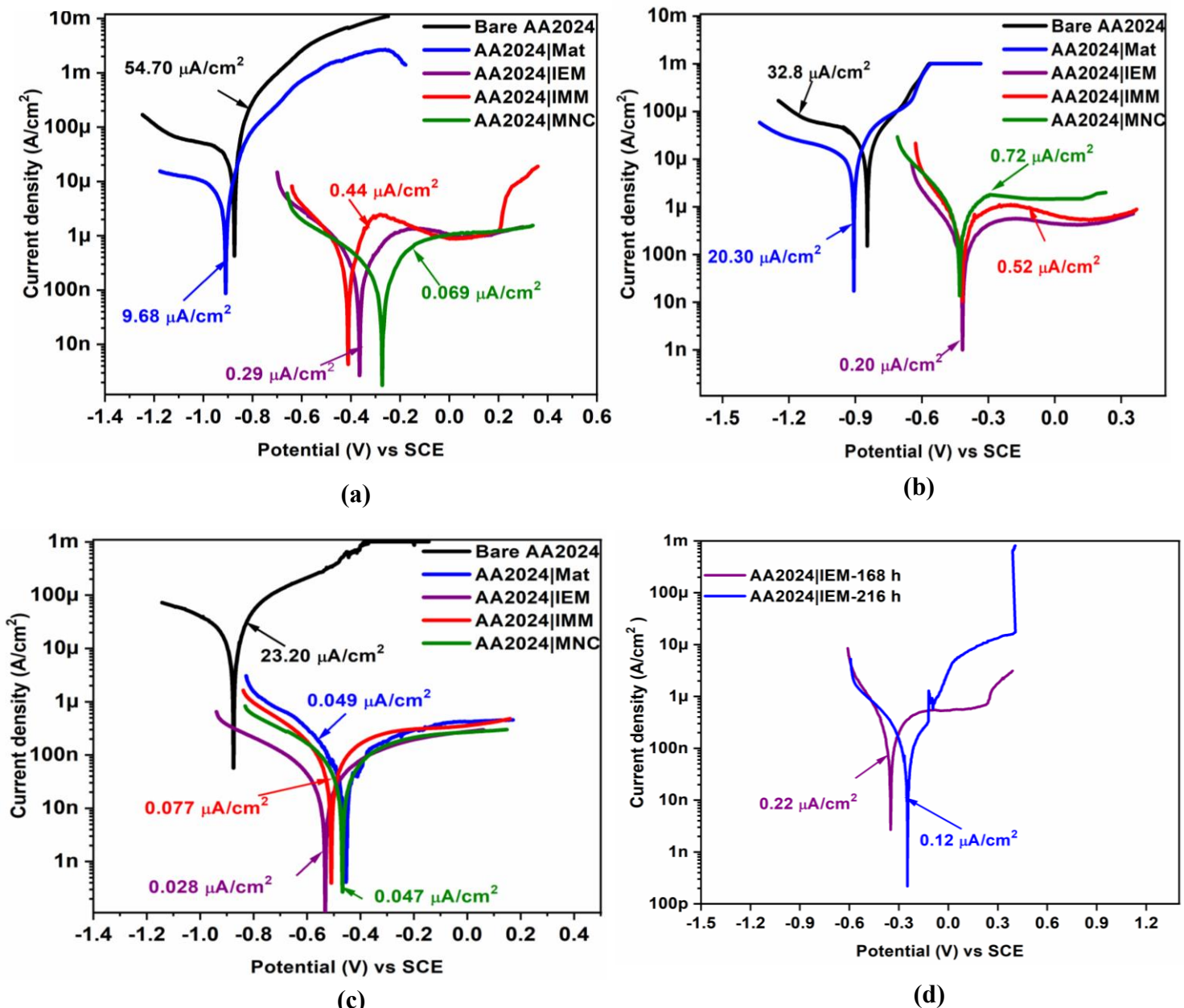


Fig. 4.9. Polarization curves of coated and uncoated AA2024-T4 substrates after a) 1 h, b) 72 h and c) 120 h and (d) IEM coated substrates after 168 h and 216 h of exposure to 3.5 wt % NaCl.

Table 4.4. Polarization data for coated and uncoated AA2024-T4 substrates at different durations of exposure to corrosive medium.

Sample	Time of immersion in 3.5 wt % NaCl	i_{corr} ($\mu\text{A}/\text{cm}^2$)	E vs SCE (Volts)
Bare	1 h	9.59	-0.835
AA2024 Mat		9.68	-0.909
AA2024 IEM		0.29	-0.361
AA2024 IMM		0.44	-0.412
AA2024 MNC		0.069	-0.316
Bare	72 h	32.8	-0.847
AA2024 Mat		20.30	-0.907
AA2024 IEM		0.20	-0.417
AA2024 IMM		0.52	-0.417
AA2024 MNC		0.72	-0.430
Bare	120 h	23.20	-0.875
AA2024 Mat		0.049	-0.455
AA2024 IEM		0.028	-0.532
AA2024 IMM		0.076	-0.510
AA2024 MNC		0.047	-0.468
AA2024 IEM	168 h	0.22	-0.350
AA2024 IEM	216 h	0.12	-0.248

The above EIS and potentiodynamic polarization results of montmorillonite-based coatings were compared with halloysite-based coatings (as discussed in chapter-3). A comparison of R_{ct} values of MNC and HNC coatings along with Mat and bare substrates as a function of duration of exposure is presented in Fig. 4.10. It can be observed from the graph that HNC and MNC sol coated substrates which contain unloaded HNTs and MMTs, respectively, exhibited equal R_{ct} initially. However, on prolonged exposure to corrosive medium, the R_{ct} value of HNC coated substrates gradually decreased, whereas the MNC sol coated substrates exhibited increased corrosion resistance. These contrasting results for HNC and MNC coatings with regard to corrosion protection made us curious to find out the reason for such behaviour. A careful literature search revealed that this could be attributed to the

orientation of the nanocontainer particles in the matrix. Huttunen-Saarivirta et al [5] have reported that montmorillonite particles when dispersed in an epoxy matrix and deposited on aluminum foil and cold-rolled carbon steel panels, orient parallel to the surface and resulting in a smooth surface. The pores present in the epoxy coating were covered by MMT particles and hence provided a better corrosion protection. However, HNTs when dispersed in epoxy matrix resulted in randomly oriented particles on the surface and thus the water permeability increased. It was found that HNTs exhibited relatively higher water permeability than MMTs. Therefore from the above studies, it is clear that why in our studies also the unloaded MMTs exhibited higher corrosion resistance than HNTs when dispersed in the sol-gel matrix.

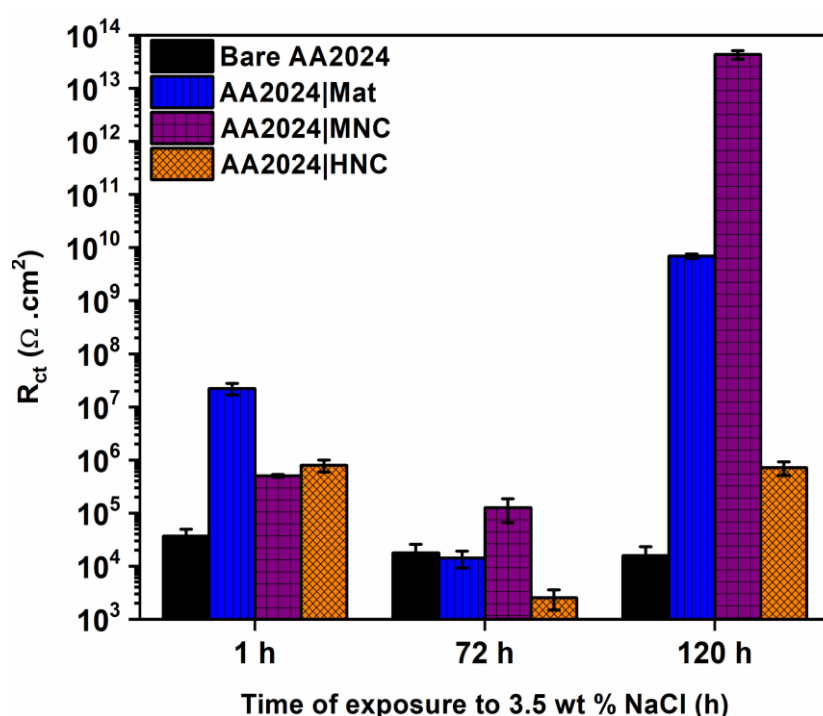


Fig. 4.10. Comparison of charge transfer resistance of coated and uncoated substrates obtained from EIS data as a function of exposure time to corrosive medium.

4.2.5 Weight loss experiments

Weight loss analysis was carried out for coated and uncoated AA2024-T4 substrates to determine the corrosion rate after 120 h of immersion in 3.5 wt % NaCl according to ASTM G31 standard procedure [6], and cleaning of the substrates after immersion was carried out by using ASTM G1 method [7]. A comparison of corrosion rates in mm/y after 120 h of exposure to corrosive medium is shown in the Fig. 4.11. IEM coated substrates exhibited

least corrosion rate among all, whereas IMM coated substrates exhibited higher corrosion rates. The decreasing order of corrosion rates after 120 h is,

Mat > IMM > MNC > Bare > IEM

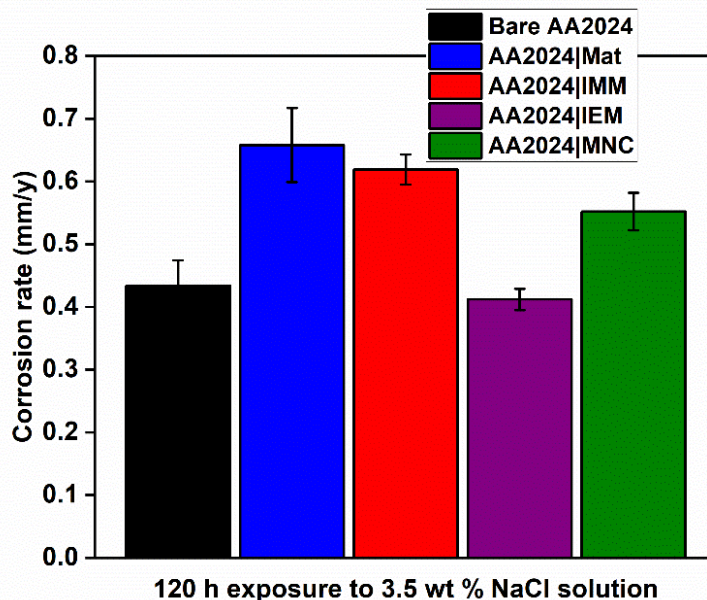


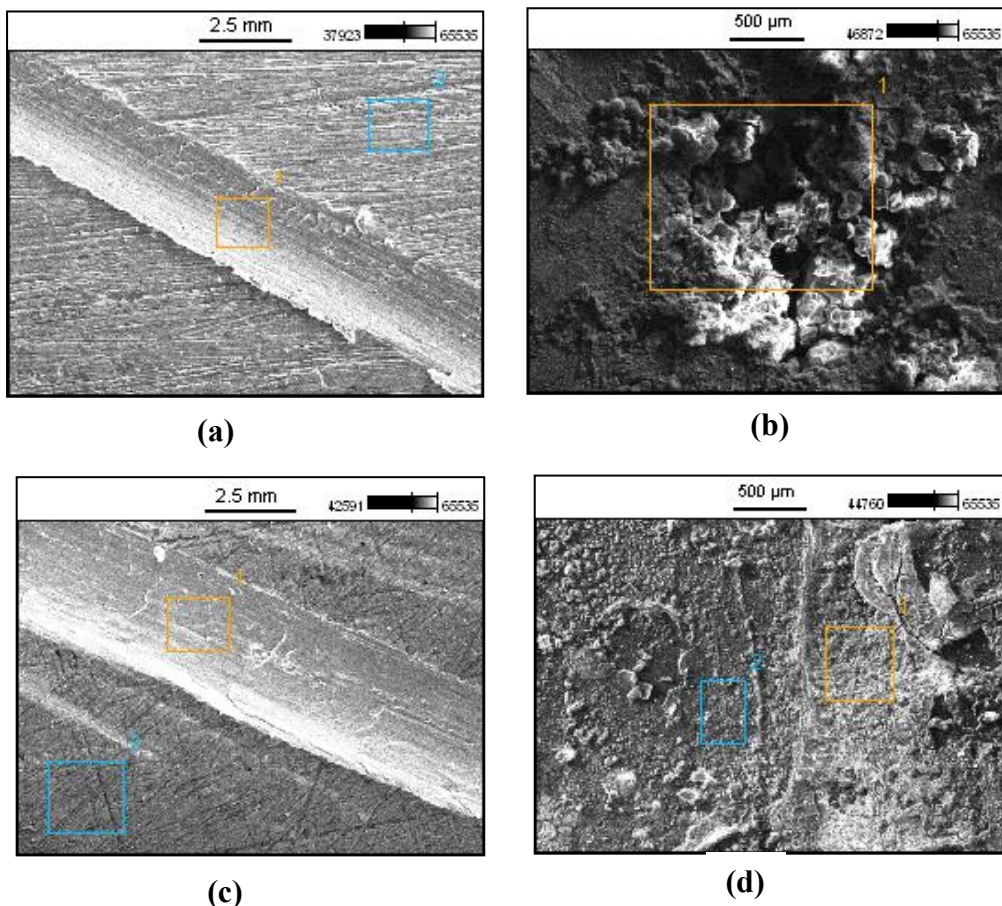
Fig. 4.11. Comparison of corrosion rates of various substrates after 120 h exposure to 3.5 wt % NaCl.

4.2.6 SST and EDS analysis

SST was carried out for uncoated and coated AA2024-T4 substrates by making an 'X' shaped artificial scratch and exposing them for 168 h to 5 wt % NaCl solution as per ASTM B117 standard [8]. SEM images of the AA2024 substrates before and after SST are depicted in Fig. 4.12. Results of EDS elemental analysis of given images are compiled in Table 4.5. Weight percentages of C, Si, O, Ce and Zr on the scribed area before and after SST were compared. Bare, Mat and IMM coated substrates have shown higher amounts of O after SST compared to IEM sol coated substrates. This indicated the formation of corrosion product. IEM coated substrates have shown increased amounts of C, Ce and Zr in the scratch area after SST as given in Fig. 4.12 (h) and Table 4.5, whereas there is almost negligible amount of Zr and no appearance of Ce after SST in the scratched area for IMM. This observation clearly indicated that, in the case of IEM coated substrates, inhibitors have got released into the scratch after the damage, forming a passive layer of ceria and zirconia. The increase in the amount of C and O could be attributed to the polymerization of the epoxy monomers present in the matrix in the presence Ce^{3+} and Zr^{4+} catalysts. MNC coated substrates also have shown an increased amount of C along with O, which is due to metal

mediated polymerization in the presence of Al^{3+} present in the scratch region. In this polymerization, epoxy monomers which were added into the matrix get polymerized after a ring opening reaction [9,10] as given in Fig 4.13. Hence, the MNC coated substrates were able to provide better corrosion protection as seen from EIS and potentiodynamic polarization studies when compared to IMM.

From SST test, it was observed that IEM coated substrates have shown the presence of cationic inhibitors in the scribed area. The increase in Ce, Zr, C and O in the scribed area after SST for IEM coated substrates confirmed both the formation of passive layers of ceria and zirconia and the formation of epoxy polymer in the scribed area.



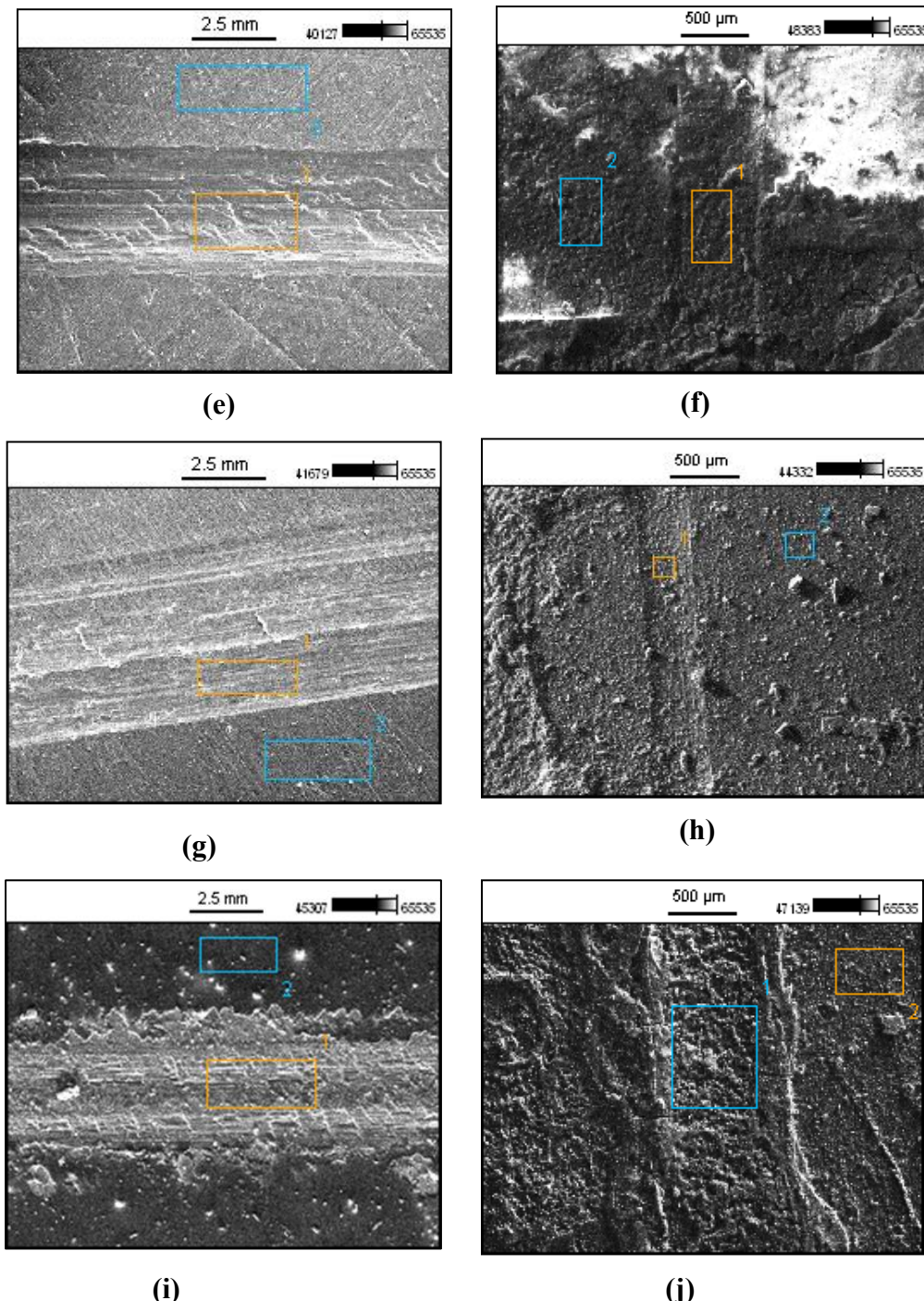


Fig. 4.12. SEM images of bare (a, b), Mat (c, d), IMM (e, f), IEM (g, h) and MNC sol coated (i, j) AA2024-T4 substrates before (a, c, e, g, i) and after (b, d, f, h, j) SST.

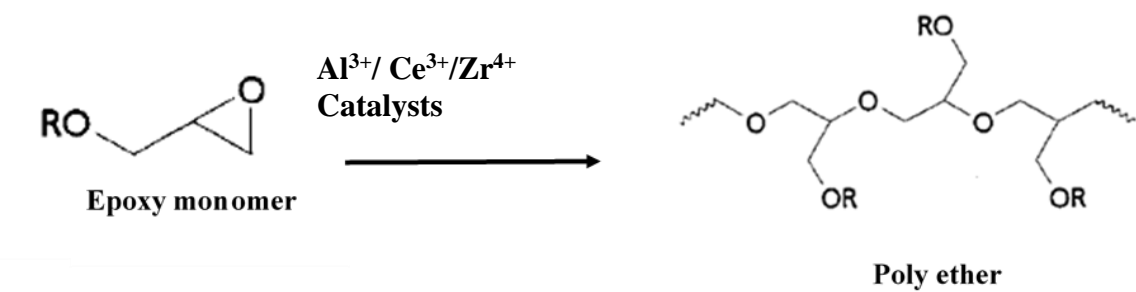


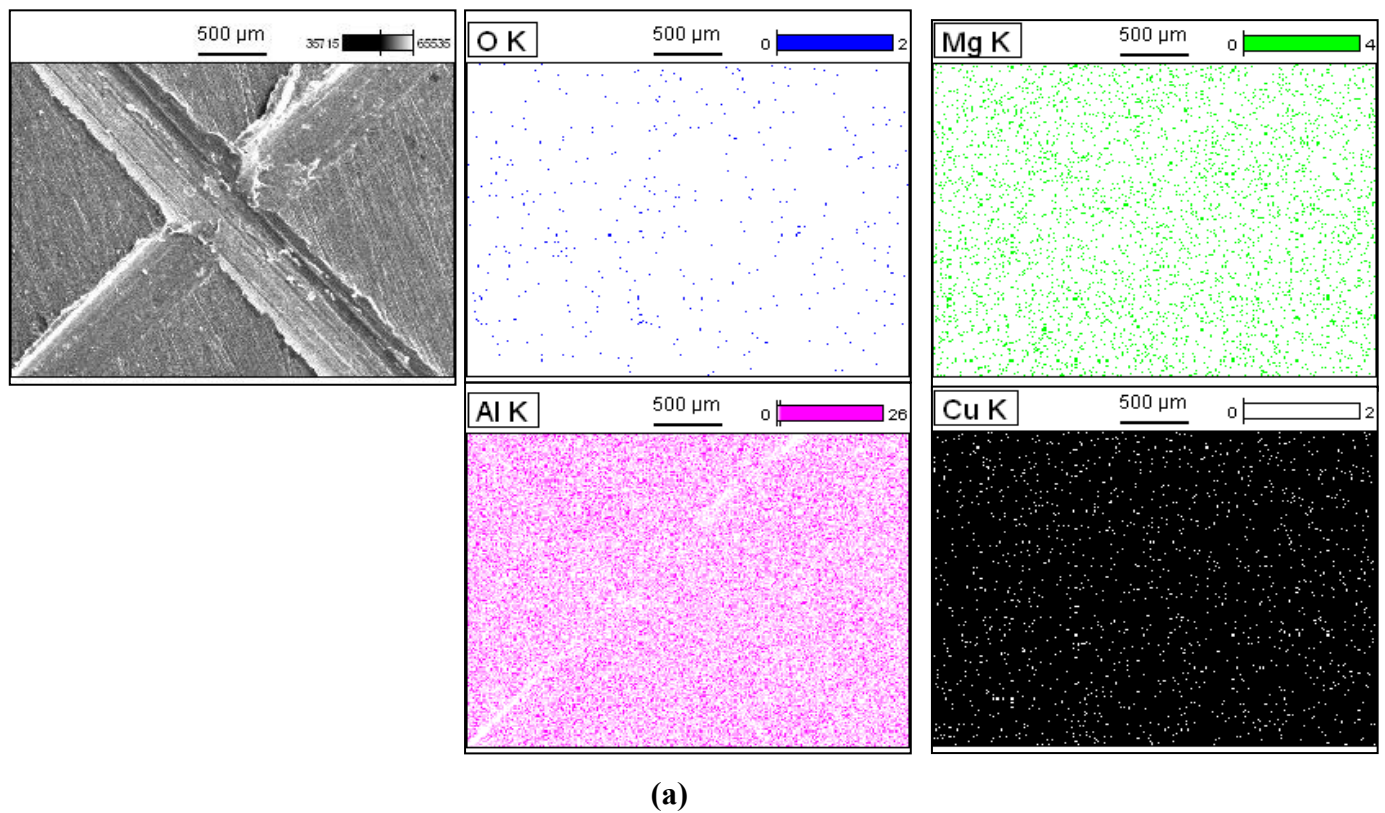
Fig. 4.13. Schematic representation of metal mediated polymerization reaction

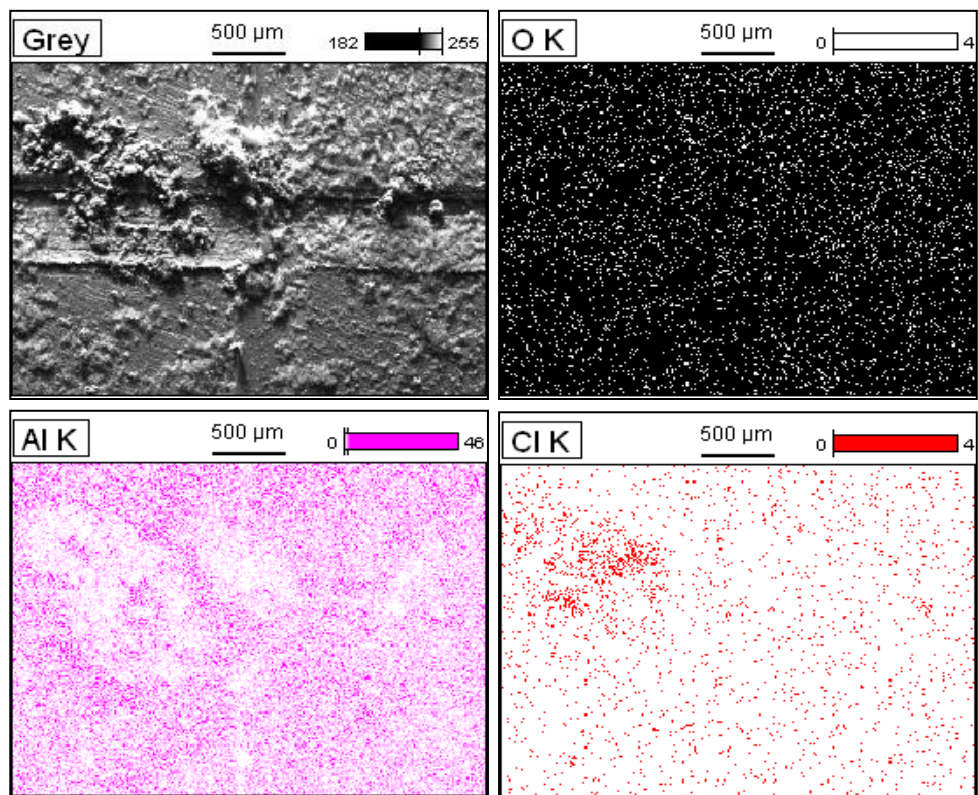
Table 4.5. EDS analysis of uncoated and coated substrates, before and after SST for 168 h in 5 wt % NaCl solution

Sample	SST	% weight ratio of elements in the scratch region									
		C	O	Na	Mg	Al	Si	Cu	Cl	Zr	Ce
Bare	Before	-	0.61	-	1.56	92.32	-	5.51	-	-	-
	After	-	42.15	-	-	40.33	0.31	7.59	9.62	-	-
Mat sol coated	Before	1.79	0.39	-	1.26	91.83	0.00	4.73	-	-	-
	After	0.00	51.34	0.01	-	45.01	0.70	2.60	0.34	-	-
IMM sol coated	Before	0.00	0.00	-	1.20	92.25	0.00	6.45	-	0.00	0.10
	After	0.00	48.64	0.45	-	50.00	0.12	0.14	0.64	0.01	0.00
IEM sol coated	Before	5.04	0.00	-	1.33	87.91	0.00	5.71	-	0.01	0.00
	After	10.70	38.22	1.41	-	45.20	0.00	2.61	1.11	0.40	0.35
MNC sol coated	Before	0.00	3.46	-	-	90.14	-	6.40	-	-	-
	After	13.15	46.14	0.37	0.51	36.31	2.72	0.16	0.64	-	-

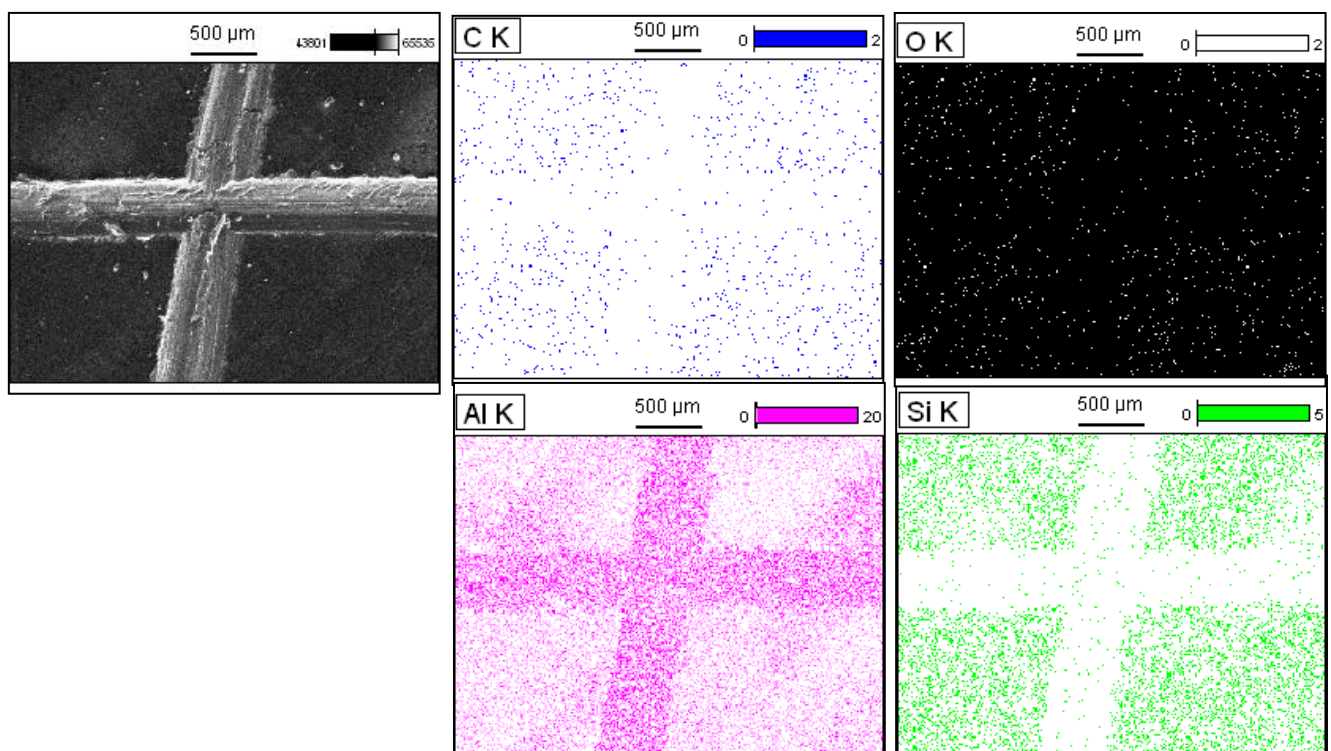
4.2.7 SIT and EDS elemental mapping

SIT was performed by making an artificial scratch on the uncoated and coated AA2024-T4 substrates and immersing them in 3.5 wt % NaCl solution for 120 h. EDS elemental mapping was carried out before and after SIT. SEM images and their respective mappings are depicted in Fig. 4.14. Bare substrate has shown an increased amount of O after SIT (Fig. 4.14 b), whereas Mat and MNC coated substrates showed increase in the amounts of O, Al and Si in the scribed area as given in Fig. 4.14 d and j, respectively. IEM sol coated substrates showed much increased amounts of Ce and Zr along with the C, O, Al and Si (Fig. 4.14 f) when compared to IMM, indicating that the corrosion inhibitors have got released into the scratch region after exposing the damage to corrosion medium. Increase in the C and O indicated that the epoxy monomers added inside the MMTs along with inhibitors have also got polymerised to form a polymeric passive layer in the presence of inhibitors. From above studies, it is clearly indicated that IEM coated substrates provide better corrosion protection and the inhibitors have got released into the damage when the chloride ions attacked. Further, the confirmation of self-healing activity was done by SVET analysis.

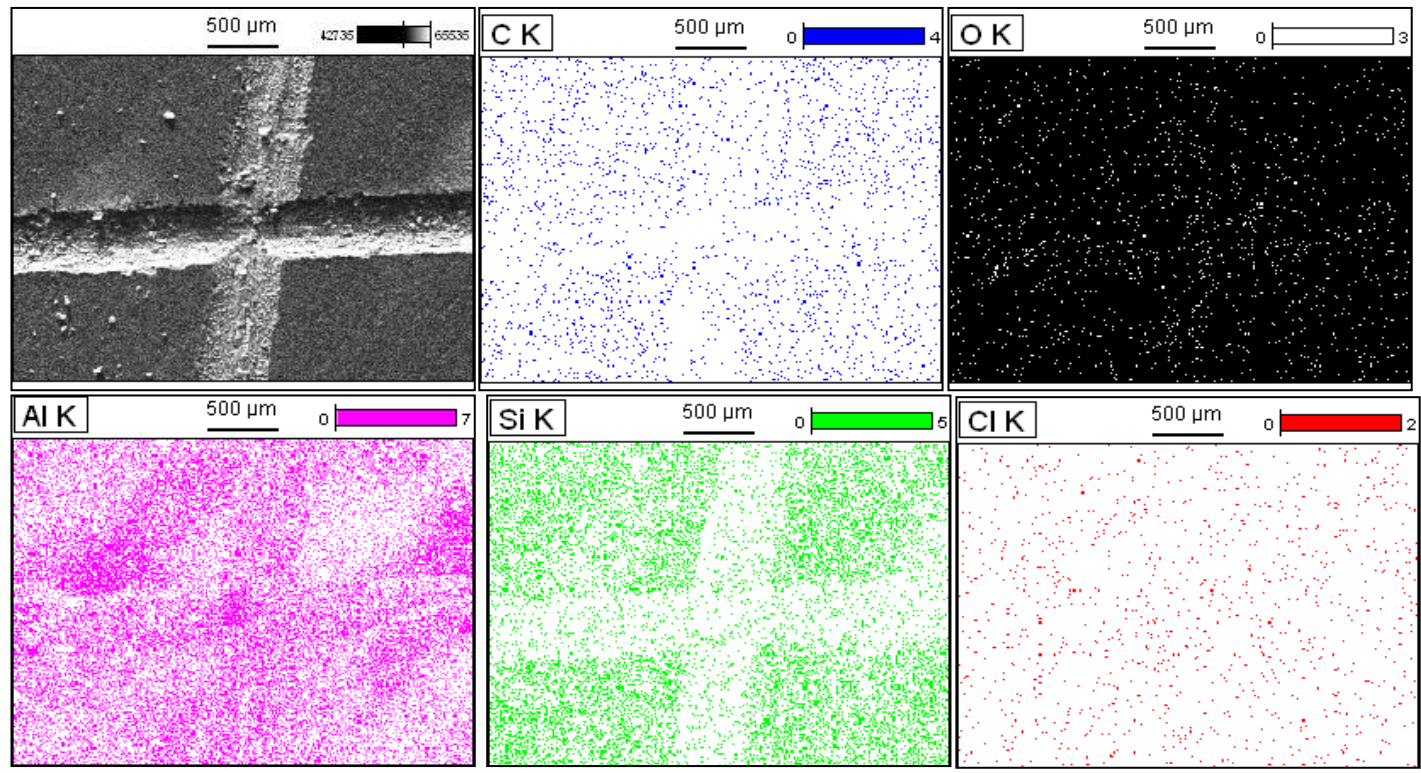




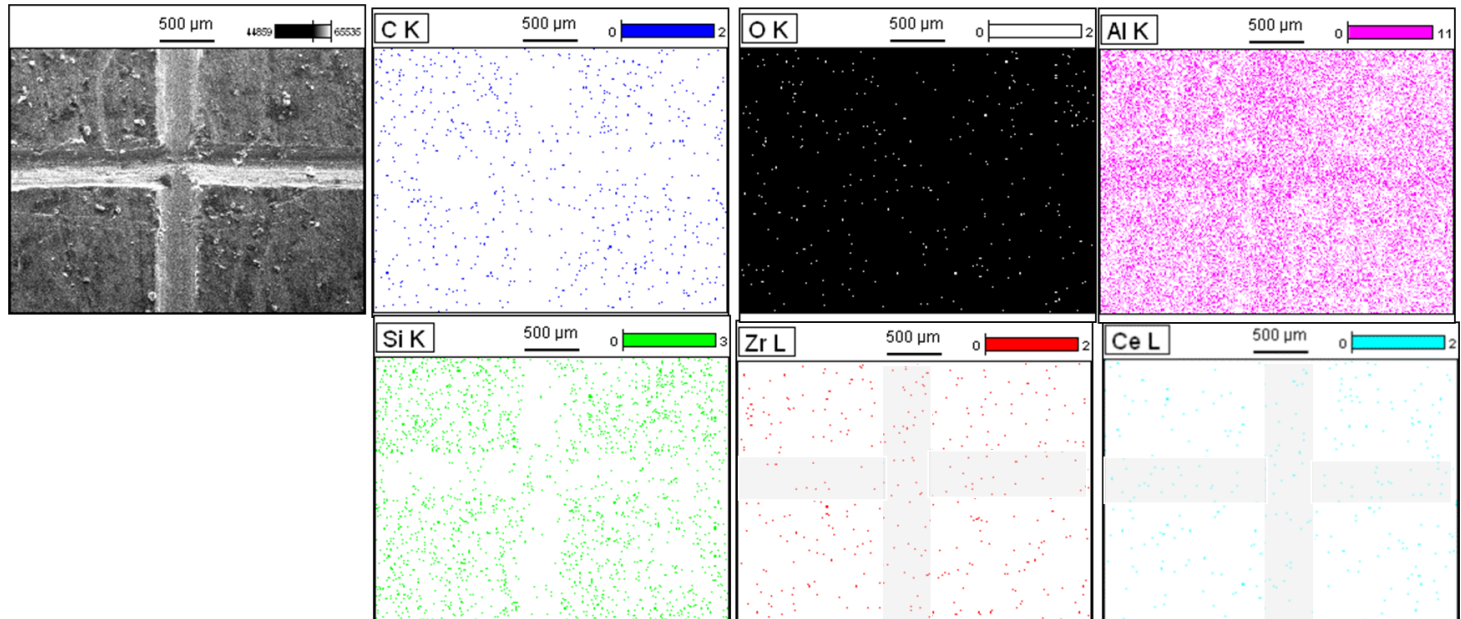
(b)



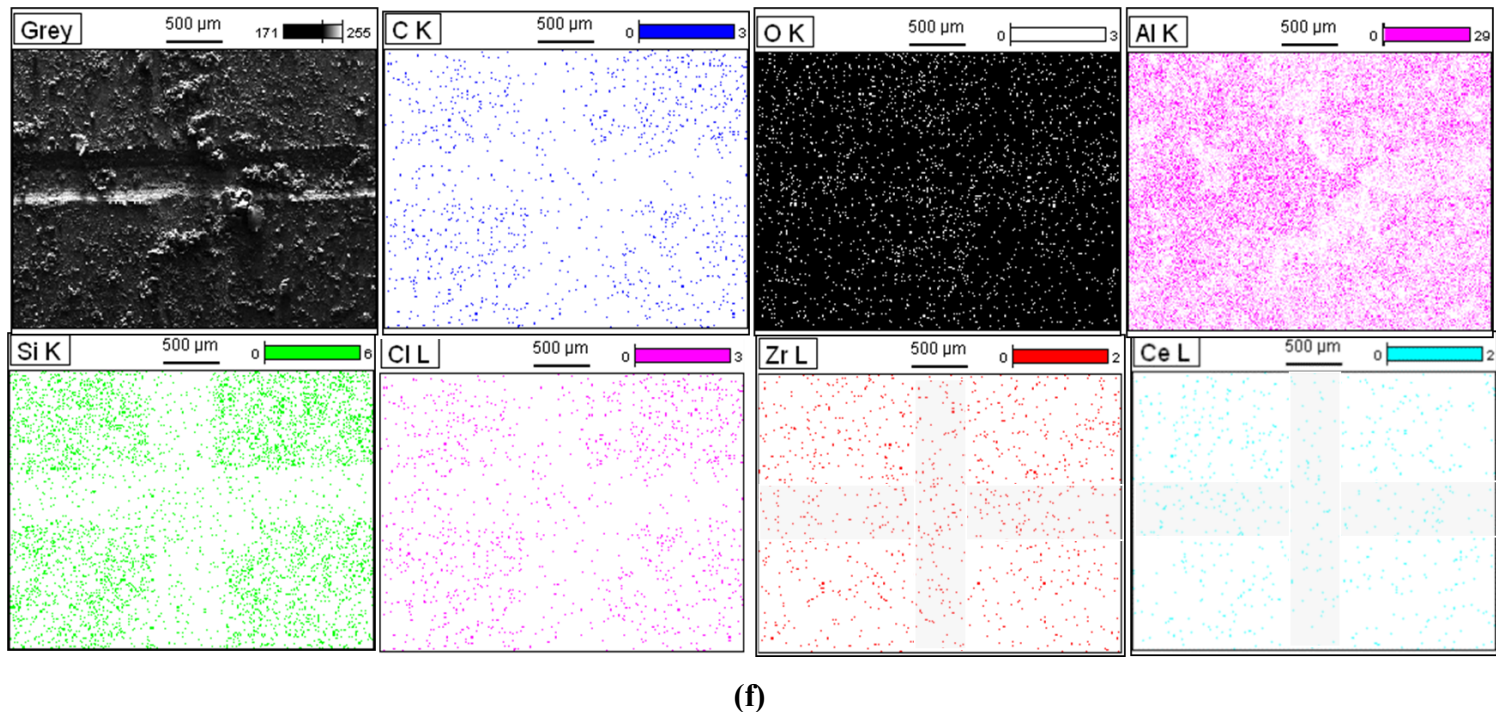
(c)



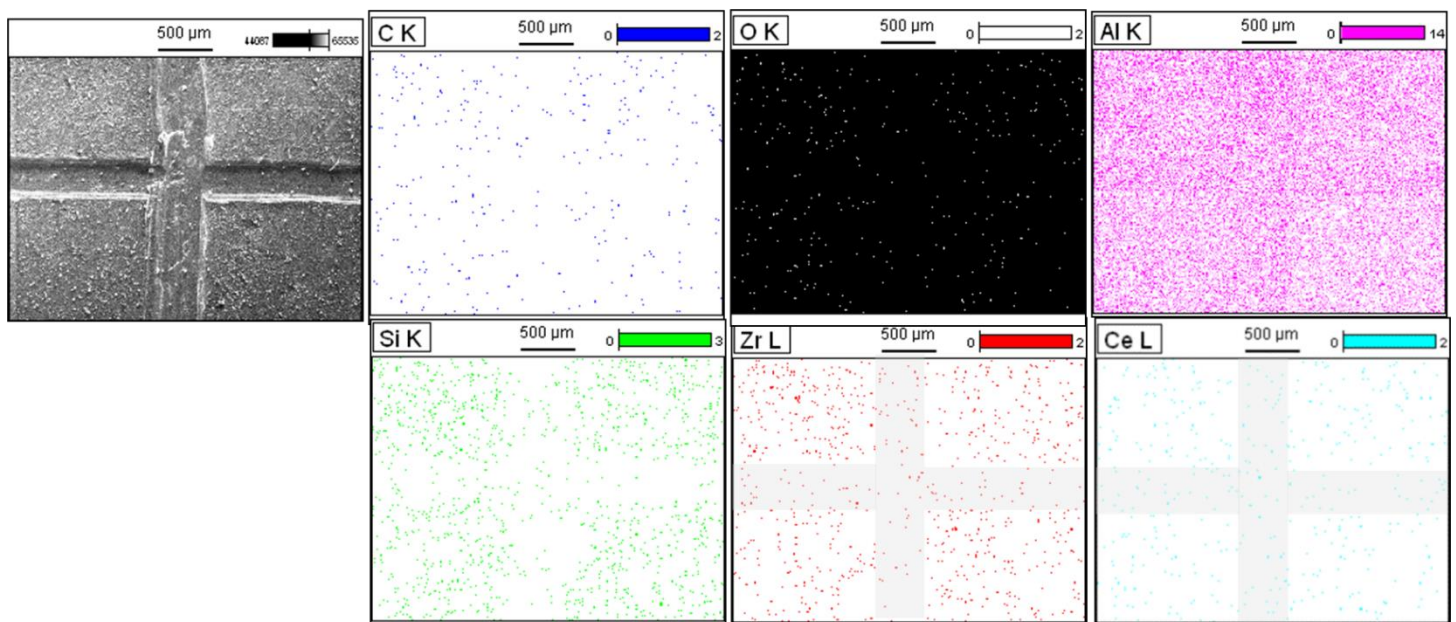
(d)



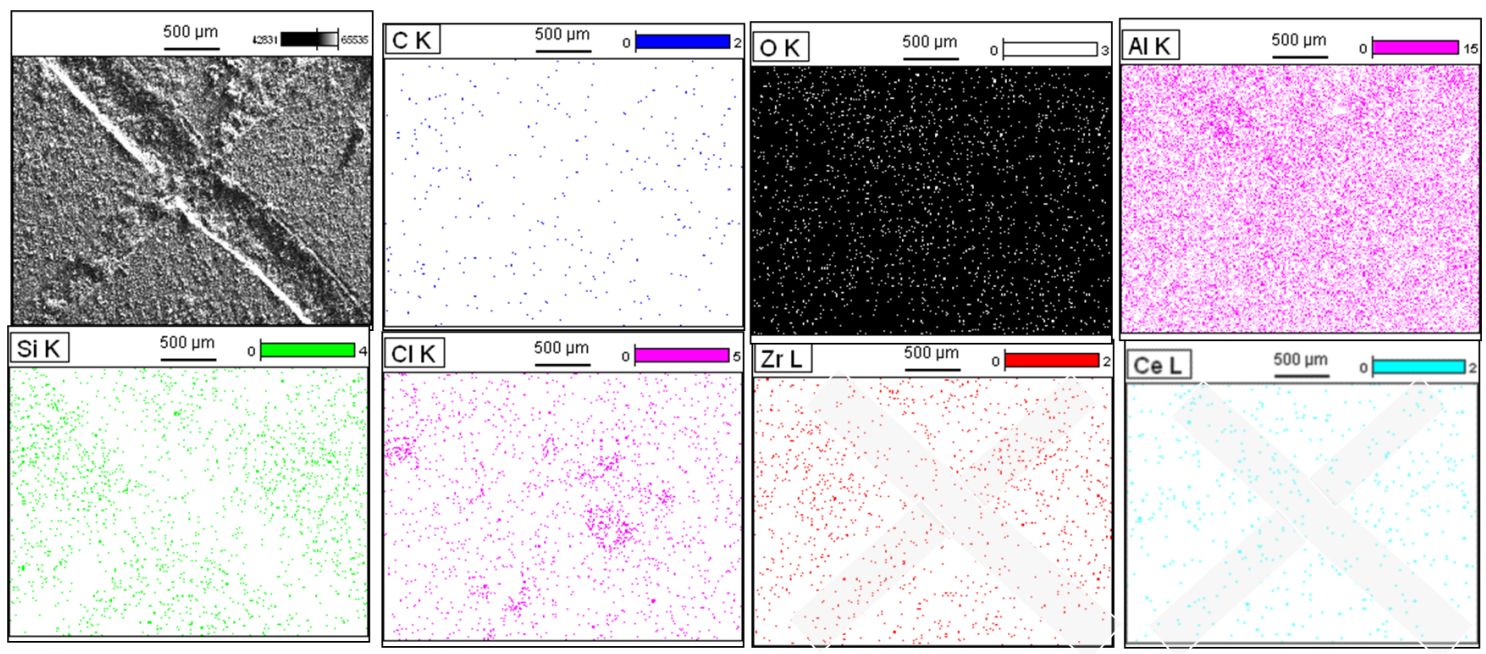
(e)



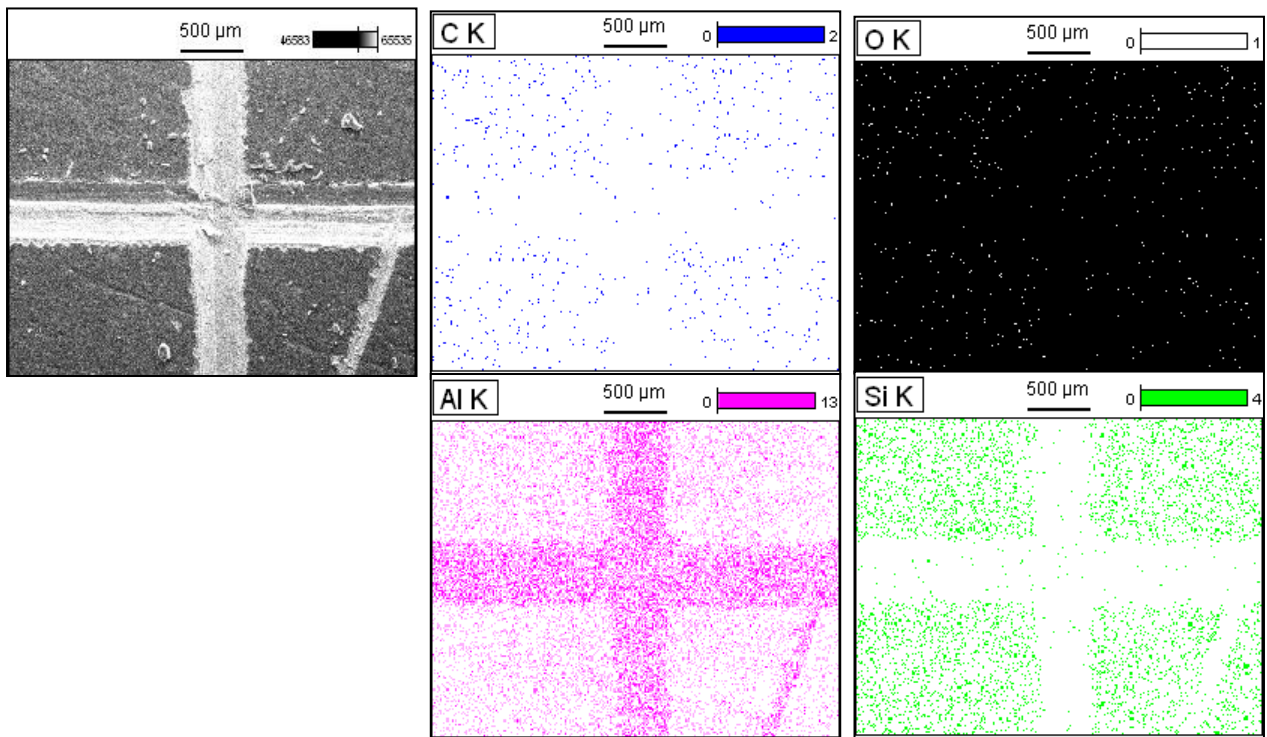
(f)



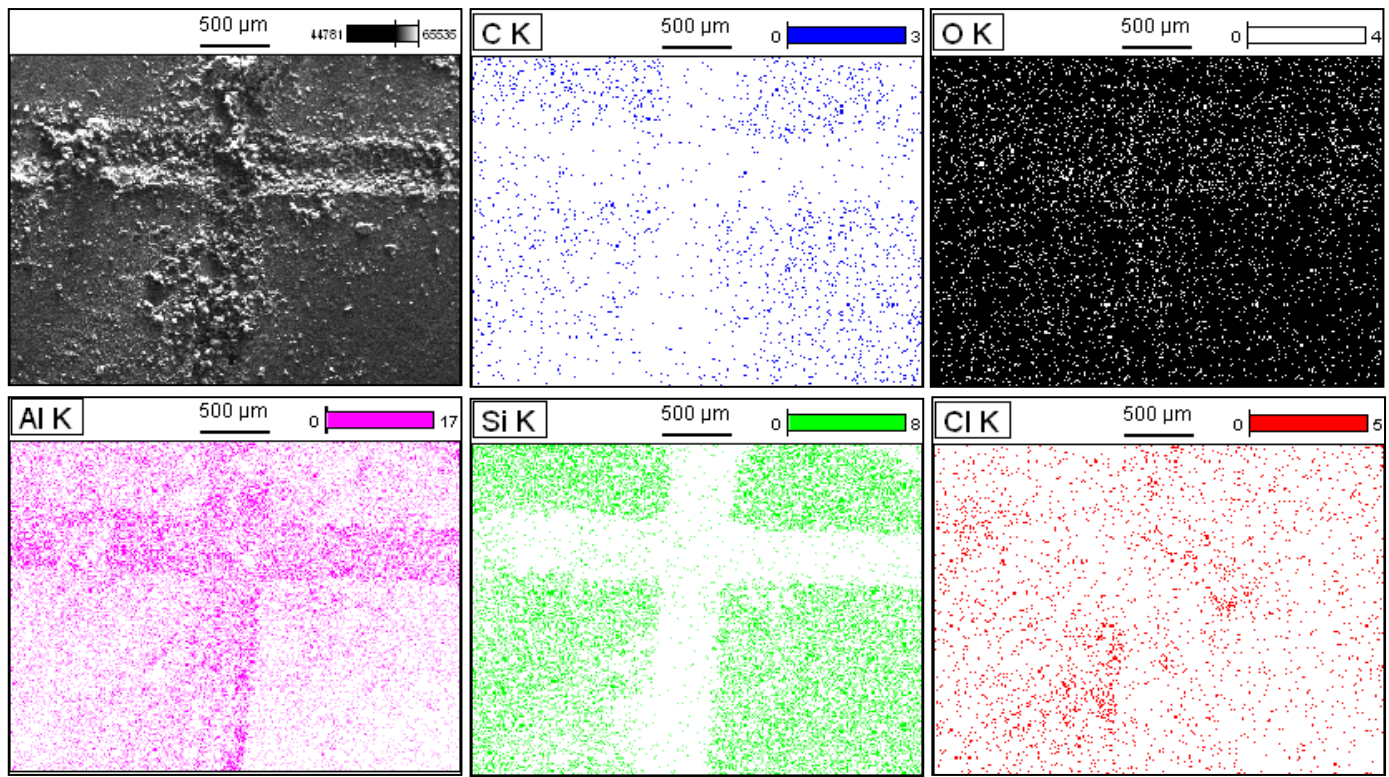
(g)



(h)



(i)



(j)

Fig. 4.14. EDS elemental mapping of bare (a, b), Mat (c, d), IEM (e, f), IMM (g, h) and MNC (i, j) coated substrates before (a, c, e, g, i) and after (b, d, f, h, j) SIT.

4.2.8 SVET analysis

Self-healing property of the developed MMT-based coatings has been evaluated by a localized electrochemical testing method, SVET. The current density maps obtained after exposing the scribed region of the substrates to 3.5 wt % NaCl solution at different time intervals are given in Fig. 4.15. For uncoated substrates, there is a rapid increase in the anodic current with time indicating that more corrosion has taken place as there is no protection. Mat sol coated substrates did not show any anodic current initially due to its barrier nature, but the anodic current got increased as the time of exposure to corrosive medium was increased. IMM sol coated substrates exhibited initially low anodic currents, but the current got increased with the time, due to the lack of extended corrosion protection. MNC sol coated substrates have shown higher anodic currents in the scribed area as the function of time. This indicated that, as there are no corrosion inhibitors present in the MNC coating, it was unable to provide corrosion protection. Although the MNC coated substrates have shown R_{ct} values closer to that of IEM coated substrates in EIS studies, the self-healing ability was not observed with MNC coated substrates. On the other hand, for IEM sol coated substrates, there

is appearance of an initial small anodic current due to the attack of corrosive species, which gets suppressed as a function of time. This indicates that IEM sol coated substrates, having cationic inhibitors, were able to provide self-healing action and hence a longer corrosion protection.

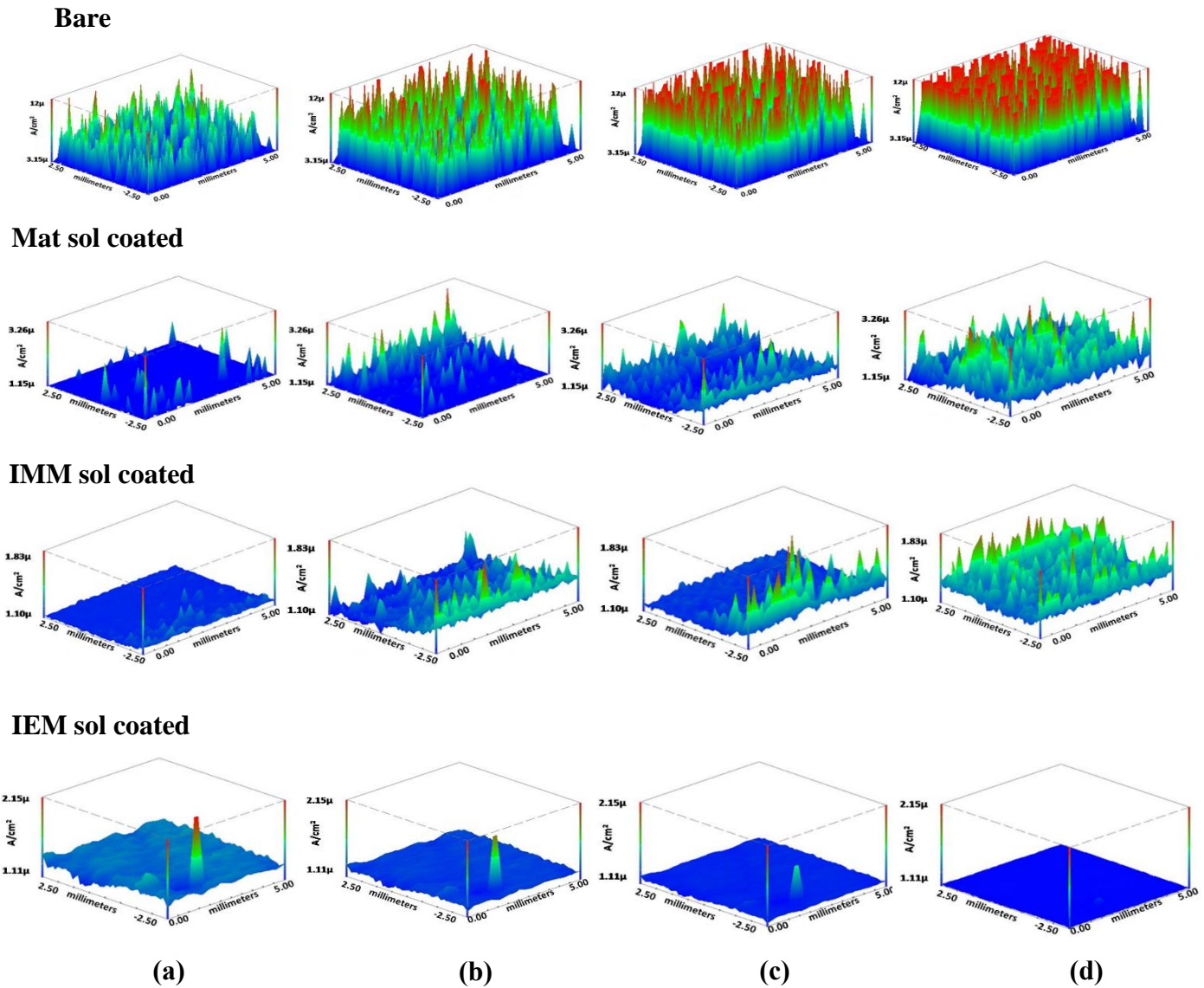


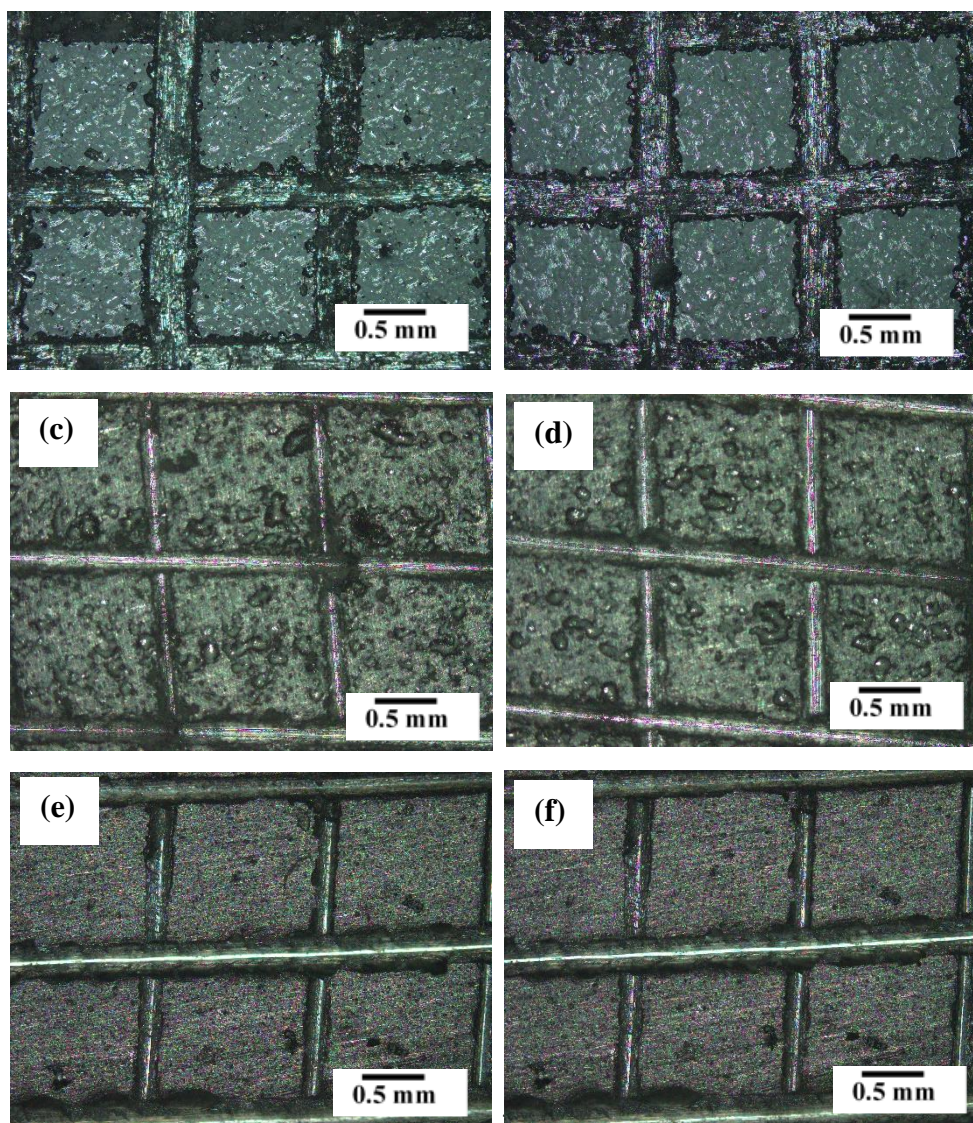
Fig. 4.15. Current density maps obtained in the scribed region at a) initially, b) 1 h, c) 12 h and d) 24 h of exposure to 3.5 wt % NaCl solution.

4.3 Results and discussion of coatings on A356.0 alloy

4.3.1 Thickness and adhesion strength of the coatings

The thickness for Mat sol coating was found to be $4.0 (\pm 0.35) \mu\text{m}$, IEM sol coating was $3.5 (\pm 0.5) \mu\text{m}$, IMM sol coating was $3.8 (\pm 0.3) \mu\text{m}$ and MNC sol coating was $3.6 (\pm 0.2) \mu\text{m}$.

The adhesion strength of Mat, IEM, IMM and MNC coatings on A356.0 substrates was determined by using tape adhesion test as per ASTM D3359-17 standard procedure [4]. The optical microscopic images of coated substrates after the adhesion test are given in Fig. 4.16. Mat coated substrates have shown up to 15 % removal of the coating along the edges of grids after the tape was peeled off, and therefore the adhesion strength of these coatings were ranked as 3B. IEM, IMM and MNC sol coated substrates have also shown slight removal of coating along the edges of the grids, and the area of removal was up to 5 %. So, the adhesion strength of the coatings was ranked as 4B.



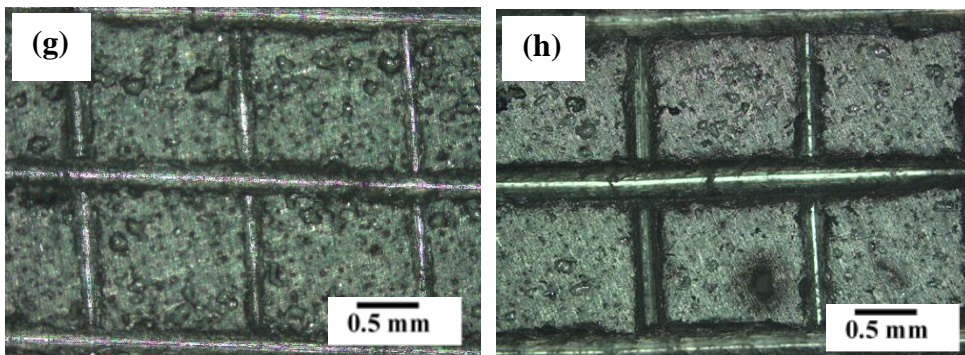


Fig. 4.16. Microscopic images of Mat sol coated (a, b), IMM sol coated (c, d), IEM sol coated (e, f) and MNC sol coated (g, h) A356.0 substrates before putting on tape (a, c, e, g) and after removal of tape (b, d, f, h).

4.3.2 EIS and potentiodynamic polarization studies

EIS studies were carried out for montmorillonite-based coatings on A356.0 substrates after 1, 72 and 120 h of exposure to 3.5 wt % NaCl solution. The equivalent electrical circuit used for fitting the EIS data is given in Fig. 4.7. Nyquist plots are depicted in Fig. 4.17 and the fit parameters are presented in Table 4.6. MNC coated substrates have shown highest R_{ct} after 1 h, which got decreased after 72 h and got increased after 120 h of exposure, as it do not contained any corrosion inhibitors. IEM coated substrates exhibited R_{ct} in the nearly same order at all durations of exposure and were found to have less R_{ct} values than IMM coated substrates. However, IMM coated substrates have shown increased R_{ct} values after 72 h and have found to exhibit highest i.e., $1026 \text{ k}\Omega\text{.cm}^2$ after 120 h R_{ct} among all. In addition, the coating resistance (R_{coat}) of IMM was also found to be highest among all at 72 h and 120 h of exposure.

The potentiodynamic polarization studies also have followed the same trend as that of EIS studies. The polarization curves have been depicted in Fig. 4.18, and polarization fit data are given in Table 4.7. MNC coated substrates have shown least corrosion currents after 1 h exposure, but it got increased on prolonged durations of exposure, whereas the IMM coated substrates have exhibited least corrosion currents after 72 h and 120 h of exposure to corrosive medium and found to be better coating system among all, for the corrosion protection of A356.0. The IEM coated substrates exhibited low i_{corr} values at 1 h of exposure, which got increased after 72 h and decreased after 120 h. The i_{corr} values of IEM coated substrates found to be less than IMM coated substrates after 72 h and 120 h of exposures.

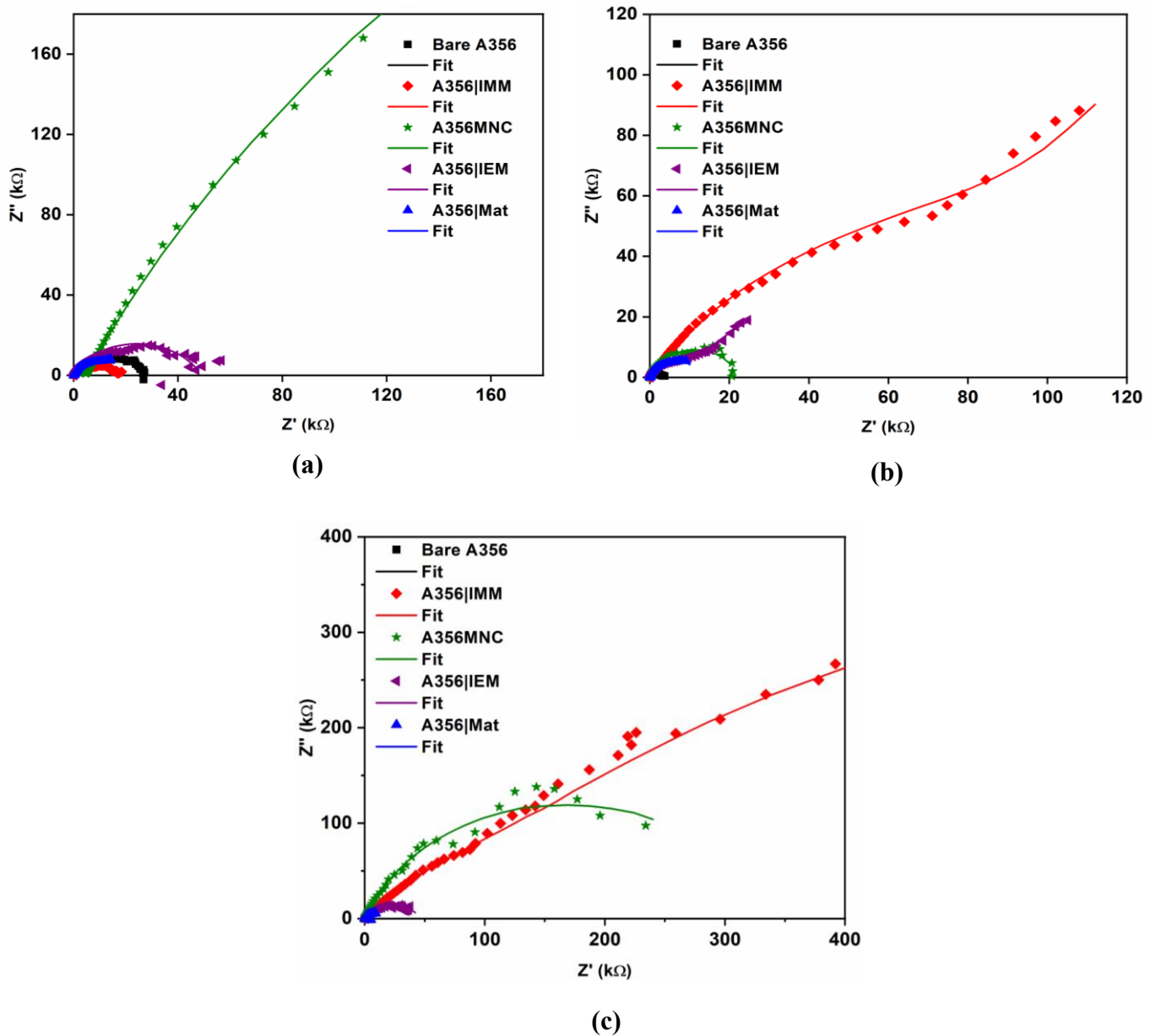


Fig. 4.17. Nyquist plots for coated and uncoated A356.0 substrates after (a) 1h, (b) 72 h and (c) 120 h of exposure to 3.5 wt % NaCl solution.

Table 4.6. EIS fit data for coated and uncoated A356.0 at different exposure durations to 3.5 wt % NaCl

Sample	Time of immersion in 3.5 wt % NaCl	$R_{Coat/Oxide}$ $k\Omega \cdot \text{cm}^2$	R_{ct} $k\Omega \cdot \text{cm}^2$	$C_{Coat/Oxide}$ $\mu\text{F}/\text{cm}^2$	C_{dl} $\mu\text{F}/\text{cm}^2$
A356 Bare	1 h	14.26	13.93	0.96	4.26
A356 Mat		0.20	20.08	3.51	7.67
A356 IEM		0.073	49.0	0.1886	3.31
A356 IMM		11.73	5.17	15.20	286.5
A356 MNC		4.55	1248.0	0.0028	5.30
A356 Bare	72 h	0.044	3.27	1.31	63.61
A356 Mat		0.0044	12.85	120.0	29.0
A356 IEM		15.47	64.98	35.15	689.80
A356 IMM		190.90	387.1	11.76	51.52
A356 MNC		18.20	3.60	141.1	50.92
A356 Bare	120 h	0.038	3.01	0.15	67.66
A356 Mat		0.072	7.17	25.40	88.9
A356 IEM		0.667	47.22	0.0043	22.07
A356 IMM		273.8	1026.0	3.04	19.0
A356 MNC		0.16	336.6	0.033	9.53

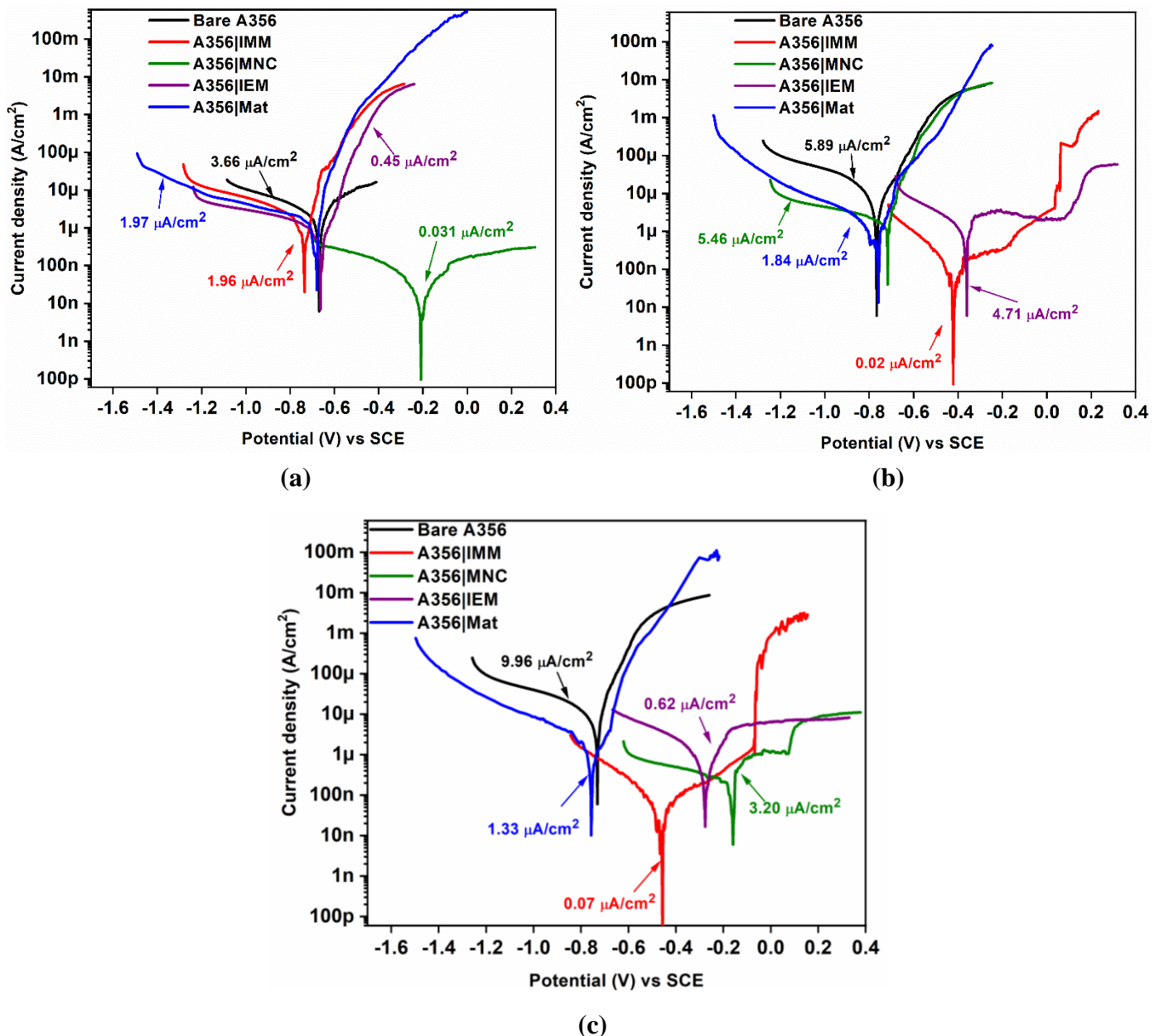


Fig. 4.18. Polarization curves of coated and uncoated A356.0 substrates after (a) 1h, (b) 72 h and (c) 120 h of exposure to corrosive medium.

Table 4.7. Corrosion currents and corrosion potential values for coated and uncoated A356.0 substrates at different exposure durations

Sample	Time of immersion in 3.5 wt % NaCl	i_{corr} ($\mu\text{A}/\text{cm}^2$)	E vs SCE (Volts)
A356 Bare	1 h	3.66	-0.669
A356 Mat		1.97	-0.686
A356 IEM		0.45	-0.663
A356 IMM		1.96	-0.736
A356 MNC		0.031	-0.210
A356 Bare	72 h	5.89	-0.767
A356 Mat		1.84	-0.763
A356 IEM		4.71	-0.360
A356 IMM		0.020	-0.421
A356 MNC		5.46	-0.717
A356 Bare	120 h	9.96	-0.731
A356 Mat		1.33	-0.756
A356 IEM		0.62	-0.277
A356 IMM		0.071	-0.457
A356 MNC		3.20	-0.159

4.3.3 Weight loss analysis

The corrosion rate of coated and uncoated A356.0 substrates was determined using weight loss experiments by immersing the substrates for 120 h of immersion in 3.5 wt % NaCl according to ASTM G31 standard procedure [6,7]. IMM coated substrates exhibited least corrosion rate among all as given in Fig. 4.19. The corrosion rate of IEM coated substrates exhibited higher corrosion rates than IMM in the case of A356.0 alloy. MNC coated substrates exhibited highest corrosion rate among coated substrates. The increasing order of corrosion rates of the coated and uncoated substrates is: IMM < IEM < MNC < Bare.

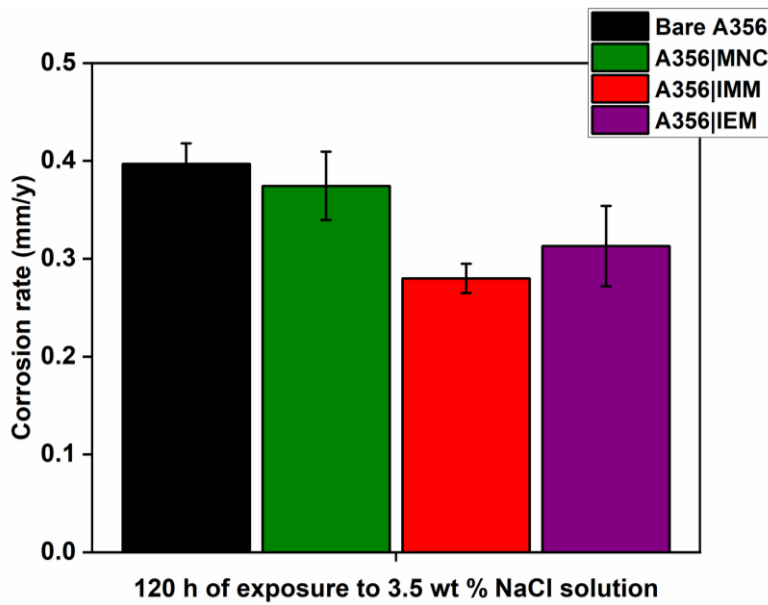
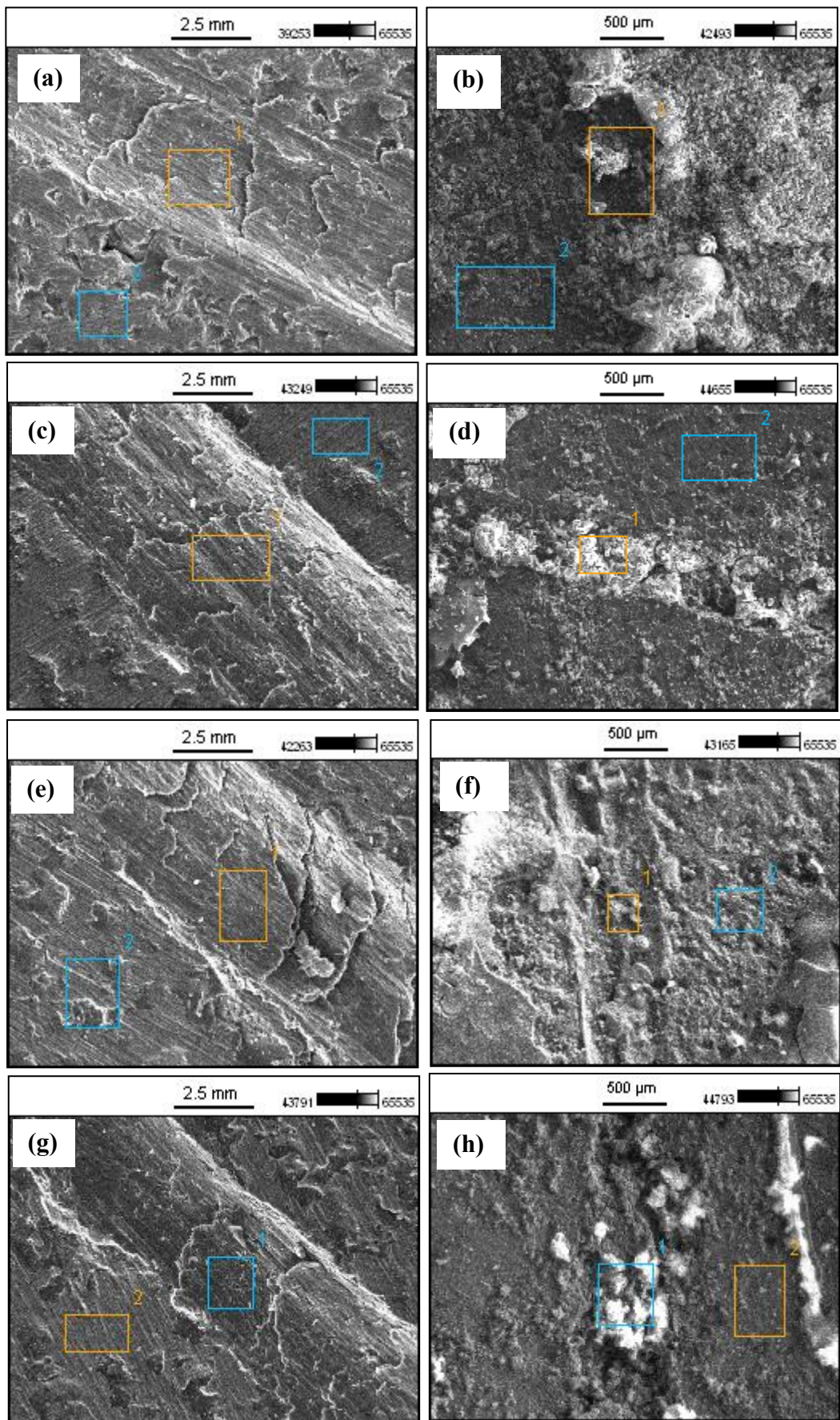


Fig. 4.19. Comparison of corrosion rate of A356.0 substrates determined by weight loss experiments.

4.3.4 SST and EDS analysis

SST was carried out for coated and uncoated A356.0 substrates after making an X shape artificial scratch and exposing them to 5 wt % NaCl for 168 h as per ASTM B117 standard [8]. SEM images of bare and coated substrates are given in Fig. 4.20 and EDS elemental analysis before and after SST in the scribed region is presented in Table 4.8. Bare (Fig. 4.20 (a, b)) and MNC coated substrates (Fig. 4.20 (i, j)) have shown an increased amount of O after SST, indicating the formation of corrosion product. Mat coated substrates have shown an increase in the amounts of C and O, which could be due to metal mediated polymerization of epoxy monomers as mentioned in the section 4.2.6. IEM coated substrates, as seen in Fig. 4.20 (e, f) and Table 4.8, have shown an increase in the amounts of C, O and appearance of Zr after SST. However, IMM coated substrates (Fig. 4.20 (g, h), and Table 4.8) have shown more amounts of Ce and Zr along with an enormous increase in C and O weight percentages. The observations clearly indicated that IMM coated substrates were able to protect the A356.0 substrates from corrosion more effectively due to the release of inhibitors into the scratch region or damaged area to form passive layer of ceria and zirconia as well as to form poly ether polymer layer.



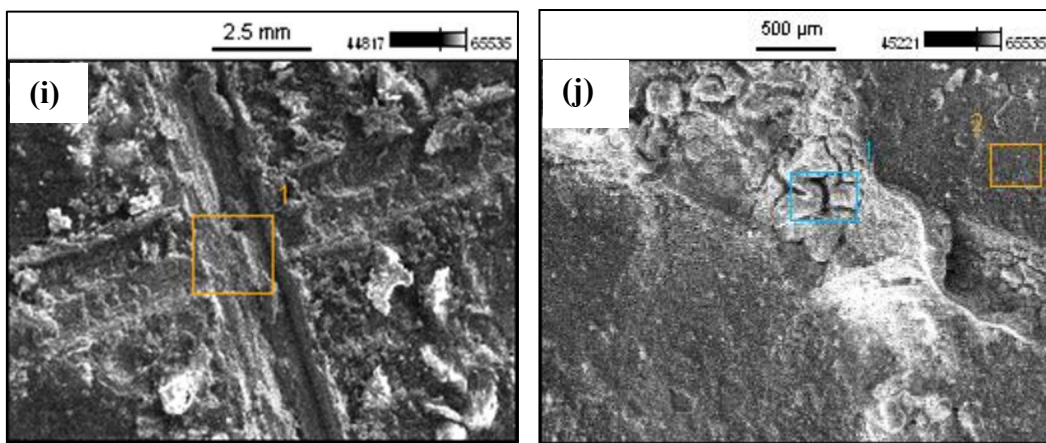


Fig. 4.20. SEM images of bare (a, b), Mat (c, d), IEM (e, f), IMM (g, h) and MNC sol coated (i, j) A356.0 substrates before (a, c, e, g, i) and after (b, d, f, h, j) SST.

Table 4.8. Weight % of elements in scratch region before and after SST of coated and uncoated A356.0 substrates.

Sample	SST	% weight ratio of elements in the scratch region								
		C	O	Na	Mg	Al	Si	Cl	Zr	Ce
Bare	Before	-	0.31	0.00	0.30	90.86	8.53	-	-	-
	After	-	41.38	1.33	1.52	41.48	9.69	4.60	-	-
Mat sol coated	Before	1.86	0.10	0.00	0.20	89.61	8.23	-	-	-
	After	8.57	46.14	0.52	0.10	36.51	3.53	4.63	-	-
IMM sol coated	Before	4.29	0.27	0.00	0.28	79.06	16.08	-	0.02	0.00
	After	26.42	28.39	1.06	0.00	32.48	7.19	2.05	0.31	2.10
IEM sol coated	Before	2.20	0.16	0.00	0.22	88.87	8.35	-	0.00	0.02
	After	8.71	40.95	1.42	0.00	46.26	2.03	0.53	0.10	0.00
MNC sol coated	Before	2.24	0.00	0.00	0.36	84.00	13.40	-	-	-
	After	0.00	40.31	2.73	2.00	49.88	1.43	3.65	-	-

4.4 Performances of corrosion protection of IEM and IMM coatings on AA2024-T4 and A356.0 alloys

Charge transfer resistances of IEM and IMM sol coatings on AA2024-T4 and A356.0 substrates were depicted in Fig. 4.21. IEM sol coatings on AA2024 have shown reliable steady increase in the corrosion resistance with the duration of exposure and have shown enormously very high R_{ct} . IEM sol coatings have outperformed compared to IMM sol coatings in the case of AA2024 substrates, whereas IMM sol coatings have shown higher corrosion resistances than IMM sol coatings in the case of A356 substrates. However, the AA2024/IEM coated substrates exhibited extremely high corrosion resistance values among all the coated substrates studied. Similarly, IEM coatings exhibited least corrosion currents than IMM when applied on AA2024-T4 as seen from Fig. 4.22, whereas, IMM coatings exhibited less i_{corr} than IEM in case of A356.0 substrates. The difference in the behavior of the same coating when applied on two alloys could be attributed to the nature of alloying element present in a particular alloy. In A356.0, the major alloying element is Si, due to which A 356.0 is less prone to corrosion when compared to AA2024-T4 that contains Cu as the major alloying element. The IMM contained more amount of Zr adsorbed on the surfaces of montmorillonite clay than in IEM. Therefore, the adsorbed inhibitors from the partially delaminated MMT surfaces might have got released to form a passive layer on the damage and which was sufficient for providing the corrosion protection for this mild corrodible alloy A356.0. However, ultimately EIS analyses reveal that the combination between IEM sol and AA2024-T4 resulted in highly protective self-healing substrates.

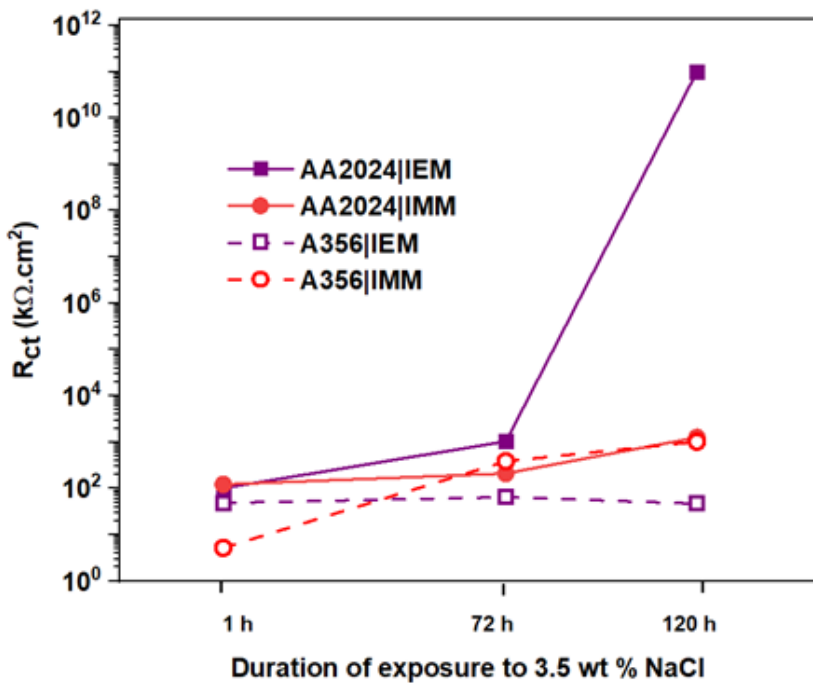


Fig. 4.21. Charge transfer resistance of IEM and IMM coatings on AA2024-T4 and A356 substrates.

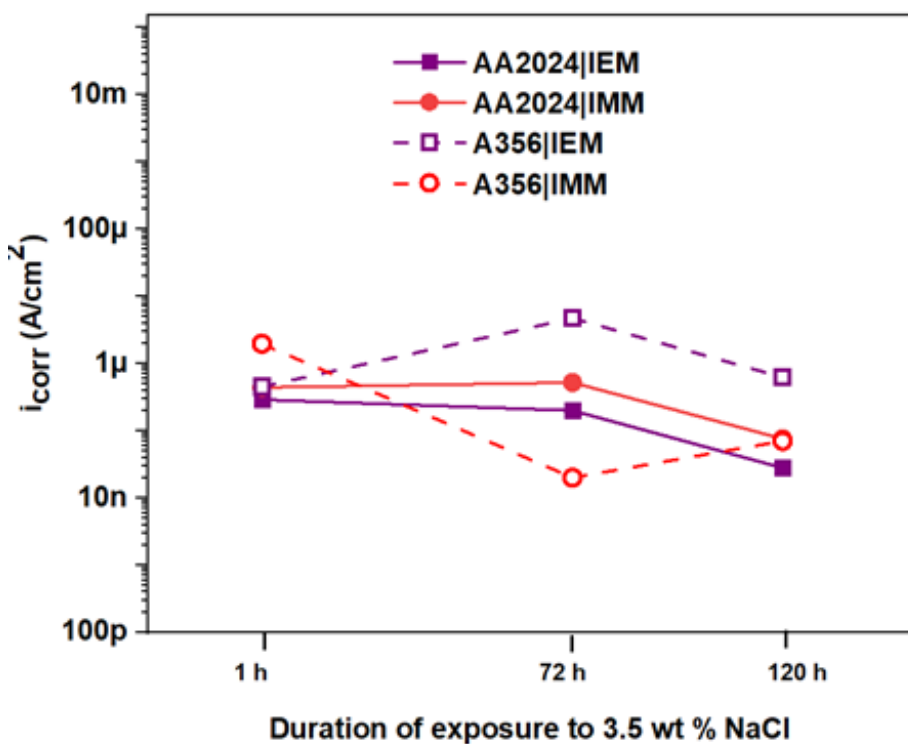


Fig. 4.22. Corrosion currents of IEM and IMM coatings on AA2024-T4 and A356.0 substrates.

References

- [1] J.T. Pinnavaia, M. Tzou, D.S. Landau, H.R. Rasik, On the pillaring and delamination of smectite clay catalysts by polyoxo cations of aluminum, *Journal of Molecular Catalysis*. 27 (1984) 195–212.
- [2] R. Mahboub, E.Y. Mouzdaahir, A. Elmchaouri, A. Carvalho, M. Pinto, J. Pires, Characterization of a delaminated clay and pillared clays by adsorption of probe molecules, *Colloids and Surfaces A: Physicochemical and Engineering Aspects*. 280 (2006) 81–87. doi:10.1016/j.colsurfa.2006.01.036.
- [3] P. Yuan, F. Annabi-bergaya, Q. Tao, M. Fan, Z. Liu, J. Zhu, H. He, A combined study by XRD, FTIR, TG and HRTEM on the structure of delaminated Fe-intercalated / pillared clay, 324 (2008) 142–149. doi:10.1016/j.jcis.2008.04.076.
- [4] ASTM D3359-17 Standard Test Methods for Rating Adhesion by Tape Test, (2009) 1–9. doi:10.1520/D3359-17.
- [5] E. Huttunen-Saarivirta, G. V Vaganov, V.E. Yudin, J. Vuorinen, Characterization and corrosion protection properties of epoxy powder coatings containing nanoclays, *Progress in Organic Coatings*. 76 (2013) 757–767. doi:10.1016/j.porgcoat.2013.01.005.
- [6] ASTM G31-12 Standard Guide for Laboratory Immersion Corrosion Testing of Metals 1, (2012). doi:10.1520/G0031-12A.
- [7] ASTM G1-90 Standard Practice for Preparing, Cleaning and Evaluation Corrosion Test Specimens, (1999).
- [8] ASTM B117-16 Standard Practice for Operating Salt Spray (Fog) Apparatus, (2016). doi:10.1520/B0117-16.2.
- [9] G. Schottner, Hybrid Sol - Gel-Derived Polymers : Applications of Multifunctional Materials, *Chemistry of Materials*. 13 (2001) 3422–3435.
- [10] D. Hoebbel, M. Nacken, H. Schmidt, On the Influence of Metal Alkoxides on the Epoxide Ring-Opening and Condensation Reactions of 3-Glycidoxypolytrimethoxysilane, *Journal of Sol-Gel Science and Technology*. 21 (2001) 177–187.

CHAPTER-5

Synergistic Effect of Halloysite and Montmorillonite Nanocontainers for the Corrosion Protection of AA2024-T4

CHAPTER-5

Synergistic Effect of Halloysite and Montmorillonite Nanocontainers for the Corrosion Protection of AA2024-T4

In this chapter-5, a combination of two different nanocontainers has been used in order to study their coordinated influences in enhancing the corrosion protection of AA2024-T4 substrates. Here, two different nanocontainers such as halloysite nanotubes and montmorillonite nanoclays were used. These nanoclays were found to be promising smart nanocarriers for accommodating corrosion inhibitors and effectively releasing them on demand, when used individually as discussed in chapter-3 and chapter-4. Use of the combination of inhibitors loaded nanocontainers is a new approach followed for the development of corrosion protection coatings for prolonged durations. There are many reports on the use of the combinations of different nanocontainers loaded with inhibitors.

5.1 Literature Survey

Darmiani et al. [1] have studied the synergistic effect of montmorillonite and cerium nitrate nanocomposite-based epoxy coatings on cold rolled steel panels. Carbonel et al. [2] have studied the barrier property and corrosion protection behavior of different inhibitors like benzotriazole, Na-(diethyl(dithiocarbamate)), piperazine and Ce(III)-montmorillonite prepared by ion exchange reaction at 65° C for 6 h. They were dispersed in a sol-gel matrix and deposited on AA2024-T3. Snihirova et al. [3] have studied the effect of binary mixtures of Ce-2,5-dimercapto-1,3,4-thiadiazolate (Ce-DMTD), 8-hydroxyquinoline-salicylaldoxime (8-HQ-SAL), 8-HQ-DMTD and Ce-SAL along with the individual inhibitors on AA2024-T3 alloy. The synergistic effect of these inhibitors was studied by exposing the AA2024-T3 substrates to aqueous solution of inhibitors as well as coating the substrates with epoxy matrix containing porous CaCO_3 microparticles loaded with different inhibitors. They have reported that the inhibitors when encapsulated and embedded in epoxy matrix provided prolonged corrosion protection than when inhibitors are added into aqueous solution. Coating with Ce-SAL loaded CaCO_3 nanocontainers was found to provide better corrosion protection due to the synergistic effect between cationic and anionic inhibitors. Montemor et al. [4] have used

the combination of layered double hydroxides (LDH) and cerium molybdate hollow spheres (CeMo) loaded with mercaptobenzothiazole (MBT). These loaded nanocontainers were dispersed in epoxy matrix and applied on to galvanised steel substrates. The corrosion inhibition activity was studied by scanning vibrating electrode technique and scanning ion selective electrode technique. They reported that the combination of two nanocontainers resulted in synergistic corrosion inhibition that combines early corrosion protection by LDH/MBT and long-term inhibition by CeMo/MBT. Izadi et al. [5] studied the synergistic inhibition between Nettle molecules (extracted from Nettle plant leaves) loaded polyaniline (PANI)/poly-acrylic acid (PAA) nanocontainers (Nettle-NC) and zinc acetate (ZA). They were dispersed in silane matrix and applied over mild steel substrates as bilayer coating having the configuration as ZA/Nettle-NC. The Nettle molecules were encapsulated by layer-by-layer deposition of PANI/PAA. The corrosion behaviour of the developed coatings was compared with that of neat silane coatings. The ZA/Nettle-NC coating was found to show enhancements in the corrosion inhibition performance, which were attributed to the synergistic effect between the active agents of Nettle constituents (Quercetin, Histamine and Serotonin moieties) and Zn^{2+} cations due to complex formation. Chen et al. [6] have intercalated phosphate (PO_4^{3-}) into the layers of hydrotalcite (PIH) and used graphene oxide (GO) to disperse the PO_4^{3-} intercalated PIH in water based epoxy coatings by electrostatic self-assembly (GO-PIH). These coatings were applied on carbon steel substrates. They have reported that the intercalated PO_4^{3-} ions present in the GO-PIH layers were released and Cl^- ions were entrapped, forming a passive film at metal-coating interface to avoid the propagation of corrosion. Serdechnova et al. [7] have used a combination of two nanocontainers such as LDH and bentonite with two different inhibitors 1,2,3-benzotriazole (BTA) and Ce^{3+} . The mixture of BTA-loaded LDH and Ce^{3+} -loaded bentonite nanocontainers were dispersed in a commercially available epoxy resin, SEEVENAX. These coatings were found to show good corrosion protection and self-healing ability due to the synergistic effect of different inhibitors loaded nanocontainers for galvanically coupled aluminum alloy AA6061 with carbon fiber reinforced plastic. Zadeh et al. [8] have studied the synergistic behavior between Ce^{3+} loaded NaY-zeolite (NaY-Ce) and MBT loaded Zn-Al LDH (LDH-MBT) containers. These loaded nanocontainers were dispersed in a water borne, room temperature curable epoxy amine and coated on AA2024-T3 substrates. A combination of these two inhibitor-loaded nanocontainers was found to have the effective corrosion protection at an optimal ratio of NaY-Ce to LDH-MBT at 90:10 in the epoxy coating. They have also observed that the individual inhibitor doped nanocontainers were able to provide

good corrosion protection, but the combination resulted in enhanced active corrosion protection due to the synergy between the two loaded nanocontainers. Hao et al. [9] have studied the corrosion protection behavior of phytic acid doped polyaniline nanofibers (PA-PANI-NF) loaded with BTA dispersed in epoxy matrix and deposited on Q235 carbon steel. They have reported that BTA loaded PA-PANI-NFs have shown excellent corrosion inhibition than phytic acid doped PANI-NFs alone, emphasizing the synergistic effect between PA and BTA inhibitors towards corrosion protection.

From all the above reported literatures, it was observed that the use of two or more inhibitors and/or nanocontainers was found to be immensely effective in protecting metal surfaces due to their synergistic behavior. In this context, the present work was designed to investigate the use of both Ce^{3+} and Zr^{4+} inhibitors loaded halloysite and montmorillonite nanocontainers that were dispersed in organic-inorganic hybrid silane matrix and applied on AA2024-T4 alloy.

5.2 Preparation of sols, coating deposition and characterization

Ce^{3+} and Zr^{4+} inhibitors loaded nanocontainers montmorillonite (M) and halloysite nanotubes (H) were mixed in 1:1 wt ratio in hybrid sol-gel matrix to make a composite coating, which is labeled as M+H. Bilayer coatings were prepared with two different configurations, such as i) montmorillonite-based coating followed by halloysite-based coating, labeled as M|H, and ii) halloysite-based coating followed by montmorillonite-based coating, labeled as H|M configuration. Preparation of inhibitor loaded nanocontainers, composite mixture, coating of bilayer and composite sols were carried out as mentioned in Chapter-2.

The bilayer and composite coatings have been characterized by FESEM and EDS for their morphology and elemental composition and cross-sectional images were investigated for determining the thickness. Adhesion strength of the coatings was determined by tape adhesion testing. Further, the corrosion behaviour of the coated samples was examined by electrochemical tests such as electrochemical impedance spectroscopy and potentiodynamic polarization studies. Weight loss analysis, salt spray test and salt immersion tests have also been carried out to study their corrosion protection performance.

5.3 Results and Discussion

5.3.1 Surface morphology of coatings by FESEM analysis

FESEM images of (a) H|M, (b) M|H and (c) M+H coatings are shown in Fig. 5.1, and the images have indicated that the nanocontainers were distributed uniformly in all the coatings. H|M coated substrates have shown the presence of few blisters, as seen from Fig. 5.1 (a). However, M|H and M+H coatings have not shown any blisters or cracks (Fig. 5.1(b,c)). Results of EDS analysis given in Table 5.1 have shown the presence of Al, Si, O corresponding to the composition of MMT and HNT clays and Ce, Zr corresponding to the corrosion inhibitors in all the three coatings.

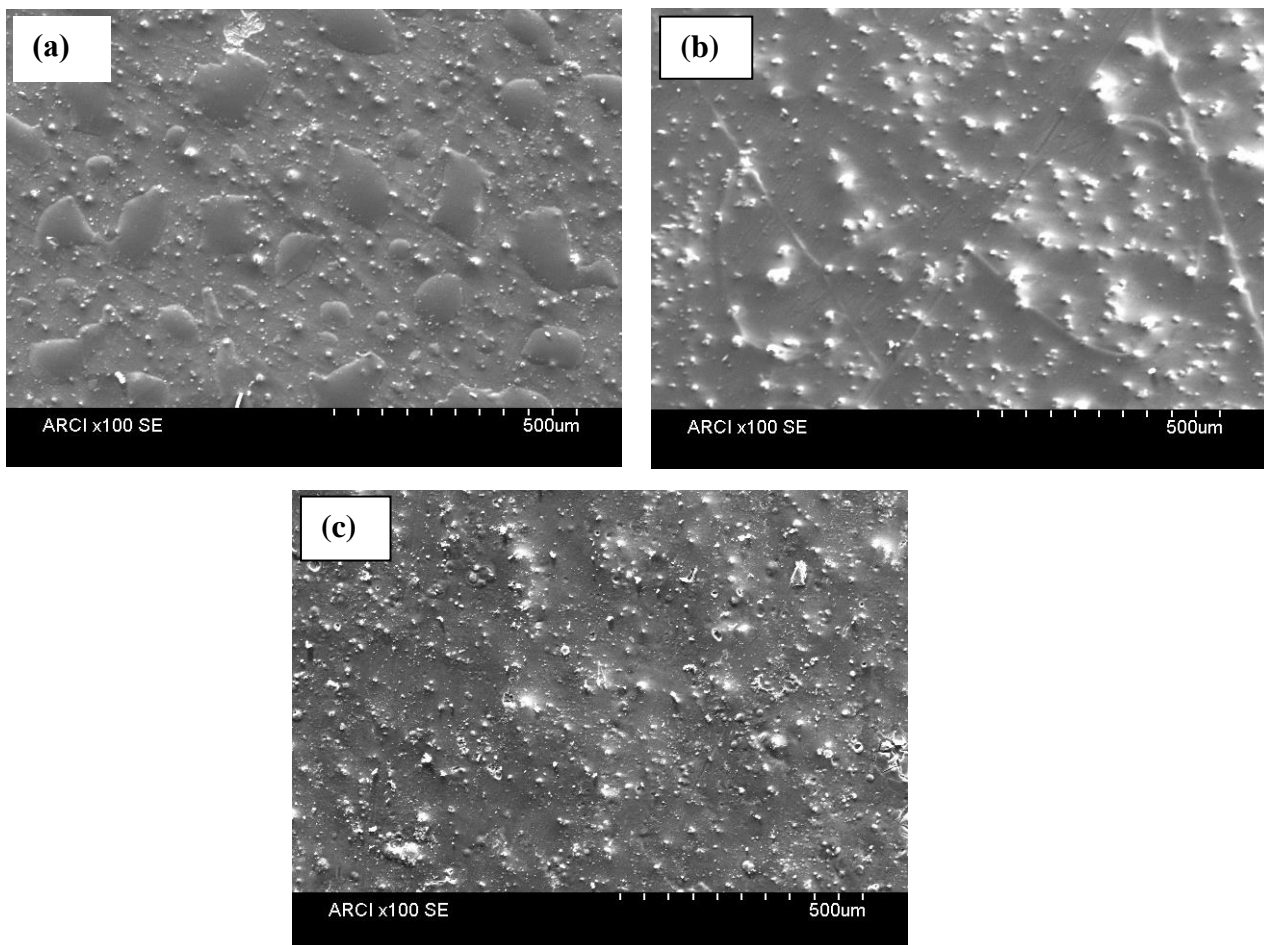


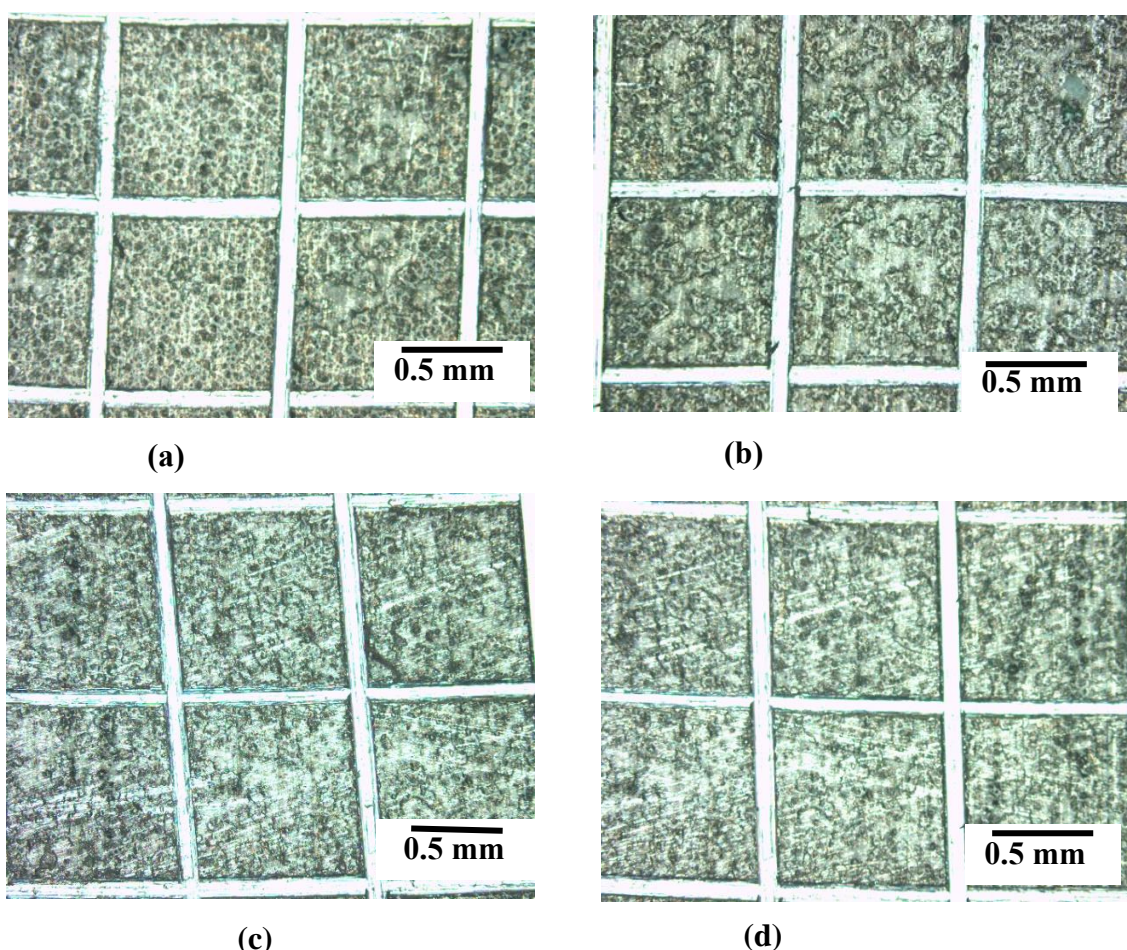
Fig. 5.1. FESEM images of (a) H|M, (b) M|H and (c) M+H coatings.

Table 5.1. Weight percentage of different elements for all the coatings obtained from EDS analysis.

Sample	C	O	Al	Si	Zr	Ce
H M	44.90	11.35	20.70	22.77	0.26	0.02
M H	43.43	10.81	23.99	21.36	0.38	0.03
M+H	45.21	15.27	12.31	26.72	0.47	0.02

5.3.2 Adhesion strength of coatings by tape adhesion test

The adhesion strength of the coatings has been tested by tape adhesion test using the cross-hatch cutter according to ASTM D3359 standard operating procedure [10]. Both the bilayer coatings H|M, M|H and the composite M+H coating have shown 5B ranking after peeling of the tape, as seen in Fig. 5.2, indicating that there is no peeling of the coating (0 % removal of the coating).



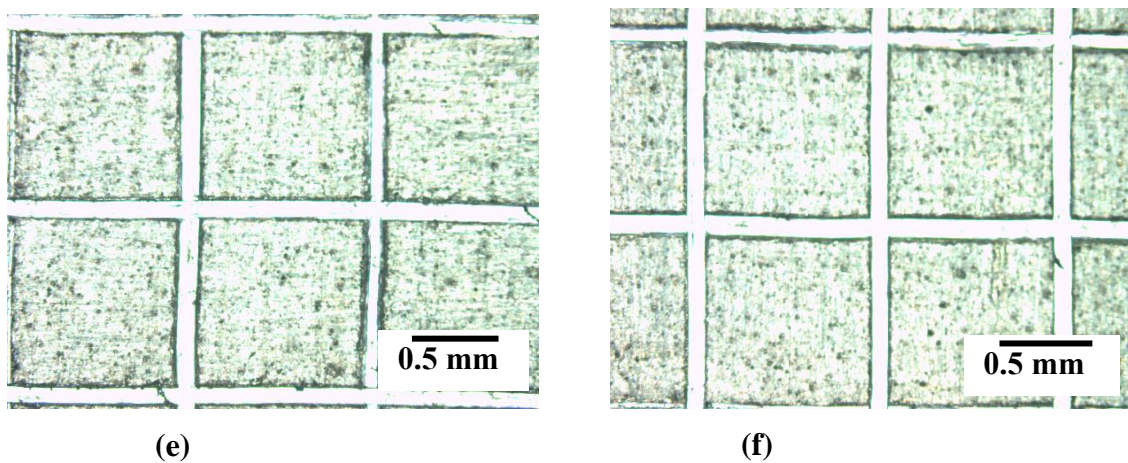


Fig. 5.2. Optical microscopic images of (a, b) H|M, (c, d) M|H and (e, f) M+H coated AA2024-T4 substrates (a, c, e) before and (b, d, f) after the tape adhesion test.

5.3.3 Thickness of the coatings by FESEM analysis

Thickness of H|M, M|H and M+H coatings was determined by FESEM analysis and the observed cross-sectional FESEM images are shown in Fig. 5.3. H|M and M|H coatings have shown two distinct layers of coating. The thickness of H|M coating (Fig. 5.3 (a)) was found to be $13.2 (\pm 0.4) \mu\text{m}$, with inner H layer of $4.6 (\pm 0.3) \mu\text{m}$ and outer M layer of $8.4 (\pm 0.2) \mu\text{m}$. In this case, the thickness of outer M layer was found to be more than inner H layer. M|H coating has shown the thickness of $6.8 (\pm 0.2) \mu\text{m}$, having inner M layer of $2.9 (\pm 0.3) \mu\text{m}$ and outer H layer of $3.8 (\pm 0.1) \mu\text{m}$, as seen in Fig. 5.3 (b). The thickness of M|H coating was found to be lesser than the H|M coating and further the M|H coating has shown nearly an equal thickness for both the inner and outer layers. In the case of composite M+H coating, the thickness of the coating was $3.8 (\pm 0.1) \mu\text{m}$. It was noted that the thickness of the inner M layer was found to be lesser than the inner H layer. Furthermore, the thickness of the composite M+H coating was lesser than the inner H layer alone of H|M coating. These observations clearly infer that the presence of montmorillonite for coatings intended to form always thinner inner coatings on the AA2024-T4 alloy substrate. Moreover, from the thicknesses of H layer in H|M and M|H coatings, it was observed that the presence of inner M layer decreased the thickness of H layer considerably from $4.6 \mu\text{m}$ to $3.8 \mu\text{m}$. All these coatings were seen to be adherent to the substrate, which again confirmed that the coatings have good adhesion with substrate.

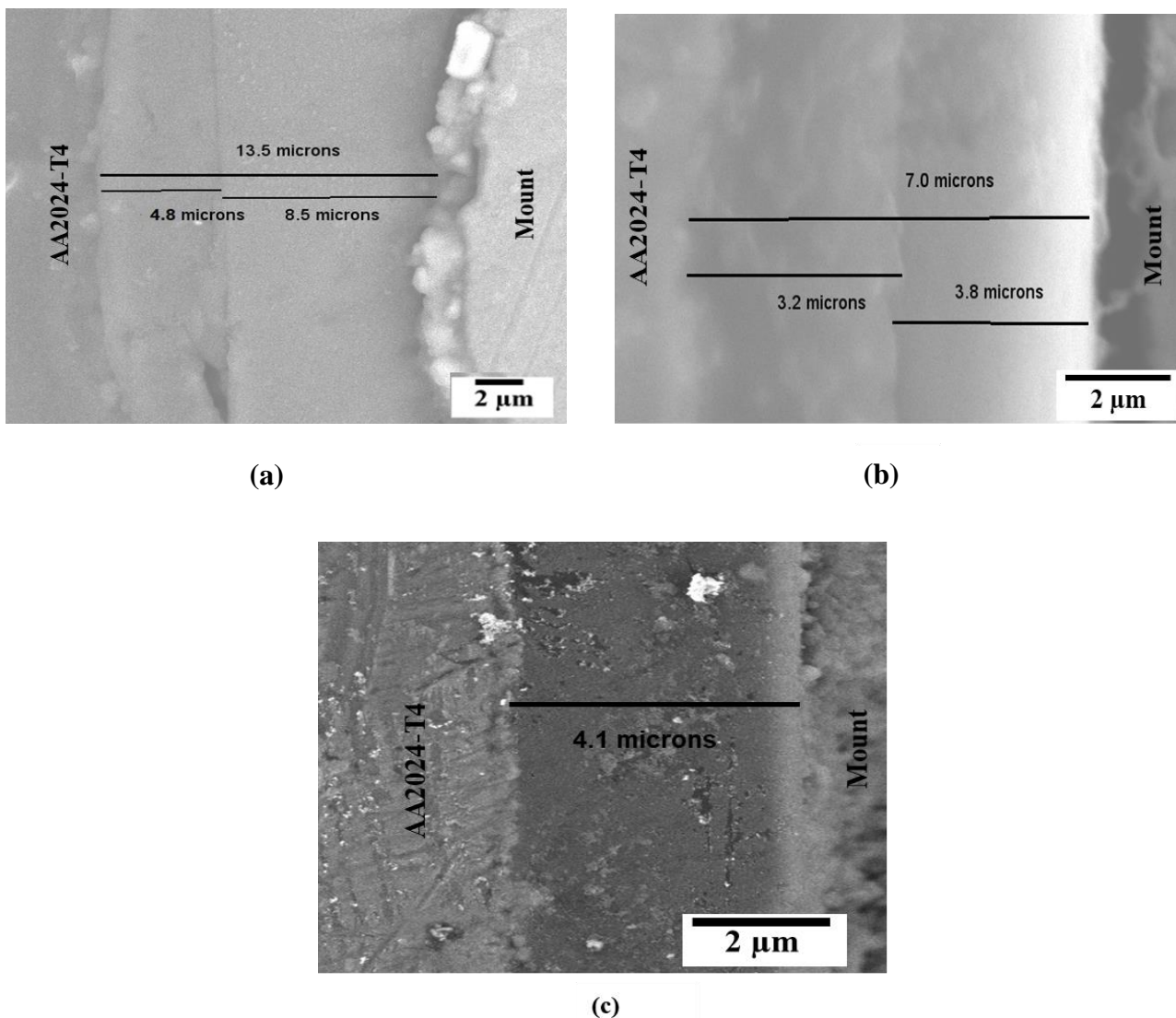


Fig. 5.3. FESEM cross-sectional images of (a) H|M, (b) M|H and (c) M+H coatings.

5.3.4 Electrochemical Impedance Spectroscopy (EIS) and potentiodynamic polarization studies

EIS and potentiodynamic polarization studies were carried out for uncoated AA2024-T4, bilayer H|M and M|H coated substrates and composite M+H coated substrates after 1, 72, 120 h and were further extended to 168 and 216 h of exposure to 3.5 wt % NaCl solution for M|H and M+H coated substrates. The EIS and polarization results of these coatings were compared with those of single layer H and M coated AA2024-T4 substrates studied in previous chapters 3 and 4.

The equivalent electrical circuit used for fitting the EIS data of bilayer coatings is given in Fig. 5.4 (a) and for composite and single layer coatings is given in Fig. 5.4 (b).

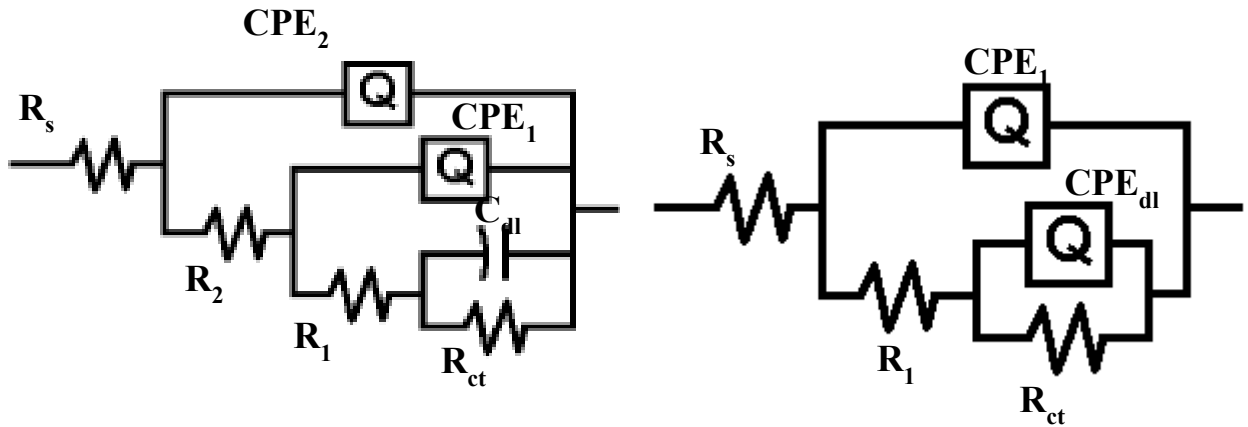


Fig. 5.4. Equivalent electric circuits used for fitting EIS data of (a) bilayer coatings and (b) composite and single layer M and H coatings.

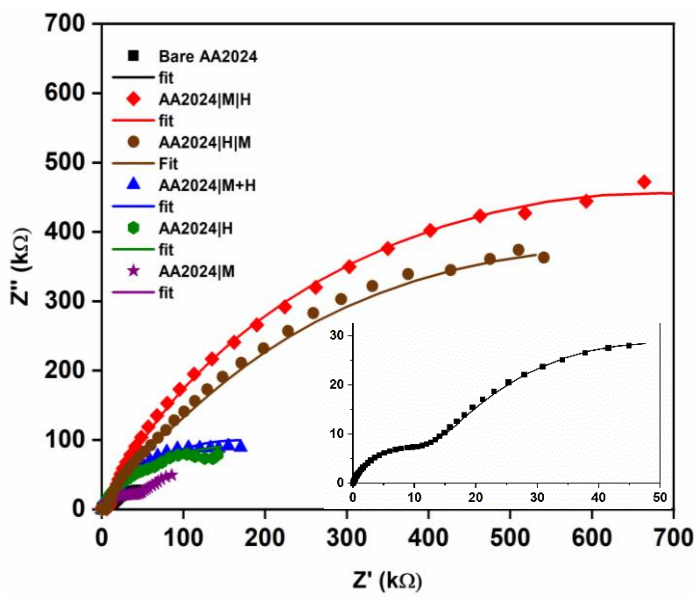
Nyquist plots for bilayer and composite coatings are shown in Fig. 5.5 and the EIS fit data is presented in Table 5.2. M|H coated substrates exhibited highest R_{ct} among all the coated and uncoated substrates at all durations of exposure. In contrast, H|M coated substrates have shown lower R_{ct} values than that of M|H and M+H coated substrates at all durations of exposure. The impedance values of all the coated and uncoated substrates decreased as the function of time till 120 h. In addition, the coating resistances, R_2 and R_1 were also found to decrease from 1 h to 120 h. In overall, R_{ct} of M|H was the highest till 120 h for all the coated substrates and also M|H coating exhibited improved coating resistances (R_2 and R_1) than H|M. From the above observations, M|H configuration was found to have better corrosion protection than H|M coatings. Therefore, the electrochemical tests were carried out further for only M|H coatings till 216 h of exposure.

The composite M+H coatings exhibited better corrosion resistance than H|M coatings, however M|H coating exhibited better corrosion resistance among all. It can be observed from the Table 5.2 and Fig. 5.6 that the M+H coating exhibited lower R_{ct} value than H and M coatings. Further, the coating resistance (R_1) of M+H coating was lower than the H and M coatings. These observations clearly indicate that there was no improvement in the corrosion protection after making the composite coating compared to single component H and M coatings.

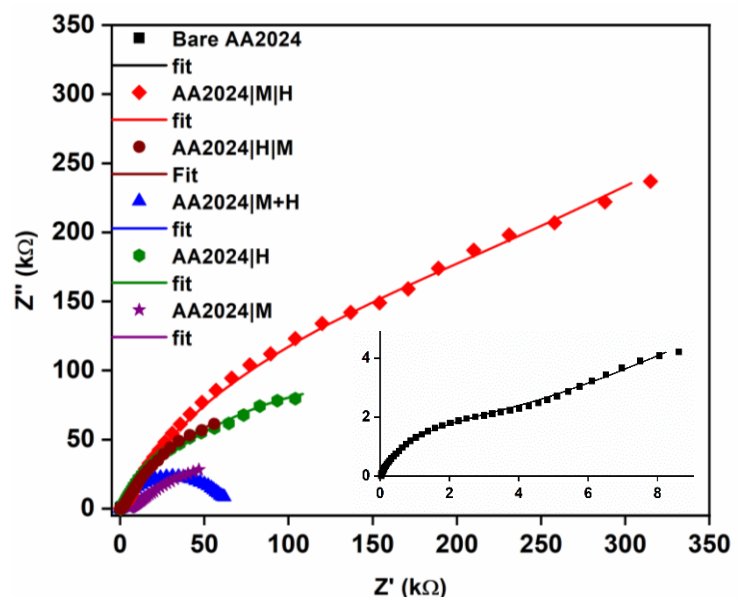
The R_{ct} of M|H coated substrates decreased from $1370 \text{ k}\Omega\text{.cm}^2$ (1 h of exposure) to $446.0 \text{ k}\Omega\text{.cm}^2$ (72 h of exposure) and then drastically to $87.5 \text{ k}\Omega\text{.cm}^2$ during 120 h exposure, and then it got increased rapidly to $500 \text{ k}\Omega\text{.cm}^2$ as the time duration prolonged to 168 h and remained nearly same after 216 h also. The observed drastic decrease in R_{ct} after 120 h

exposure and then increase in R_{ct} on prolonged exposure to 168 and 216 h implies that there would be an initiation of corrosion due to the penetration of Cl^- ions which in turn triggered the self-healing action to increase the charge-transfer resistant at the interface. The coating resistances, R_2 and R_1 also decreased after 120 h (due to the penetration of electrolyte) and further increased after 168 h and were the highest even after 216 h. The single layer H exhibited higher R_{ct} than all except M|H, but it decreased after the prolonged duration of exposure for 216 h, as observed in Fig. 5.6. Single layer M showed better coating resistance (R_1) than that of H. From above observations, it is clearly indicating that M|H coated substrates exhibited enhanced corrosion protection because of inner M having better coating resistance and outer H layer exhibiting good R_{ct} .

The potentiodynamic polarization curves after different times of exposure shown in Fig. 5.7 and the polarization fit data given in Table 5.3 have followed the same trend as that of EIS data that the least i_{corr} values were measured for bilayer M|H coating at all durations of exposure. In addition, it also has been observed that this M|H coating exhibited more positive corrosion potential values (E_{corr}) compared to all the coated electrodes at all durations of exposure, indicating that there is an ennoblement of corrosion potentials with M|H coating. Moreover, the anodic tafel slope became more passive for M|H coated substrates till 168 h and it showed slightly active region after 216 h. In contrary, the i_{corr} values for H|M coated substrates have got increased with the increase in the duration of exposure to corrosive medium till 120 h. M+H coated substrates have also exhibited higher i_{corr} values than the single layered coatings.



(a)



(b)

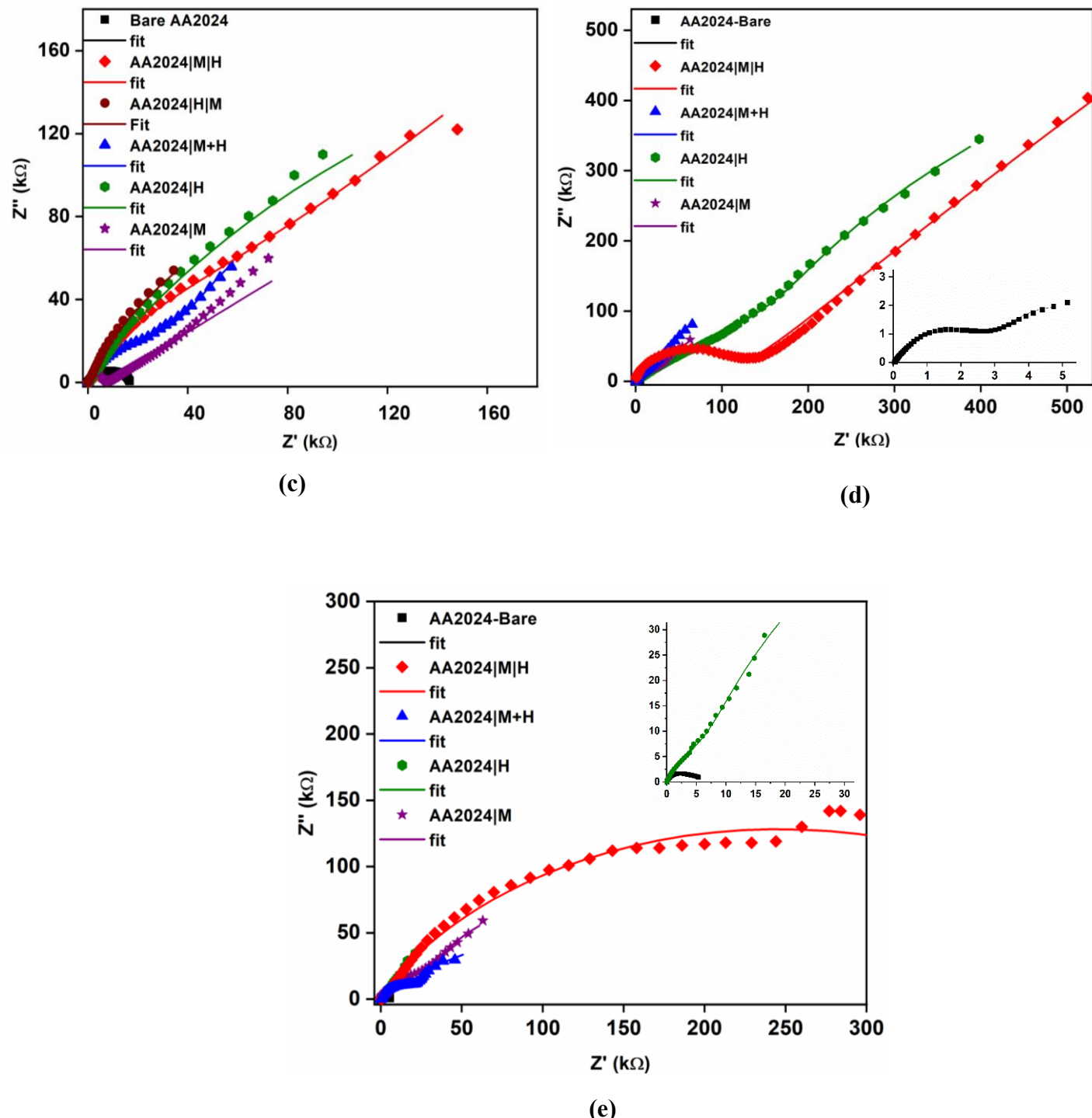


Fig. 5.5. Nyquist plots for coated and uncoated AA2024-T4 substrates at different durations of exposures to 3.5 wt % NaCl.

Table 5.2. EIS data of coated and uncoated AA2024-T4 obtained after fitting with equivalent electrical circuit.

Duration of exposure to 3.5 wt% NaCl	Sample	R_2 k Ω .cm 2	R_1 k Ω .cm 2	R_{ct} k Ω .cm 2	C_2 μ F/cm 2	C_1 μ F/cm 2	C_{dl} μ F/cm 2	CHI square error
1 h	Bare	-	6.04	36.7	-	12.6	40.9	1.37×10^{-3}
	AA2024 M H	5.93	7.58	1370	0.0029	0.57	0.63	1.09×10^{-3}
	AA2024 H M	1.72	0.10	148	0.14	0.97	11.10	0.65×10^{-3}
	AA2024 M+H	-	0.10	337.0	-	0.0093	13.1	1.87×10^{-3}
	AA2024 H	-	1.64	340	-	0.470	0.110	6.92×10^{-3}
	AA2024 M	-	68.0	102.0	-	11.03	0.199	2.78×10^{-3}
72 h	Bare	-	5.34	17.9	-	49.6	932.0	3.64×10^{-3}
	AA2024 M H	0.31	6.38	446.0	42.0	1.21	4.28	0.42×10^{-3}
	AA2024 H M	0.28	1.53	33.8	0.024	1.19	9.99	0.35×10^{-3}
	AA2024 M+H	-	0.009	66.4	-	0.00034	13.9	0.26×10^{-3}
	AA2024 H	-	5.75	234.0	-	1.03	1.15	1.57×10^{-3}
	AA2024 M	-	110.0	104.0	-	127.0	63.6	4.58×10^{-3}
120 h	Bare	-	1.36	15.8	-	6.34	3.80	0.44×10^{-3}
	AA2024 M H	0.23	1.86	87.5	0.0072	1.09	11.9	0.36×10^{-3}
	AA2024 H M	0.21	0.29	13.7	0.21	1.64	0.80	1.50×10^{-3}
	AA2024 M+H	-	5.44	30.40	-	33.7	265.0	1.07×10^{-3}
	AA2024 H	-	2.25	65.5	-	0.72	0.45	4.59×10^{-3}
	AA2024 M	-	5.87	34.8	-	8.02×10^{-5}	10.60	1.45×10^{-3}
168 h	Bare	-	3.72	3.35	-	11.7	410.0	0.49×10^{-3}
	AA2024 M H	3.73	5.52	500.0	1.5×10^{-4}	5.87×10^{-8}	0.02	4.73×10^{-3}
	AA2024 M+H	-	36.0	152.0	-	28.2	817.0	0.32×10^{-3}
	AA2024 H	-	7.83	441.0	-	331.0	6.23	1.43×10^{-3}
	AA2024 M	-	53.5	143.0	-	36.6	182.0	2.29×10^{-3}
216 h	Bare	-	5.34	17.9	-	49.6	932.0	3.64×10^{-3}

	AA2024 M H	1.68	14.5	498.0	0.04	0.23	0.34	1.89×10^{-3}
	AA2024 M+H	-	2.88	73.0	-	15.70	267.0	0.27×10^{-3}
	AA2024 H	-	2.28	48.0	-	162.0	2.22	1.59×10^{-3}
	AA2024 M	-	0.079	79.0	-	1.52	7.93	1.23×10^{-3}

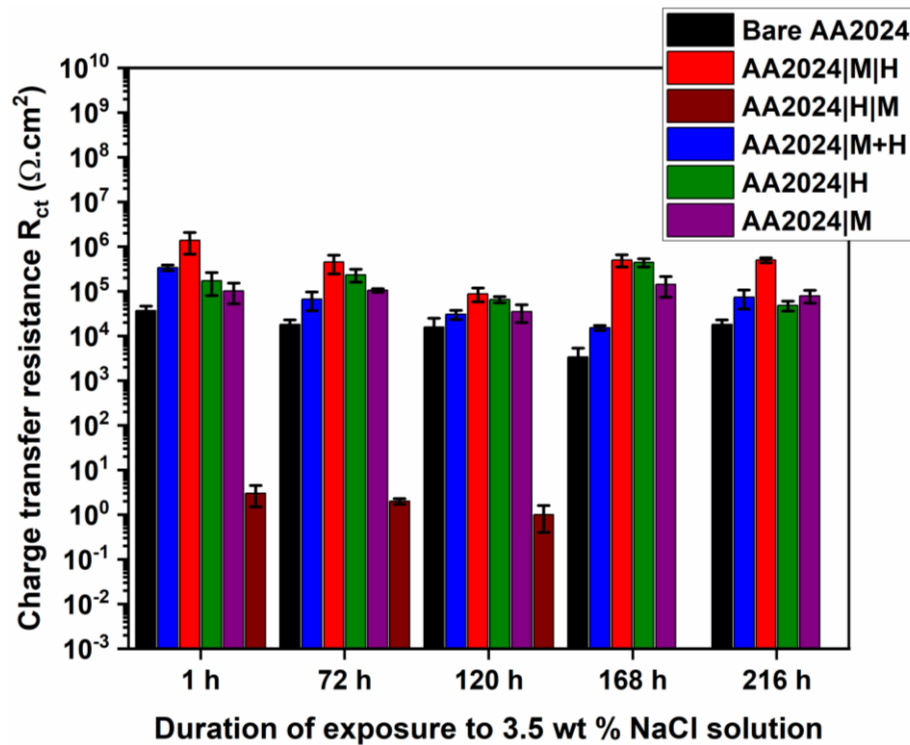
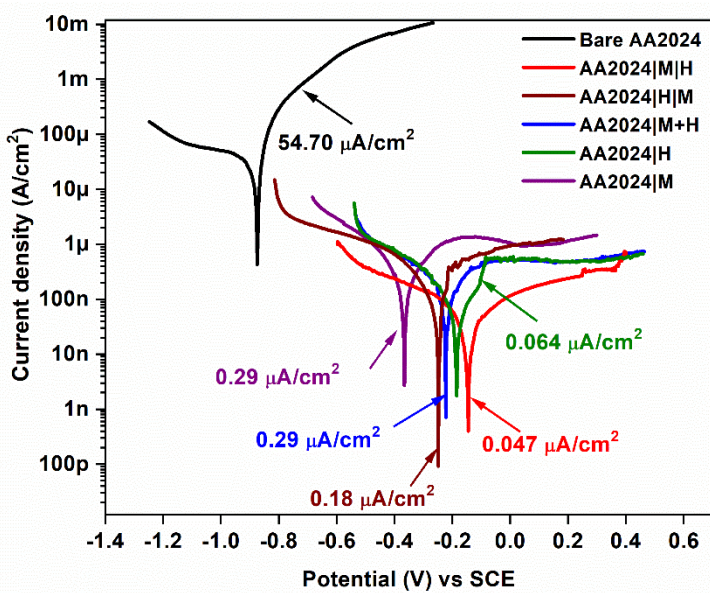
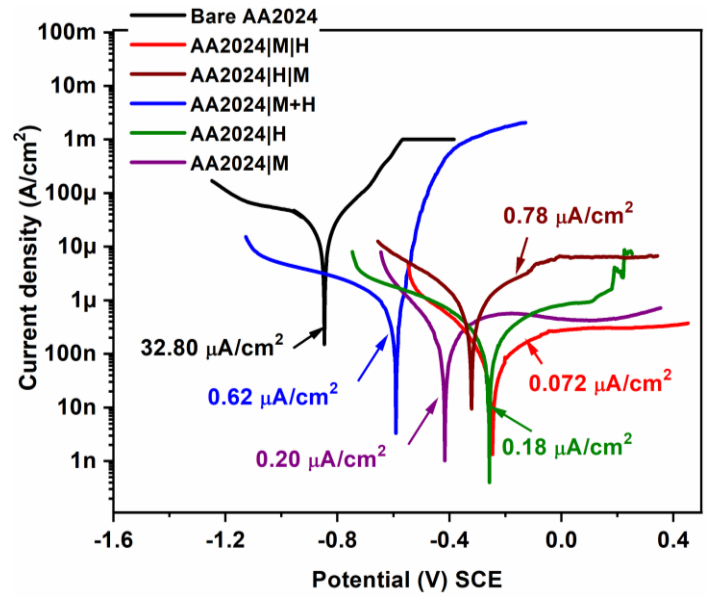


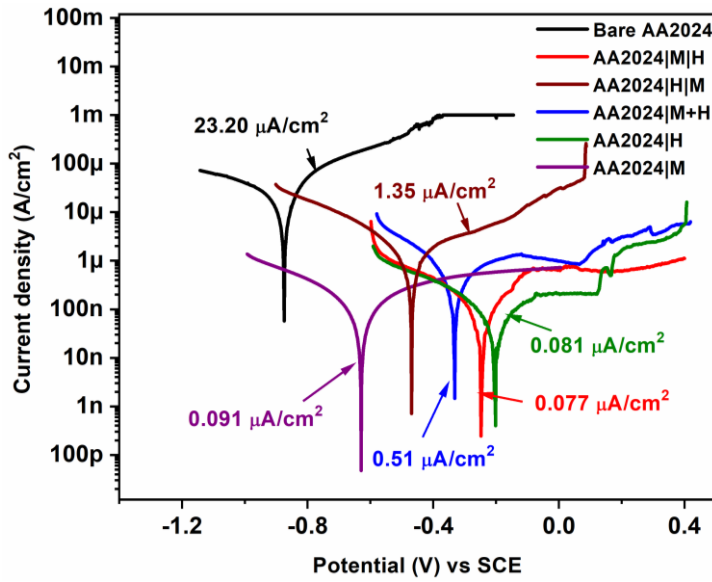
Fig. 5.6. Comparison of R_{ct} at different durations of exposure to corrosive medium.



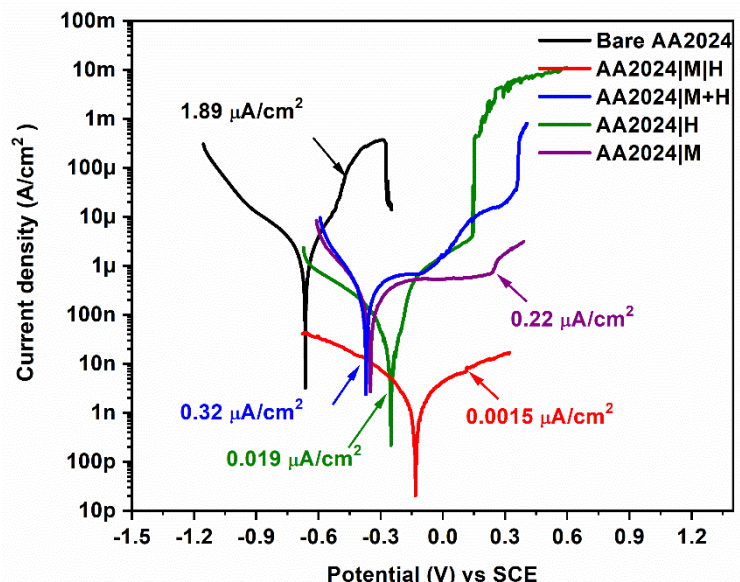
(a)



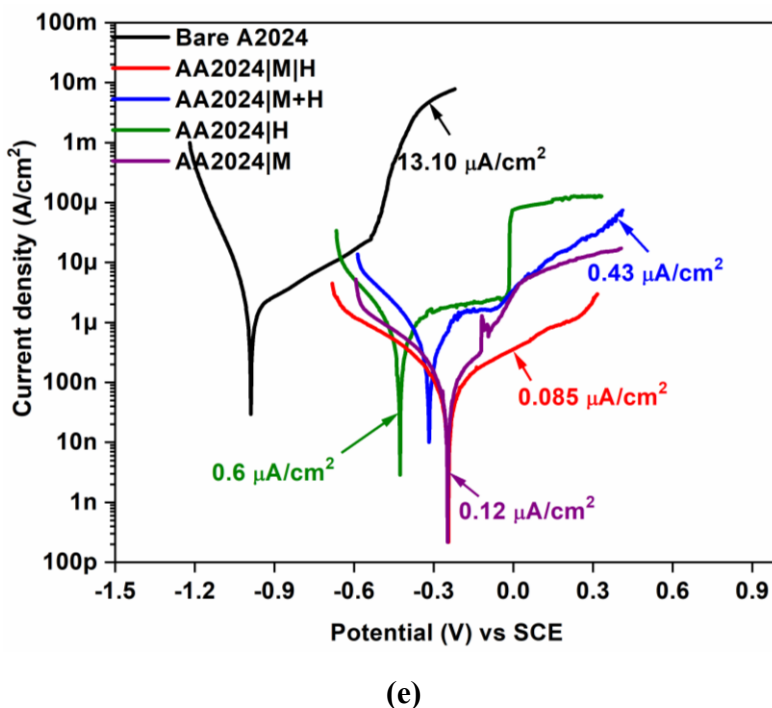
(b)



(c)



(d)



(e)

Fig. 5.7. Polarization curves of AA2024 substrates after (a) 1 h, (b) 72 h, (c) 120 h, (d) 168 h and (e) 216 h of exposure to 3.5 wt % NaCl solution.

Table 5.3. Potentiodynamic polarization data for coated and uncoated AA2024-T4 substrates at different durations of exposure to corrosion medium.

Sample	Time of immersion in 3.5 wt % NaCl	E_{corr} (V) vs SCE	i_{corr} ($\mu\text{A}/\text{cm}^2$)
Bare	1 h	-0.869	54.7
AA2024 M H		-0.145	0.05
AA2024 H M		-0.248	0.19
AA2024 M+H		-0.222	0.29
AA2024 H		-0.185	0.060
AA2024 M		-0.366	0.29
Bare	72 h	-0.847	32.80
AA2024 M H		-0.246	0.07
AA2024 H M		-0.321	0.78
AA2024 M+H		-0.581	0.62

AA2024 H		-0.257	0.18
AA2024 M		-0.417	0.20
Bare	120 h	-0.875	23.2
AA2024 M H		-0.248	0.08
AA2024 H M		-0.469	0.13
AA2024 M+H		-0.332	0.51
AA2024 H		-0.202	0.08
AA2024 M		-0.630	0.09
Bare		-0.664	1.89
AA2024 M H	168 h	-0.133	0.0015
AA2024 M+H		-0.372	0.32
AA2024 H		-0.251	0.019
AA2024 M		-0.350	0.22
Bare		-0.746	13.10
AA2024 M H	216 h	-0.245	0.08
AA2024 M+H		-0.318	0.43
AA2024 H		-0.427	0.60
AA2024 M		-0.248	0.12

The corrosion protection performance of the single layer coatings developed from halloysite and montmorillonite nanocontainers without any loaded corrosion inhibitors was also investigated to find out the reason for enhanced corrosion protection of M|H over H|M coating, though both are of bilayer configuration. Coatings developed from unloaded HNT and unloaded MMT nanocontainers are labelled as HNC and MNC, respectively. The i_{corr} obtained from potentiodynamic polarization studies of HNC and MNC coatings are compared and depicted in Fig. 5.8. The HNC coated substrates exhibited higher i_{corr} than MNC at initial exposure (1 h), but as the exposure duration increased to 72 and 120 h, MNC coated substrates exhibited lower i_{corr} values than HNC. Similarly, the R_{coat} values of MNC coated substrates were found to be higher than those of HNC at the long exposure durations of 72 and 120 h as seen from Table 5.4. This indicated that, MMT nanocontainers when present as adjacent layer to substrate provided good corrosion protection rather than HNT as adjacent coating to the substrate. The variation in the behavior of coatings based on two unloaded nanocontainers could be attributed to the orientation of these nanoparticles in the matrix sol as reported by

Huttunen et al [11]. They have dispersed HNT and MMT independently in an epoxy matrix and studied the corrosion protection of coatings deposited from these nanocomposite formulations on cold rolled steel substrates and on aluminum foil. According to their findings, halloysite nanoparticles get oriented randomly in the epoxy matrix and resulted in the increased water permeability. However, montmorillonite nanoparticles when dispersed in the epoxy matrix and deposited, oriented themselves parallel to the coating surface, thus exhibiting less water permeability and hence, providing good coating and corrosion resistance. The schematic representation of HNC and MNC coatings and comparison of their coating resistance is depicted in Fig. 5.9.

Therefore, based on the above observations, the improved corrosion protection of M|H coatings over H|M can be explained because of the synergistic behavior of inner M layer which had a good coating resistance and outer H layer having higher R_{ct} . These two nanocontainers exhibited enhanced release of the corrosion inhibitors and provided prolonged corrosion protection to the substrate, due to the combined effect of both the nanocontainers, which release inhibitors from each layer only on demand (on the onset of damage to the coating).

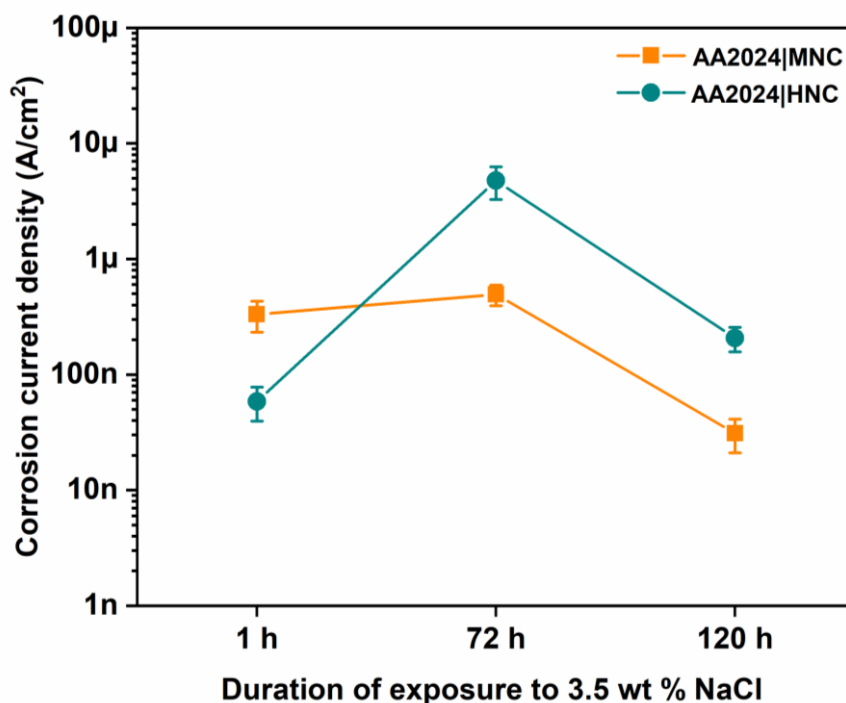


Fig. 5.8. Variation of corrosion current density of HNC and MNC coated AA2024-T4 substrates at different exposure durations

Table 5.4. Coating resistance values of HNC and MNC coated substrates obtained from EIS data.

Sample	Duration of exposure to 3.5 wt % NaCl	R_{coat} (k Ω .cm 2)
AA2024 HNC	1 h	276.0
AA2024 MNC		8.54
AA2024 HNC	72 h	0.52
AA2024 MNC		15.6
AA2024 HNC	120 h	34.3
AA2024 MNC		620.0

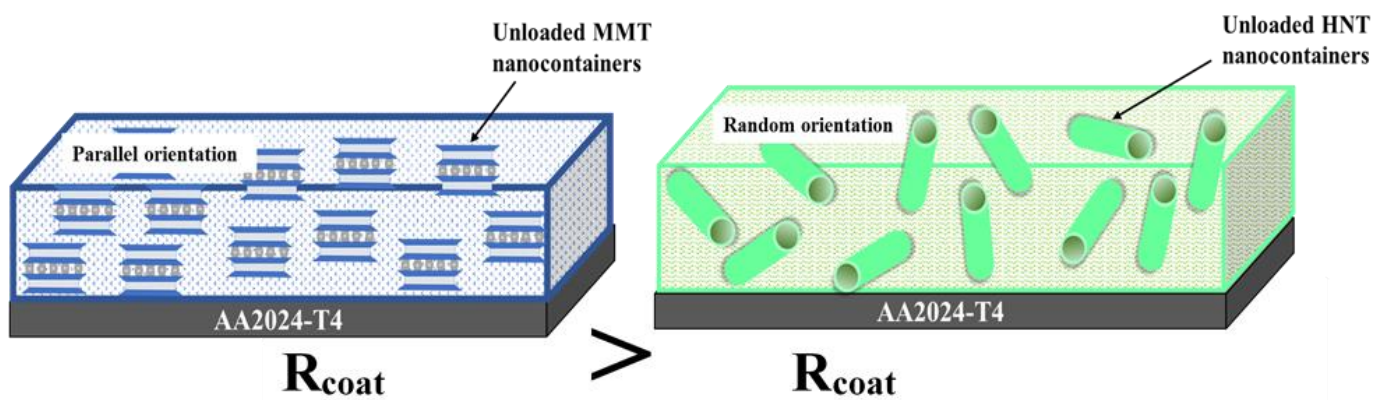


Fig. 5.9. Schematic representation of HNC and MNC coated AA2024-T4 substrates at different exposure durations.

5.3.5 Weight loss studies

Weight loss studies were carried out for bilayer and composite coatings along with bare AA2024-T4 substrates for 120 h by immersing in 3.5 wt % NaCl solution as per ASTM G31 standard operating procedure [12,13]. M|H coated substrates have shown least corrosion rate as shown in Fig. 5.10. On the other hand, H|M and M+H coated substrates exhibited high corrosion rates.

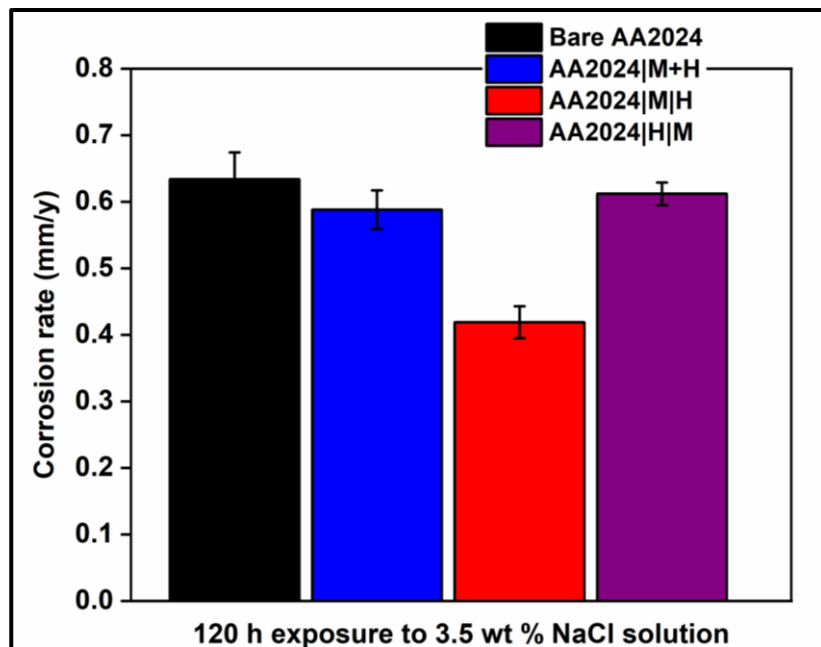


Fig. 5.10. Comparison of corrosion rates of AA2024-T4 substrates.

5.3.6 Salt spray test (SST)

SST was carried out by exposing the substrates to 5 wt % NaCl solution for 168 h as per ASTM B117 standards [14]. Photographs taken before and after SST are shown in Fig. 5.11 and Fig 5.12. H|M and M+H coated substrates have got corroded completely and appeared similar to bare substrate after SST, as shown in Fig 5.12. However, M|H substrate was better even after 168 h of SST with only a small number of pits in it. This clearly indicates that M|H coated substrates have better corrosion protection than H|M and M+H substrates.

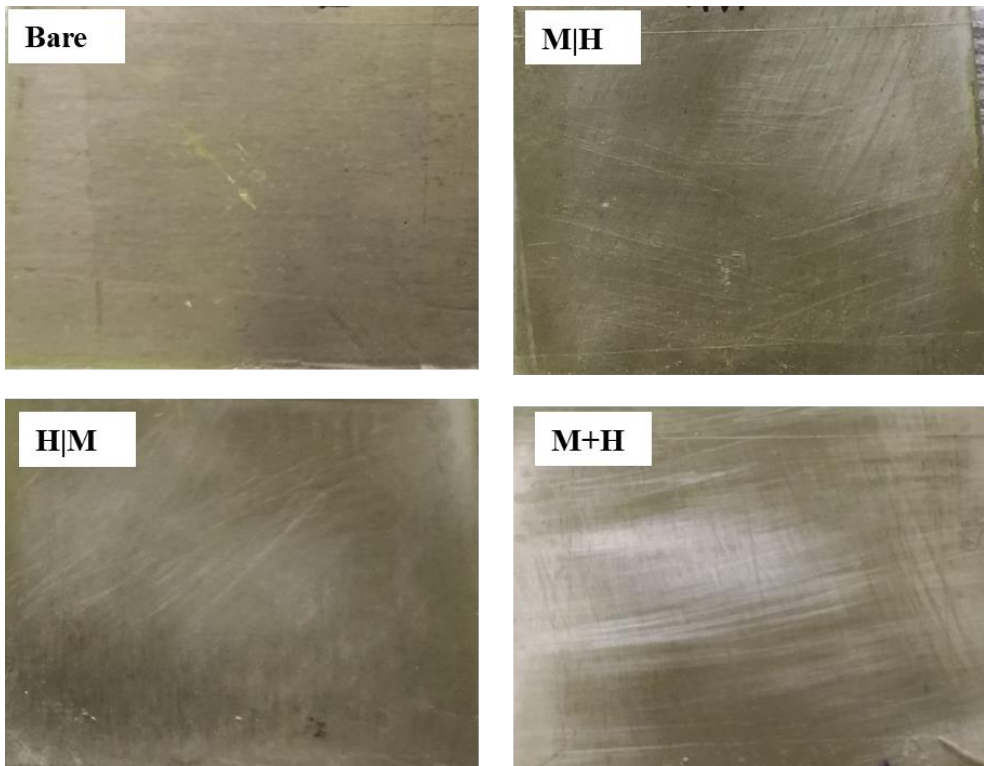


Fig. 5.11. Photographs of AA2024-T4 substrates before SST.

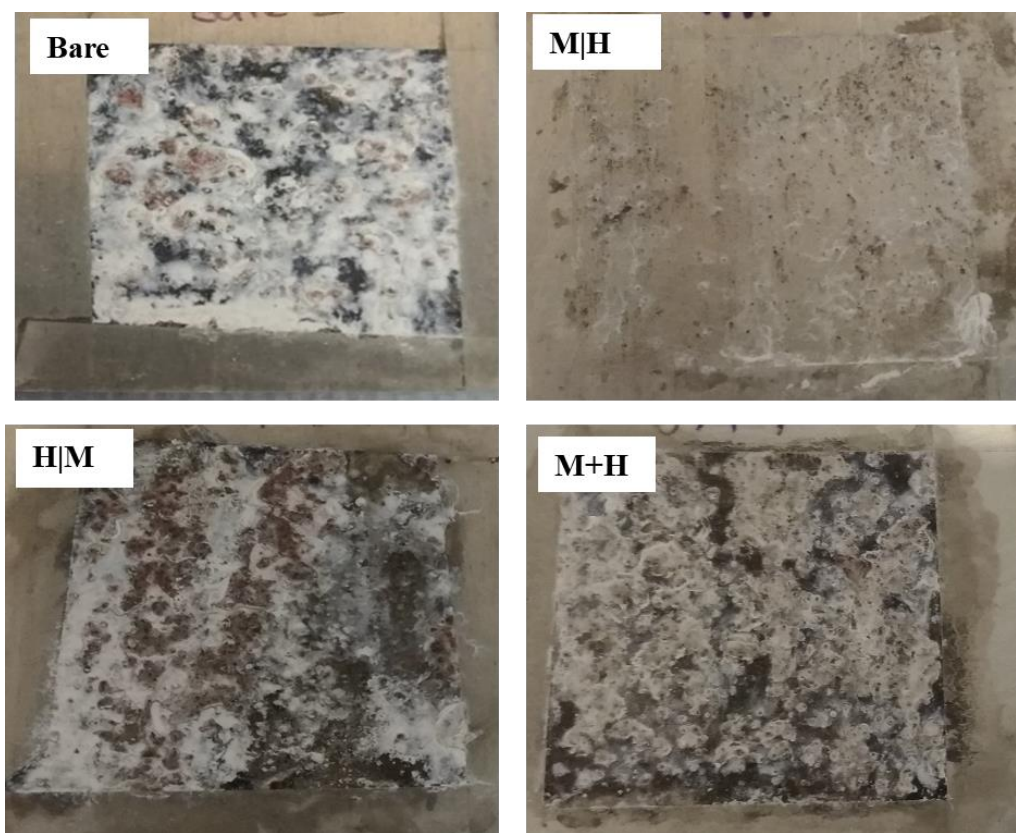
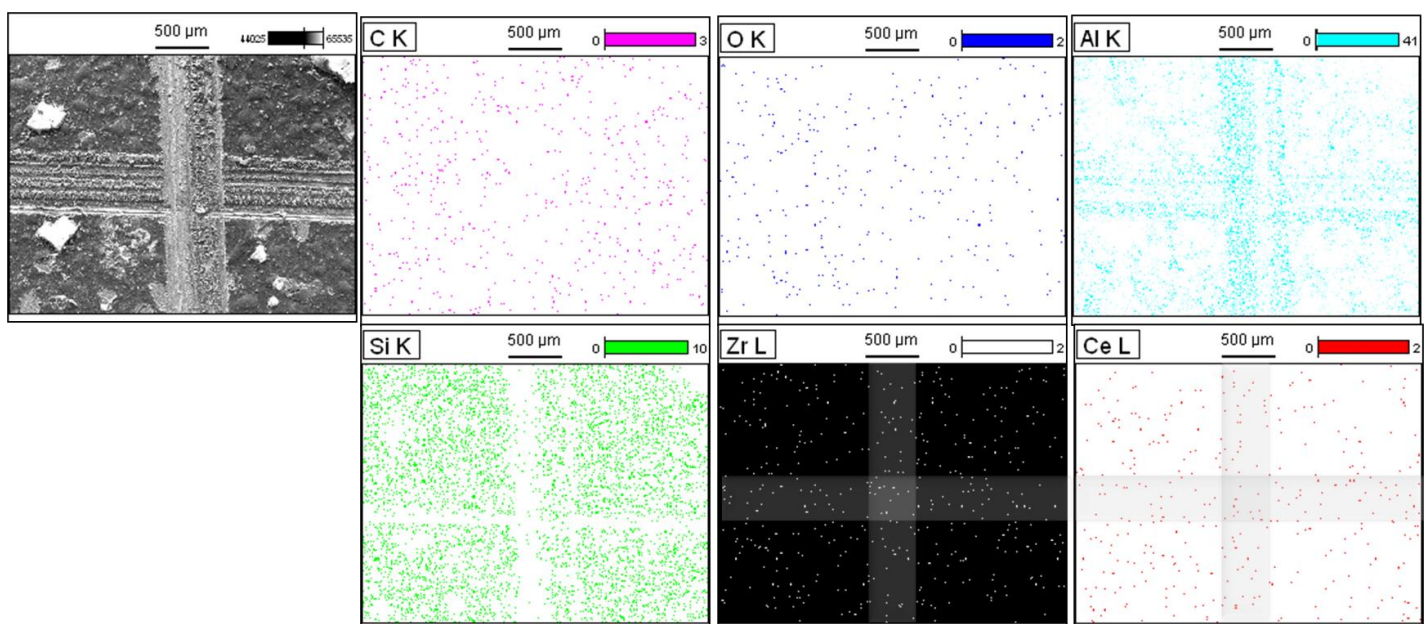


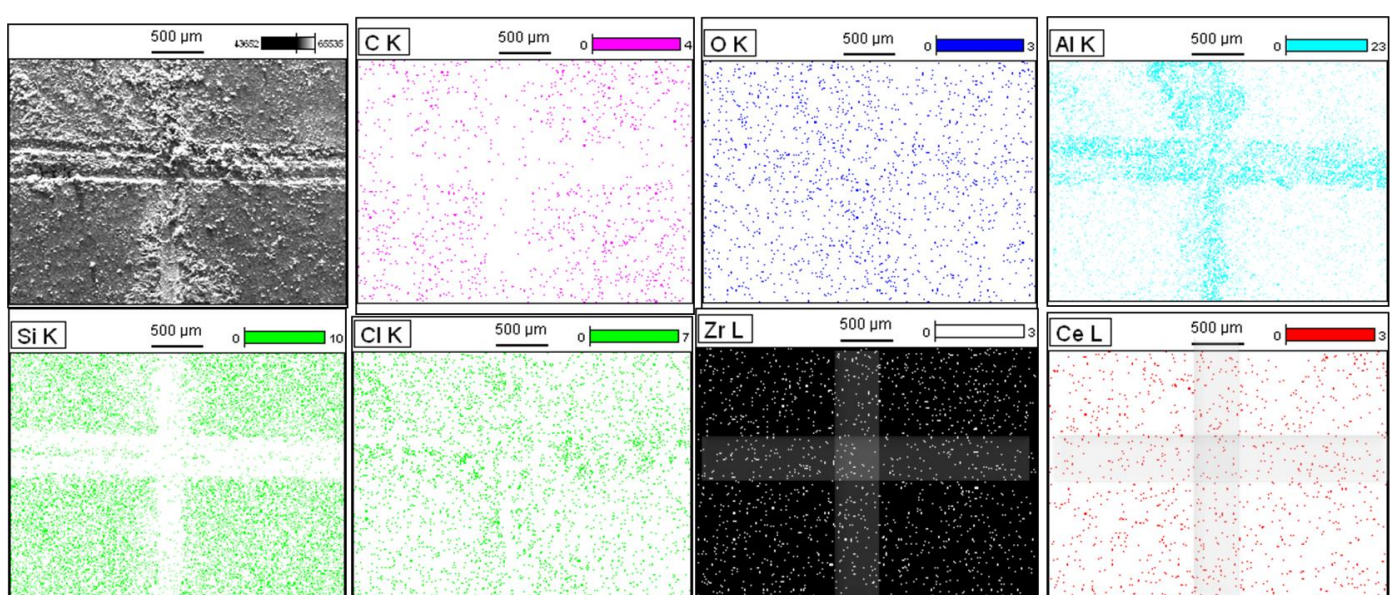
Fig. 5.12. Photographs of AA2024-T4 substrates after SST in 5 wt % NaCl solution for 168 h.

5.3.7 Salt immersion test (SIT)

Salt immersion test (SIT) was carried out for M|H coated substrates by making 'X' shaped artificial scribe on the substrates and exposing them to 3.5 wt % NaCl solution for 120 h. The elemental mapping by EDS analysis was carried out on the scribed area before and after the SIT and the results are shown in Fig. 5.13. The elemental mapping of M|H coated substrate has shown an increase in the amounts of Ce and Zr in the scribed area after SIT (Fig. 5.13b). Thus, this test confirms that inhibitors have got released into the scratch region to self-heal the damage by forming passive layers of CeO_2 and ZrO_2 .



(a)



(b)

Fig. 5.13. Elemental mapping of M|H coatings (a) before and (b) after salt immersion test.

Hence, based on observations from above all studies, the schematic representation of release of corrosion inhibitors from nanocontainers and self-healing of damage by formation of passive layer in case of bilayer M|H coated substrate is depicted in Fig.5.14 (a) and nanocontainers loaded with Ce^{3+} and Zr^{4+} is given in Fig. 5.14 (b).

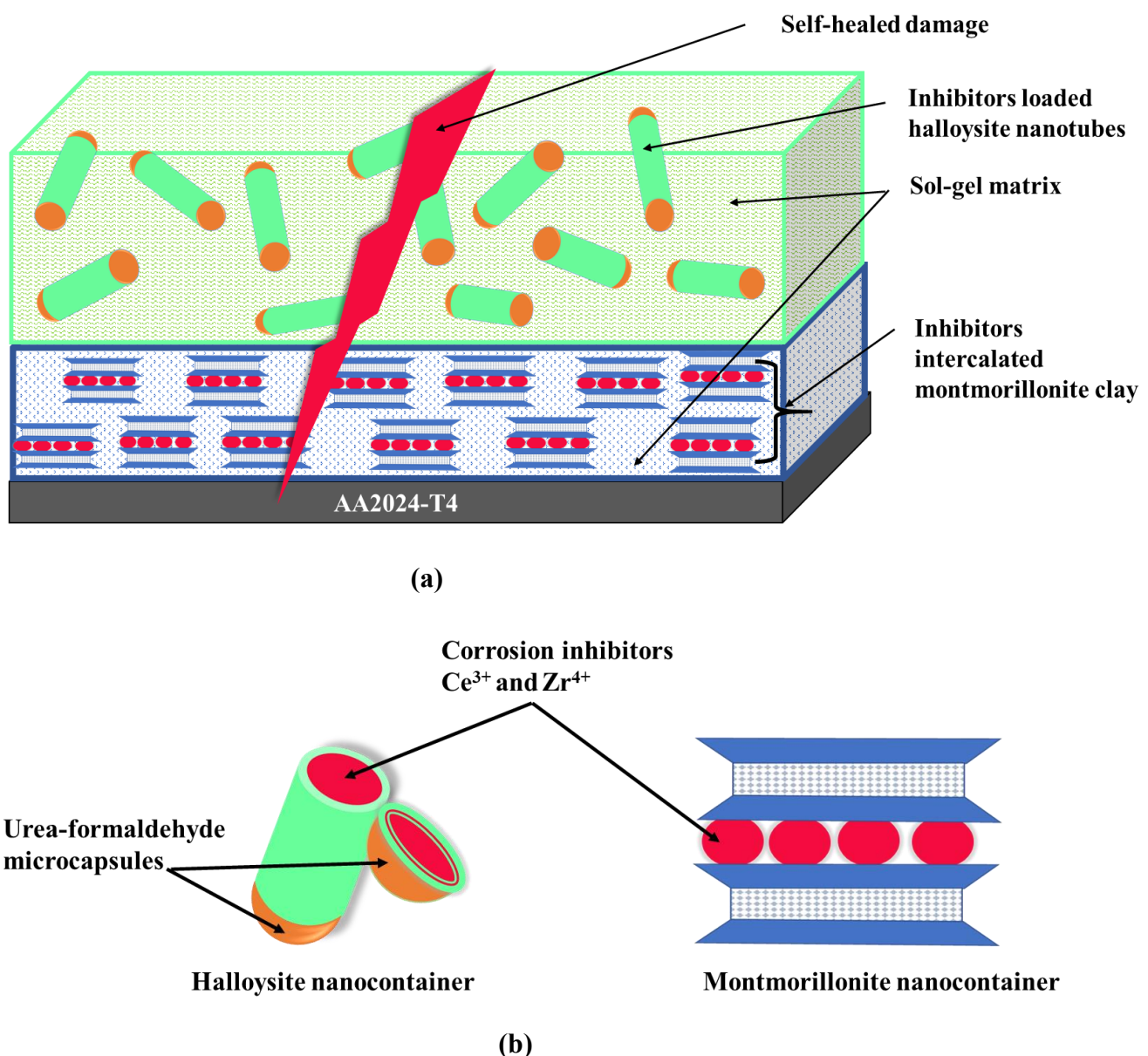


Fig. 5.14. (a) Proposed mechanism of self-healing in M|H coated AA2024-T4 substrate and (b) Halloysite and montmorillonite nanocontainers loaded with corrosion inhibitors.

References

- [1] E. Darmiani, G.R. Rashed, D. Zaarei, I. Danaee, Synergistic Effects of Montmorillonite/Cerium Nitrate Additives on the Corrosion Performance of Epoxy-Clay Nanocomposite Coatings, *Polymer - Plastics Technology and Engineering*. 52 (2013) 980–990. doi:10.1080/03602559.2013.763373.
- [2] D.J. Carbonell, A. García-Casas, J. Izquierdo, R.M. Souto, J.C. Galván, A. Jiménez-Morales, Scanning electrochemical microscopy characterization of sol-gel coatings applied on AA2024-T3 substrate for corrosion protection, *Corrosion Science*. 111 (2016) 625–636. doi:10.1016/j.corsci.2016.06.002.
- [3] D. Snihirova, S. V Lamaka, P. Taheri, J.M.C. Mol, M.F. Montemor, Comparison of the synergistic effects of inhibitor mixtures tailored for enhanced corrosion protection of bare and coated AA2024-T3, *Surface & Coatings Technology*. 303 (2016) 342–351. doi:10.1016/j.surfcoat.2015.10.075.
- [4] M.F. Montemor, D. V. Snihirova, M.G. Taryba, S. V. Lamaka, I.A. Kartsonakis, A.C. Balaskas, G.C. Kordas, J. Tedim, A. Kuznetsova, M.L. Zheludkevich, M.G.S. Ferreira, Evaluation of self-healing ability in protective coatings modified with combinations of layered double hydroxides and cerium molibdate nanocontainers filled with corrosion inhibitors, *Electrochimica Acta*. 60 (2012) 31–40. doi:10.1016/j.electacta.2011.10.078.
- [5] M. Izadi, T. Shahrabi, B. Ramezan-zadeh, Electrochemical investigations of the corrosion resistance of a hybrid sol–gel film containing green corrosion inhibitor-encapsulated nanocontainers, *Journal of the Taiwan Institute of Chemical Engineers*. 81 (2017) 356–372. doi:10.1016/j.jtice.2017.10.039.
- [6] C. Chen, Y. He, G. Xiao, F. Zhong, H. Li, Y. Wu, J. Chen, Synergistic effect of graphene oxide@phosphate- intercalated hydrotalcite for improved anti-corrosion and self-healable protection of waterborne epoxy coating in salt environments, *Journal of Materials Chemistry C*. 7 (2019) 2318–2326. doi:10.1039/c8tc06487c.
- [7] M. Serdechnova, S. Kallip, M.G.S. Ferreira, M.L. Zheludkevich, Active self-healing coating for galvanically coupled multi-material assemblies, *Electrochemistry Communications*. 41 (2014) 51–54. doi:10.1016/j.elecom.2014.01.023.
- [8] M.A. Zadeh, J. Tedim, M. Zheludkevich, S. Van Der Zwaag, S.J. Garcia, Synergistic active corrosion protection of AA2024-T3 by 2D- anionic and 3D- cationic nanocontainers loaded with Ce and mercaptobenzothiazole, *Corrosion Science*. 135

(2018) 35–45. doi:10.1016/j.corsci.2018.02.018.

[9] Y. Hao, Y. Zhao, X. Yang, B. Hu, S. Ye, L. Song, R. Li, Self-healing epoxy coating loaded with phytic acid doped polyaniline nanofibers impregnated with benzotriazole for Q235 carbon steel, *Corrosion Science.* 151 (2019) 175–189. doi:10.1016/j.corsci.2019.02.023.

[10] ASTM D3359-17 Standard Test Methods for Rating Adhesion by Tape Test, (2009) 1–9. doi:10.1520/D3359-17.

[11] E. Huttunen-Saarivirta, G. V Vaganov, V.E. Yudin, J. Vuorinen, Characterization and corrosion protection properties of epoxy powder coatings containing nanoclays, *Progress in Organic Coatings.* 76 (2013) 757–767. doi:10.1016/j.porgcoat.2013.01.005.

[12] ASTM G31-12 Standard Guide for Laboratory Immersion Corrosion Testing of Metals 1, (2012). doi:10.1520/G0031-12A.

[13] ASTM G1-90 Standard Practice for Preparing, Cleaning and Evaluation Corrosion Test Specimens, (1999).

[14] ASTM B117-16 Standard Practice for Operating Salt Spray (Fog) Apparatus, (2016). doi:10.1520/B0117-16.2.

CHAPTER-6

Effect of Etching of Halloysite Nanotubes on Loading and Corrosion Protection of AA2024-T4

CHAPTER-6

Effect of Etching of Halloysite Nanotubes on Loading and Corrosion Protection of AA2024-T4

The present investigation was aimed at modification of halloysite nanotubes by selectively etching the inner lumen and studying the effect of etching on lumen diameter, pore volume, surface area and the morphology of nanotubes. In addition, corrosion behavior of etched HNTs when loaded with cationic corrosion inhibitors and dispersed in sol-gel matrix for the protection of AA2024-T4 alloy was also studied. Here, two different concentrations of sulphuric acid (H_2SO_4) was used for etching HNTs. The degree of etching of HNTs was analyzed by FT-IR spectroscopy. The morphology and lumen diameter of the etched nanotubes were observed through TEM. Pore volume and surface area of etched and etched loaded HNTs were determined by BET analysis. XRD analysis was carried out to check the presence of etchant residues in the interlayers of HNTs, if any. Electrochemical experiments such as electrochemical impedance spectroscopy and potentiodynamic polarization studies were carried to study the effect of etching on corrosion protection behavior of AA2024-T4.

6.1 Literature Survey

Halloysite nanoclay is a hydrated mineral that occurs in nature and is biocompatible. It has a tubular morphology with lumen, containing rolled sheets of aluminosilicates. The inner lumen of halloysite nanotubes (HNTs) is positively charged because of alumina layers and the outer surface is negatively charged due to the presence of silicate layers. Various active agents such as corrosion inhibitors, enzymes, drugs, antimicrobial agents, flame retardants, catalysts and magnetic compounds can be loaded into the lumen of halloysite clay nanotubes and can be adsorbed on its surface due to its high surface area and pore volume [1,2]. Enlargement of lumen of HNT leads to enhanced capacity of loading, which in turn is expected to result in the prolonged release of active agents. Various chemical agents such as acids and alkali are used for etching the inner lumen and outer surface of HNTs. A systematic literature survey has been carried out on etching of HNTs as mentioned below.

Wang et al [3] have carried out alkaline etching using Na_2CO_3 and NaNO_3 to roughen the outer surface of HNTs for depositing Pt nanocatalysts over roughened HNTs surface (Pt@RHNT). The catalytic performance of Pt@RHNTs was evaluated by selective hydrogenation of cinnamaldehyde to cinnamyl alcohol and were compared with that of Pt deposited on unetched HNTs (Pt@HNTs). The conversion and selectivity of catalytic hydrogenation for Pt@RHNTs were 93.02% and 83.39%, respectively, whereas for Pt@HNTs, they were 49.03% and 68.78% within 5 min, respectively. Moreover, complete hydrogenation had taken place within 30 min using Pt@RHNTs. The improved catalytic performance of Pt@RHNTs was found to be because of enhanced surface area and hence more amount of Pt particles loaded on the active sites of RHNTs surface. Li et al [4] have used mesoporous halloysite nanorods supported Co^{2+} as catalyst for solvent-free selective oxidation of cyclohexane to allylic products. In this study, HCl was used as etchant for selective etching of inner alumina layer for 18 h, such that the complete removal inner alumina layer has occurred and resulted in the formation of mesoporous nanorods with the loss of tubular structure. FT-IR results showed that, the peak corresponding for aluminol Al_2OH bending at 912 cm^{-1} disappeared after 18 h and Si-O stretching vibration at 1032 cm^{-1} of halloysite nanotubes completely disappeared. The peak at 1092 cm^{-1} corresponding to Si-O-Si deformations has increased in intensity. These mesoporous etched HNTs were used as the support for Co^{2+} catalyst for the solvent free oxidation. The highest cyclohexane conversion was reported at optimal catalyst to etched HNTs ratio of 2:1. Alkaline etching of HNTs using NaOH for adsorption and release of ofloxacin drug was studied by Wang et al [5]. FT-IR results showed that etching with alkali removed some of inner Al-OH and outer Si-OH groups from halloysite. They reported that the ofloxacin loaded HNTs showed effective and prolonged release of the drug in simulated gastric fluid, because the drug got adsorbed on the surface via electrostatic interactions and also loaded inside the lumen by complex formation with inner amorphous Al^{3+} .

Garcia-Garcia et al [6] have used different acids such as sulphuric, acetic and acrylic acid to study the effect of these acids on the selective surface etching of HNTs. They have reported that the sulphuric acid etching was aggressive, and the BET surface area and lumen diameter have increased from $52.9\text{ m}^2/\text{g}$ to $132.4\text{ m}^2/\text{g}$ and $13.8 \pm 1.4\text{ nm}$ to $31.6 \pm 6.7\text{ nm}$, respectively. For acetic acid and acrylic acid etched HNTs, the lumen diameter increased to 18.4 ± 2.9 and $17.1 \pm 2.1\text{ nm}$, respectively. TEM results showed that sulphuric acid etching resulted in highly porous and partially decomposed structures. Zhang et al [7] have carried out systematic investigation on the effect of sulphuric acid on physico-chemical and pore

characteristics of HNTs for adsorption of methylene blue. They have studied the effect of 3 M sulphuric acid treatment on halloysite lumen etching for 21 h. BET analysis has shown that the surface area and pore volume increased till 13 h and decreased thereafter, which was found to be due to disaggregation of silica layers. TEM analysis showed that, after acid treatment, the obtained HNTs were in the form of porous nanorods of amorphous silica. Abdullayev et al [8] have studied the kinetics of selective lumen etching of HNTs using 0.5 M, 1 M and 2 M sulphuric acid concentrations at different temperatures from 18-90° C for 3 days. The optimum concentration of acid and temperature of etching was found to be 1 M and 50-80° C, respectively. They reported that selective and uniform dissolution of inner alumina layers occurred below 70° C using 1 M H₂SO₄ as etchant. The etched HNTs were checked for increased lumen diameter at regular intervals for different % of dealumination. HNTs lumen diameter increased from 10.0 ± 1.0 nm to 21.5 ± 2.0 nm after removal of 20% aluminum and to 36.3 nm upon 65% dealumination. Kinetics study revealed that chemical interaction is the rate-determining step with the activation energy of 68.0 kJ/mol and pseudo-zeroth order below 70° C. After 30-40 % dealumination, the HNTs found to have porous silica particles and transform to nanorods and holes were formed above 60% etching. The loading capacity of benzotriazole (BTA) was studied at different % of etching. The maximum loading of BTA was found to be at 40-50 % etching, after which efficiency got decreased. Moeinpour et al [9] have carried out selective etching of HNT lumen using 2 M H₂SO₄ and calcined HNT to increase loading capacity of losartan, a high blood pressure controlling drug. The BET surface area and pore volume of HNT increased by etching from 25.288 to 42.209 m²/g and 0.0742 to 0.0976 cm³/g, respectively. It has been found that loading of drug increased for etched HNT and decreased for calcined HNT. They have reported that the presence of water molecules inside the lumen plays a key role in loading of active materials. Dodecyl amine encapsulated HNTs for the corrosion protection of carbon steel AISI 1020 CS plates have been studied by Falcón et al [10]. The HNTs were etched previously with sulphuric acid before loading to increase the loading efficiency and were embedded in alkyd paint after loading. They observed that loaded HNTs have shown higher corrosion resistance as compared to that of paint without loaded HNTs. Duce et al [11] have carried out thorough and detailed modern kinetic study on the thermal behaviour and lumen enlargement of etched halloysite using scanning electron microscopy (SEM), scanning transmission electron microscopy (STEM) and thermogravimetry (TG) techniques. The HNTs were etched using 2 M H₂SO₄ at 50° C for 48 h and compared with pristine halloysite (unetched) for their lumen diameter and mass loss. The lumen diameter increased from 15-20 nm to 30-40 nm after

etching and the walls of the etched halloysite nanotubes preserved their rod like structure, but appeared as more porous than pristine halloysite and contained some broken points. Kinetic studies revealed that dehydration and dihydroxylation of inner alumina sheets and enlargement of lumen by acid etching of halloysite are complex multi-step processes, which were much more similar to kaolinite. They have reported that the structural changes in halloysite are responsible for change in their thermal behaviour. White et al [12] studied the stability of HNTs in various acid and alkaline environments at different concentrations. They found that HNTs are stable in water, weak or dilute organic and inorganic acids as well as alkaline solutions at room temperature. However, in concentrated solutions using strong acids (H_2SO_4), the dissolution occurs leading to the formation of SiO_2 nanoparticles inside the tubes. In strong base $NaOH$ solution, it resulted in the formation of flake like particles having layers of $Al(OH)_3$.

From the above reported literature, it was found that the selective etching can be carried out using a specific acid or alkali. Most of literature were reported on inner aluminol etching to increase lumen diameter and H_2SO_4 was reported to be an effective etchant for the lumen. Hence, the present investigation was carried out by using H_2SO_4 as etchant for selective etching of HNTs inner lumen. Here, we have used two different concentrations of sulphuric acid i.e., 1 M and 2 M to study the effect of concentration of H_2SO_4 on etching of HNTs.

6.2 Experimental

6.2.1 Etching of HNTs and loading of etched HNTs with corrosion inhibitors

As-received HNTs were etched by using 1 M and 2 M H_2SO_4 solutions for selective etching of inner alumina lumen. For this, 1 g of as-received HNT powder was added to 500 ml of 1 M/2 M sulphuric acid solution and stirred for 3 days by maintaining the temperature at 60°C. Centrifugation was carried out after etching process by repeated washing with DI water until the pH became 7 and the powder was further dried. The HNTs etched with 1 M and 2 M H_2SO_4 were labeled as EH-1M and EH-2M, respectively. After etching, these EH-1M and EH-2M were loaded with cationic corrosion inhibitors and stoppered at the ends with urea-formaldehyde microcapsules to prevent the leakage of corrosion inhibitors, using the same procedure as described in sections 2.2.1 and 2.2.2 of chapter-2, which will be abbreviated as ELSH-1M and ELSH-2M henceforth.

6.2.2 Preparation of sols based on modified HNTs and coating deposition

Etched HNTs and etched loaded and stoppered HNTs were dispersed in an organic-inorganic hybrid sol-gel matrix to prepare their respective sols. All the sols contained 2 wt % of modified (etched or etched loaded and stoppered) HNTs. Procedure for synthesis of matrix sol and dispersion of HNTs in matrix sol are mentioned in sections 2.1 and 2.2.2. Prepared sols were deposited on 2.5 cm × 2.5 cm × 0.3 cm size AA2024-T4 substrates by dip coating technique at 1 mm/s withdrawal speed. All the coatings were cured at 130° C for 1 h for densification of coatings.

6.2.3 Characterization of etched HNTs and etched loaded and stoppered HNTs

HNTs while etching with 1 M and 2 M H₂SO₄ were characterized by FT-IR technique by collecting the etched HNTs at regular intervals of 0, 8, 24, 32, 48, 56 and 72 h. They were analyzed to find out the extent of etching with respect to time and concentration of acid. XRD and BET surface area and pore volume analyses were carried out for EH-1M and -2M as well as for ELSH-1M and -2M to find out the change in the crystallinity of the nanotube, surface area and pore volume after etching and loading with corrosion inhibitors. TEM analysis was performed to determine the lumen diameter and morphology of nanotubes.

The coatings developed from EH-1M and -2M and ELSH-1M and -2M on AA2024-T4 substrates were tested for their corrosion protection behavior by carrying out the electrochemical experiments such as electrochemical impedance spectroscopy and potentiodynamic polarization studies.

6.3 Results and Discussion

6.3.1 FT-IR analysis

Figure 6.1 represents the FT-IR spectra of HNT powders etched with 1 M and 2 M H₂SO₄ for various time durations. The peaks at 3695 and 3617 cm⁻¹ correspond to the inner OH stretching vibrations of aluminol groups of halloysite [13]. For etched HNT with 1 M acid (EH-1M), these peak intensities got slightly decreased after 72 h, indicating partial removal of inner aluminol layer. In case of EH-2M, the peak intensities at 3695 and 3617 cm⁻¹ started decreasing just after 8 h itself, and they were very little after 48 h and disappeared after 72 h. This observation indicated the complete removal of alumina layer. A broad peak from 3742-3152 cm⁻¹ corresponds to SiO-H vibrations [14]. The broad peak appeared for EH-

2M, indicating the formation of silica nanoparticles. The intensity of the peak at 1100 cm^{-1} , corresponding to in-plane Si-O-Si deformations, was seen to increase upon increasing the duration of etching for EH-2M. However, EH-1M has shown no increase in the intensity of this peak.

The peak at 754 cm^{-1} , corresponding to the Si-O-Al perpendicular stretching, was retained for EH-1M at all etching levels, whereas it disappeared for EH-2M, indicating complete dissolution of aluminol with 2 M H_2SO_4 etching. FT-IR peak at 795 cm^{-1} , corresponding to symmetric Si-O-Si stretching [8], slightly shifted to 802 cm^{-1} upon increasing the duration for EH-2M. Therefore, from the FT-IR analysis of all samples, it could be inferred that etching with 1 M H_2SO_4 led to a partial removal of alumina layer in HNT, whereas etching with 2 M H_2SO_4 resulted in complete removal of inner alumina layer.

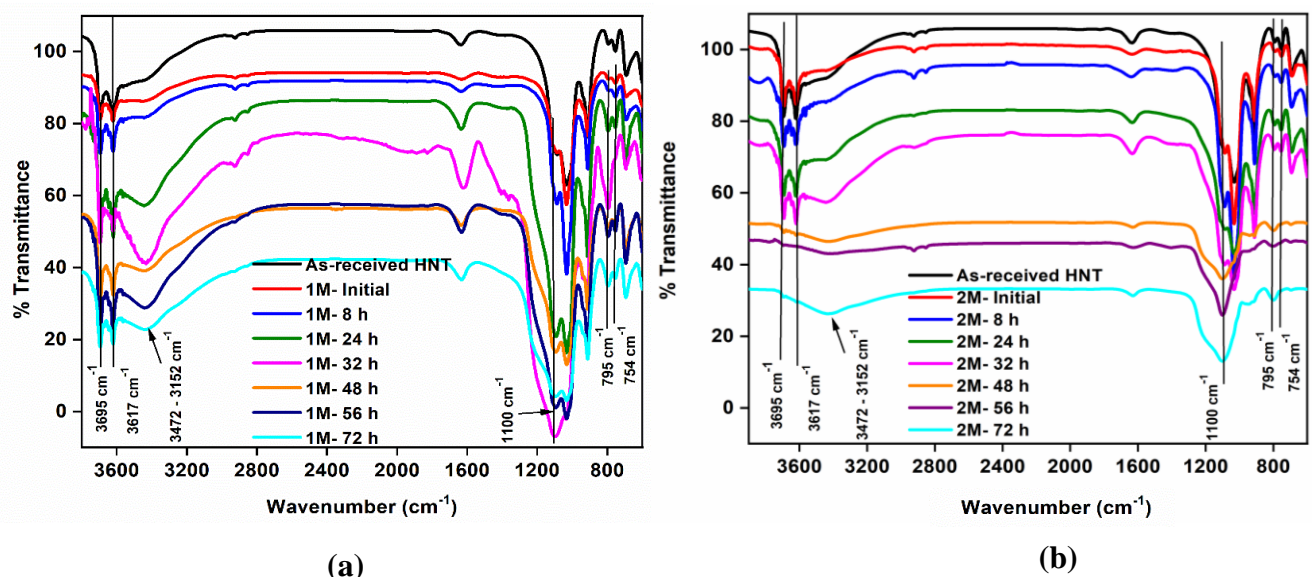


Fig. 6.1. FT-IR spectra of (a) EH-1M and (b) EH-2M powders at different time intervals.

6.3.2 XRD analysis

XRD spectra of as-received HNT (ARH), and EH and ELSH-1M and -2M nanoclays etched for 72 h are depicted in Fig 6.2. The d_{001} peak at 7.3 \AA corresponds to the multilayer wall packing, and d_{002} at 4.5 \AA corresponds to the tubular nature of HNT [8,15–17]. It was observed from Fig. 6.2 (a) that, after etching for EH-1M and EH-2M, there was no shift in the peak positions of d_{001} plane, indicating no intercalation of etchant (sulphuric acid) remnants in the interlayers of HNT. This also indicated that a layer-by-layer etching has taken place, starting from innermost alumina layer to outer silicate layers but not simultaneously from outside and inside which could result in an intercalation of sulphate ions between the

interlayers. In a similar way, loaded HNTs after etching, i.e., ELSH-1M and ELSH-2M, showed the peak positions of d_{001} at the same 2θ value as that of ARH as seen from Fig. 6.2 (b), indicating that there was no intercalation of corrosion inhibitors in the interlayers of the HNT but got loaded into the lumen. The intensities of the above mentioned two peaks for EH-2M have decreased, indicating the partial loss of crystalline nature of tubes because of etching.

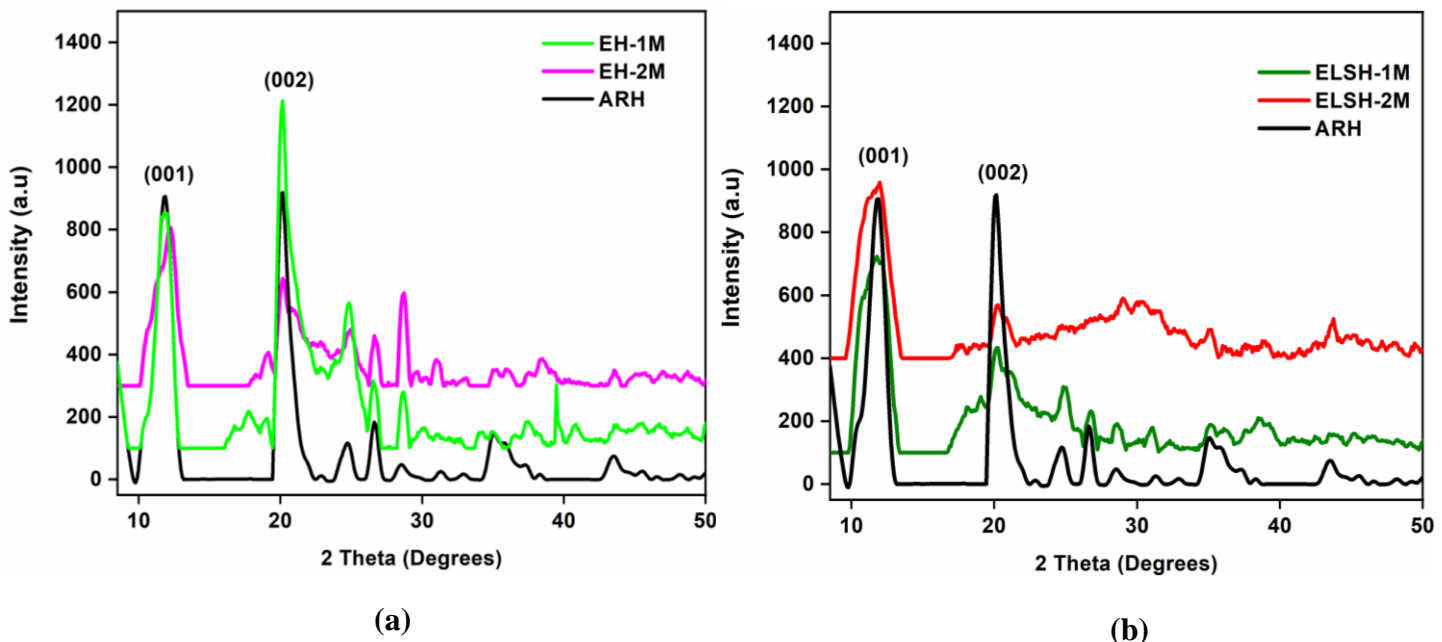


Fig. 6.2. X-ray diffraction patterns of (a) EH-1M, EH-2M and (b) ELSH -1M, ELSH-2M in comparison with ARH.

6.3.3 BET analysis

The surface area and pore volume of etched and etched loaded and stoppered HNTs were determined by BET analysis. BET surface area and pore volume data are given Table 6.1, and the variation in pore volumes of ARH, EH (1M, 2M) and ELSH (1M, 2M) is shown in Fig. 6.3. It was observed that the surface area and pore volume increased for EH-1M and EH-2M. The % increase in surface area and pore volume of EH-1M are 71.5 % and 42.9 %; and for EH-2M, the values are 69.04 % and 42.86 %, respectively. This indicated that there is no much difference in the surface area and pore volume by increasing the concentration of sulphuric acid from 1 M to 2 M. However, after loading and stoppering, the surface area and pore volume values have got decreased. The % decrease in the surface area and pore volume for ELSH-1M are 12.8 % and 9.96 %, and for ELSH-2M, are 23.86 % and 12.28 %,

respectively. The decrease in the surface area and pore volume values for ELSH-2M are more than that for ELSH-1M.

Table 6.1 BET surface area and pore volume data of as-received, etched and etched loaded and stoppered HNTs

Sample	BET surface area (m ² /g)	Pore volume (cm ³ /g)
ARH	50.62	0.235
EH-1M	175.46	0.412
ELSH-1M	152.98	0.371
EH-2M	163.52	0.4115
ELSH-2M	124.49	0.360

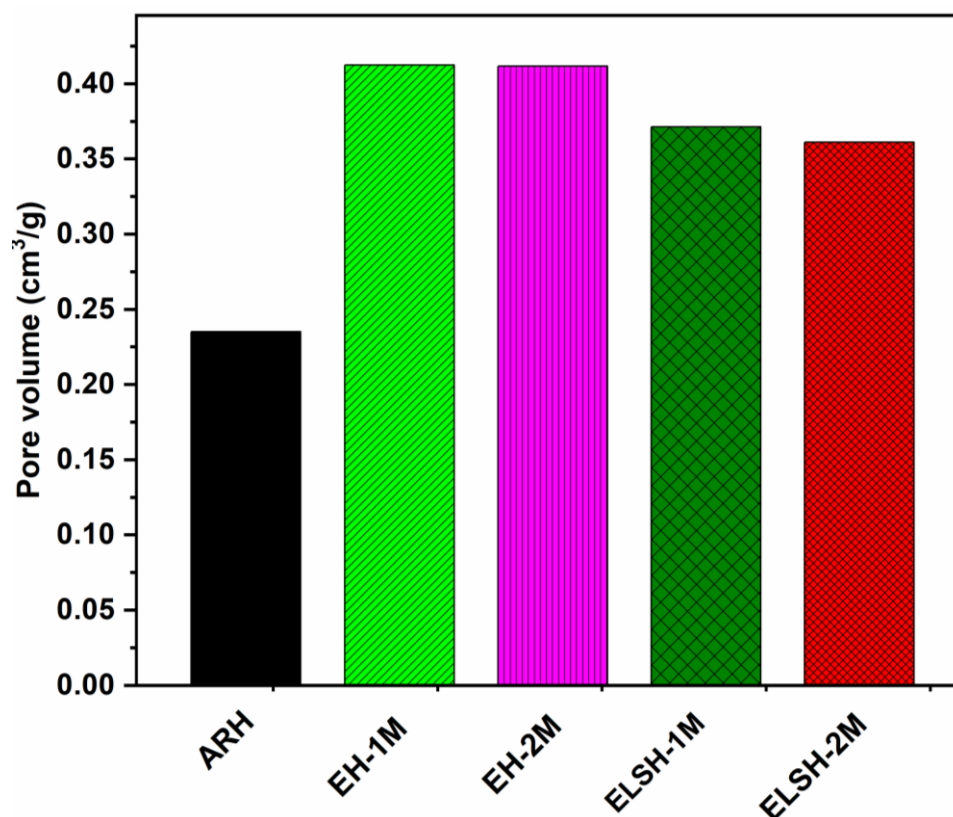
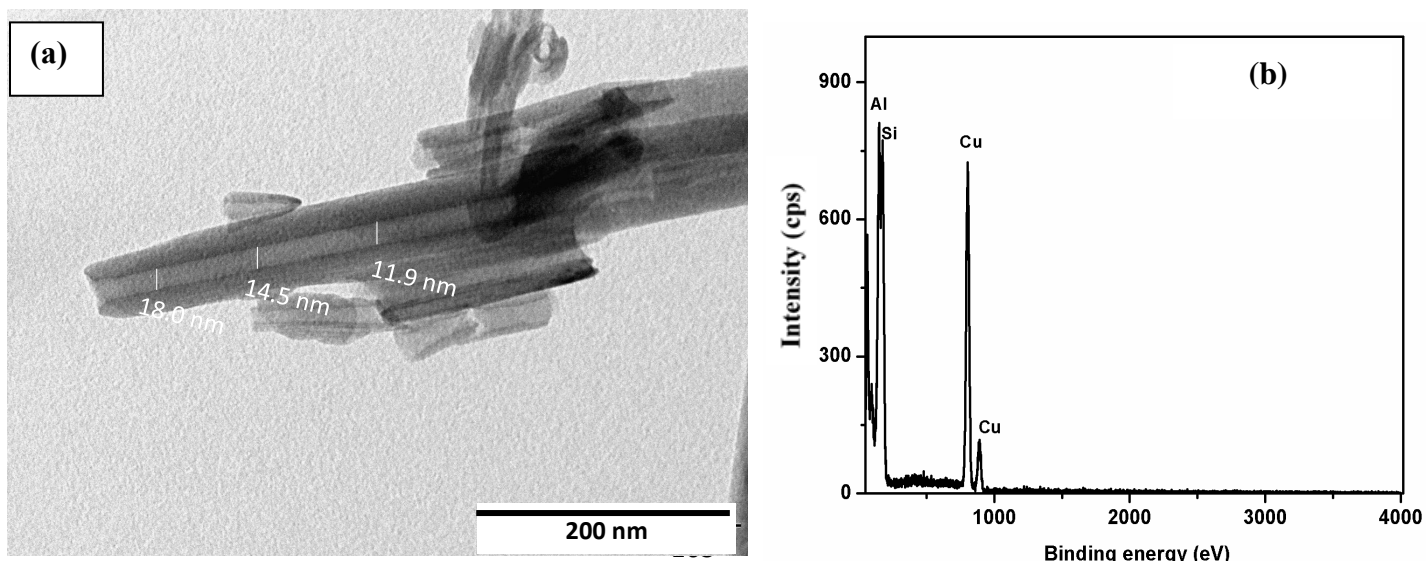
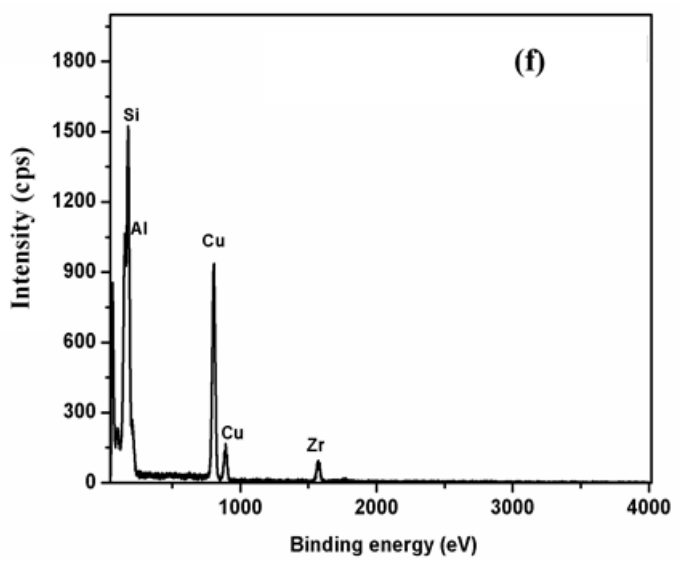
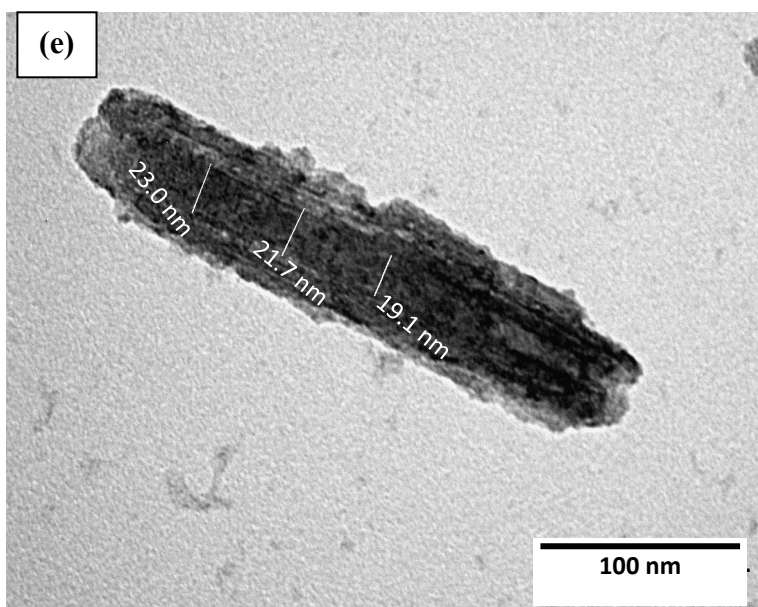
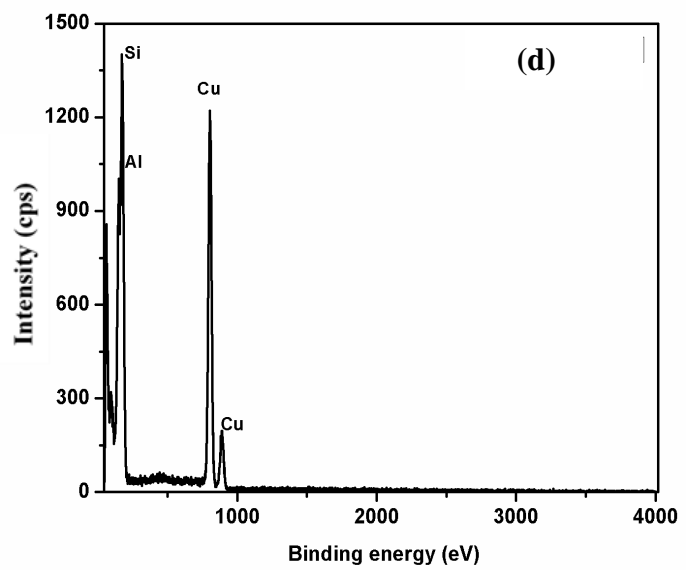
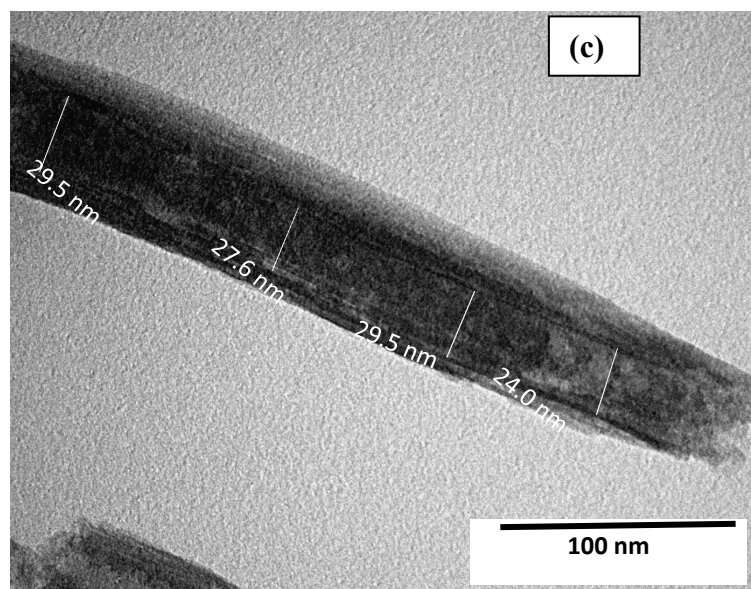


Fig. 6.3. Comparison of pore volumes for ARH, EH-1M, -2M and ELSH-1M, -2M.

6.3.4 TEM analysis

TEM analysis of HNTs was carried out for observing the change in the tube morphology and lumen diameter after etching and loading. In addition to these, loaded and stoppered HNTs without etching (labeled as LSH) were also analyzed along with ARH, for comparison. TEM images and EDS spectrum of ARH, EH-1M and ELSH-1M are shown in Fig. 6.4. The average lumen diameter was ranging from 12-18 nm for ARH as given Fig. 6.4 (a). The EDS spectrum, as given in Fig. 6.4 (b), has shown the presence of Al and Si, indicating HNTs is aluminosilicate, and the presence of Cu was from Cu grid used for sample preparation. The lumen diameter for EH-1M was in the range from 24.0-29.5 nm (Fig. 6.4 (c)). The inner diameter of ELSH-1M was found to be in the range of 19.1-23.0 nm as given in Fig. 6.4 (e). The EDS mapping as given in Fig. 6.4 (f) has shown the presence of Zr along with Al and Si, confirming the HNTs to be loaded with corrosion inhibitors. The presence of Ce was not identified by EDS mapping as the amount was lower than the detectable limit, hence EELS (electron energy loss spectroscopy) analysis was carried out and is depicted in Fig. 6.4 (g). Presence of two M₅ and M₄ edges at 880 and 900 eV were seen in Fig. 6.4 (g). The M-edge region of EELS spectrum gives the information of about initial state 4f level occupancy in rare-earth elements and thus reveals the valency state of it. The edge lines appear due to the spin-orbit splitting. The relative intensities of these lines were associated with the 4f-shell occupancy [18]. Presence of two M₅ and M₄ edges at 880 and 900 eV with M₅ being sharper than M₄ edge, were seen in Fig. 6.4 (g) and which are corresponding to the presence of Ce³⁺ valency. The % increase in the lumen diameter after etching for EH-1M was ~45.7 %, which is in accordance with the increase in pore volume i.e., 42.9 % obtained from BET results.





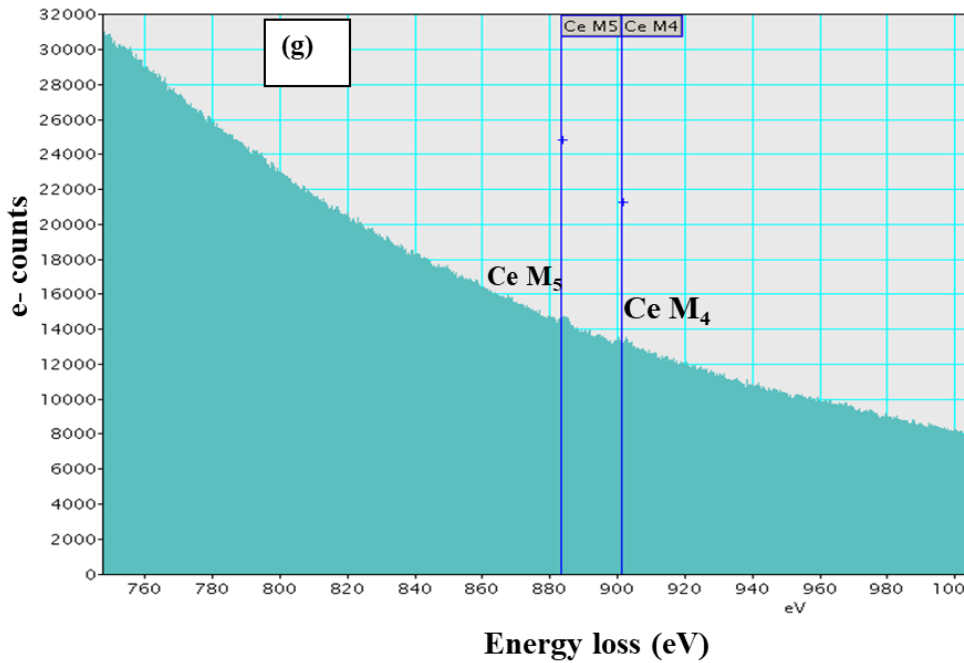


Fig. 6.4. (a, c, e) TEM images and (b, d, f) EDS spectra of (a, b) ARH, (c, d) EH-1M and (e, f) ELSH-1M, and (g) EELS of ELSH-1M.

TEM images of EH-2M and ELSH-2M along with LSH are depicted Fig. 6.5. The lumen diameter for EH-2M was increased to 29-32 nm from 12-18 nm when compared to ARH. Moreover, it can be observed from Fig. 6.5 (a, b) that the tube walls of HNTs have got partially destroyed and showing presence of some material inside the tubes. However, the inner diameter of tubes for ELSH-2M was found to be in the range of 12.8-15.2 nm as given in Fig. 6.5 (c, d), which is less than that of ELSH-1M (19.1-23.0 nm). The % decrease in the diameter of ELSH-1M and -2M compared to EH-1M and EH-2M are 21.4 % and 44.1 %, respectively.

FT-IR analysis in section 6.3.1 showed that there is formation of SiO_2 particles, and from XRD analysis in section 6.3.2 partial loss of tube crystallinity for EH-2M can be seen. These results are in support with inferences from TEM data. Hence, it is clear from the aforementioned that the tube walls were destroyed with 2 M sulphuric acid etching and that the amorphous silica particles remained inside the tubes. This could be the reason for increase in the lumen diameter for EH-2M when compared to EH-1M and further for decrease in lumen diameter and pore volumes (from BET analysis as mentioned in 6.3.3) for ELSH-2M when compared to ELSH-1M. The nanotubes appeared as diffused tubes and the inhibitor materials got adsorbed all over the surface as seen from Fig. 6.5 (c) for ELSH-2M. Thus,

there is a large decrease in the BET surface area (section 6.3.3) of ELSH-2M than ELSH-1M.

The lumen diameter for LSH got decreased from 12-18 nm (ARH) to 9-11 nm as shown in Fig. 6.5 (e), which is less than both ELSH-1M and ELSH-2M. The % decrease in lumen diameter for LSH is 27.6 %.

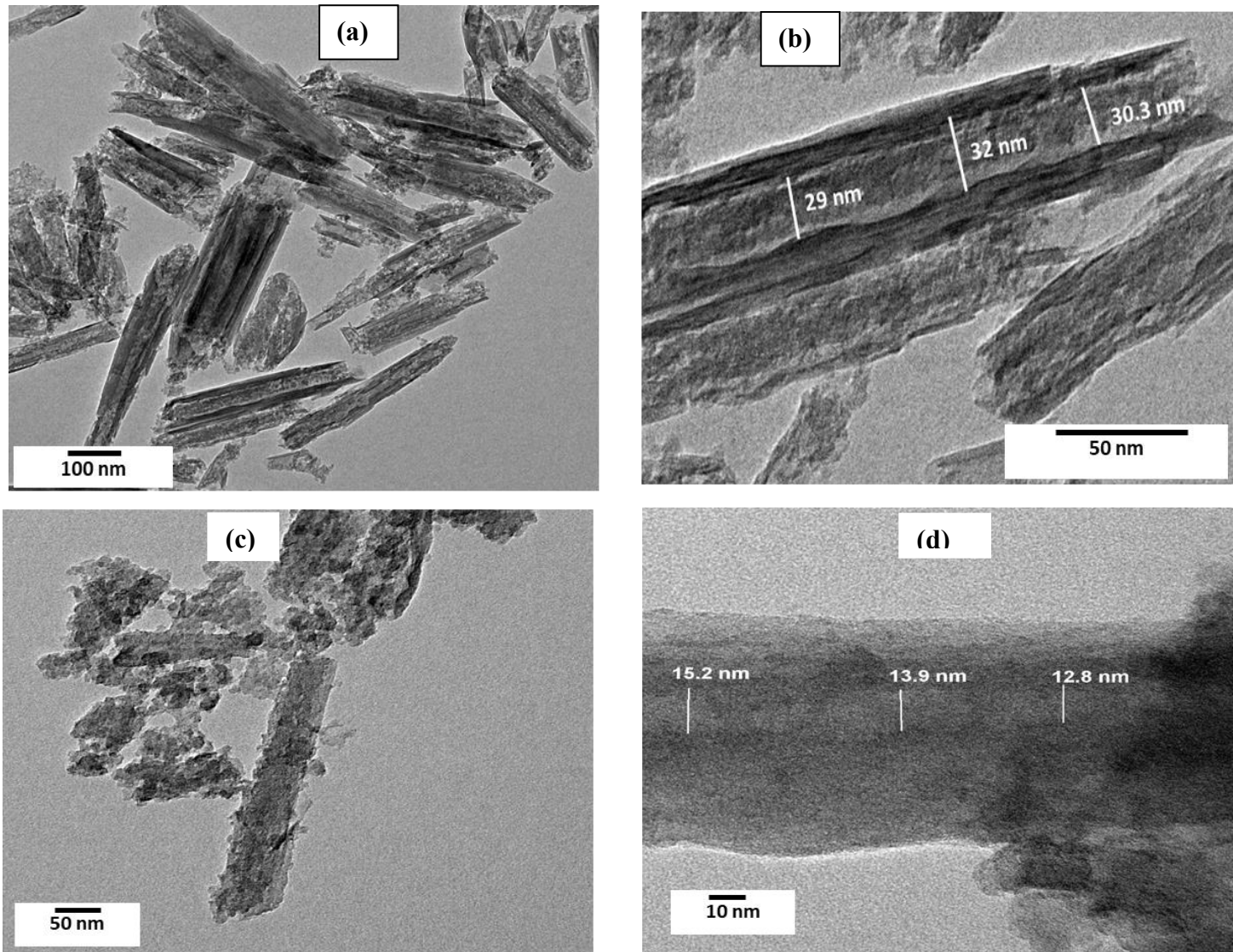


Fig. 6.5 TEM images of (a) and (b) EH-2M, (c) and (d) ELSH-2M and (e) and (f) LSH.

After the detailed characterization of etched and etched, loaded and stoppered HNT powders, the corrosion protection behavior of the coatings developed from inhibitor loaded etched HNTs on AA2024-T4 were studied.

6.3.5 Electrochemical impedance spectroscopy (EIS) and potentiodynamic polarization studies

EIS and potentiodynamic polarization studies have been carried out for ELSH-1M and ELSH -2M coated substrates for 1, 72, 120, 168 and 216 h of exposure to 3.5 wt % NaCl solution. The results were compared with that of LSH and uncoated substrates. Equivalent electrical circuit used for fitting the impedance data is shown in Fig. 6.6. Nyquist plots of coated and uncoated AA2024-T4 substrates are given in Fig. 6.7, and EIS fit data are presented in Table 6.2. All the coated substrates exhibited higher impedance values than uncoated substrates at all durations of exposure. The R_{ct} values of the coated and uncoated AA2024-T4 substrates were plotted against the duration of exposure to 3.5 wt% NaCl in Fig. 6.8. ELSH-1M coated substrates have shown the highest R_{ct} initially at 1 h and after 120 h than all coated and uncoated substrates. On prolonging the duration of exposure to 168 h, R_{ct} decreased to $350.6 \text{ k}\Omega \cdot \text{cm}^2$ and further decreased to $36 \text{ k}\Omega \cdot \text{cm}^2$ after 216 h. The impedance values of ELSH-2M were found to be lower than ELSH-1M coated substrates, indicating that these coatings provide less protection than ELSH-1M. This could be attributed to the destroyed tube structure and to the presence of SiO_2 particles inside the lumen, because of which the inhibitors got adsorbed more on the surface of the tubes rather than getting loaded inside the lumen.

However, the R_{ct} values of LSH have steadily increased from 72 h to 120 h, after which it got decreased slightly to $441 \text{ k}\Omega \cdot \text{cm}^2$ at 168 h from $655 \text{ k}\Omega \cdot \text{cm}^2$ at 120 h. After 168 h, the R_{ct} of LSH remained highest among all substrates and thereby providing prolonged corrosion protection.

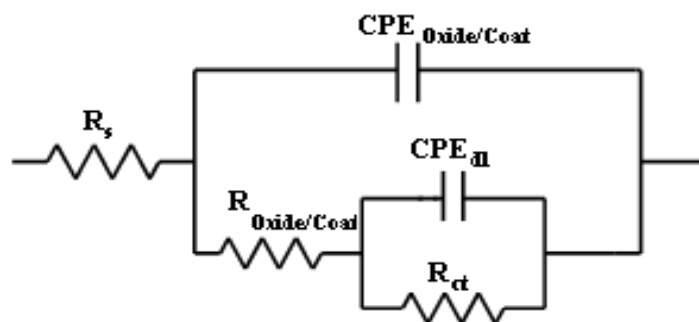


Fig. 6.6. Equivalent electrical circuit used for fitting the EIS data.

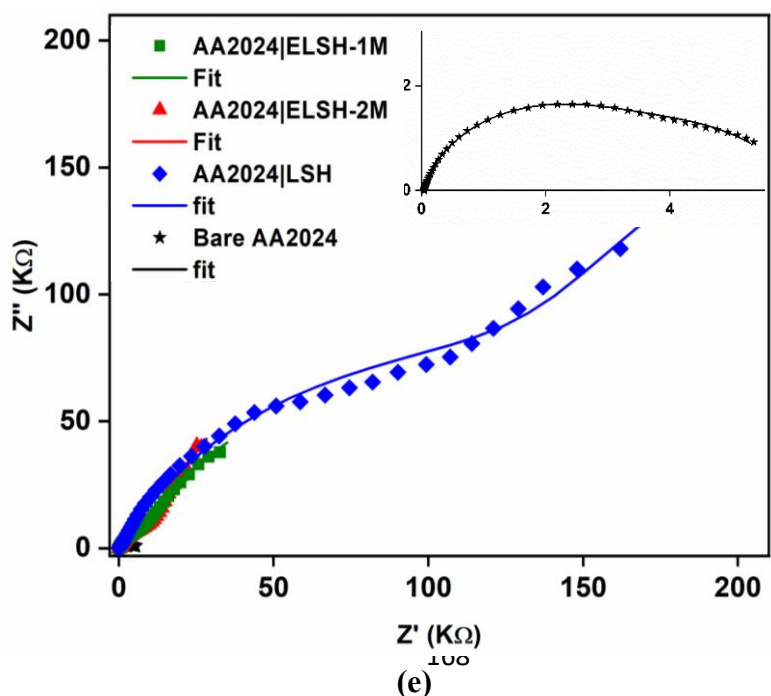
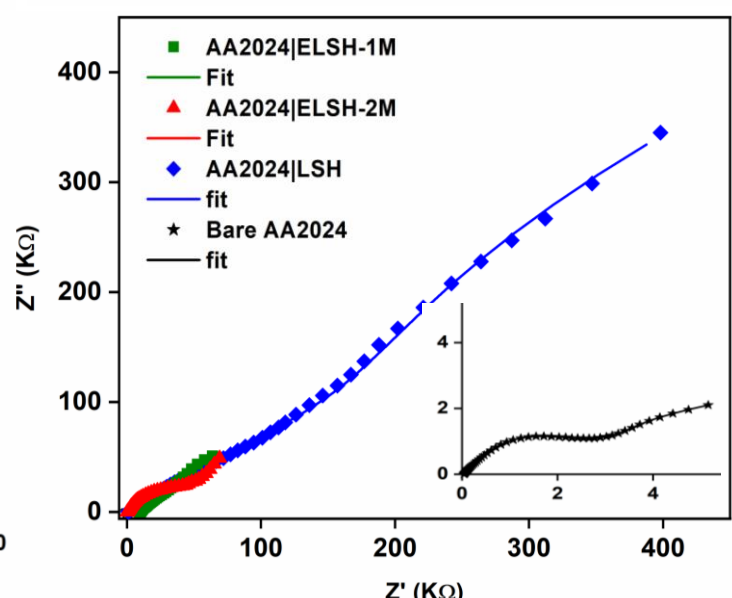
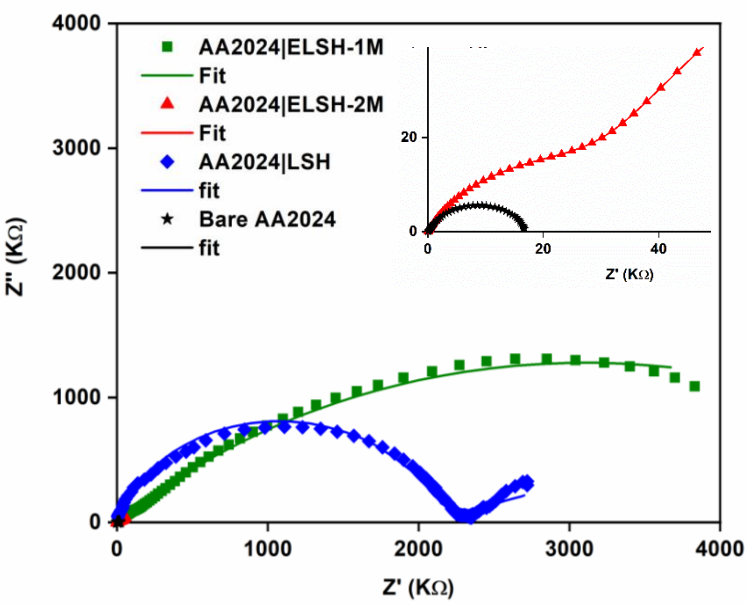
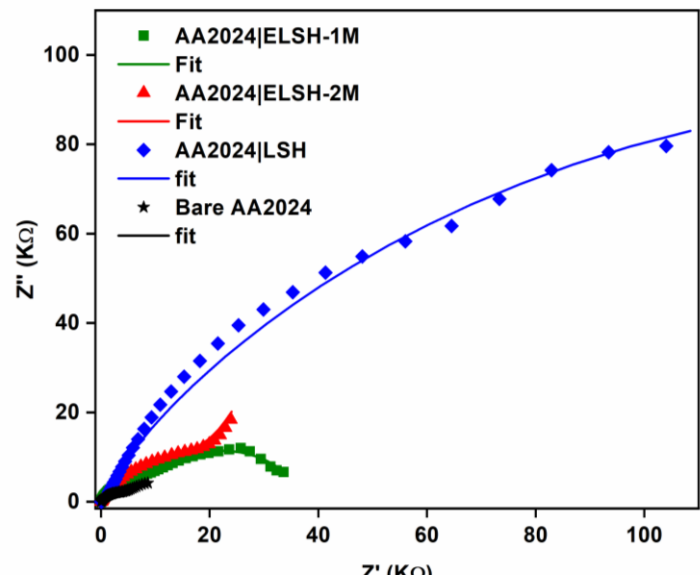
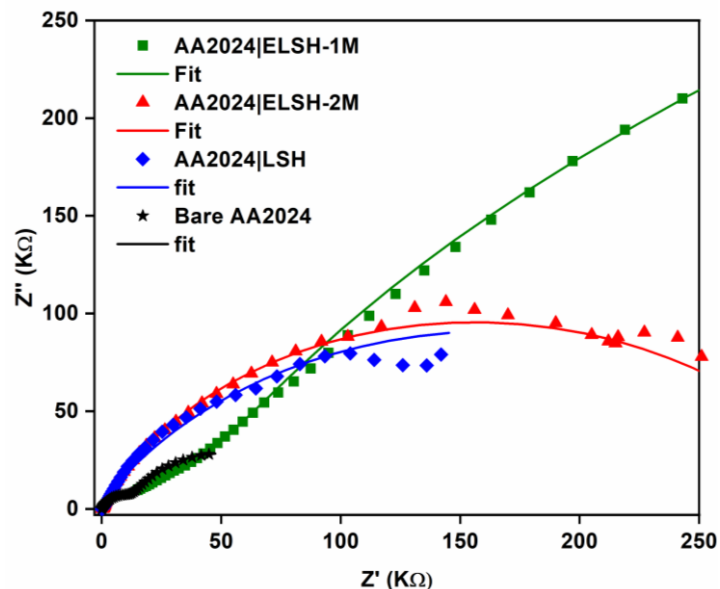


Fig. 6.7. Nyquist plots of coated and uncoated AA2024-T4 substrates after (a) 1 h, (b) 72 h, (c) 120 h, (d) 168 h and (e) 216 h of exposure to 3.5 wt % NaCl.

Table. 6.2. EIS fit data for coated and uncoated AA2024-T4 substrates at various durations of exposure to corrosive medium.

Sample	Duration of exposure to 3.5 wt% NaCl	$R_{oxide/Coat}$ K Ω .cm 2	R_{ct} K Ω .cm 2	$C_{oxide/Coat}$ μ F/cm 2	C_{dl} μ F/cm 2	CHI square error
Bare	1 h	6.04	36.7	12.6	409.0	0.35×10^{-3}
ELSH-2M		6.89	323.0	0.096	0.014	2.56×10^{-3}
ELSH-1M		0.16	1800	0.0014	0.0013	1.87×10^{-3}
LSH		1.64	340	0.47	1.10	6.92×10^{-3}
Bare	72 h	5.34	17.9	49.6	932.0	3.64×10^{-3}
ELSH-2M		2.68	18.30	17.1	11000	1.74×10^{-3}
ELSH-1M		12.90	24.40	15.7	154.0	0.56×10^{-3}
LSH		5.75	234.0	1.03	1.15	1.57×10^{-3}
Bare	120 h	1.36	15.8	6.34	3.80	0.21×10^{-3}
ELSH-2M		43.4	209.0	26.9	371.0	0.78×10^{-3}
ELSH-1M		619.0	3520	0.0051	13.90	4.40×10^{-3}
LSH		2.25	655.0	0.72	0.45	4.59×10^{-3}
Bare	168 h	3.72	3.35	117.0	4100	0.49×10^{-3}
ELSH-2M		33.48	232.70	66.94	114.3	1.84×10^{-3}
ELSH-1M		37.7	350.6	37.06	293.2	0.67×10^{-3}
LSH		783.0	441.0	33.1	6.23	1.43×10^{-3}
Bare	216 h	5.34	17.9	49.6	932.0	3.64×10^{-3}
ELSH-2M		74.0	146.9	20.38	276.0	2.82×10^{-3}
ELSH-1M		138.90	36.56	102.2	142.5	3.24×10^{-3}
LSH		225.3	372.3	16.87	111.6	4.74×10^{-3}

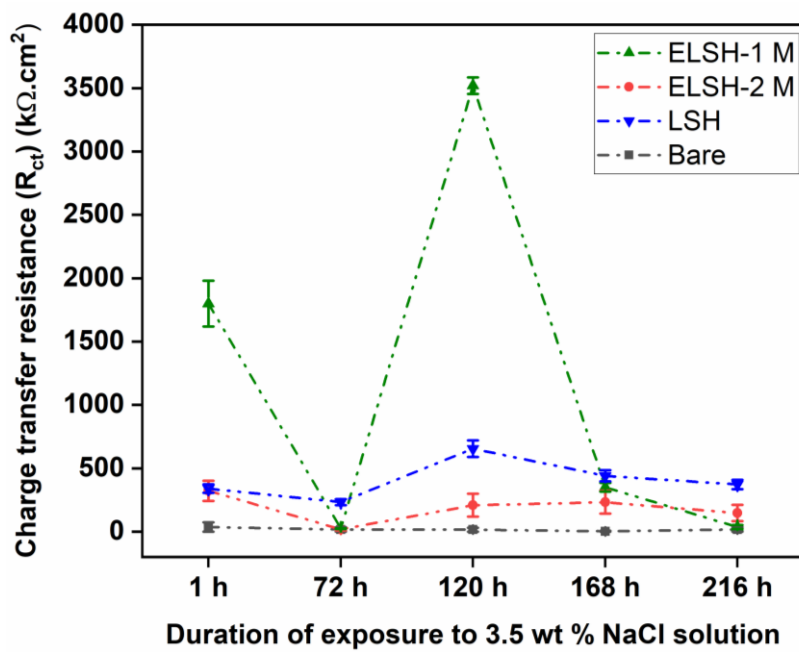
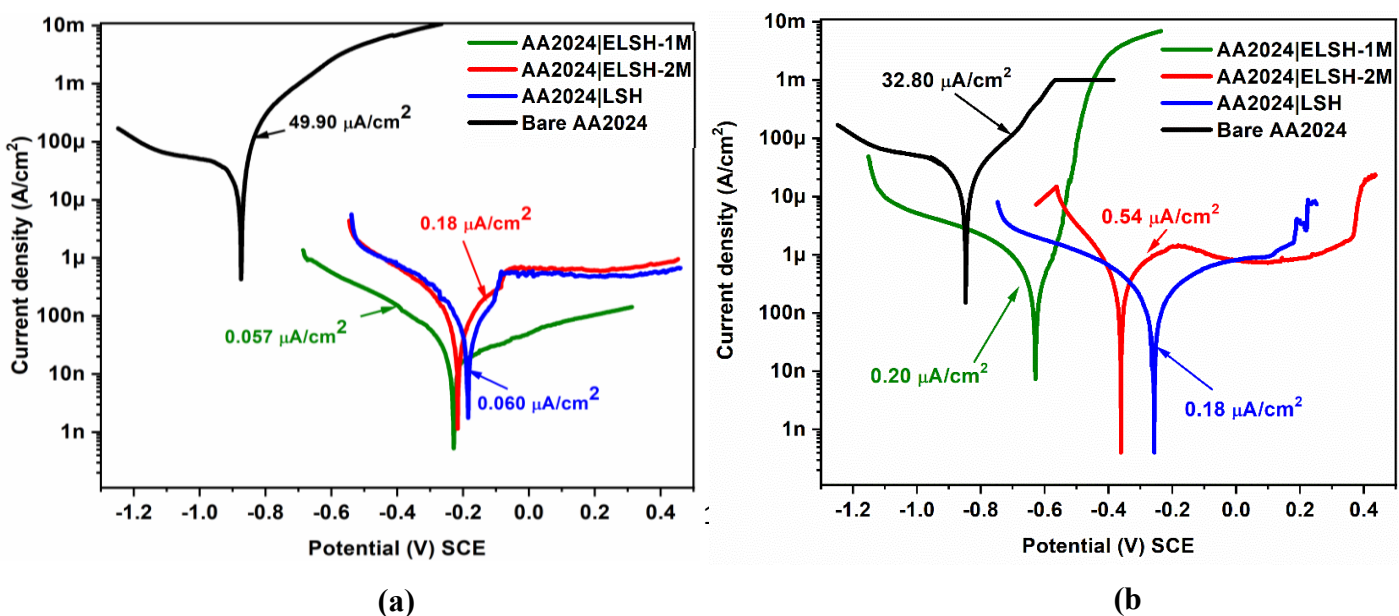


Fig. 6.8. Comparison of charge transfer resistance of different coatings at various durations of exposure to corrosive medium (Note: The lines connecting the data points are just guidelines for the eye).

Potentiodynamic polarization results as given in Fig. 6.9 and Table 6.3 indicated that ELSH-1M coated substrates have shown low i_{corr} values compared to LSH and ELSH-2M after 1 and 120 h of exposures. These results were in accordance with EIS results. However, ELSH-2M were found to have higher corrosion currents than LSH and ELSH-1M at all durations of exposure. i_{corr} of ELSH-1M though were near to that of LSH till 120 h, upon prolonging the duration of exposure to 168 h and 216 h, LSH only exhibited the least corrosion currents, in concurrence with the observed highest R_{ct} values of LSH compared to all substrates at the durations of 168 and 216 h exposure. Moreover, the corrosion potential (E_{corr}) values for LSH were more positive than all other coatings at all durations.



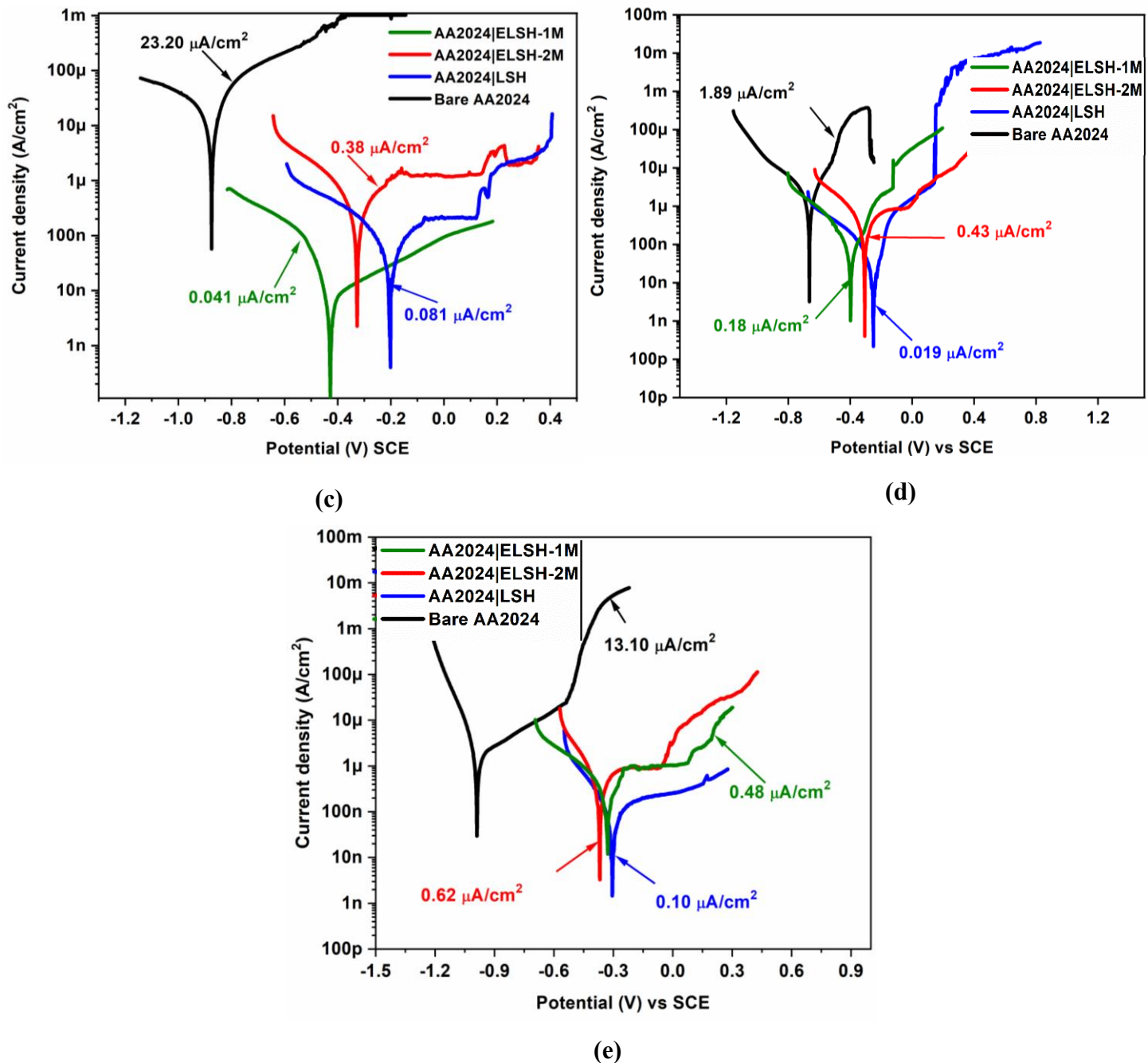


Fig. 6.9. Polarization curves for ELSH-1M and 2M, LSH and uncoated substrates after (a) 1 h, (b) 72 h, (c) 120 h, (d) 168 h and (e) 216 h of exposure.

Table 6.3. Polarization data of bare, ELSH-1M and 2M and LSH coated substrates at different exposure durations.

Sample	Time of immersion in 3.5 wt % NaCl	i_{corr} ($\mu\text{A}/\text{cm}^2$)	E_{corr} (V) vs SCE
Bare	1 h	0.49	-0.194
ELSH-1M		0.057	-0.229
ELSH-2M		0.18	-0.217
LSH		0.060	-0.185
Bare	72 h	32.8	-0.847
ELSH-1M		0.20	-0.629
ELSH-2M		0.54	-0.361
LSH		0.188	-0.257
Bare	120 h	23.2	-0.875
ELSH-1M		0.014	-0.428
ELSH-2M		0.38	-0.327
LSH		0.081	-0.202
Bare	168 h	1.89	-0.664
ELSH-1M		0.18	-0.341
ELSH-2M		0.43	-0.306
LSH		0.019	-0.168
Bare	216 h	13.1	-0.746
ELSH-1M		0.48	-0.328
ELSH-2M		0.62	-0.368
LSH		0.10	-0.248

Hence, these observations indicate that, etching of HNTs does not exhibit significant improvement in the corrosion protection of AA2024-T4 when prolonged exposure to corrosion medium is considered. However, for short durations of exposure, the coatings based on 1M etched HNT exhibited the highest corrosion protection, indicating that the etching indeed helps in loading more corrosion inhibitor, and hence, releasing more. However, perhaps the inhibitor release in the case of etched HNTs is probably not taking place at a steady rate, so as to prolong the self-healing mechanism. Release rate studies as a function of pH may help in better understanding of the role of etching.

References

- [1] R.R. Price, B.P. Gaber, Y. Lvov, In-vitro release characteristics of tetracycline HC1, khellin and nicotinamide adenine dinucleotide from halloysite; a cylindrical mineral, *Journal of Microencapsulation*. 18 (2001) 713–722. doi:10.1080/02652040010019532.
- [2] E. Abdullayev, Y. Lvov, Halloysite clay nanotubes as a ceramic “skeleton” for functional biopolymer composites with sustained drug release, *Journal of Materials Chemistry B*. 1 (2013) 2894–2903. doi:10.1039/c3tb20059k.
- [3] Q. Wang, Y. Wang, Y. Zhao, B. Zhang, Y. Niu, X. Xiang, R. Chen, Fabricating roughened surfaces on halloysite nanotubes via alkali etching for deposition of high-efficiency Pt nanocatalysts, *CrystEngComm*. 17 (2015) 3110–3116. doi:10.1039/C5CE00189G.
- [4] C. Li, Y. Zhao, T. Zhu, Y. Li, J. Ruan, G. Li, Effective solvent-free oxidation of cyclohexene to allylic products with oxygen by mesoporous etched halloysite nanotube supported Co²⁺, *RSC Advances*. 8 (2018) 14870–14878. doi:10.1039/C7RA11245A.
- [5] Q. Wang, J. Zhang, A. Wang, Alkali activation of halloysite for adsorption and release of ofloxacin, *Applied Surface Science*. 287 (2013) 54–61. doi:10.1016/j.apsusc.2013.09.057.
- [6] D. Garcia-Garcia, J.M. Ferri, L. Ripoll, M. Hidalgo, J. Lopez-Martinez, R. Balart, Characterization of selectively etched halloysite nanotubes by acid treatment, *Applied Surface Science*. 422 (2017) 616–625. doi:10.1016/j.apsusc.2017.06.104.
- [7] A.B. Zhang, L. Pan, H.Y. Zhang, S.T. Liu, Y. Ye, M.S. Xia, X.G. Chen, Effects of acid treatment on the physico-chemical and pore characteristics of halloysite, *Colloids and Surfaces A: Physicochemical and Engineering Aspects*. 396 (2012) 182–188. doi:10.1016/j.colsurfa.2011.12.067.
- [8] E. Abdullayev, A. Joshi, W. Wei, Y. Zhao, Y. Lvov, Enlargement of Halloysite Clay Nanotube Lumen by Selective Etching of Aluminum Oxide, *ACS Nano*. 6 (2012) 7216–7226. doi:10.1021/nn302328x.
- [9] F. Moeinpour, F. Soofivand, F.S. Mohseni-Shahri, Controlled release of losartan from acid- and heat-treated halloysite nanotubes, *Medicinal Chemistry Research*. 28 (2019) 160–168. doi:10.1007/s00044-018-2273-y.
- [10] J.M. Falcón, T. Sawczen, I.V. Aoki, Dodecylamine-Loaded Halloysite Nanocontainers for Active Anticorrosion Coatings, *Frontiers in Materials*. 2 (2015) 1–13. doi:10.3389/fmats.2015.00069.

- [11] C. Duce, S. Vecchio Ciprioli, L. Ghezzi, V. Ierardi, M.R. Tinè, Thermal behavior study of pristine and modified halloysite nanotubes, *Journal of Thermal Analysis and Calorimetry*. 121 (2015) 1011–1019. doi:10.1007/s10973-015-4741-7.
- [12] R.D. White, D. V. Bavykin, F.C. Walsh, The stability of halloysite nanotubes in acidic and alkaline aqueous suspensions, *Nanotechnology*. 23 (2012). doi:10.1088/0957-4484/23/6/065705.
- [13] P. Yuan, P.D. Southon, Z. Liu, M.E.R. Green, J.M. Hook, S.J. Antill, C.J. Kepert, Functionalization of halloysite clay nanotubes by grafting with γ -aminopropyltriethoxysilane, *Journal of Physical Chemistry C*. 112 (2008) 15742–15751. doi:10.1021/jp805657t.
- [14] U. Vijayalakshmi, A. Balamurugan, S. Rajeswari, Synthesis and characterization of porous silica gels for biomedical applications, *Trends in Biomaterials and Artificial Organs*. 18 (2005) 101–105.
- [15] K. Tazaki, Microbial formation of a halloysite-like mineral, *Clays and Clay Minerals*. 53 (2005) 224–233. doi:10.1346/CCMN.2005.0530303.
- [16] A. Joshi, E. Abdullayev, A. Vasiliev, O. Volkova, Y. Lvov, Interfacial modification of clay nanotubes for the sustained release of corrosion inhibitors, *Langmuir*. 29 (2013) 7439–7448. doi:10.1021/la3044973.
- [17] S. Manasa, A. Jyothirmayi, T. Siva, S. Sathiyanarayanan, K. V. Gobi, R. Subasri, Effect of inhibitor loading into nanocontainer additives of self-healing corrosion protection coatings on aluminum alloy A356.0, *Journal of Alloys and Compounds*. 726 (2017) 969–977. doi:10.1016/j.jallcom.2017.08.037.
- [18] L. Wu, H.J. Wiesmann, A.R. Moodenbaugh, R.F. Klie, Y. Zhu, D.O. Welch, M. Suenaga, Oxidation state and lattice expansion of CeO_{2-x} nanoparticles as a function of particle size, *Physical Review B*. 69 (2004) 125415. doi:10.1103/PhysRevB.69.125415.

CHAPTER-7

Summary and Conclusions

CHAPTER-7

Summary and Conclusions

In the present research study, self-healing corrosion protection coatings have been developed using Ce^{3+} and Zr^{4+} as cationic corrosion inhibitors for loading into the two nanocontainers, such as a tubular nanocontainer, halloysite nanotubes and a layered nanoclay, montmorillonite clay. Inhibitor loaded nanocontainers individually and together as a composite were dispersed into an organic-inorganic sol-gel matrix. The prepared sols were deposited on two aluminum alloys AA2024-T4 and A356.0. We have developed four different coating systems using these cationic inhibitors loaded nanocontainers as given below in Table 7.1.

Table 7.1. Details of various coating systems developed on aluminum alloys.

S. No.	Coating system/configuration	Substrate
1.	Ce^{3+} and Zr^{4+} corrosion inhibitors loaded and stoppered halloysite nanotubes dispersed in sol-gel matrix-single layer	AA2024-T4 and A356.0
2.	Ce^{3+} and Zr^{4+} loaded montmorillonite clay dispersed in sol-gel matrix-single layer	AA2024-T4 and A356.0
3.	Bilayer and single layer composite coatings developed using inhibitor loaded halloysite and montmorillonite clay dispersed in sol-gel matrix	AA2024-T4
4.	Etching of halloysite nanotubes inner lumen and loading of corrosion inhibitors into etched HNTs and their dispersion into sol-gel matrix-single layer	AA2024-T4

Chapter-1 describes the introduction of aluminum alloys, the mechanism of their corrosion and various strategies employed for protection of metal/alloys from corrosion. Moreover, a detailed literature survey was carried out on different types of nanocontainers and corrosion inhibitors used for corrosion protection of various metal/alloys. The detailed

experimental procedure for all the coatings along with the characterization techniques used for analysis of inhibitor loaded nanoclay powders and coatings generated from them was mentioned in the chapter-2. The four coating systems mentioned above in Table 7.1 were investigated and results obtained are discussed in four chapters.

The inhibitor loaded halloysite nanoclays and montmorillonite nanoclays were individually dispersed in matrix sol and applied over a wrought alloy AA2024-T4 and a cast alloy A356.0. The corrosion protection performance of these coatings was studied in chapter-3 and chapter-4. A combination of inhibitor loaded halloysite and montmorillonite nanoclays to make a composite and bilayer coatings and their corrosion inhibition performance on AA2024-T4 was investigated in chapter-5. Modification of halloysite nanoclay's lumen in order to increase its diameter by selective etching the inner lumen, loading of corrosion inhibitors after etching was investigated. The corrosion behaviour of the coatings developed from the etched loaded HNTs deposited on AA2024-T4 was carried out in chapter-6.

The coatings developed from inhibitor loaded halloysite nanotubes (HNTs) on AA2024-T4 and A356.0 alloys were the first coating systems to be studied. The HNTs after loading with corrosion inhibitor were stoppered at ends by urea-formaldehyde microcapsules to prevent the leakage of loaded inhibitors. Loading of corrosion inhibitors into the lumen of halloysite nanotubes was confirmed by TEM, BET pore volume and XRD analyses. After the confirmation of loading of corrosion inhibitors into the lumen of HNTs, the loaded HNT powder was dispersed into sol-gel matrix and coated on AA2024-T4 and A356.0 substrates. The corrosion protection behaviour of these coatings was studied by electrochemical tests such as electrochemical impedance spectroscopy (EIS) and potentiodynamic polarization studies, weight loss analysis, salt spray test and salt immersion test. Scanning vibrating electrode technique (SVET), a localized electrochemical testing, was used for evaluating the self-healing ability of the coatings.

The pore volume of inhibitor loaded HNTs decreased drastically from 0.145 to 0.029 cm³/g after loading with the corrosion inhibitors. TEM analysis confirmed the decrease in lumen diameter after loading. XRD analysis indicated that, inhibitors have got loaded only into the lumen and have not got intercalated into interlayers of the tubes. Coatings developed from the inhibitor loaded HNTs when deposited on both the alloys showed very good adhesion strength and thickness of coatings ranged from 4-5 µm. From the EIS results, matrix coated substrates showed higher corrosion resistance at the initial duration of exposure to 3.5 wt % NaCl, indicating the good barrier property of sol-gel matrix. The coatings based on inhibitor loaded HNTs when deposited over AA2024-T4 and A356.0 alloys showed higher

charge transfer resistance and coating resistance when compared with that of coatings based on unloaded HNTs and matrix sol. The potentiodynamic polarization studies were performed to study the corrosion protection of coatings under applied voltage. Results of potentiodynamic polarization studies indicated that, the corrosion potential values shifted towards positive side for the coatings containing inhibitor loaded HNTs for AA2024-T4 alloy. This indicates the ennoblement of corrosion potentials. Least corrosion rate was observed in gravimetric weight loss analysis for the inhibitor loaded HNT-based coated substrates. Release of corrosion inhibitors from HNTs into the scratch area was confirmed by elemental mapping and EDS analysis in the scratch region after salt immersion test and salt spray test. SVET results showed suppression of anodic currents with increasing the exposure duration in case of inhibitor loaded HNT based coating in both the alloys, indicating the self-healing of the damage by formation of a passive layer. Moreover, the formation of passive layer by forming the oxides of cerium (CeO_2) and zirconium (ZrO_2) was confirmed by Micro-Raman spectroscopic analysis on pure Al and A356.0 alloys. The coated substrates after exposure to 3.5 wt% NaCl solution showed the presence of peaks corresponding to ceria and zirconia in the scribed area.

The second coating system was developed by using the layered clay i.e., montmorillonite clay (MMT) as the nanocontainer for loading the corrosion inhibitors. The loaded nanocontainers were dispersed into matrix sol and deposited over AA2024-T4 and A356.0 alloys. Here, loading of corrosion inhibitors into MMT clays was carried out by two methods, i) physical mixing of inhibitors into MMT (IMM) and ii) intercalation of inhibitors into interlayers of MMT (IEM). SEM and TEM along with EDS analyses of MMT powders showed that, IMM had more amount of Zr but the layered structure of clay nanoparticles is lost during the process. IEM showed an increase in Ce and Zr contents and the layered structure is retained. XRD analysis indicated that, broadening of peak at 2θ value 4.9° for IMM was due to the delamination of layered structure of some of MMTs, whereas IEM showed no broadening of the peak, indicating the retention of layered structure. BET analysis showed a drastic decrease in the pore volume for IMM, which could be attributed to the adsorption of corrosion inhibitors on the delaminated layers rather than intercalation into interlayer spaces. However, both these modified MMT based coatings exhibited good adhesion strength when coated on AA2024-T4.

It could be inferred from EIS results that, the coatings developed from IEM exhibited enhanced corrosion resistance even after prolonged durations of exposure to corrosive medium when deposited on AA2024-T4 alloy. Potentiodynamic polarization studies showed

that, IEM coated substrates exhibited lower corrosion currents when compared to IMM coated substrates. Moreover, the anodic curves for IEM coated substrates were having passive region till 120 h. Weight loss studies also showed that corrosion rate for IEM coated substrates was least among all coated substrates. Salt immersion test and salt spray tests showed that more amount of inhibitors have got released into the scratch region for IEM coated substrates. SVET analysis indicated that there is a fine suppression of anodic currents for IEM coated substrates with increasing immersion time to 3.5 wt % NaCl from 0 to 24 h, thereby confirming the self-healing of the damage in IEM coated substrates. In case of MMT based coatings on A356.0, IMM coated substrates exhibited enhanced corrosion protection than IEM coatings. This can be attributed to the nature of alloying element present in A356.0 which is Si, due to which A 356.0 is less prone to corrosion when compared to AA2024-T4 that contains Cu as the major alloying element. The IMM contained more amount of Zr adsorbed on the surfaces of montmorillonite clay than in IEM. Therefore, the adsorbed inhibitors from the partially delaminated MMT surfaces might have got released to form a passive layer on the damage and which was sufficient for providing the corrosion protection for this mild corrodible alloy A356.0. Weight loss studies also indicated that IMM coated substrates had least corrosion rate than IEM, in case of A356.0 substrates.

The third coating system investigated was a combination of inhibitor loaded HNT and MMT to make different configurations such as mixing of both loaded nanocontainers to prepare a composite single layer coating and bilayer deposition of each inhibitor loaded nanocontainers in different configurations such as H|M and M|H. The coating thickness of H|M coatings was 13.2 (± 0.5) μm and showed few blisters when observed through SEM. M|H coatings have shown thickness of 8.6 (± 0.2) μm and having a uniform distribution of nanocontainers in the matrix. However, the thickness of single layered composite M+H coating was 3.8 (± 0.1) μm . All the coatings have shown excellent adhesion strength when applied on AA2024-T4 alloy. Analysis of EIS results showed that, M|H bilayer configuration coated substrates exhibited higher charge transfer resistance than H|M and M+H coatings. On the other hand, H|M coated substrates found to show increased corrosion resistance than even single layer H and M coatings. The enhanced corrosion protection of M|H coatings over H|M coatings was found to be because of the inner M layer possessing good coating resistance and outer H layer having excellent charge transfer resistance. Release of inhibitors from both the nanocontainers to self-heal the damage was confirmed by elemental mapping of scribed region after immersion in corrosive medium for 5 days.

Fourth coating system was based on etched HNTs. Selective etching of the inner halloysite lumen was carried out using sulphuric acid in order to increase the lumen diameter. Here, two different concentrations of sulphuric acid 1 M and 2 M were investigated to study the effect of concentration of acid on the extent of etching. HNTs after etching were loaded with corrosion inhibitors and stoppered with urea-formaldehyde microcapsules. FT-IR spectroscopic analysis of etched HNT indicated that, for etched HNT with 1 M sulphuric acid (EH-1M), partial etching of inner lumen has occurred. Complete inner lumen etching was found to have taken place with 2 M H_2SO_4 and the presence of silica particles was observed for 2 M etched HNTs (EH-2M). BET analysis indicated that pore volume got reduced after etching, but this decrease in the pore volume from EH-1M to 2M was very less (~ 0.2 %). However, after loading the etched HNTs with corrosion inhibitors, the decrease in the surface area and pore volume for ELSH-2M was 23.86% and 12.28% which is higher than ELSH-1M (12.8% and 9.96%). XRD results showed that, etching and loading has occurred solely inside lumen without any intercalation of etching remnants and corrosion inhibitors into the interlayer spaces of rolled alumino silicate sheets. There was a partial loss of tube crystallinity for EH-2M and ELSH-2M. TEM analysis showed that lumen diameter increased after etching. HNTs of EH-2M appeared as partially destroyed outer walls with some particles inside the lumen. From all the analyses, it was concluded that etching with 2 M H_2SO_4 resulted in complete etching of nanotubes, destruction of outer tube walls and presence of silica particles inside the lumen. The coatings were developed using the sols based on ELSH-1M and ELSH-2M powders and applied over AA2024-T4 to study the corrosion protection behaviour.

EIS and potentiodynamic polarization results of ELSH-1M and ELSH-2M were studied and compared with that of unmodified HNT based coatings (LSH). ELSH-1M coated substrates exhibited superior corrosion resistance than ELSH-2M till the duration of 120 h exposure to 3.5 wt% NaCl. However, on prolonged durations of exposure to corrosive medium, LSH coated substrates found to have good corrosion resistance than ELSH-1M and ELSH-2M.

Conclusions

Sol-gel matrix was found to be a potential coating material that provided good barrier protection to AA2024-T4 and A356.0. The halloysite nanotubes and montmorillonite nanoclay served as good host nanocontainers for accommodating cationic corrosion

inhibitors. The smart coatings developed by using inhibitor loaded HNT and MMT provided prolonged corrosion protection by self-healing the damage.

1. HNT-based coating system

The corrosion inhibitors Ce^{3+} and Zr^{4+} were successfully loaded into the halloysite nanotubes, which was confirmed by TEM, BET pore volume and XRD analyses. The developed self-healing coatings exhibited enhanced corrosion resistance and least corrosion currents for both the alloys AA2024-T4 and A356.0. The coatings developed from unloaded HNT showed higher corrosion rate and least corrosion resistance when compared to the control coatings derived from only the sol-gel matrix. The mechanism of self-healing by the formation of passive layer on the damage site of the coatings was confirmed by micro-Raman analysis and EDS analysis.

2. MMT-based coating system

MMT based coatings showed good corrosion resistance when inhibitors were intercalated into MMT layers, whereas, inhibitors mixed MMT exhibited increased corrosion current and poor corrosion resistance in case of AA2024-T4 alloy. Coatings with unloaded MMT exhibited higher corrosion currents and poor corrosion resistance. IMM coated substrates have shown better corrosion protection than IEM, when deposited on A356.0 alloy.

3. Bilayer and composite coating system

Bilayer coatings with M|H configuration provided superior and prolonged resistance against corrosion due to the synergistic effect of two different nanocontainers. Composite coatings M+H resulted in the increased corrosion rate and decreased corrosion resistance on AA2024-T4 alloy. H|M coated substrates exhibited increased corrosion rate and poor corrosion protection than even single layer H and M coatings. The enhanced corrosion protection of M|H over H|M is due to the inner M layer possessing better coating resistance than outer H layer.

4. Etched HNT-based coating system

Etching of HNTs with 1 M and 2 M H_2SO_4 resulted in the increased lumen diameter, which got decreased after loading with corrosion inhibitors. Partial etching of alumina layer occurred for etching with 1 M H_2SO_4 , whereas complete etching of the inner lumen and remnants of etching remained inside the nanotubes by etching with 2 M H_2SO_4 . The coatings developed from ELSH-1M showed higher corrosion resistance than that of ELSH-2M. However, these both coatings exhibited higher corrosion currents than the coatings of control experiments without etching (LSH) at prolonged durations of exposure to corrosive medium.

Hence, the self-healing, sol-gel based coatings developed by using Ce^{3+} and Zr^{4+} loaded halloysite and montmorillonite nanoclays were environmental friendly chrome-free alternatives for providing very effective corrosion protection of aluminum alloys AA2024-T4 and A356.0 even for prolonged duration of exposure to corrosive medium.

Future scope of the work

- The developed self-healing coatings are promising to be used on aircraft structural parts made from AA2024-T4 alloy and automobile components made of A356.0 alloy.
- Studies on corrosion protection performance of these self-healing coatings can be extended to other highly corroding metals such as mild steel and carbon steel.

LIST OF PUBLICATIONS

Publications in Peer-Reviewed/Refereed International Journals

1. "Nanoclay based self-healing corrosion protection coatings on aluminum, A356.0 and AZ91 substrates", **S. Manasa**, A. Jyothirmayi, T. Siva, B. V. Sarada, M. Ramakrishna, S. Sathiyanarayanan, K. V. Gobi, R. Subasri, **Journal of Coatings Technology and Research**, **2017 14 (5) 1195-1208**.
2. "Effect of Inhibitor Loading into Nanocontainer Additives of Self-healing Corrosion Protection Coatings on Aluminum alloy A356.0", **S. Manasa**, A. Jyothirmayi, T. Siva, S. Sathiyanarayanan, K. V. Gobi, R. Subasri, **Journal of Alloys and Compounds**, **2017 726 969-977**.
3. "Montmorillonite Nanoclay-based Self-Healing Coatings on AA2024-T4", **S. Manasa**, T. Siva, S. Sathiyanarayanan, K. V. Gobi, R. Subasri, **Journal of Coatings Technology and Research**, **2018 15 (4) 721-735**.
4. "Smart Nanocontainers for Anticorrosion applications", R. Subasri, Swapnil H. Adsul, **S. Manasa**, a chapter in a book titled "**Smart Nanocontainers**" edited by "Phuong Nguyen-Tri, Trong-On Do, Tuan Anh Nguyen." **Elsevier 2020, 399-412. ISBN No. 9780128167700**.

National and International conferences attended

1. "Montmorillonite Nanoclay-Based, Self-Healing, Corrosion Protection Coatings on Aluminum Alloys A356.0 and AA2024-T4" **S. Manasa**, **K. V. Gobi**, **R. Subasri**, Poster presentation at **Frontiers in Chemical Sciences and Technologies (FCST)**, Organized by Department of chemistry, NIT, Warangal, Telangana, India, from 28-29th January 2016.
2. Attended **workshop on Advanced Coating Technology: Opportunity for Indian industries**, held at CSIR- IMMT, Bhubaneswar, India, from 25 -26th February, 2016.
3. "Nanoclay- Based Sol- Gel Coatings for Corrosion Protection of Aluminum Alloys" **S. Manasa**, **A. Jyothirmayi**, **K. V. Gobi**, **R. Subasri**, oral presentation in **CORCON-2016** organized by NACE International Gateway India, from 18-21st September-2016 at New Delhi, India.
4. "Smart Nanocontainer-Based Self-Healing Corrosion Protection coatings on AA2024-T4" **S. Manasa**, **K. V. Gobi**, **R. Subasri**, poster presentation at "**Second International Conference on**

Electrochemical Science and Technology (ICONEST)-2017, held at IISc, Bengaluru, India, from 10-12th August, 2017.

5. “Development of Self-Healing, Corrosion Protection coatings on AA2024-T4 by Electrophoretic Deposition”. **S. Manasa, K. V. Gobi, R. Subasri**, oral presentation in **National conference on Frontiers in Corrosion Control and Materials (FCCM) 2018**, held at NIT Warangal, Telangana, India, from 28th- 29th June, 2018.
6. “Synergistic Effect of Different Nanocontainers for Self-healing Corrosion Protection Coatings on AA2024-T4”. **S. Manasa, K. V. Gobi, R. Subasri**, oral presentation in **International Surfaces, Coatings and Interfaces Conference-2019 (SURFCOAT KOREA-2019)**, held at Songdo Convensia, Incheon, Korea from 27th-29th, March 2019.

Awards Received

1. **Received Runner up 1-Young Scientist Award in Chemistry** for the oral presentation on “Sol-Gel Derived, Smart, Self-Healing Coatings for Corrosion Protection of Aluminum Alloy A356.0.” **S. Manasa, K.V. Gobi, R. Subasri**, in **Dr. K. V. Rao Scientific awards for the year 2018**, held at Hyderabad, Telangana, India on April 14, 2018.
2. **Received third prize** for the oral presentation on “Development of Self-Healing, Corrosion Protection coatings on AA2024-T4 by Electrophoretic Deposition” **S. Manasa, K. V. Gobi, R. Subasri** in FCCM-2018.

BIO-DATA

Personal Information:

MANASA SAMAVEDAM



Senior Research Fellow (SRF), Centre for Sol-Gel Coatings, International Advanced Research Centre for Powder Metallurgy and New materials (ARCI), Balapur, Hyderabad, Telangana, India, 500005

+91-9014298831

manasasamavedam2@gmail.com,

Web link: <https://www.arci.res.in/centres-about-sol-gel-coatings>
https://www.researchgate.net/profile/Manasa_Samavedam

Gender: Female | **Date of Birth:** 22-01-1990 | **Nationality:** Indian
Languages known: Telugu, English, Tamil & Hindi

Education and Training:

July 2015 - Present:

Ph.D. thesis submitted

External research scholar from Department of Chemistry
 National Institute of Technology, Warangal.

Thesis Title: “Nanoclay Based, Self-healing Corrosion Protection Coatings on Aluminum Alloys AA2024-T4 and A356.0”

Course Work: As a part of PhD programme, a mandatory course work has been undergone on the following relevant subjects for one semester

1. Principles of corrosion and corrosion control
2. Advanced Analytical techniques
3. Surface Analytical Techniques
4. Advanced Electrochemical Methods
5. English for Scientific Communication

March 2014- January 2015

Graduate Trainee at Centre for Sol-Gel Coatings, ARCI, Hyderabad, Telangana, India.

July 2011- May 2013

Master of Science in Chemistry (organic chemistry)
 Nizam college, Hyderabad

Cumulative Grade Point Average (CGPA): **7.3 (First Division)**

July 2008- June 2011

Bachelor of science (Microbiology, Biotechnology, Chemistry)
Ideal Degree College for Women, Hyderabad. Telangana, India.
Percentage of marks: **75.6 % (First Division)**

July 2006- April 2011

Intermediate (Biology, Physics, Chemistry)
Ideal Junior College, Hyderabad. Telangana, India.
Percentage of marks: **84.3 % (First Division)**

June 2005 -March 2006

Secondary School Certificate (High School)
Divya Teja Public School, Mahaboobnagar.
Percentage of marks: **80.0 % (First Division)**

Achievements:

- **Received Runner up 1-Young Scientist Award in Chemistry** for the oral presentation entitled “**Sol-Gel Derived, Smart, Self-Healing Coatings for Corrosion Protection of Aluminum Alloy A356.0.**” authors: S. Manasa, K.V. Gobi, R. Subasri, in **Dr. K. V. Rao Scientific awards for the year 2018.**
- **Received third prize** for the oral presentation entitled “**Development of Self-Healing, Corrosion Protection coatings on AA2024-T4 by Electrophoretic Deposition**” authors: S. Manasa, K. V. Gobi, R. Subasri in **FCCM-2018 conference** at NIT W.
- **Received consolation prize** for the science for the talk entitled **Orange diaper-A happy diaper** in **National Science Day flash talk-2020** at ARCI, Hyderabad.
- Secured 133 rank in OU PGCET in 2011 for M. Sc admission.

Work Experience:

- Having Five years of research experience in the field of corrosion protection coatings, sol-gel synthesis and one-year experience in development solar control coatings.
- Good expertise in synthesis of various sols via sol-gel method.
- Well expertise in operating a wide variety of instruments for physicochemical characterizations.
- Familiar with XRD, BET, SEM, EDAX, TEM, Raman spectroscopy techniques and interpreting the data.

Hands on Experience:

- Electrochemical work station in operating electrochemical impedance spectroscopy and Potentiodynamic polarization studies.
- Dip coating and electrophoretic deposition.
- Different ovens and furnaces: Carbolite oven, muffle furnace, Nabertherm furnace, conveyor belt furnace Therelec furnace.
- Thickness measurement by Filmetrics, Positector.
- Scratch Test, Abrasion Test, Adhesion test, Water contact angle, Ellipsometer, UV-Vis-NIR spectrophotometer

Research Interest:

- Corrosion protection coatings, Self-healing, Sol-gel derived coatings.

Computer Skills:

- Zsimpwin and Thales softwares for fitting electrochemical impedance data
- TF Calc software for simulating multilayered stacks for solar control coatings
- End Note and Mendeley Reference Manager.
- Origin 8.0 and 9.0, Microsoft Office.
- For a broad range of data measurement, plotting, analyses and publication writings.